Imperial College of Science, Technology and Medicine
Department of Electrical and Electronic Engineering

On-CMOS Microelectrode Systems for Enhanced ISFET-Based Detection of DNA

Lewis Keeble

Submitted in part fulfilment of the requirements for the degree of
Doctor of Philosophy in Electrical and Electronic Engineering of Imperial College London
March 2023

Declaration of Originality

I hereby declare that this thesis and the work reported herein was composed by and originated entirely from me. Information derived from the published and unpublished work of others has been appropriately referenced. Any contribution made to this research by others is explicitly acknowledged in the text.

Copyright Declaration

The copyright of this thesis rests with the author. Unless otherwise indicated, its contents are licensed under a Creative Commons Attribution-NonCommercial 4.0 International Licence (CC BY-NC).

Under this licence, you may copy and redistribute the material in any medium or format. You may also create and distribute modified versions of the work. This is on the condition that: you credit the author and do not use it, or any derivative works, for a commercial purpose.

When reusing or sharing this work, ensure you make the licence terms clear to others by naming the licence and linking to the licence text. Where a work has been adapted, you should indicate that the work has been changed and describe those changes.

Please seek permission from the copyright holder for uses of this work that are not included in this licence or permitted under UK Copyright Law.

Le mieux est l'ennemi du bien.

To all those who have loved and supported me along the way.

Abstract

Ion-sensitive field-effect transistors (ISFETs) can detect DNA via pH changes during amplification reactions, creating a complementary metal-oxide-semiconductor (CMOS)-based diagnostic platform that is portable, accessible, and accurate. Incorporating on-chip microelectrode systems has the potential to improve the speed and functionality of the device.

Firstly, by moving DNA towards the ISFET sensing array prior to amplification using electrokinetics, a reduced time-to-positive (ttp) is expected due to localised pH production. To estimate this effect, proton diffusion was modelled as part of novel monte-carlo first-passage and finite-element simulations. The monte-carlo simulation predicted a $96\,s$ reduction in ttp with all DNA trapped at the sensing surface rather than randomly distributed throughout the reaction solution.

To realise these anticipated improvements, on-CMOS interdigitated electrodes were fabricated through photolithography. These electrodes demonstrated the first electrokinetic DNA trapping on active CMOS. However, DNA trapping in amplification reaction solutions was not observed due to its high conductivity. Further CMOS integration was attempted by designing electrodes in the top-metal of a microchip, an approach that, whilst unsuccessful, guided further work.

Another role that on-CMOS electrodes can perform is providing the reference potential required for ISFET operation. For the first time, bond-pads of a commercial CMOS process were used as a base on which a fully electroplated $Ag/AgCl$ quasi-reference electrode (QRE) was produced. This QRE demonstrated a drift rate of $0.3\,mV/hr$, which is comparable to literature values, and promises better integration and scalability of the manufacturing process.

Finally, the ability of electrode systems to carry out sample preparation inspired a conceptual electrokinetic lab-on-CMOS diagnostic device. A microchip-based system comprising an array of 3D carbon electrodes on bond-pads, combined ISFET and impedance sensing, and CMOS-based $Ag/AgCl$ QREs was devised. This was supported by the first demonstration of electrokinetic DNA trapping using gold-plated bond-pads, thus achieving full CMOS-integration of a DNA trapping system.

Acknowledgements

For as long as I have been doing my PhD I have always been immensely looking forward to writing my acknowledgements. It is such a joy to read through the acknowledgements section of theses from people in the group, or even those sourced randomly on the internet. I got the impression that it was a massively cathartic process - a period of reflection and thankfulness at the end of a long, arduous process. As such I have taken the time to come out to my favourite cafe in London, Curators Coffee in Leadenhall Market, on this my thesis deadline day, to dedicate time at the end of my PhD to express my gratitude to all the people who got me here. I intend to edit this section as little as possible, so that it may serve as a time-capsule of this moment.

To my family, I thank you for all of the support you have given me, during the PhD and in the 22 years prior. You provided the solid foundations upon which I have been able to live my life relatively stress-free and explore the world without fear.

My scientific mind is no doubt the doing of my dad, Andrew. He would infuriate me no end growing up by never telling me the answers to my homework when I asked, instead trying to guide me towards the answer. I did not have the necessary patience at the time, but looking back I can see that it was the right approach and will likely apply this to my own children. So dad, I thank you for persisting through a tirade of abuse hurled in your direction and nurturing my curiosity.

My mum, Sally, had a tough job trying to get me to apply myself through my school career and use this brain of mine. Thank you mum for encouraging me to be the best version of myself. I would hope that this thesis is evidence enough that you can rest assured that I will need no coaxing to apply myself from here on out. In the same breath, I must apologise to various teachers who copped flak from my mum due to my laziness and/or disinterest at school rather than any fault of their own.

My sister, Eleanor, is currently blazing a trail across various African governments and NGOs. Eleanor, I look up to you massively and thank you for looking out for me like any good big sis would. This naturally includes encouraging me to enjoy life and I treasure the many special experiences we have had together.

Turning my attention more towards my scientific pursuits, I must first start with my physics teacher, Mr. Jones, who taught me for 6 out of my 7 years during senior school. I still have such a romanticised memory - think a physics Dead Poets Society - of our A-level physics classes. These lessons, to this day, remain some of my most enjoyed scientific experiences. To Mr. Jones, I thank you for reinforcing my love of physics and you played no small part in my decision to study physics at university.

A mention must be given to the University of Manchester, which I feel so fortunate to have gone to: It truly was the right university for me. I had originally wanted to go to Imperial for undergrad, but got rejected (This thesis thus completes my redemption arc). I only applied to Manchester 30 minutes before the UCAS deadline whilst sat in the bath, off a recommendation from a friend. Few baths in history - bar Archimedes' maybe - have had such a ripple effect in time.

I never intended to pursue a PhD (I even first tried to get on the civil service fast track - failing at the personality questionnaire). It was only during my master's project with the Advanced Technology group at the University of Manchester that I discovered my passion for research. To Lucio, Mark, Dan, and the rest of the team who hosted me, I thank you for providing me with such an interesting project and encouraging my enthusiasm. I still look back at my master's project with such pride at what I achieved.

Having decided on doing a PhD, Pantelis' group was one that stood out instantly. I know one is told not to put all their eggs in one basket, but come the summer of 2018, my application to Imperial was all I could bring myself to care about. To my co-supervisor Pantelis, I thank you for seeing something in me and bringing me onto your team. Huge credit must go to you for the culture that you have built at CBiT, which is one of such friendliness and collaboration, but also one of success, and I am so glad that I have been able to be a part of it over these last four and a half years. You have always backed my ideas without question and that has been a massive factor in the enjoyment of my PhD.

To Jesus, my co-supervisor, it is a shame that I didn't advance as far into the biological applications of my work, but I'm sure we will get there, and I thank you for all the bio-related insight that you have been able to give me over the course of my PhD. The 2019 away-day is a particular highlight, when you came up to me in the evening and prophesised that I would be great in the bio-lab because I was able to cook such nice scotch eggs. Those black-pudding

scotch eggs remain one of the greatest achievements of my PhD.

Whilst not on my official list of supervisors, Nick was pivotal in bedding me into the group when I joined, and remains the first port of call when I have an issue or an idea. To Nick, I thank you for all the help you have given and time you have dedicated to me, without which this thesis would look remarkably different. I have also enjoyed the growth of our friendship, helped, as everything is in life, with cake.

There are many people from the group who have made major contributions to this thesis. To Kenny, I thank you for all your help with the experimental data for the simulations in Chapter 3. I am supremely impressed with your levels of organisation, epitomised when you told me the exact location, to the exact position in the drawer, of the YOYO dye that I hadn't touched for almost a year. You truly are so great.

The idea for the simulations in this thesis stem from a lovely tale of chance collaboration, when Ahmad and I realised over a conversation in the office that the LAMP model in Ahmad's thesis exactly fit my needs. I thank you Ahmad for all the help you gave me in implementing this, on top of all the fun we had together at the union.

Another stroke of good fortune for my PhD came from Daryl and his brilliant microchip, DAPPER. I came up with the idea for my plated bond-pad reference electrode without a platform to test it on, only to find out that Daryl had already foreseen this research avenue and had designed DAPPER accordingly. Without this serendipity, Chapter 5 would not be in my thesis. On a personal level, Daryl was an absolute beacon of light during my PhD and I know that he has had a huge hand in making the group what it is today. I don't think you could find two people with more opposite world-views than me and Daryl, but I always enjoyed our conversations and cherished all the heartfelt advice you have proffered over the years. Thank you for all of this Daryl.

For a long time, I consigned my idea for Chapter 5 to something that would have to wait until I had finished my PhD. In addition to Daryl's help, I must also thank Arthur for all his work on the ENIG plating process. The stars really did align with Arthur coming over from EPFL for his master's project, as he needed to ENIG-plate CMOS bond-pads for his work and I had a process and chemicals ready to go. I have such happy memories of our long sessions working in the cleanroom and on the SEM. We got on instantly, but it was only over time that we grew to

realise how similar not just our mindsets and personalities were, but also our life experiences. You came into my world at just the perfect time, and I am eternally grateful to the forces that made it happen. Arthur, thank you for being you.

Microfabrication forms a massive part of this thesis and it is the field that I have most enjoyed progressing in. This is entirely down to Flo and Kasia, my microfab gurus, who together provide the perfect blend of chaotic and rational energies - spend 5 minutes with either and I'm sure you will work out who those statements refer to. There is not much more to say than to thank you for all the guidance you have continually provided since I joined CBiT. You are both forces to be reckoned with and I doubt I will ever stop looking up to you.

The past year or two has witnessed a sea change in my life, but Tash, Kat, and Costanza have been absolute rocks throughout. It is hard to overemphasise just how important they have all become to me and many times I have looked forward to coming in to the office if only because I get to hang out with them. To Tash, Kat, and Costanza, I thank you for being such good friends to me and I want you to know that I am appreciative for all that you have done for me.

Many more people at CBiT, past and present, will have contributed to the both the work in and enjoyment of my PhD than I have time or space to mention here. Just know that, even if I have not named you, I could read a list of all the people at CBiT and think of a funny anecdote, a happy memory, or helpful advice that they have provided.

Outside of PhD world, I have many great friends who have helped me to get away from it all when I needed a breather. I want to give particular thanks to Joe, who has developed the ability to chill me out like no other. Our friendship, over 20 years strong, has made you like a brother to me and you must not underestimate the positive effect that you have had on my life. I also want to give thanks to Annie, who has been there for me during my hardest times and has always given me something to look forward to. To Annie, the love I have for you is immeasurable.

Now all that is left is to click submit on this thesis. To those reading, I hope that you enjoy it and appreciate, if nothing else, that it is written with sincere passion and enthusiasm for the science contained within.

Contents

1 Introduction **5**

1.1 Motivation 5

1.1.1 From Laboratory to the Point-of-Care: The Role of Rapid Molecular Diagnostics in Meeting Modern Healthcare Challenges 5

1.1.2 The Lab-on-Chip Revolution: CMOS-based ISFETs as a Portable DNA Detection Platform 7

1.2 Research Objectives 9

1.3 Thesis Organisation 10

1.3.1 Chapter 2: DNA, Amplification Reactions, and the ISFET Sensing Mechanism 11

1.3.2 Chapter 3: Spatio-Temporal Simulation of ISFET-based DNA Detection 11

1.3.3 Chapter 4: Electrokinetic Manipulation of DNA to Enhance ISFET-based Detection 11

1.3.4 Chapter 5: An Electroplated ***Ag/AgCl*** Reference Electrode based on CMOS Top-Metal 12

1.3.5 Chapter 6: Conceptualisation of an Electrokinetic Lab-on-CMOS Diagnostic Device 12

2 DNA, Amplification Reactions, and the ISFET Sensing Mechanism 17

2.1 DNA . . . 17

2.2 DNA Amplification Reactions . . . 17

2.2.1 Polymerase Chain Reaction . . . 19

2.2.2 Loop-Mediated Isothermal Amplification . . . 19

2.3 Ion-Sensitive Field-Effect Transistors . . . 20

2.3.1 The Insulator-Electrolyte Interface . . . 21

2.3.2 ISFET non-idealities . . . 24

2.4 Lab-on-Chip Implementation of ISFET-Based DNA Detection . . . 26

2.4.1 ISFET Array Design . . . 26

2.4.2 Lab-on-Chip System Design . . . 28

2.5 Summary . . . 29

3 Spatio-Temporal Simulation of ISFET-based DNA Detection 34

3.1 Introduction . . . 34

3.2 LAMP Model . . . 35

3.2.1 DNA Dynamics . . . 35

3.2.2 Proton Production . . . 37

3.3 Diffusion . . . 40

3.4 Approaches to Simulating ISFETs with Spatio-Temporal Dependency . . . 41

3.4.1 ISFET Simulations . . . 43

3.4.2 Other Electrochemical Simulations . . . 44

3.5 Monte-Carlo Implementation . . . 46

3.5.1 Random Walk Model 46

3.5.2 First-Passage Model 47

3.5.3 ISFET Output Voltage 49

3.5.4 Hardware 49

3.6 Finite-Element Implementation 49

3.6.1 Level-Set Method 50

3.6.2 Simulation Parameters 51

3.6.3 MATLAB Scripts 52

3.6.4 Surface Site Concentration: 1D Stationary Model 52

3.6.5 Hardware 52

3.7 Results 52

3.7.1 Parameter Estimation 53

3.7.2 Monte-Carlo First-Passage Model Validation 55

3.7.3 First-Passage and FEM Model Comparison 58

3.7.4 Variation of ISFET Signal with DNA Copy Number 64

3.7.5 Variation of ISFET Signal with DNA Trapping 66

3.8 Discussion 68

3.8.1 Assessment of Models 68

3.8.2 Discussion of Results 69

3.9 Future Vision: Towards Detection of Amplification ‘Hotspots’ on ISFET Arrays 70

3.10 Summary 71

4 Electrokinetic Manipulation of DNA to Enhance ISFET-based Detection 76

4.1 Introduction . . . 76

4.2 Electrokinetics . . . 77

4.2.1 Electrophoresis . . . 78

4.2.2 Dielectrophoresis . . . 78

4.2.3 Electro-osmosis . . . 81

4.2.4 Electrothermal . . . 81

4.3 Electrode Systems for Electrokinetic Manipulation of DNA . . . 82

4.3.1 Castellarnau *et al.* 2006: A Case study in ISFET-DEP Combination to Monitor Bacterial Digestion . . . 82

4.3.2 DEP Trapping Systems . . . 83

4.3.3 Other Electrokinetic Trapping Systems . . . 91

4.3.4 Challenges in ISFET-DEP Combination for DNA Detection . . . 92

4.3.5 Electrode System Design . . . 93

4.4 Photolithographically Fabricated On-CMOS Electrodes . . . 94

4.4.1 Design and Simulation . . . 94

4.4.2 Method and Materials . . . 96

4.4.3 Results . . . 100

4.4.4 Discussion . . . 106

4.5 Commercial CMOS Top-Metal Electrodes: The FRY Microchip . . . 107

4.5.1 Design and Simulation . . . 107

4.5.2 Methods and Materials . . . 110

4.5.3 Results . . . 112

4.5.4 Discussion . . . 114

4.6 Future Vision: An Electrokinetic System Utilising Bond-pads Towards a Lab-on-CMOS Diagnostic Device . . . 116

4.7 Summary . . . 117

5 An Electroplated *Ag/AgCl* Reference Electrode based on CMOS Top-Metal 124

5.1 Introduction . . . 124

5.2 Thin-film fabrication approaches for ***Ag/AgCl*** reference electrodes . . . 127

5.3 Materials and Methods . . . 129

5.3.1 CMOS Test Platform . . . 129

5.3.2 Fabrication Process . . . 130

5.3.3 Characterisation . . . 135

5.4 Results . . . 138

5.4.1 Fabricated Prototypes . . . 138

5.4.2 Electrochemical Performance . . . 141

5.5 Discussion . . . 145

5.6 Future Vision: Towards Multi-wafer Level, Electroless RE Fabrication for Wireless ISFET Arrays . . . 145

5.7 Summary . . . 146

6 Conceptualisation of an Electrokinetic Lab-on-CMOS Diagnostic Device 153

6.1 Electrokinetic Sample Preparation . . . 154

6.1.1 Cell Lysis . . . 154

6.1.2 Sample Purification . . . 154

6.1.3 DNA Concentration . . . 156
6.1.4 Sample Transport and Mixing . . . 157
6.2 Alternative Electrochemical Sensing Modalities . . . 158
6.3 On-CMOS 3D Carbon Electrodes . . . 159
6.4 BUFFY: An Electrokinetic Lab-on-CMOS Diagnostic Device . . . 160
6.5 DNA DEP Using ENIG-Plated Bond-pads . . . 164
6.6 Summary . . . 164

7 Conclusion **170**

7.1 Contributions . . . 170
7.2 Recommendations for Future Work . . . 172
7.2.1 Amplification Model and Hotspot Validation . . . 172
7.2.2 Electrokinetic DNA trapping in LAMP Solutions . . . 173
7.2.3 On-CMOS 3D Carbon Electrode Fabrication for Electrokinetics . . . 173
7.2.4 Standard CMOS-Compatible High-Voltage Electrokinetics . . . 173
7.2.5 Fabrication of Full Sample-to-Result Electrokinetic Lab-on-CMOS . . . 174

A Publications Arising from this Thesis **175**

B GitHub Repository **176**

C Supplementary Data for Section 3.7.2 **177**

D Supplementary Data for Section 4.4.3 **179**

E Supplementary Data for Section 5.4.1 **182**

List of Tables

2.1 A summary of the ISFET LoC platforms presented in the literature for DNA sequencing or detection. 27

3.1 A table containing studies where ISFET simulation was a major part of the work and considered the insulator-electrolyte interface as part of pH detection. 42

3.2 A table collating the parameters used within the FEM simulation. 51

3.3 A table of parameters used to build the reaction chamber and sensing array for the two simulated microchips.* Only the set of ISFETs within the reaction chamber are simulated. 53

3.4 A table containing 1D stationary simulation results for OH site concentrations for the initial and final pH values from the 1×10^3 DNA copy experiments in Malpartida Cardenas *et al.* 2019 [45]. 53

3.5 A table showing the fitting parameters, the mean and variance respectively, for the normal distributions displayed in the right of Figure 3.8a. 55

3.6 A table containing reduced-χ^2 values comparing first-passage and random walk simulation results for both reflecting and absorbing boundaries and at different heights from the sensing plane. 57

3.7 A table showing the fitting parameters, the mean and variance respectively, of the normal distributions displayed in the right of Figures 3.8b and 3.8c for reflecting and absorbing boundary conditions respectively. 57

3.8 A table showing the values, as simulated by the different models, of final, cumulative number of protons released, the total number of protons detected by all sensors, and the corresponding detection probability. 60

3.9 Fitting parameters of the form $y = mx + c$ for plots of ttp against log_{10}(DNA copy number), compared for experimental and simulated data. For experimental data, fluorescence is output from a thermal cycler, whereas for simulated data fluorescence is equated to the cumulative release of protons from clusters. In both experimental and simulated data, voltage refers to the mean threshold voltage change across the ISFET array. Experimental data is from Malpartida Cardenas *et al.* 2019 [45]. 65

3.10 A table containing the average simulated ttp and associated standard deviation for various trapping percentages of DNA. 67

4.1 A table comparing the electrokinetic effects and their relationship with different variables. * The case for DNA. 81

4.2 Electrode systems used for electrokinetic manipulation of DNA free in solution. Systems manipulating of DNA origami, DNA nanoparticles, or DNA bonded to microspheres, nanotubes, or surfaces have not been considered. Systems involving nanotweezers or nanopipettes have also been excluded. [1] Estimation based on deionised water. [2] Graphene. 90

4.3 A summary of FEM simulation estimates of electric field variables for the designed electrodes. 96

4.4 A table showing the conductivity of the solutions used for experiments. 106

4.5 A summary of electrode system FEM simulation results. 109

4.6 Summary of FRY microchip specifications 110

5.1 A table of thin-film $Ag/AgCl$ quasi-REs in the literature. These are papers where the fabrication of the RE is a focus of the study. S = Sputtering, Ev = Evaporation, El = Electroplating. 128

5.2 A table summarising parameters for CV experiments on the Au-coated slide, ENIG-coated pad, and $AgCl$-coated pad, averaged over all scan rates, for which parameter values are independent. 141

6.1 Table presenting concentration factors that have been either been quoted in the literature or can be discerned from graphs provided in the text. Both the voltage used and the time that the DEP field was applied to achieve it are shown for context. 156

List of Figures

1.1 Schematic outlining the processes behind a NAAT sample-to-result diagnostic device, illustrating the key concepts involved and how they interlink. 7

1.2 A schematic outlining the structure of the ISFET in unmodified CMOS technology and the process of DNA detection, including electrodes to move DNA close to the sensor surface with electric field interactions to achieve a signal boost. The graph shows the change in ISFET threshold voltage (**blue**) in response to DNA amplification and decreasing solution pH (**red**), and compares the expected signals of systems with (**solid blue line**) and without (**dashed blue line**) an electric field actuation system. Adapted from [29] and [35]. 9

1.3 A flowchart representing the organisation of this thesis. The links between chapters are illustrated by the red arrows. 13

2.1 An illustration of the structure of DNA, which contains the four nucleotide types. The three components of a nucleotide: a PO_4 group, a deoxyribose sugar, and a nitrogeneous base, are highlighted. Hydrogen bonds between bases are denoted by dashed red lines, and the 3' and 5' endings are labelled. Adapted from [2]. . . 18

2.2 Illustration of PCR for cyclic DNA amplification [3]. Taq is a thermostable DNA polymerase. 18

2.3 An illustration of CMOS implementations of a MOSFET (**left**) compared to an ISFET using an extended gate approach (**right**), with key concepts denoted. . . 20

2.4 An illustration of the various layers of an ISFET, including the electrolyte and RE. An equivalent circuit is provided, representing each layer with a circuit element. A representation of the electric potential moving through the system is contained in the bottom graph. From left to right, D and S are the source and drain respectively, C_{ox} is the capacitance across the gate oxide, $V_{G''}$ is the potential at the extended gate, C_P is the capacitance across the passivation layer, $V_{G'}$ is the potential at the insulator-electrolyte interface, C_{IHP} and C_{OHP} are the capacitance of the inner and outer Helmholtz plane respectively, C_{Dif} is the capacitance across the diffuse layer, and V_{ref} is the reference potential. . . . 23

2.5 ISFET-based LoC platforms for DNA-based applications with a chip microphotograph, cross-section diagram, front-end schematic and encapsulation picture [3]. **(a)** Ion Torrent system for DNA sequencing [29], **(b)** DNAe/Imperial College (IC) chip for multiple gene detection [32, 35], **(c)** High signal resolution IC chip integrating 4,368 sensors for DNA detection and temperature regulation [26] and **(d)** IC chip integrating 12,800 sensors for DNA detection [33]. 30

3.1 (**a**) A schematic of the experiment in Liu *et al.* 2014 and (**b**) a graph of progress of the reaction front along the microfluidic channel, measured using fluorescence microscopy, against time, showing the constant velocity of DNA LAMP reaction-diffusion [3]. 36

3.2 A schematic illustrating how protons are generated according to the LAMP model in [2]. 37

3.3 The PDF (**a**) and CDF (**b**) for the first-passage distribution of protons in water hitting the $z = 0$ plane, calculated for Δz values 0.25×, 0.5×, and 0.75× the solution height used in experiments of $2.5\,mm$. 41

3.4 (**a**) A representation of the FEM geometry used in Aoun *et al.* 2016 and (**b**) a graph of ISFET threshold voltage against time, with varying distances between the Pt electrode and the ISFET, d, for a $30\,s$ electrode polarisation time [27]. . . 43

3.5 (**a**) A schematic of the generator-collector ETOF system used in Slowinska *et al.* 2003 and (**b**) a graph of change in collector electrode potential against time, with varying distances between the generator and collector [38]. The inter-electrode distance, g, increases from lines A to D. The solid line shows the experimental data, whilst the theoretical model is denoted with open circles. 44

3.6 A graph of the time response of electrode current due to collision of molecular random walks with varying adsorption time, τ, from Krause *et al.* 2014 [41]. . . 45

3.7 An illustrative graph of the level-set phase field (ϕ, **red**) and delta function (δ, **blue**) against distance, showing the two phases for DNA and water and the transition region that defines the interface, with the thickness parameter, ϵ. . . . 50

3.8 A comparison of temporal (**left**) and spatial (**right**) results for protons absorbed at the $z = 0$ plane for the random walk (**dashed lines**) and first-passage (**solid lines**) simulations with no boundary conditions (**a**), reflecting boundary conditions (**b**), or absorbing boundary conditions (**c**). Where boundary conditions were applied, no ceiling was used so that the semi-infinite approximation held. 1×10^5 protons were released from $0.9\times$ the nominal chamber height of $2.5\,mm$ in all cases, and at $0.1\times$ and $0.5\times$ for the cases with boundary conditions. Boundary conditions were applied at x and y-coordinates of $2.2\,mm$ and $1.5\,mm$ respectively as well as at $x, y = 0$. Protons were released from the middle of these x and y dimensions. The lines in spatial graphs represent normal distributions fitted to histograms of the x-coordinate of protons absorbed at the $z = 0$ plane with 100 bins. 56

3.9 A comparison of temporal signals from random walk (**dashed lines**) and first-passage (**solid lines**) simulation of 1×10^5 protons released from $0.1\times$ (**red**), $0.5\times$ (**blue**), and $0.9\times$ (**green**) the chamber height of $2.5\,mm$. Reflecting boundary conditions were used on the side walls, with x and y chamber dimensions of $2.2\,mm$ and $1.5\,mm$. Protons were released from the middle of these x and y dimensions. Both reflecting (**dashed**) and absorbing (**dot-dashed**) boundary conditions were applied to the ceiling, in the positive z dimension. 59

3.10 A graph of normalised number of protons against time comparing the random walk (**blue**), first-passage (**red**), and FEM (**green**) simulated output of two amplifying DNA clusters. 60

3.11 Plots from the FEM benchmarking simulation for: (**a**) the level set interface ($\phi = 0.5$), showing the surface of the DNA cluster; (**b**) the change in proton concentration from initial value in a vertical plane bisecting the two DNA clusters; and (**c**) the change in surface concentration of SiO^- from the initial value on the bottom plane of the reaction chamber. The times from top to bottom are: $0\,s$, $20\,s$ (before cluster overlap), $30\,s$ (after cluster overlap), $100\,s$ (after the reaction has ended). Where only a single number exists on the scale, the variation is negligibly small. 61

3.12 (**a**) A graph of cumulative total cluster surface area against time as estimated by the first-passage and FEM models and (**b**) the standard deviation of the normalised signal over the sensing array for the FEM and first-passage simulations, plotted on a logarithmic y-axis. 62

3.13 Surface plots of sensor output over the course of the reaction as simulated by the (**left**) first-passage and (**right**) FEM models. The times sampled, running from top to bottom, are: $20\,s$, $40\,s$, $100\,s$. All output is normalised to the maximum final value. 63

3.14 (**a**) A graph of simulated threshold voltage change versus time curves for varying DNA copy number. The shaded regions indicate the standard deviation for each time point. (**b**) A graph of simulated ttp-log_{10}(DNA copy number) based on simulated fluorescence and ISFET threshold voltage. Linear fits were conducted for both sets of data points with fitting parameters and r^2 values provided in each case. 64

3.15 A graph of simulated threshold voltage against time with varying percentages of trapped DNA. 67

4.1 A diagram outlining the electrostatic interactions of DNA and surrounding counterions in (**a**) uniform and (**b**) non-uniform electric fields . F_- and F_+ are the electrostatic forces on negative and positive charges respectively, with F_{DEP} indicating the direction of the pDEP force in case (**b**). Adapted from [8]. 78

4.2 A graph plotting the CM function for DNA in deionised water (conductivity $2\,mSm^{-1}$) and 0.1× PBS ($160\,mSm^{-1}$) [13]. 80

4.3 A diagram illustrating ACEO for a pair of oppositely polarised electrodes. E_X and F_C denote the electric field tangential to the electrode and electrostatic force respectively. Ions move in the direction of F_C and drag the surrounding fluid, causing fluid flow as shown in the figure. Adapted from [14]. 80

4.4 (**a**) A graph of FEM simulated electric field strength for the 'U' and 'T' shaped electrode pair used in Castellarnau *et al.* 2006 with an ISFET sensor in the trough of the 'U' electrode [20]; (**b**) A graph of pH against time as sensed by the ISFET with (**red**) and without (**blue**) a DEP field applied to the electrodes, with a commercial pH meter (**grey**) used as a reference. Edited from [21]. . . . 82

4.5 A fluorescence microscope image of YOYO1-stained, 45 *kbp* λ-DNA during DEP trapping in Asbury *et al.* 2002 [5]. 84

4.6 (**a**) An optical microscope image of the sawtooth electrodes used in Dewarrat *et al.* 2002 and (**b**) a fluorescence microscope image of YOYO-dyed 48.5 *kbp* λ-phage DNA; (**c**) is a close-up image of (**b**) [28]. 84

4.7 A SEM image of the electrode array used in Velmanickam *et al.* 2018, showing the opposing thin rectangular and curved castellations used to maximise field gradients [31]. 85

4.8 Fluorescence microscope images from Bakewell et. al 1998 [34] showing avidin trapped under (**a**) pDEP and (**b**) nDEP between adjacent polynomial quadrupole electrodes. 87

4.9 A comparison of the DEP force direction for (**left**) quadropoles and (**right**) square-ring traps [8]. 87

4.10 Fluorescence microscope images from Krishnan *et al.* 2008 showing (**a**) nanoparticles trapped under nDEP at the centre of circular quadrupoles and (**b**) DNA trapped under pDEP at the edges of circular electrodes [35]. 87

4.11 A diagram showing the polarisation of the carbon pillar electrodes from Martinez-Duarte *et al.* 2013 and the simulated electric field strength gradients ($\nabla|E|^2$) they produce [37]. 89

4.12 The simulated electric field strength gradients produced in Tuukkanen *et al.* 2006 both with and without the carbon nanotube. The gap between the nanotube and the opposing electrode is $100\,nm$ and the white scale bars represent $50\,nm$ [38]. 89

4.13 (**a**) A schematic of the parallel plate set-up including graphene and an electrode used in Barik *et al.* 2017 and (**b**) the electric field strength gradients produced by the graphene sheet [39]. 89

4.14 Figures from Du *et al.* 2008 showing (**top**) the direction of vortices created via ACEO on the 'T'-shaped quadropoles and (**bottom**) the subsequent trapping of $T4$-DNA [51]. 91

4.15 A schematic detailing the design features of the (**top**) line and (**bottom**) one-sided sawtooth electrode arrays. Values are given in micrometres. ISFETs are represented by orange squares and electrode separations are provided for designs with one and two ISFETs between neighbouring electrodes. 95

4.16 A schematic illustrating the lift-off and etching approaches to producing patterned metal. 97

4.17 A schematic depicting the creation of photopatterns with different types of photoresists. 97

4.18 Fluorescence microscope image of line electrodes with a $4\,V$, $500\,Hz$ electric field applied, trapping $400\,pM$ YOYO-1-dyed λ-DNA. The images show the electrodes (**a**) before, (**b**) during, and (**c**) just after the electric field is applied. 101

4.19 Fluorescence microscope image of line electrodes with a $4\,V$, $10\,kHz$ electric field applied, trapping $400\,pM$ YOYO-1-dyed λ-DNA. 101

4.20 (**a**) Brightfield image of a gold electrode array on a TITAN microchip. (**b**) A plot of ISFET output voltage in mV for an array with surface electrodes. 103

4.21 Plots of average ISFET output voltage against time. (**a**) shows how ISFET output voltage changes with the application of a $500\,Hz$ voltage to the electrodes and then the addition of HCl to reduce the pH of the solution. (**b**) shows how varying frequency of the signal applied to the electrodes affects mean ISFET output. 103

4.22 Plots of ISFET output voltage in mV for an array with surface electrodes after DEP trapping, whilst (**a**) a $500\,Hz$ and (**b**) a $100\,kHz$ voltage is being applied to the electrodes. 104

4.23 A fluorescence microscope image of the photolithographic, on-chip line IDEs with a $2\,V$, $500\,Hz$ electric field applied, trapping $400\,pM$ YOYO-1-dyed λ-DNA. . . 104

4.24 Fluorescence microscope images of photolithographic one-sided sawtooth IDEs with a $2\,V$, $500\,Hz$ electric field applied, trapping YOYO-dyed λ-DNA. (**a**) shows trapping of $400\,pM$ DNA with (**b**) and (**c**) using $40\,pM$ DNA. (**c**) is a close-up of (**b**). 105

4.25 A graph containing fluorescence profiles of a control with (**blue**) no electric field applied and the photolithographic, on-chip (**red**) one-sided sawtooth and (**green**) line IDEs $3\,mins$ after the electric field has been applied. A $2\,V$, $500\,Hz$ voltage is used to trap $400\,pM$ λ-DNA stained with YOYO-1. The data is normalised to the background, which is taken as the first reading. 105

4.26 The Cadence layout of the FRY microchip, consisting of three 5×2 arrays of extended gate configuration ISFETs situated between IDEs, two of which contain wide and thin rectangular castellations. All dimensions are quoted in μm. The pad regions of the $800\,\mu m \times 400\,\mu m$ chip are omitted from this Figure. 108

4.27 A schematic showing the top level system architecture for the FRY microchip. . 108

4.28 Plots of electric field strength as simulated in COMSOL for the (**a**) line electrode, (**b**) wide rectangular castellated electrode, and (**c**) thin rectangular castellated electrode. A logarithmic scale is used and grey areas denote the electrodes. . . . 109

4.29 An annotated image of the motherboard and cartridge set-up used for testing FRY. A microphotograph of the fabricated microchip is provided in the bottom-right. 111

4.30 EDX signal intensity for (**red**) Al and (**blue**) O with increasing FIB milling depth. The lines get darker for increasing etch depth. The line marked with crosses denotes the etch depth chosen for electrodes that have a thin SiO_2 layer still covering them, which is $1\,\mu m$. 112

4.31 Scanning electron microscope images with EDX analysis overlaid, showing the exposure of Al top metal with FIB etching currents of (**a**) $10\,nA$ to $3\,\mu m$ depth and (**b**) $40\,nA$ to $1.5\,\mu m$ depth. 113

4.32 Characterisation of a FRY microchip. (**a**) shows a graph of source voltage against gate voltage, with a pH 7 buffer. (**b**) shows a graph of source voltage against time, exhibiting sensor drift that was fitted (**red**). The inset shows the drift corrected signal (**green**), with a pH change from 8.1 to 0.75. 114

4.33 Florescence microscopy of $40\,pM$, $45\,kbp$ λ-DNA with (**a**) exposed and (**b**) unexposed sets of electrodes on FRY. A $10\,V$ DC voltage was applied to an ITO-coated slide held just above the chip surface and the electrodes were held at ground. . . 115

4.34 Images of a FRY microchip with exposed top-metal, after a DEP trapping voltage has been applied and significant dissolution of the metal has occurred. (**a**) shows a microscope image of the electrodes and (**b**) a SEM image with EDX analysis overlaid, showing a lack of aluminium signal. 115

5.1 An illustration of a basic $Ag/AgCl$ glass RE, with the reference potential applied by the $Ag/AgCl$ electrode and established across the porous membrane due to ion exchange. 125

5.2 Micrograph of the $0.18\,\mu m$ TSMC microchip used as a test platform in this study. The pads for the ISE, WE, RE, and CE are highlighted. 130

5.3 SEM images of CMOS bond-pads after (**a**) first zincation for $150\,s$ with a $5\,s$ etch in both $NaOH$ and NHO_3 and (**b**) second zincation for $50\,s$ with a $5\,s$ etch in NHO_3. SEM images were obtained with a $10\,kV$ beam energy. 131

5.4 SEM images of Au coated microscope slides electroplated with Ag in a $1\,M$ NH_3 and $0.3\,M$ $AgNO_3$ bath and a (**a**) pulsed ($2\,s$ on, $20\,s$ off) or (**b,c**) constant $13\,mAcm^{-2}$ current applied. (**b**) and (**c**) show repeats of plating with a constant current, demonstrating the lower reliability of the process. SEM images were obtained with a $10\,kV$ beam energy. 133

5.5 A schematic showing the composition of the pad (**a**) before and (**b**) after post-processing, with the approximate thicknesses of the electroplated layers provided. 134

5.6 An illustrated example of a cyclic voltammetry curve, with the direction of the scan given by the arrows on the curve and the regions of (**blue**) oxidation and (**red**) reduction labelled. The peak cathodic and peak anodic currents, i_p^c and i_p^a respectively, are annotated, along with the current, i_λ, at the switching voltage, V_{switch}. 137

5.7 A microscope image of an ENIG-plated and an $AgCl$-plated pad. SEM close-up images of the surface topology were obtained with a beam energy of $10\,kV$. The white scale bars in the SEM images represent $2\,\mu m$. EDX spectra of the surfaces are provided, annotated with the elements corresponding to certain peaks. . . . 139

5.8 A graph of surface profiles of the DAPPER ISE, WE, RE, and CE. Profiles are shown for the (**green**) bare chip and the chip (**blue**) after ENIG plating of all electrodes and Ag plating of the RE only (**red**). 140

5.9 Scanning electron microscope images of an ENIG plated pad with a bonded wire, and after this wire has been pulled, causing bond failure. (**a**) shows successful wirebonding and (**b**) shows delamination of the underlying Al bondpad from the silicon and Al vias underneath after the wire has been pulled off. SEM images were obtained with a $10\,kV$ beam energy. White scale bars have been provided. 140

5.10 CV analysis for the (**a**) *Au*-coated slide, (**b**) ENIG-plated pad, and (**c**) *AgCl*-plated pad. (**left**) Graphs of five-point moving means of CV curves using a commercial $Ag/AgCl$ RE. A Pt mesh was used as a counter electrode and the solution is $0.1\,M\ KCl$, $0.1\,mM\ K_3FeCN_6$, and $1\,mM\ K_4FeCN_6$. 10 scan rates from $10-100\,mV/s$ were run. Increasing scan rate direction is shown by increasing opacity of the line and is annotated on the graphs, along with the direction of the scans. (**right**) Graphs of (**red**) absolute peak cathodic and (**blue**) anodic current against the square-root of scan rate. Linear fits are provided, along with their r^2 values. 142

5.11 Electrochemical characterisation of the plated $Ag/AgCl$ RE. (**a**) A graph of OCP versus time measured over an $18\,hr$ period. A linear fit is provided along with the drift rate. (**b**) A polarisation curve. Both are measured against a commercial $Ag/AgCl$ glass electrode in $100\,mM\ KCl$ solution. 143

5.12 CV curves for (**blue**) on-chip and (**red**) off-chip three-electrode systems. The on-chip system used ENIG-plated WE and CE pads and an $Ag/AgCl$-plated RE pad. The off-chip system used an ENIG-plated WE pad, a platinised titanium mesh CE, and a commercial glass RE. The test solution was $0.1\,M\ KCl$, $0.1\,mM\ K_3FeCN_6$, and $1\,mM\ K_4FeCN_6$. A scan rate of $25\,mV/s$ was used. 144

6.1 A series of diagrams detailing the process of DNA isolation from blood carried out in Sonnenberg *et al.* 2012 [14], using an array of circular electrodes to form quadrupoles. 155

6.2 Simulated electric field strength and ACEO fluid flow direction caused by asymmetric electrode pairs [28]. 157

6.3 A graphical summary of the combined ISFET-impedance pixel for DNA detection, with integrated DEP positioning, developed in Wang *et al.* 2021. 158

6.4 Examples of carbonised 2PP structures produced in Haque *et al.* 2020 [43]. . . . 159

6.5 A schematic illustrating the sample-to-result pipeline envisaged in BUFFY. . . . 160

6.6 A schematic illustrating the planned electrode polarisations and the electrokinetic effects for which they are used. 161

6.7 An illustration of the square pillar electrode design imagined for the BUFFY microchip. 162

6.8 A system-level illustration of the planned BUFFY chip. 163

6.9 Fluorescence microscope images of an ENIG-plated bond-pad before (**a**) and during (**b**) the application of a $2\,V$, $500\,Hz$ electric field, trapping $400\,pM$ YOYO-1-dyed $\lambda-$DNA. 164

C.1 A comparison of first passage simulations with absorbing (red) and reflecting (blue) boundary conditions with experimental results (green). 1×10^3 DNA copies were used. 178

D.1 Fluorescence microscope image of line electrodes with a 4V, 10kHz electric field applied, trapping 400pM YOYO-1-dyed $\lambda-$DNA. 180

D.2 Fluorescence microscope image of line electrodes with a 500Hz electric field applied, trapping 400pM YOYO-1-dyed $\lambda-$DNA and an applied voltage of $900mV_{pp}$ with a 900mV offset (varying from 0-1.8V). 180

D.3 Fluorescence microscope image of line electrodes with a 500Hz electric field applied, trapping 400pM YOYO-1-dyed $\lambda-$DNA and an applied voltage of $1.8V_{pp}$. 181

E.1 Microscope images of two tape tests with (a) before and (b) after. 182

E.2 Microscope images of ENIG plated pads with bonded wires, and after these wires have been pulled, causing bond failure. (b) shows the bond wire breaking after being pulled. (c) shows delamination between the bonded wire and the Au surface. 183

Abbreviations

AMR	Anti-microbial resistance
PCR	Polymerase chain reaction
PoC	Point-of-care
LFT	Lateral flow tests
LMIC	Lower and middle income countries
WHO	World Health Organisation
LoC	Lab-on-Chip
CMOS	Complementary metal-oxide-semiconductor
ELISA	enzyme-linked immunosorbent assay
LAMP	Loop-mediated isothermal amplification
NAAT	Nucleic acid amplification testing
EIS	Electrochemical impedance spectroscopy
LoD	Limit of detection
FET	Field-effect transistor
ISFET	Ion-sensitive field-effect transistor
RE	Reference electrode
QRE	Quasi-reference electrode
DNA	Deoxyribose nucleic acid
A	Adenine
G	Guanine
T	Thymine
C	Cytosine
ssDNA	Single-stranded DNA
$\boldsymbol{PO_4}$	Phosphate
$\boldsymbol{OH}$	Hydroxyl
dsDNA	Double-stranded DNA
dNTP	Nucelotide
RNA	Ribonucleic acid

MOSFET	Metal-oxide-semiconductor field-effect transistor
p-Si	p-type silicon
n-Si	N-type silicon
EDL	Electrical double layer
$\boldsymbol{SiO_2}$	Silicon dioxide
$\boldsymbol{Si_3N_4}$	Silicon nitride
$\boldsymbol{HfO_2}$	Hafnium dioxide
$\boldsymbol{O^-}$	Deprotonated hydroxyl
$\boldsymbol{OH_2^+}$	Protonated hydroxyl
$\boldsymbol{NH_2}$	Amine
$\boldsymbol{e}$	Electron charge
IHP	Inner Helmholtz plane
OHP	Outer Helmholtz plane
PDF	Probability density function
CDF	Cumulative density function
GCS	Guoy-Chapman-Stern
ttp	Time-to-positive
ADC	Analogue-to-digital converter
TIA	Trans-impedance amplifier
OTA	Operational trans-conductance amplifier
$\boldsymbol{Ag}$	Silver
HMDS	Hexamethyldisilazane
FEM	Finite-element method
CAD	Computer-aided design
ETOF	Electrochemical time-of-flight
bp	Base-pair
DEP	Dielectrophoresis
pDEP	Positive DEP
nDEP	Negative DEP
CM	Clausius-Mossotti
ACEO	AC electro-osmosis
IDE	Interdigitated electrode
$\boldsymbol{Au}$	Gold
$\boldsymbol{Al}$	Aluminium
$\boldsymbol{Pt}$	Platinum
TSMC	Taiwan Semiconductor Manufacturing Company
$\boldsymbol{O_2}$	Oxygen

Cr	Chromium
N_2	Nitrogen
Ar	Argon
DI	Deionised
KCl	Potassium chloride
HCl	Hydrochloric acid
$NaOH$	Sodium hydroxide
ITO	Indium tin oxide-coated
MCU	Microcontroller
SPI	Serial peripheral interface
SEM	Scanning electron microscope
EDX	Energy dispersive X-ray
FIB	Focussed ion beam
ENIG	Electroless nickel, immersion gold
Ti	Titanium
Al_2O_3	Aluminium oxide
Ni	Nickel
Zn	Zinc
Cu	Copper
Si	Silicon
PI	Polyimide
Pd	Palladium
PET	Polyethylene terephthalate
SAM	Self-assembled monolayer
PSA	Pressure-sensitive adhesive
PEN	Polyethylene naphthalate
PVB	Polyvinyl butyral
LCP	Liquid-crystal polymer
PA	Polyamide
Pb	Lead
PDMA	Polydimethylsiloxane
$NaClO$	Sodium Hypochlorite
$FeCl_3$	Iron (III) chloride
ISE	Ion-sensitive electrode
WE	Working electrode
CE	Counter electrode
ZnO	Zinc oxide

$\boldsymbol{HNO_3}$	Nitric acid
$\boldsymbol{H_2PO_2^-}$	Hypophosphite
$\boldsymbol{NH_4OH}$	Ammonium hydroxide
$\boldsymbol{AgNO_3}$	Silver nitrate
$\boldsymbol{Cl}$	Chlorine
OCP	Open circuit potential
CV	Cyclic voltammetry
2PP	Two-photon polymerisation
ESD	Electrostatic discharge

Chapter 1

Introduction

1.1 Motivation

1.1.1 From Laboratory to the Point-of-Care: The Role of Rapid Molecular Diagnostics in Meeting Modern Healthcare Challenges

"If health has stopped improving, society has stopped improving."

Professor Sir Michael Marmot
Director of UCL Institute of Health Equity

Accurate and quick diagnosis will always be pivotal in the effective management of infectious diseases. On the level of the individual, it allows early treatment and increases the chances of a positive outcome. However, on a nationwide level, diagnostic technology is the linchpin for health security in the face of two major health crises: pandemics and the rise of anti-microbial resistance (AMR).

With the rapid spread of a new or mutated disease that occurs during pandemics, a quick and flexible testing program is required to efficiently identify and isolate infected people to prevent them from further spreading the disease. The sensitivity (true positive rate) of the diagnostic technology needs to be high to avoid false negatives and prevent people with the disease not isolating. However, from an economic and mental health viewpoint, it is also important to avoid people isolating unnecessarily due to false positives, which requires high specificity (true negative rate). Quick turnaround times will also cut down on isolation whilst waiting for results and will likely improve community participation in testing due to the increased convenience [1].

One of the main sticking points for national-level testing programs is the logistics involved. The

current gold-standard of diagnostic testing using the molecular technique polymerase chain reaction (PCR) to replicate and detect fluorescence from infectious deoxyribose nucleic acid (DNA) takes around an hour to deliver results [2]. However, the transportation and processing of the sample means that results take multiple days to get back to people after the sample was taken.

As such, there is a clear motivation to move test processing out of laboratories and into the community, ideally to the point-of-care (PoC) - the person who requires testing - to shorten logistic chains. This can be achieved using lateral flow tests (LFTs), which can detect proteins (antigens or antibodies) in a sample deposited on a strip of paper in under $10\,mins$. Whilst undoubtedly offering quick and convenient testing, there is a trade-off for test accuracy, with LFTs showing a broad spread of sensitivities between $43-99\,\%$ and specificities between $93-100\,\%$ [3], whereas PCR can achieve between $70-98\,\%$ sensitivity and $95-100\,\%$ specificity [4] [5]. For effective control of the spread of diseases, the sensitivity and specificity of diagnostic testing should both be over 85% [6].

The ideal scenario would involve the more accurate molecular diagnostic techniques being available as part of a more convenient PoC device. This would also provide a key advantage in tackling AMR, as molecular techniques have the ability to identify resistant strains of diseases. By arming clinicians with more accurate and informative diagnostic data, without long turnaround times, incorrect usage of antimicrobials can be curbed and AMR slowed and reduced [7].

> “Rapid diagnostics are the single biggest potential game-changer in the fight against anti-microbial resistance.”
>
> Lord Jim O’Neill
> Chair of Wellcome Trust’s AMR Review

But in an increasingly globalised world, the threat posed by pandemics and AMR can only be diminished with a co-ordinated worldwide approach to testing. It is not sufficient for more affluent countries to simply eradicate diseases within their own borders, whilst leaving less affluent countries unsupported and allowing pathogens to proliferate, mutate, and develop resistance. As such, it is important that portable molecular diagnostic devices are developed with the aim of being accessible to healthcare systems in lower and middle income countries (LMIC). Devices should adhere to the World Health Organisation’s (WHO) ASSURED criteria: Affordable, sensitive, specific, user-friendly, rapid and robust, equipment-free, and deliverable to end-users [8]. These criteria help a diagnostic device overcome infrastructure and resource limitations that affect supplies, from electricity to consumables, as well as access to trained clinicians and laboratory equipment [6].

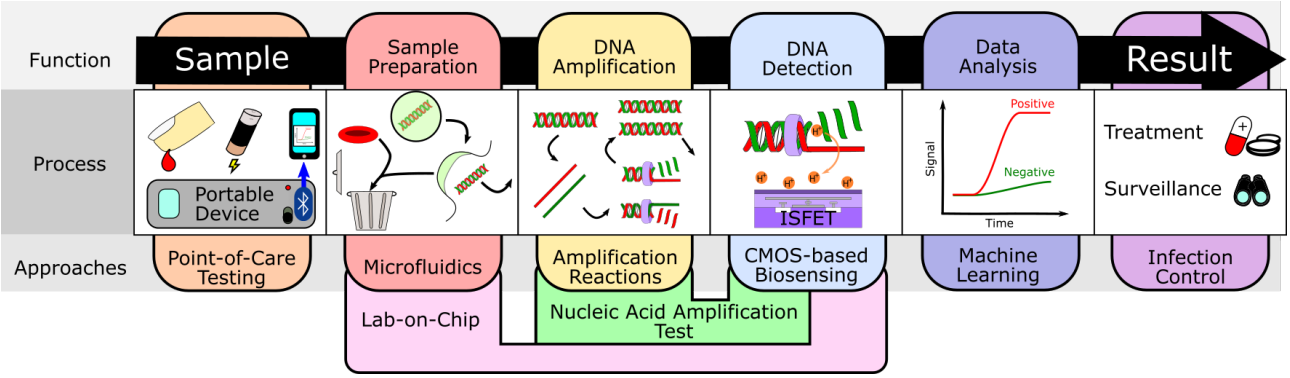


Figure 1.1: Schematic outlining the processes behind a NAAT sample-to-result diagnostic device, illustrating the key concepts involved and how they interlink.

1.1.2 The Lab-on-Chip Revolution: CMOS-based ISFETs as a Portable DNA Detection Platform

Lab-on-Chip (LoC) devices aim to scale down laboratory processes so that multiple stages of sample handling and target detection can occur within the confines of a single, handheld device[1]. Sample processing occurs entirely within the device, which reduces requirements for separate pieces of laboratory equipment and trained clinicians, as well as making the device more robust by limiting contamination. Combining LoC approaches with integrated circuitry based on complementary metal-oxide-semiconductor (CMOS) provides a promising platform for PoC diagnostic devices that can process microlitre samples and detect biomarkers.

CMOS technology has repeatedly been demonstrated for use in various biosensing applications, including DNA detection, cell monitoring, and neurosensing, with a variety of signal transduction mechanisms [9, 10]. CMOS is favoured due to its low power consumption, low noise, and high scalability of production, making it the ideal platform for a low-cost, PoC diagnostic device capable of detecting pathogens in test samples.

Pathogen detection typically targets two types of molecules: nucleic acids (DNA and RNA) and antigens. Pathogens produce antigens, a group of molecules that are foreign to a body and trigger the host immune response to infection. Antigens can include proteins, amino acids, and lipids, amongst others. Antibodies form part of the host immune response and can bind to specific antigens. Antibody-antigen reactions can be leveraged to detect the presence of a pathogen within a patient. This can be in the form of LFTs, which give visually determined results based on capillary flow through paper, sacrificing sensitivity for affordability, speed, and portability [11]. Enzyme-linked immunosorbent assays (ELISA) use an enzyme-labelled antibody that catalyses a colour-changing reaction in the solution. ELISAs are capable of higher sensitivity and specificity than LFTs, but are a labour-intensive laboratory technique

[1]The use of the word chip here can cause confusion and typically refers to a microfluidic chip rather than a CMOS microchip. Lab-on-CMOS is a separate concept that will be introduced later.

[12].

DNA-based diagnosis is usually performed by identifying the presence of a certain genetic sequence associated with the pathogen. This can be done using probes that exhibit specific binding to the target DNA [13, 14, 15]. However, such approaches are potentially limited by the small quantities of the target that may be present in the sample, demanding high sensitivity from the detection system. Instead, by using amplification reactions such as PCR and loop-mediated isothermal amplification (LAMP), the number of target DNA strands in the sample can be increased, easing the process of detection. This is often referred to as nucleic acid amplification testing (NAAT) [16].

Detecting post-amplification DNA is the next challenge. Many optical methods of detecting DNA have been developed, often utilising fluorescent dyes but also including Raman scattering and plasmon resonance [17, 18]. The sensitivity of these techniques means that they are favoured for bench-top applications and they currently dominate the gold-standard practises for DNA detection. However, the required optical equipment adds bulk, cost, and power demands, which are challenges when translating the technology to the PoC [19, 20, 21].

As an alternative to optical DNA sensing, electrochemical approaches have been gaining increasing attention due to their label-free sensing mechanism and the easy integration of electrochemical sensors within a CMOS architecture. Electrochemical impedance spectroscopy (EIS) is an electrochemical technique that detects a change in impedance of the sensing system due to the presence of DNA, typically involving its interaction with functionalised surfaces or particles [22, 23, 24]. EIS is straightforward to implement, but suffers from a high limit-of-detection (LoD) [25]. DNA can also be detected via the interaction of its electrostatic charge with field-effect transistors (FETs) [26].

While FETs detect DNA via electrostatic charge, it is possible to detect DNA through the hydrogen ions (protons, H^+) produced during amplification reactions using ion-sensitive field-effect transistors (ISFETs) [27, 28, 29]. The ISFET's implementation in unmodified CMOS technology relies on stacking vias from the floating gate of the underlying metal-oxide-semiconductor field-effect transistor (MOSFET) to the top-metal, known as the extended-gate approach, then using the standard passivation layer as a sensing material. Protons in solution bind to hydroxyl (OH) groups on the surface, thereby modifying the overall surface charge and shifting the threshold voltage of the device, providing sensitivity to pH changes. To date, ISFET-based DNA sensing platforms have been successfully applied to the rapid diagnosis of malaria [30], cancer [31], and anti-microbial resistance [32]. A summary of the key concepts and approaches involved in creating a sample-to-result device for diagnosis via ISFET-based DNA detection can be seen in Figure 1.1.

Much research has been conducted into improving ISFET performance, focusing on sensor non-

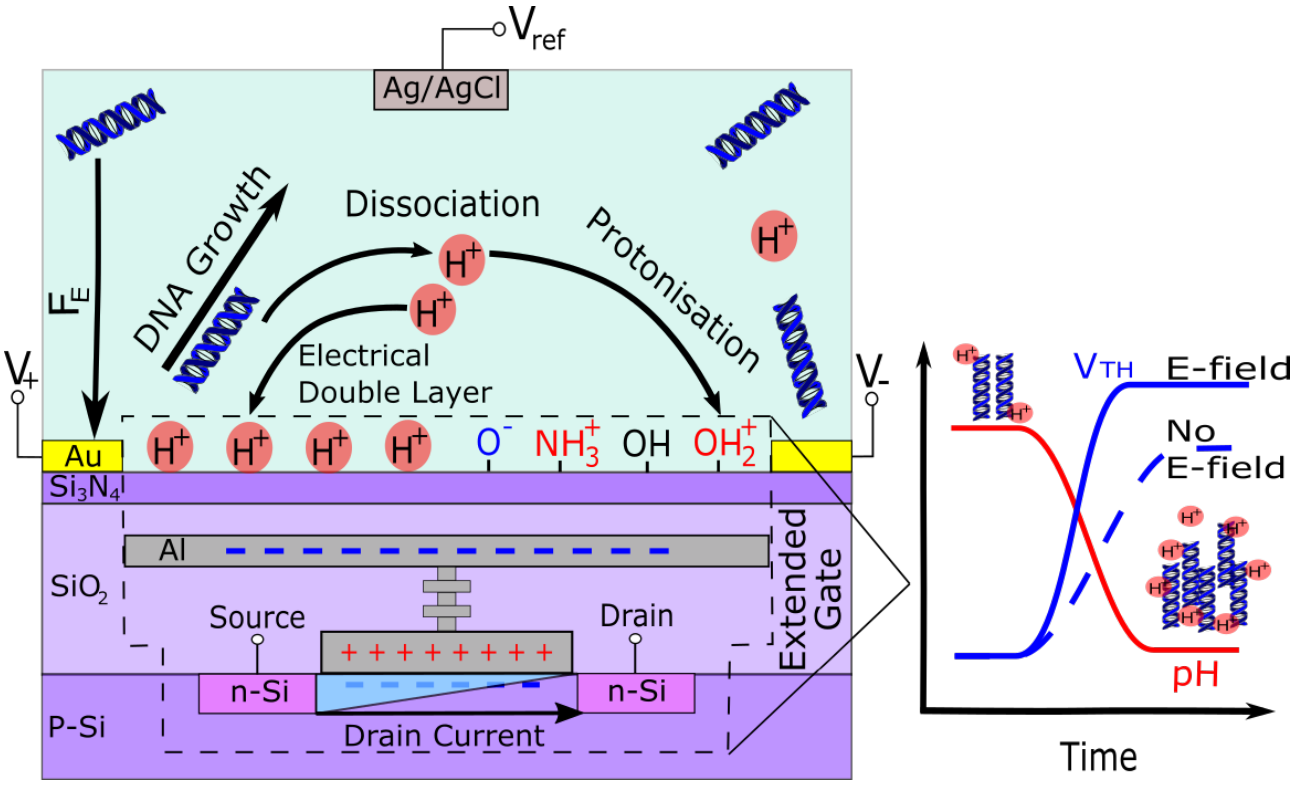


Figure 1.2: A schematic outlining the structure of the ISFET in unmodified CMOS technology and the process of DNA detection, including electrodes to move DNA close to the sensor surface with electric field interactions to achieve a signal boost. The graph shows the change in ISFET threshold voltage (**blue**) in response to DNA amplification and decreasing solution pH (**red**), and compares the expected signals of systems with (**solid blue line**) and without (**dashed blue line**) an electric field actuation system. Adapted from [29] and [35].

idealities [33] or modifying the microchip surface to improve signal [34]. However, there are many opportunities to improve device performance and functionality by changing the way in which the chip interacts with the test electrolyte through the use of on-chip electrodes and electric field interactions.

1.2 Research Objectives

The primary objective of this thesis is to use on-chip electrodes to spatially manipulate DNA within the test solution using electric field interactions and boost the ISFET signal by moving DNA towards sensors prior to amplification. Currently, DNA is randomly distributed within the test solution. For DNA that originates far from the chip surface, protons that are produced during amplification must rely on transport mechanisms, such as diffusion and convection, to bring them within ISFET sensing regions. If instead, DNA is moved towards the chip's surface prior to amplification, then the subsequently produced protons will have a higher detection probability and quicker detection rate. Overall, this is expected to increase the size and speed

of the signal [36], as outlined in Figure 1.2. To estimate this change in ISFET signal, new models are required that incorporate the spatial and temporal dependencies of both DNA amplification and proton transport.

Whilst initial efforts will focus on producing photolithographic, on-chip electrodes, a key aim of this thesis is to explore the extent to which these DNA-manipulating electrodes can be incorporated as part of commercial CMOS processes. It is possible that the top-metal of a CMOS microchip, as fabricated by the CMOS foundries, can be leveraged as an electrode for electric field trapping of DNA and two approaches to achieve this will be presented. By demonstrating electrokinetics using a CMOS top-metal electrode system, future research avenues towards on-CMOS sample preparation can be explored.

This top-metal electrode approach also opens up opportunities for further CMOS-integration of the device. The ISFET requires a reference electrode (RE) to provide a stable biasing potential, without which signals are lost. Through surface processing of exposed CMOS top-metal, a quasi-RE (QRE) can be fabricated as part of the IC with minimal effort.

Over the course of this thesis, the following research questions will be answered:

Research Questions

1. Can ISFET-based DNA detection be improved by using electric field manipulation to position DNA close to sensing regions prior to amplification?
2. To what extent can DNA-manipulating electrode systems be integrated within CMOS IC? What is the best approach to achieve this whilst minimising CMOS modification and post-processing?
3. Can the impact of DNA positioning on ISFET output be estimated through models? What simulation approach is best suited for ISFET-based DNA detection?
4. Can an electroplated on-chip Ag/AgCl QRE be fabricated on CMOS top-metal?
5. What sample preparation processes can be conducted by on-CMOS electrodes? How much of this functionality can be handled by a single electrode system?

1.3 Thesis Organisation

The organistion of this thesis is represented in Figure 1.3 and consists of the following chapters:

1.3.1 Chapter 2: DNA, Amplification Reactions, and the ISFET Sensing Mechanism

In Chapter 2, the mechanism that enables ISFETs to detect DNA is explained in more detail. Particular attention will be paid to the insulator-electrolyte interface, how surface charges form, and the equations that govern them. This will be of importance for the modelling conducted in Chapter 3 and motivates the direct simulation of surface proton concentration instead of using a bulk approxmation.

1.3.2 Chapter 3: Spatio-Temporal Simulation of ISFET-based DNA Detection

In Chapter 3, spatio-temporal simulations for ISFET-based DNA detection will be developed, building on an existing model for DNA amplification. The first approach incorporates proton diffusion through a Monte-Carlo first-passage method. The second approach uses the finite-element method (FEM) software COMSOL. Results from the two approaches will be compared and evaluated against experimental data. The Monte-Carlo approach is proved to be highly efficient, demonstrates an ability to replicate experimental data, and predicts an improvement in device speed with DNA positioned at the ISFET surface, which supports and provides estimates for the work in Chapter 4.

1.3.3 Chapter 4: Electrokinetic Manipulation of DNA to Enhance ISFET-based Detection

In Chapter 4, on-chip electrode systems will be developed for electric field manipulation of DNA. The first approach uses photolithographic techniques to fabricate electrodes on existing microchips. These electrodes demonstrate an ability to trap DNA in low conductivity solutions, but not in high conductivity amplification solutions. The second approach uses electrodes that are designed in the top-metal of a CMOS process and exposed using a focussed ion beam (FIB). The CMOS top-metal experiments were ultimately unsuccessful and highlighted the need for surface processing and inspires the work in Chapter 5.

1.3.4 Chapter 5: An Electroplated *Ag/AgCl* Reference Electrode based on CMOS Top-Metal

In Chapter 5, an on-chip $Ag/AgCl$ QRE will be fabricated using CMOS bond-pads as a base for a fully-electroplated process. Electrochemical characterisation of the bond-pad QRE shows that it is capable of producing a stable potential with a sufficiently long lifetime. The ENIG-plating that forms part of the QRE fabrication process sees further application in Chapter 6.

1.3.5 Chapter 6: Conceptualisation of an Electrokinetic Lab-on-CMOS Diagnostic Device

In Chapter 6, the work conducted over the course of the thesis will be brought together in the concept for an electrokinetic lab-on-CMOS diagnostic device. The scope for sample preparation conducted via electric field interactions will be outlined, along with opportunities for on-CMOS 3D carbon electrodes and alternative sensing modalities. To demonstrate the viability of the proposed design, electrokinetic trapping with gold (Au)-plated bond-pads will be demonstrated.

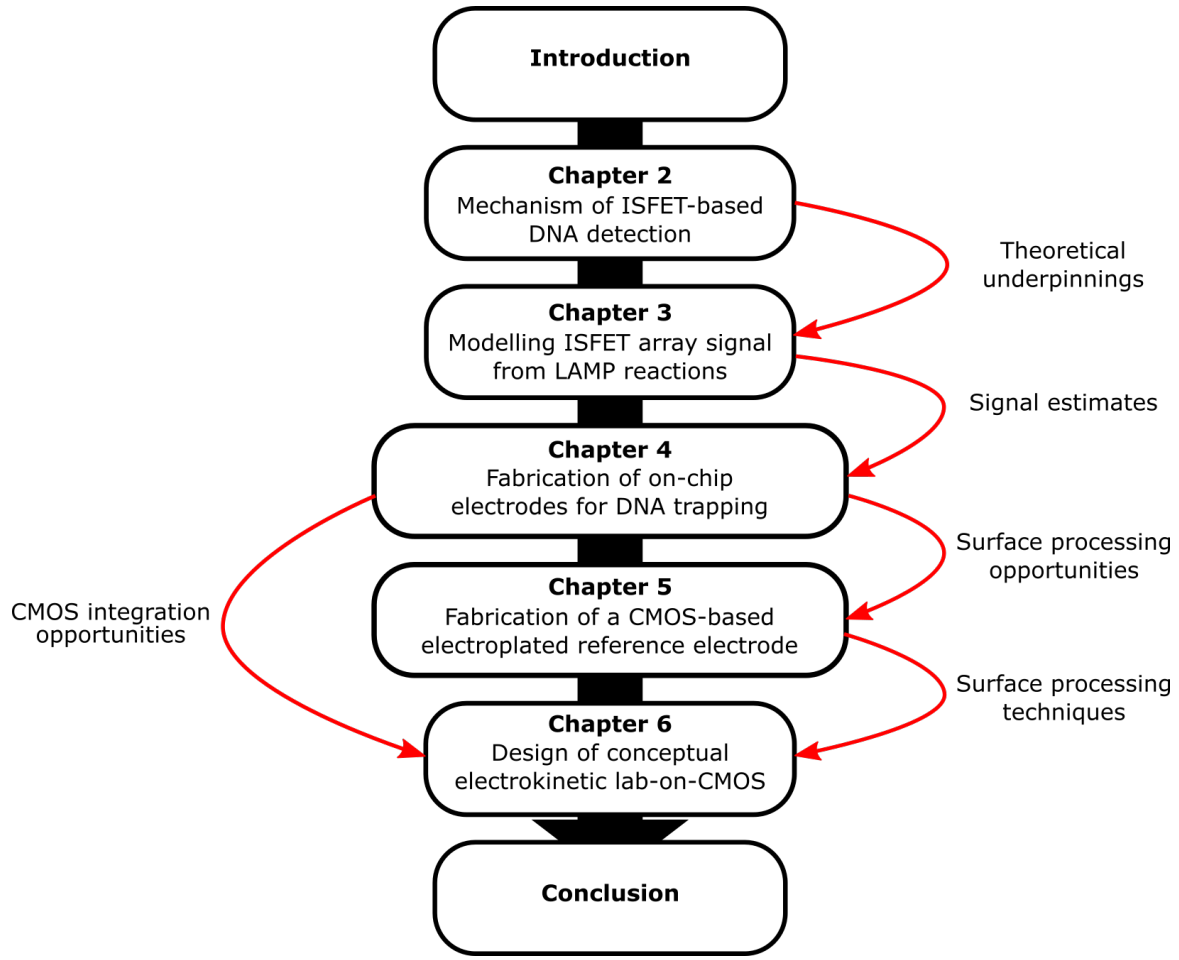


Figure 1.3: A flowchart representing the organisation of this thesis. The links between chapters are illustrated by the red arrows.

Bibliography

[1] D. Ming et al. "Connectivity of rapid-testing diagnostics and surveillance of infectious diseases". In: *Bulletin of the World Health Organization* 97 (Mar. 2019), pp. 242–244.

[2] P. Craw and W. Balachandran. "Isothermal nucleic acid amplification technologies for point-of-care diagnostics: A critical review". In: *Lab on a Chip* 12.14 (2012), pp. 2469–2486.

[3] D. Mistry et al. "A systematic review of the sensitivity and specificity of lateral flow devices in the detection of SARS-CoV-2". In: *BMC Infectious Diseases* 21 (828 2021).

[4] J. Watson, P. F. Whiting, and J. E. Brush. "Interpreting a covid-19 test result". In: *BMJ* 369 (2020).

[5] K. B. Pouwels et al. "Community prevalence of SARS-CoV-2 in England: Results from the ONS Coronavirus Infection Survey Pilot". In: *medRxiv* (2020).

[6] M. Urdea et al. "Requirements for high impact diagnostics in the developing world." In: *Nature* 444 Suppl 1 (2006), pp. 73–79.

[7] J. O'Neill. *Review on Antimicrobial Resistance: Rapid Diagnostics*. Tech. rep. Wellcome Trust, 2015.

[8] R. W. Peeling et al. "Rapid tests for sexually transmitted infections (STIs): the way forward". In: *Sexually Transmitted Infections* 82.suppl 5 (2006), pp. v1–v6. ISSN: 1368-4973.

[9] K. M. Lei et al. "CMOS biosensors for in vitro diagnosis – transducing mechanisms and applications". In: *Lab on a Chip* 16 (19 Sept. 2016), pp. 3664–3681.

[10] H. Li et al. "CMOS electrochemical instrumentation for biosensor microsystems: A review". In: *Sensors (Switzerland)* 17 (1 Jan. 2017).

[11] P. Estrela, K. M. Koczula, and A. Gallotta. "Lateral flow assays". In: *Essays in Biochemistry* 60.1 (June 2016), pp. 111–120. ISSN: 0071-1365.

[12] S. Hosseini et al. "Advantages, Disadvantages and modifications of conventional ELISA". In: *SpringerBriefs in Applied Sciences and Technology* (9789811067655 2018), pp. 67–115.

[13] R. Lenigk et al. “Plastic biochannel hybridization devices: a new concept for microfluidic DNA arrays”. In: *Analytical Biochemistry* 311.1 (2002), pp. 40–49. ISSN: 0003-2697.

[14] N. M. Hom, C. Promptmas, and K. Wat-Aksorn. “Detection of DNA Hybridization Using Protein A Modified Ion Sensitive Field Effect Transistor”. In: *Analytical Letters* 48.7 (2015), pp. 1128–1138.

[15] C. Cheng et al. “Capacitive DNA sensor for rapid and sensitive detection of whole genome human herpesvirus-1 dsDNA in serum”. In: *Electrophoresis* 38.12 (2017), pp. 1617–1623.

[16] M. G. Mauk et al. “Simple Approaches to Minimally-Instrumented, Microfluidic-Based Point-of-Care Nucleic Acid Amplification Tests”. In: *Biosensors* 8.1 (2018). ISSN: 2079-6374.

[17] K. Hering et al. “SERS: a versatile tool in chemical and biochemical diagnostics”. In: *Analytical and Bioanalytical Chemistry* 390.1 (2008), pp. 113–124. ISSN: 1618-2650.

[18] E. Primiceri et al. “Key Enabling Technologies for Point-of-Care Diagnostics”. In: *Sensors* 18.11 (2018). ISSN: 1424-8220.

[19] H. Norian et al. “An integrated CMOS quantitative-polymerase-chain-reaction lab-on-chip for point-of-care diagnostics”. In: *Lab Chip* 14 (20 2014), pp. 4076–4084.

[20] J. Song et al. “Smartphone-Based Mobile Detection Platform for Molecular Diagnostics and Spatiotemporal Disease Mapping”. In: *Analytical Chemistry* 90.7 (2018), pp. 4823–4831. ISSN: 0003-2700.

[21] A. Hassibi et al. “Multiplexed identification, quantification and genotyping of infectious agents using a semiconductor biochip”. In: *Nature Biotechnology* 36 (2018), p. 738.

[22] T. S. Bronder et al. “Detection of PCR-Amplified Tuberculosis DNA Fragments with Polyelectrolyte-Modified Field-Effect Sensors”. In: *Analytical Chemistry* 90.12 (2018), pp. 7747–7753. ISSN: 15206882.

[23] C. F. Chang and M. S. Lu. “CMOS Ion Sensitive Field Effect Transistors for Highly Sensitive Detection of DNA Hybridization”. In: *IEEE Sensors Journal* 20 (16 Aug. 2020), pp. 8930–8937. ISSN: 15581748.

[24] B. Zribi et al. “A microfluidic electrochemical biosensor based on multiwall carbon nanotube/ferrocene for genomic DNA detection of Mycobacterium tuberculosis in clinical isolates”. In: *Biomicrofluidics* 10.1 (2016), p. 014115.

[25] E. O. Blair and D. K. Corrigan. “A review of microfabricated electrochemical biosensors for DNA detection”. In: *Biosensors and Bioelectronics* 134 (2019), pp. 57–67. ISSN: 0956-5663.

[26] B. Veigas, E. Fortunato, and P. V. Baptista. “Field Effect Sensors for Nucleic Acid Detection: Recent Advances and Future Perspectives”. In: *Sensors* 15.5 (2015), pp. 10380–10398. ISSN: 1424-8220.

[27] P. Bergveld. "Thirty years of ISFETOLOGY: What happened in the past 30 years and what may happen in the next 30 years". In: *Sensors and Actuators B: Chemical* 88.1 (2003), pp. 1–20. ISSN: 0925-4005.

[28] J. M. Rothberg et al. "An integrated semiconductor device enabling non-optical genome sequencing". In: *Nature* 475.7356 (2011), pp. 348–352. ISSN: 0028-0836.

[29] C. Toumazou et al. "Simultaneous DNA amplification and detection using a pH-sensing semiconductor system". In: *Nature Methods* 10 (2013), pp. 641–646.

[30] K. Malpartida-Cardenas et al. "Quantitative and rapid Plasmodium falciparum malaria diagnosis and artemisinin-resistance detection using a CMOS Lab-on-Chip platform". In: *Biosensors and Bioelectronics* 145 (2019), p. 111678. ISSN: 0956-5663.

[31] M. Kalofonou et al. "A novel hotspot specific isothermal amplification method for detection of the common PIK3CA p.H1047R breast cancer mutation". In: *Scientific Reports* 10 (2020).

[32] J. Rodriguez-Manzano et al. "Rapid Detection of Mobilized Colistin Resistance using a Nucleic Acid Based Lab-on-a-Chip Diagnostic System". In: *Scientific Reports* 10 (2020).

[33] N. Moser et al. "ISFETs in CMOS and Emergent Trends in Instrumentation: A Review". In: *IEEE Sensors Journal* 16.17 (2016), pp. 6496–6514. ISSN: 1530-437X.

[34] N. Moser et al. "ISFET Arrays for Lab-on-Chip Technology: A Review". In: *2019 26th IEEE International Conference on Electronics, Circuits and Systems (ICECS)*. 2019, pp. 57–60.

[35] N. Moser et al. "A Scalable ISFET Sensing and Memory Array With Sensor Auto-Calibration for On-Chip Real-Time DNA Detection". In: *IEEE Transactions on Biomedical Circuits and Systems* 12.2 (2018), pp. 390–401. ISSN: 1932-4545.

[36] M. H. M. Abdulwahab et al. "A CMOS Bio-Chip combining pH Sensing, Temperature Regulation and Electric Field Generation for DNA Detection and Manipulation". In: *2018 IEEE International Symposium on Circuits and Systems (ISCAS)*. May 2018, pp. 1–5.

Chapter 2

DNA, Amplification Reactions, and the ISFET Sensing Mechanism

2.1 DNA

DNA forms the basis of all life, providing the information required for the specialised protein production that drives cellular processes. The building block of DNA, known as a nucleotide, consists of a deoxyribose sugar, a phosphate group, and one of the four bases: Adenine (A), guanine (G), thymine (T), or cytosine (C), in a structure that is displayed in Figure 2.1.

Nucleotides bond in a chain to form single-stranded DNA (ssDNA), which has two distinct ends, denoted as 5' and 3' in Figure 2.1, that terminate in phosphate (PO_4) and OH groups respectively. Hydrogen bonding, only allowed between A-T and C-G base pairs, results in the formation of double-stranded DNA (dsDNA) from two complementary ssDNA molecules.

The PO_4 groups that form the backbone of DNA are acidic, losing a proton when in a solution, and they account for the overall negative charge of aqueous DNA molecules [1].

2.2 DNA Amplification Reactions

Amplification reactions are used to carry out targeted replication of specific DNA strands in laboratory conditions, thus increasing the concentration of that DNA in a sample.

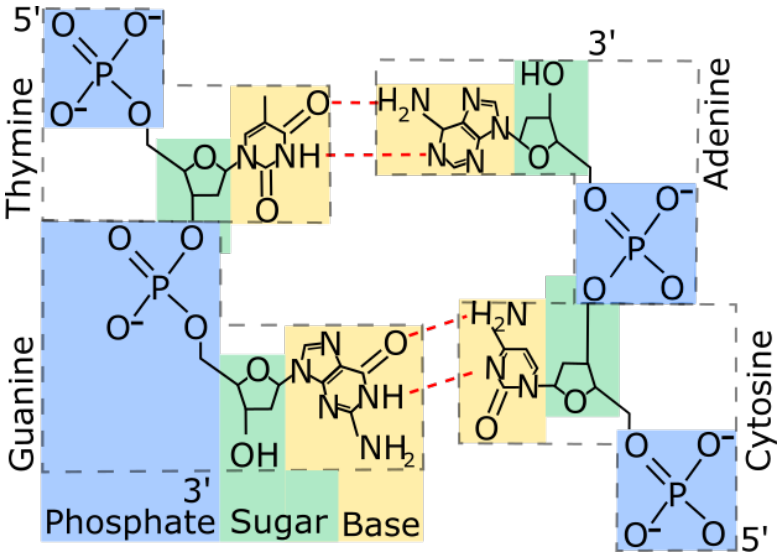


Figure 2.1: An illustration of the structure of DNA, which contains the four nucleotide types. The three components of a nucleotide: a PO_4 group, a deoxyribose sugar, and a nitrogeneous base, are highlighted. Hydrogen bonds between bases are denoted by dashed red lines, and the 3' and 5' endings are labelled. Adapted from [2].

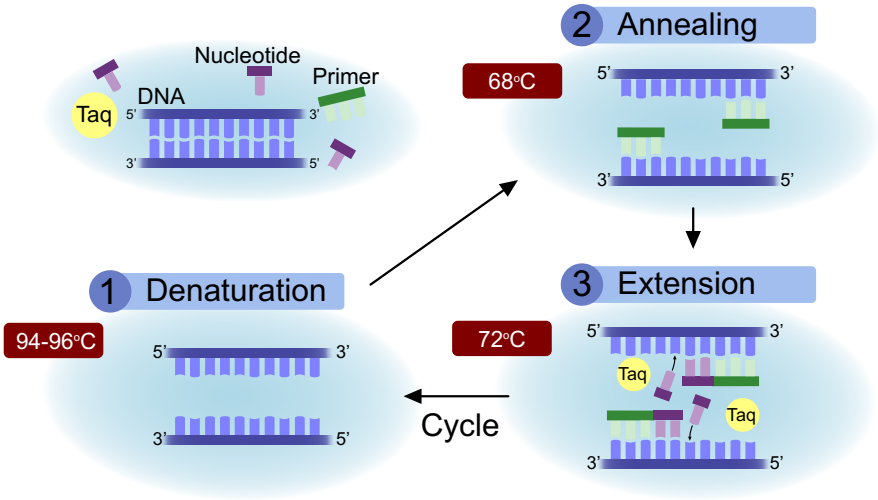


Figure 2.2: Illustration of PCR for cyclic DNA amplification [3]. Taq is a thermostable DNA polymerase.

2.2.1 Polymerase Chain Reaction

PCR was developed in 1983 by Kary Mullis [4] and uses a process that is illustrated in Figure 2.2 and consists of three steps:

1. **Denaturation:** Denaturation is the splitting of dsDNA into its two ssDNA constituents, achieved by heating the sample to $95°C$.
2. **Annealing:** Primers are short lengths of ssDNA that bond to the denatured DNA and provide an OH group at the 3' end, which acts as the origin for strand growth. Primers are synthesised to complement a genetic sequence that is unique to the target DNA, so that the reaction is specific. Annealing (bonding) of the primers occurs at a temperature of $55°C$, which can then be raised to remove primers that have not annealed in the correct locations, improving the specificity of the process.
3. **Extension:** Nucleotides (dNTP) from the amplification solution are incorporated into the strand at the OH group provided by the primer, catalysed by DNA polymerase. The dependence on the OH group results in strand growth only occurring in the 5' to 3' direction. The temperature during this stage, typically between 70-75^oC is chosen to ensure high enzyme activity and thus high DNA strand growth rate.

At the end of the cycle, two copies of the original template DNA are formed, giving exponential growth of strand numbers as the cycle, steps 1 to 3, is repeated [5].

2.2.2 Loop-Mediated Isothermal Amplification

In contrast to PCR, LAMP is conducted at a constant temperature of around $63°C$. LAMP also produces more DNA copies[1] at reaction saturation. In the case of pH-based detection, this results in a larger quantity of protons in the solution and thus a greater signal.

The LAMP reaction begins with 4-6 different primers targeting 6-8 locations on the DNA strand. This leads to primer design being significantly more challenging for LAMP than PCR. During amplification, a dumbbell-shaped DNA molecule is first produced upon which a second, cycling step acts to create a zig-zagged molecule that increases in length with each cycle[2].

LAMP is typically conducted within a buffer solution to limit the variation of pH over the course of the reaction. A buffer is solution of an acid (HA) and its conjugate base (A^-) that

[1] RT-LAMP is a technique for detecting ribonucleic acids (RNA) that first uses reverse transcription to convert the RNA to DNA. RNA is a nucleic acid that is similar in structure to DNA, with a U base replacing the T. RT-LAMP is used in many modern diagnostic applications.

[2] full LAMP process is overly complex for discussion. A good explanation of the process can be found at the Eiken Genome website [6].

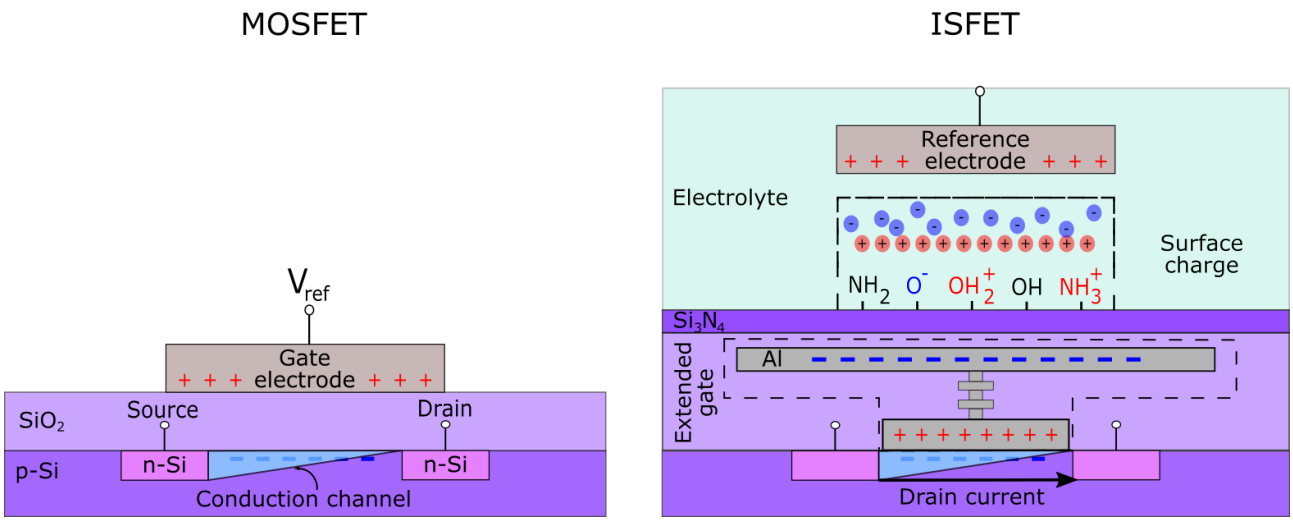


Figure 2.3: An illustration of CMOS implementations of a MOSFET (**left**) compared to an ISFET using an extended gate approach (**right**), with key concepts denoted.

takes part in an equilibrium reaction of the form $HA \rightleftharpoons H^+ + A^-$, which acts to neutralise pH changes. ISFET-based DNA detection relies upon this pH change and thus requires a weakly buffered LAMP reaction, referred to as pH-LAMP.

2.3 Ion-Sensitive Field-Effect Transistors

An ISFET is a chemically sensitive analogue to the MOSFET. In a MOSFET, a voltage applied at the gate electrode can be used to draw electrons towards the surface of the semiconductor, create a conduction channel within the p-type silicon (p-Si), and allow a current between two n-type silicon (n-Si) regions, called the source and the drain[3]. The voltage at which the conduction channel is created and a drain current flows is known as the threshold voltage (V_{Th}).

In the case of the ISFET, the gate electrode is replaced by an insulating membrane in contact with the electrolyte, with a reference electrode used to bias the system. In this case, the potential experienced by the underlying semiconductor is modified by the interaction of ions with the insulating membrane. The threshold voltage of the ISFET is that of the standard MOSFET with an additional, electrolyte-dependent voltage term,

$$V_{Chem} = V_{ref} - \psi_0 + \chi_{sol} - \frac{\phi_m}{q} \tag{2.1}$$

where V_{ref} is the reference electrode potential, ψ_0 is the chemical potential of the electrolyte, ϕ_m is the work function of the metal gate electrode that the electrolyte has replaced, and

[3]This describes the more popular NMOS implementation of a MOSFET. For a PMOS implementation, p-Si is used for the source and drain, n-Si forms the bulk, and the charge carriers are holes.

χ_{sol} is a potential contribution from electric dipoles at the electrolyte-insulator interface. ψ_0 is negatively correlated with solution pH and is thus responsible for the pH-sensitivity of the ISFET's threshold voltage. A simplified representation of equation 2.1 is given by,

$$V_{Chem} = \gamma + \alpha S_N pH \tag{2.2}$$

where γ is a collection of constants that do not vary with ionic concentration and α is a constant, varying from 0-1, that dictates the deviation of the system from the Nernstian sensitivity, $S_N = 59\,mV/pH$. Nernstian sensitivity defines the change in cell potential induced by a decade change in species concentration, in this case, the change in surface potential caused by a pH change of one.

The overall mechanism for ISFET-based DNA detection is that as amplification progresses, protons are released and the solution pH decreases, causing ISFET threshold voltage to decrease. The specificity of the amplification reaction, due to careful design of the primers, means that an increase in threshold voltage can be attributed to the presence of the target DNA.

2.3.1 The Insulator-Electrolyte Interface

It is the interaction of protons and other charged species in the electrolyte with the insulating layer of the ISFET, referred to as its passivation, that gives rise to pH-sensitivity. This involves an assortment of chemical and physical phenomena.

Surface Reactions

Common materials used for the insulating layer of an ISFET include silicon dioxide (SiO_2), silicon nitride (Si_3N_4), and hafnium dioxide (HfO_2). The surfaces of these insulating layers contain OH groups that are amphoteric surface sites, meaning that they can act as an acid or a base and either donate or accept protons through a reaction. As such, the OH groups can occupy 3 states: Deprotonated (O^-), neutral (OH), and protonated (OH_2^+). This thus describes the so called two-site binding model with the reversible reaction equations,

$$\mathrm{O^- + H_s{}^+ \rightleftharpoons OH}$$

$$\mathrm{OH + H_s{}^+ \rightleftharpoons OH_2{}^+}$$

where H_s^+ denotes hydrogen ions at the surface as opposed to the bulk solution. The equilibrium state of these reversible reactions can be described by their equilibrium constants,

$$K_a = \frac{[H_s^+][O^-]}{[OH]} \tag{2.3}$$

$$K_b = \frac{[H_s^+][OH]}{[OH_2^+]} \tag{2.4}$$

where square brackets denote species concentration and $pK = -log_{10}(K)$ is often quoted.

In addition to these OH groups, S_3N_4 surfaces contain amine (NH_2) groups that can take part in the reaction,

$$\mathrm{NH_2 + H_s{}^+ \rightleftharpoons NH_3{}^+}$$

with the equilibrium determined by the equation,

$$K_N = \frac{[H_s^+][NH_2]}{[NH_3^+]} \tag{2.5}$$

For SiO_2, pK_a is often given between 6-9 and pK_b between $-2.9 - -1.9$ [7, 8, 9, 10] whilst pK_N has been estimated to be around 10 [11].

The surface charge at the insulator-electrolyte interface is then determined by the configuration of states for the surface sites, and is given by the relation,

$$\sigma = qn_{OH}\left(\frac{[H_s^+]^2 - K_aK_b}{K_aK_b + K_b[H_s^+] + [H_s^+]^2}\right) + qn_{NH}\left(\frac{[H_s^+]}{[H_s^+] + K_N}\right) \tag{2.6}$$

where n_{OH} and n_{NH} are the density of surface sites for OH and NH_2 groups respectively, and q is the charge of a proton, equal to one electron charge (e) [11]. For surfaces that do not contain NH_2 groups, the second term is omitted.

Typically, the surface concentration of protons is related to that of the bulk solution, $[H^+]$, by the Boltzmann relation,

$$[H_s^+] = [H^+]exp\left(-\frac{q\psi_0}{k_bT}\right) \tag{2.7}$$

where k_b is Boltzmann's constant, T is the temperature of the solution, and $pH = -log_{10}([H^+])$ [12].

The Electrical Double Layer

In response to the surface charge that arises at the insulator-electrolyte interface from surface reactions, counterions within the electrolyte will move to form an electrical double layer (EDL),

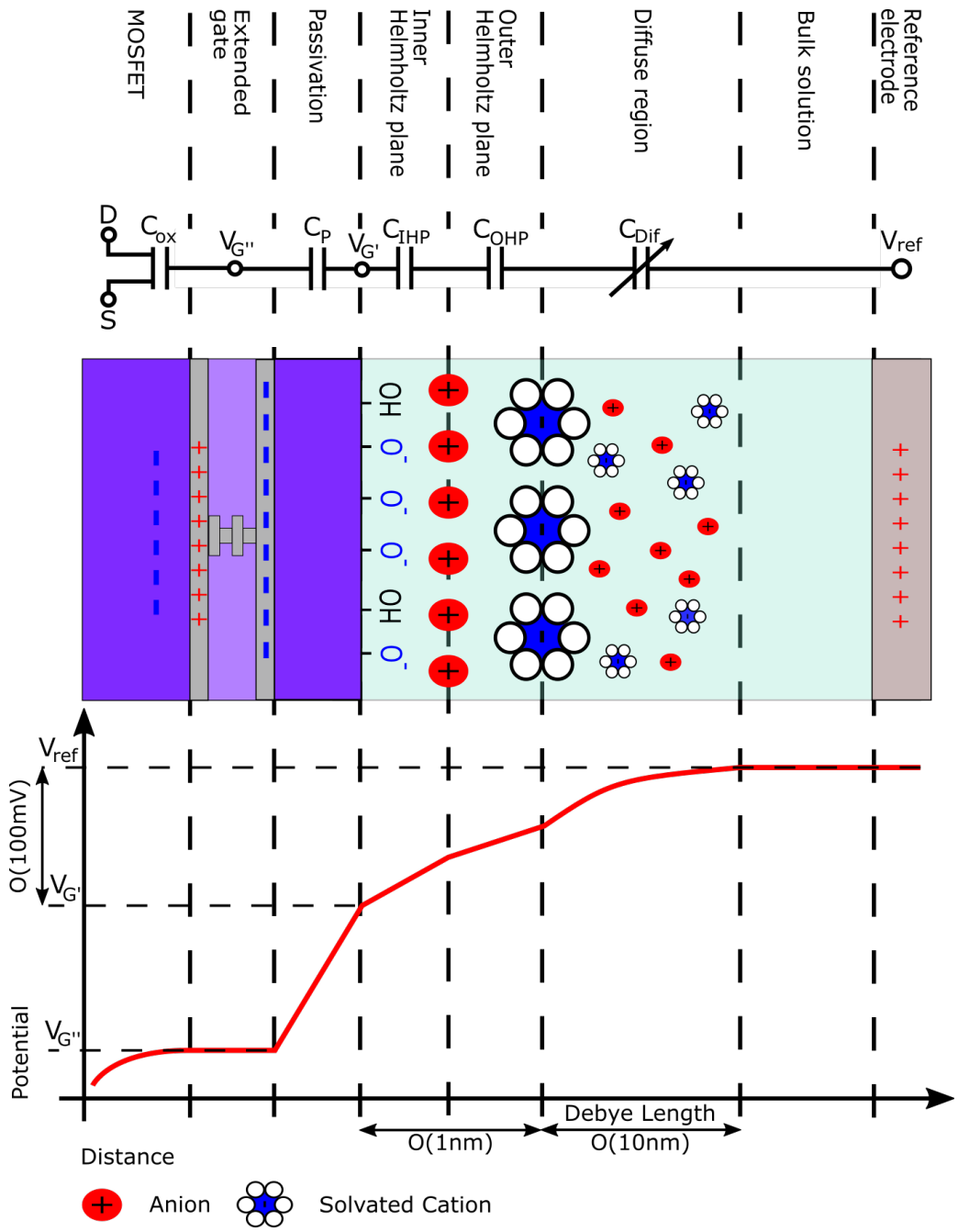


Figure 2.4: An illustration of the various layers of an ISFET, including the electrolyte and RE. An equivalent circuit is provided, representing each layer with a circuit element. A representation of the electric potential moving through the system is contained in the bottom graph. From left to right, D and S are the source and drain respectively, C_{ox} is the capacitance across the gate oxide, $V_{G''}$ is the potential at the extended gate, C_P is the capacitance across the passivation layer, $V_{G'}$ is the potential at the insulator-electrolyte interface, C_{IHP} and C_{OHP} are the capacitance of the inner and outer Helmholtz plane respectively, C_{Dif} is the capacitance across the diffuse layer, and V_{ref} is the reference potential.

due to electrostatic interaction between opposite charges.

The Helmholtz model is the simplest representation of the EDL, consisting of a single, planar layer of opposite charge residing just above the surface. This situation is analogous to a parallel plate capacitor, and as such a Helmholtz capacitance, C_{Helm}, can be defined between the electrolyte and the surface, and the potential drops linearly across the layer according to,

$$\psi_{Helm} = \frac{\sigma}{C_{Helm}} \tag{2.8}$$

For SiO_2, C_{Helm} is often quoted as $0.2\,F/m^2$ [13], however there have been arguments that this should be as high as $0.8\,F/m^2$ or $1.6\,F/m^2$ [14]. No values exist in the literature for Si_3N_4, but since the total surface site density is believed to be the same as SiO_2, it is reasonable to assume that C_{Helm} will not vary hugely between the two surfaces [11].

The different effective sizes of hydrated ions that are fully surrounded by solvent molecules creates two distinct layers of the Helmholtz plane: the inner Helmholtz plane (IHP) consisting of non-hydrated counterions and the outer Helmholtz plane (OHP) consisting of hydrated cations [15].

To incorporate the effect of diffusive particle motion, the Guoy-Chapman-Stern (GCS) model depicts a diffuse, continuous layer of charge, beyond the compact Helmholtz layer. This diffuse layer exhibits an exponential decay of potential, due to electrostatic screening, over the characteristic Debye length, which can extend up to 10-100 nm in solutions and is dependent on the ionic strength of the electrolyte [16, 17].

Grahame determined the relation for the charge density across the diffuse layer to be,

$$\sigma = \sqrt{8c_0\epsilon_s\epsilon_0 k_b T}\,sinh(\frac{e\psi_D}{2k_bT}) \tag{2.9}$$

where ψ_D is the potential across the diffuse layer, ϵ_s and ϵ_0 are the dielectric permittivity of the solution and of free space respectively, and c_0 is the ionic concentration of the solution [18]. Combining this with equation 2.8, the total potential difference across the EDL is given by,

$$\psi_0 = \frac{2k_bT}{q}\sinh^{-1}(\frac{-\sigma_0}{\sqrt{8c_0\epsilon_s\epsilon_0 k_b T}}) + \frac{\sigma_0}{C_{Helm}} \tag{2.10}$$

2.3.2 ISFET non-idealities

When attempting to use an ISFET to detect the shift in chemical potential that occurs with pH changes, there are several sensor non-idealities that will be encountered and which confound detection:

- **Trapped Charge:** A random threshold voltage offset is caused by the trapping of charge between each layer deposited during the fabrication process of CMOS-based ISFET arrays [19]. The offset varies between processes, ranging between $\pm 10\,V$ [20] and $\pm 0.5\,V$ [21].

- **Temporal Drift:** Temporal drift is characterised by a monotonic decrease in ISFET threshold voltage over time, caused by ionic bonding at buried OH sites within the first few atomic layers of the passivation. This charge build-up increases capacitance between the surface of the passivation and the floating gate, causing a decrease in the threshold voltage of the ISFET. The drift-induced change in threshold voltage, ΔV_{Th}, follows an exponential function of time, t, that can be described by,

$$\Delta V_{Th} = \Delta V_{Th}^{\infty}(1 - exp(-\frac{t}{\tau})^{\beta}) \tag{2.11}$$

  where ΔV_{Th}^{∞}, τ, and β are parameters that are fit to experimental data [22].

- **Capacitive Attenuation:** The insulating passivation layers that coat the chip above the floating gate cause a decay in electric potentials passing across them, reducing the measured threshold voltage. The attenuation that the passivation causes can be modelled by a series capacitor between the surface potential and the floating gate, C_{Pass}. The attenuation coefficient is given by,

$$A = \frac{V_G''}{V_G'} = \frac{C_{pass}}{C_{pass} + C_d} \tag{2.12}$$

  where C_d is the combination of parasitic capacitance between the gate and the source, the drain, and the bulk, and $V_{G'}$ and $V_{G''}$ are the chemical and extended gate potential respectively and are represented in Figure 2.4 [23].

- **Chemical Noise:** Stochastic particle motion at the passivation-electrolyte interface adds a characteristic $1/f$ noise to ISFET output. Other contributions to this noise exist, including drain current noise [24].

- **Temperature Variation:** ISFET threshold voltage varies with temperature, due to temperature dependency in the underlying MOSFET and the chemical reaction at the RE.

2.4 Lab-on-Chip Implementation of ISFET-Based DNA Detection

Though the theoretical operation of an ISFET as a DNA detector is sound, there are challenges in translating the technique to practical applications [3, 25].

2.4.1 ISFET Array Design

The ISFETs must be designed with sensor characteristics that are suitable for real-time DNA detection and be robust to, or able to compensate for, non-ideal behaviour.

- **Signal resolution:** Signal resolution, which defines the smallest detectable pH change, will impact the LoD and time-to-positive (ttp) of an ISFET-based diagnostic device. Larger sensing areas, as defined by the dimensions of the floating gate, will provide a greater signal to the underlying MOSFET. Alternatively, in-pixel encoding is a candidate for improved signal resolution [26, 27].

- **Temporal resolution:** The sensors must be capable of quick sampling, on the order of $1\,s$ and below, to allow readout of the entire array with a high frame rate. This will enable the ISFET array to capture fast changes in the chemical reaction. Typically, the bottleneck lies with high speed sampling at the array level and the requirement for sensor offset compensation schemes [28].

- **Spatial resolution:** The dimensions of the ISFET pixel must balance the high spatial resolution obtained by using small pixels, with the greater signal obtained by large pixels. The pixel area also defines the space available for underlying circuitry, with the use of smaller pixels potentially coming at the cost of in-pixel functionality [29, 30].

- **Non-ideality compensation:** The most critical ISFET non-idealities are offset and drift. Large offsets from trapped charge may require an analogue-to-digital converter (ADC) with more bits. The main alternative is device level compensation, such as using UV irradiation to remove trapped charges. Drift has proven the most challenging effect to compensate for since it tends to lie in a similar frequency range as the chemical signal (around $10\,mHz - 10\,Hz$). As such, it is typically accounted for in the post-processing of data [31]. Capacitive attenuation reduces the measurable signal and can be reduced through surface processing or the use of high-κ dielectrics as the passivation. Noise will impact the device LoD but is largely intrinsic to the device.

Year	Paper	Tech (μm)	Array size	Pixel (μm)	Readout method	Compensation	Sensitivity (pH)	Heating
2011	J.Rothberg *et al.* [29]	0.35	$1.5\,M$	5.1×5.1	Source follower	None	< 0.02	None
2013	C.Toumazou *et al.* [32]	0.35	40×1	104×34	Differential readout	Drift, temperature	–	On-chip heaters
2018	N.Moser *et al.* [26]	0.35	78×56	37×31	Time-encoded APS	Offset, drift	0.017	Off-chip Peltier
	N.Miscourides *et al.* [33]	0.35	64×200	6.5×7.8	Velocity saturation	None	0.101	Thermal instrument
2020	M.Cacho Soblechero *et al.* [27]	0.18	32×32	40×40	Linear OTA, sawtooth oscillator	Offset, drift	0.11	Thermal instrument

Table 2.1: A summary of the ISFET LoC platforms presented in the literature for DNA sequencing or detection.

The ISFET array-based platforms reported for DNA detection are summarised in Table 2.1. Ion Torrent [29] appeared in 2011 as a pioneer of large-scale DNA sequencing using ISFET arrays[4]. For high-throughput sequencing, the Ion Torrent ISFET pixel utilises a simple source-follower structure that fits within a small area. Each DNA target is then attached to a microbead and is contained in a well at the surface of a single pixel. Having demonstrated its value as a DNA sequencing platform, ISFET arrays were then developed for DNA detection by Toumazou *et al.*, with 40 sensors used to perform PCR on several different primers concurrently [32].

The amplification reaction of choice for ISFET-based DNA detection transitioned in 2018 from PCR to LAMP, which better matches requirements for PoC applications due to the lack of thermal cycling, on top of the superior performance of LAMP reactions. Moser *et al.* optimised for signal resolution by implementing larger pixels and encoding the ISFET current in time inside the pixel [26]. Introducing in-pixel digital computation offers prospects for scalability. Miscourides *et al.* integrated more than 12,000 pixels based on a current-mode topology with the ISFET biased in velocity saturation and the output voltage processed by a current conveyor and a transimpedance amplifier (TIA) [33]. The system was demonstrated for detection of malaria [34]. Cacho Soblechero *et al.* continued the concept of in-pixel quantisation with a system that integrated a dual thermal and chemical imaging 32×32 array that performed frequency encoding.

2.4.2 Lab-on-Chip System Design

To form an ISFET-based diagnostic device that can be operated at the PoC, the encapsulation of the microchip presents a challenge. Ion Torrent [29] designed a moulded fluidic lid that was placed on top of the ceramic package for loading the reaction solution on the chip. In Miscourides *et al.* 2018 and Moser *et al.* 2018, manifolds were created using laser-cut acrylic that contained a flow cell and a static chamber respectively [33, 26]. Sealing was achieved by applying pressure through double-sided tape on the chip. Further development of the microfluidic sample handling presents opportunities for multiplexed DNA detection on ISFET arrays. A compilation of schematics and pictures of LoC ISFET-based DNA detection systems is provided in Figure 2.5.

The RE used by Miscourides *et al.* and Moser *et al.* was a chlorinated silver (Ag) wire which was either placed under the manifold or between the inlet and outlet [33, 26]. This is the most common form of RE used for ISFET arrays, but alternative REs are becoming more prominent, particularly for microchip-based applications. The current trends in RE fabrication will be covered in Chapter 5.

[4]DNA sequencing is used to determine the genetic sequence of a DNA strand. ISFET-based DNA sequencing involves passing alternating flows of the four different nucleotides over the target ssDNA and observing a spike in sensor output when a nucleotide is incorporated into the strand.

The amplification reactions on which ISFET-based DNA detection depends, require carefully maintained temperatures. The majority of thermal regulation systems utilise temperature sensors that are implemented as part of the CMOS design and form a feedback loop with the heating system. Heating can be provided off-chip with a Peltier module, as in Miscourides *et al.* 2018 and Moser *et al.* 2018 [33, 26], or on-chip with resistive heating circuits as part of the CMOS IC, as in Toumazou *et al.* [32].

2.5 Summary

Over the course of this chapter, the mechanism of ISFET-based detection of DNA has been explained. The structure of the DNA molecule and the basic processes of amplification reactions were introduced. The operation of the ISFET as a sensor was presented, with a particular focus on the formation of surface charges at the insulator-electrolyte interface. This information was contextualised with a brief review of ISFET-based LoC devices for DNA detection. The concepts laid out in this chapter form the fundamental knowledge required for the work in this thesis and will be of particular importance for the modelling carried out in Chapter 3.

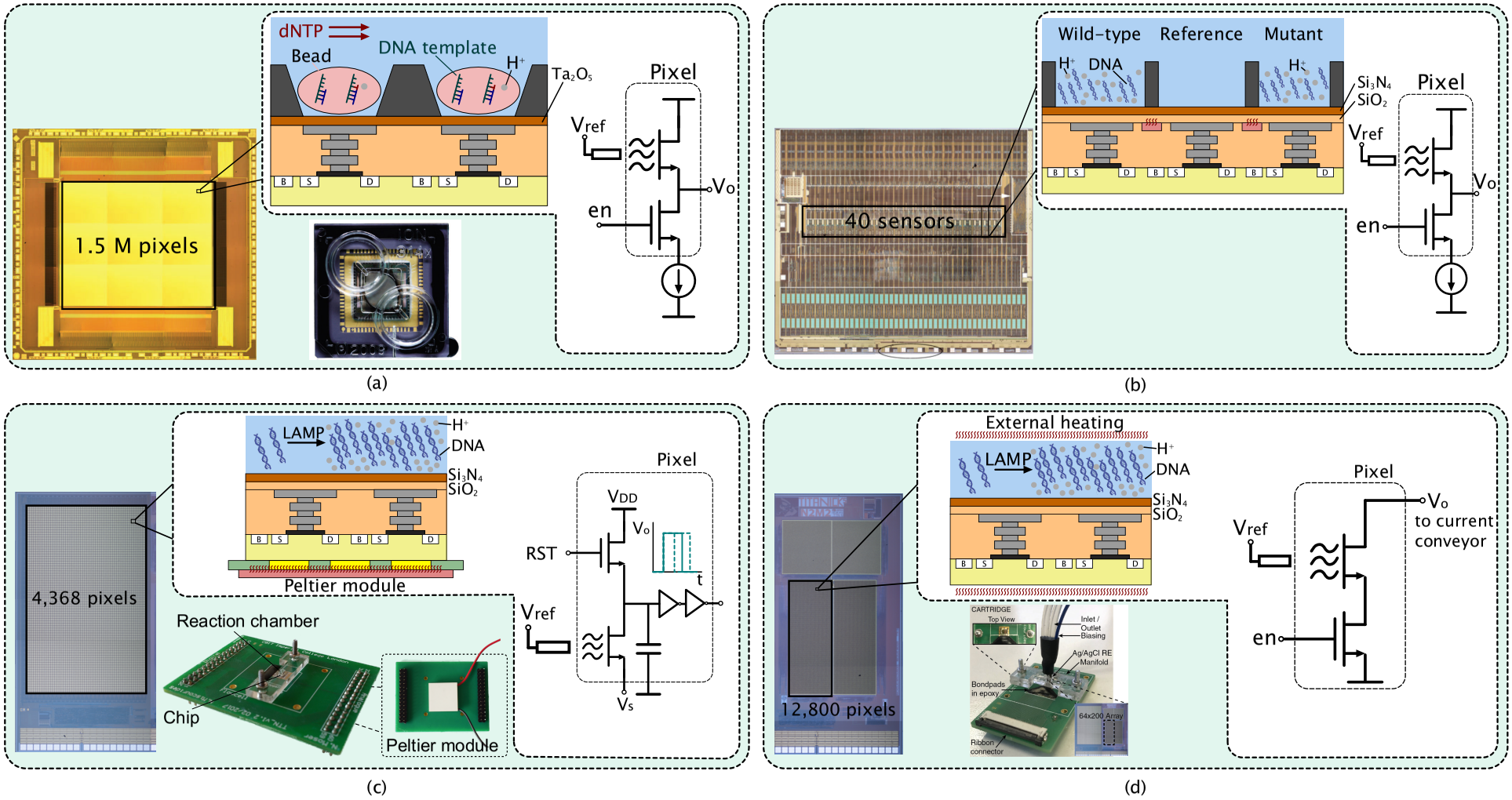


Figure 2.5: ISFET-based LoC platforms for DNA-based applications with a chip microphotograph, cross-section diagram, front-end schematic and encapsulation picture [3]. **(a)** Ion Torrent system for DNA sequencing [29], **(b)** DNAe/Imperial College (IC) chip for multiple gene detection [32, 35], **(c)** High signal resolution IC chip integrating 4,368 sensors for DNA detection and temperature regulation [26] and **(d)** IC chip integrating 12,800 sensors for DNA detection [33].

Bibliography

[1] R. R. Sinden. *DNA structure and function*. eng. 1st ed. San Diego ; London: Academic Press, 1994. ISBN: 0126457506.

[2] L. Bartee. *Principles of Biology:Biology 211, 212, and 213: DNA Structure*. 2017.

[3] L. Keeble et al. "ISFET-Based Sensing and Electric Field Actuation of DNA for On-Chip Detection: A Review". In: *IEEE Sensors Journal* 20.19 (2020), pp. 11044–11065.

[4] K. Mullis et al. "Specific enzymatic amplification of DNA in vitro: the polymerase chain reaction". In: *Cold Spring Harbor symposia on quantitative biology* 51 Pt 1 (1 1986), pp. 263–273. ISSN: 0091-7451.

[5] R. Saiki et al. "Primer-directed enzymatic amplification of DNA with a thermostable DNA polymerase". In: *Science* 239.4839 (1988), pp. 487–491. ISSN: 0036-8075.

[6] *Principle of LAMP method: Basic Principle*. Eiken Genome Site. 2005.

[7] J. A. Davis, R. O. James, and J. O. Leckie. "Surface ionization and complexation at the oxide/water interface: I. Computation of electrical double layer properties in simple electrolytes". In: *Journal of Colloid and Interface Science* 63.3 (1978), pp. 480–499. ISSN: 0021-9797.

[8] T. Hiemstra, W. Van Riemsdijk, and G. Bolt. "Multisite proton adsorption modeling at the solid/solution interface of (hydr)oxides: A new approach: I. Model description and evaluation of intrinsic reaction constants". In: *Journal of Colloid and Interface Science* 133.1 (1989), pp. 91–104. ISSN: 0021-9797.

[9] L. Koopal, W. Van Riemsdijk, and M. Roffey. "Surface ionization and complexation models: A comparison of methods for determining model parameters". In: *Journal of Colloid and Interface Science* 118.1 (1987), pp. 117–136. ISSN: 0021-9797.

[10] A. Revil and P. W. J. Glover. "Theory of ionic-surface electrical conduction in porous media". In: *Phys. Rev. B* 55 (3 Jan. 1997), pp. 1757–1773.

[11] M. Grattarola, G. Massobrio, and S. Martinoia. "Modeling H/sup +/-sensitive FETs with SPICE". In: *IEEE Transactions on Electron Devices* 39 (4 Apr. 1992), pp. 813–819. ISSN: 00189383.

[12] D. Chan, T. W. Healy, and L. R. White. "Electrical double layer interactions under regulation by surface ionization equilibria-dissimilar amphoteric surfaces". In: *Journal of the Chemical Society, Faraday Transactions 1: Physical Chemistry in Condensed Phases* 72 (0 Jan. 1976), pp. 2844–2865. ISSN: 03009599.

[13] G. Kovacs. "Introduction to the theory, design, and modeling of thin-film microelectrodes for neural interfaces". In: *Enabling technologies for cultured neural networks* (1994).

[14] T. Hiemstra and W. Van Riemsdijk. "Physical chemical interpretation of primary charging behaviour of metal (hydr) oxides". In: *Colloids and Surfaces* 59 (1991), pp. 7–25. ISSN: 0166-6622.

[15] J. N. Israelachvili and P. M. McGuiggan. "Forces Between Surfaces in Liquids". In: *Science* 241 (4867 Aug. 1988), pp. 795–800. ISSN: 00368075.

[16] H.-J. Butt and M. Kappl. *Electrostatic Double-Layer Forces*. Wiley-VCH Verlag GmbH Co. KGaA, Apr. 2018, pp. 99–129.

[17] P. C. Hiemenz. *Principles of colloid and surface chemistry.* eng. 3rd ed., rev. and expanded / Paul C. Hiemenz, Raj Rajagopalan. Undergraduate chemistry ; 14. New York: Marcel Dekker, 1997. ISBN: 0824793978.

[18] D. C. Grahame. "The electrical double layer and the theory of electrocapillarity." In: *Chemical reviews* 41 3 (1947), pp. 441–501.

[19] P. Georgiou and C. Toumazou. "ISFET characteristics in CMOS and their application to weak inversion operation". In: *Sensors and Actuators B: Chemical* 143.1 (2009), pp. 211–217. ISSN: 0925-4005.

[20] Y. Liu et al. "An Extended CMOS ISFET Model Incorporating the Physical Design Geometry and the Effects on Performance and Offset Variation". In: *IEEE Transactions on Electron Devices* 58.12 (2011), pp. 4414–4422.

[21] B. P. Degnan, P. Hasler, and C. M. Twigg. "Trapped charge characterization and removal on floating-gate transistors". In: *2008 51st Midwest Symposium on Circuits and Systems*. 2008, pp. 617–620.

[22] P. Hammond and D. S. Cumming. "Performance and system-on-chip integration of an unmodified CMOS ISFET". In: *Sensors and Actuators B: Chemical* 111-112 (2005). Eurosensors XVIII 2004, pp. 254–258. ISSN: 0925-4005.

[23] N. Miscourides and P. Georgiou. "Impact of Technology Scaling on ISFET Performance for Genetic Sequencing". In: *IEEE Sensors Journal* 15.4 (2015), pp. 2219–2226.

[24] A. Hassibi et al. "Comprehensive study of noise processes in electrode electrolyte interfaces". In: *Journal of Applied Physics* 96.2 (2004), pp. 1074–1082.

[25] N. Moser et al. "ISFET Arrays for Lab-on-Chip Technology: A Review". In: *2019 26th IEEE International Conference on Electronics, Circuits and Systems (ICECS)*. 2019, pp. 57–60.

[26] N. Moser et al. "A Scalable ISFET Sensing and Memory Array With Sensor Auto-Calibration for On-Chip Real-Time DNA Detection". In: *IEEE Transactions on Biomedical Circuits and Systems* 12.2 (2018), pp. 390–401. ISSN: 1932-4545.

[27] M. Cacho-Soblechero et al. "A Dual-Sensing Thermo-Chemical ISFET Array for DNA-Based Diagnostics". In: *IEEE Transactions on Biomedical Circuits and Systems* (2020), pp. 1–1.

[28] J. Zeng, N. Miscourides, and P. Georgiou. "A 128×128 Current-Mode Ultra-High Frame Rate ISFET Array for Ion Imaging". In: *2018 IEEE International Symposium on Circuits and Systems (ISCAS)* (2018), pp. 1–5.

[29] J. M. Rothberg et al. "An integrated semiconductor device enabling non-optical genome sequencing". In: *Nature* 475.7356 (2011), pp. 348–352. ISSN: 0028-0836.

[30] M. J. Milgrew and D. R. S. Cumming. "Matching the Transconductance Characteristics of CMOS ISFET Arrays by Removing Trapped Charge". In: *Electron Devices, IEEE Transactions on* 55.4 (2008), pp. 1074–1079. ISSN: 0018-9383.

[31] N. Moser et al. "ISFETs in CMOS and Emergent Trends in Instrumentation: A Review". In: *IEEE Sensors Journal* 16.17 (2016), pp. 6496–6514. ISSN: 1530-437X.

[32] C. Toumazou et al. "Simultaneous DNA amplification and detection using a pH-sensing semiconductor system". In: *Nature Methods* 10 (2013), pp. 641–646.

[33] N. Miscourides et al. "A 12.8 k Current-Mode Velocity-Saturation ISFET Array for On-Chip Real-Time DNA Detection". In: *IEEE Transactions on Biomedical Circuits and Systems* 12.5 (2018), pp. 1202–1214.

[34] K. Malpartida-Cardenas et al. "Quantitative and rapid Plasmodium falciparum malaria diagnosis and artemisinin-resistance detection using a CMOS Lab-on-Chip platform". In: *Biosensors and Bioelectronics* 145 (2019), p. 111678. ISSN: 0956-5663.

[35] D. M. Garner et al. "A multichannel DNA SoC for rapid point-of-care gene detection". In: *Digest of Technical Papers - IEEE International Solid-State Circuits Conference* 53 (2010), pp. 492–493. ISSN: 01936530.

Chapter 3

Spatio-Temporal Simulation of ISFET-based DNA Detection

3.1 Introduction

Accurate models are required to design ISFET arrays and ensure that they are fit for purpose. This must take into consideration the front-end of the system, namely the interaction between the insulating oxide and the electrolyte that gives rise to ion-sensitivity. Commonly, models relate the surface concentration of protons to that of the bulk through the Boltzmann relation (Equation 2.7). This is an adequate approximation for homogeneous solutions where there is little spatial variation in pH.

However, in the case of detecting DNA amplification, where proton production is localised to regions of replicating DNA, there may be significant space and time (spatio-temporal) dependence of surface proton concentration. When this reaction is imaged using an array of ISFETs, the output of individual sensors will be dependent on their position relative to amplifying DNA. ISFETs far from the amplifying DNA will likely measure a smaller threshold voltage change than those closer to where the protons are being produced, due to the finite diffusion times of protons across the array. This information will be lost by the use of a bulk-approximation and so it is vital to estimate surface proton concentration directly by simulating reactions and proton transport.

The concept of a Monte-Carlo simulation of proton transport was tested by Kunal Katarya as part of their master's project and many pieces of code developed during that project are used in the Monte-Carlo first passage simulation presented in this chapter [1]. Many thanks to Dr. Malpartida Cardenas for providing experimental data. Large batches of simulations were run using Imperial College London's High Performance Computing cluster. Other contributions are explicitly stated.

A model of LAMP reactions, generation of protons, and ISFET detection was developed by Dr. Moniri [2] that exhibits spatio-temporal dependence and underpins the work in this chapter. However, in this model, protons were projected onto the underlying array at the time and position at which they were produced. Such an approximation was appropriate for the intended application of the model, to generate datasets on which algorithms could be tested. But to estimate the effect of DNA positioning on ISFET signal during amplification, there must be a spatio-temporal dependence of the detection of a proton based on where it originated. Protons starting further from the sensors will tend to be detected later and will travel further laterally to the sensing surface than those generated close to the sensors and this must be reflected in the model.

Three simulation approaches that incorporate proton diffusion will be presented in this chapter. The first utilises probabilistic first-passages as part of a novel Monte-Carlo simulation. The second uses a level-set simulation implemented in the commercial FEM software, COMSOL Multiphysics.

3.2 LAMP Model

To assess what simulation approaches might be suitable, the existing LAMP model, developed by Dr. Moniri, must first be introduced.

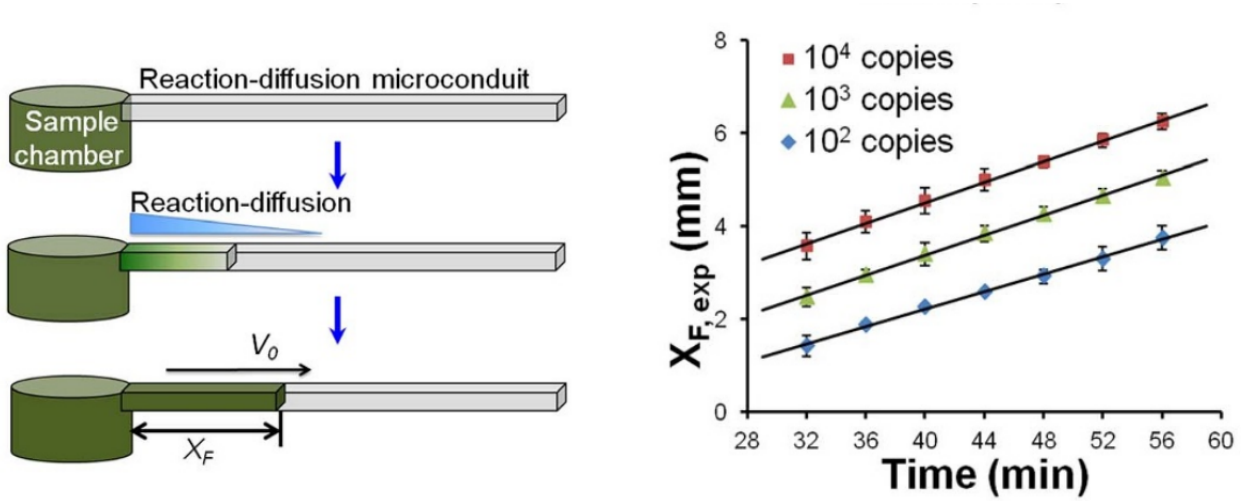
3.2.1 DNA Dynamics

The complete mechanism of DNA amplification via LAMP is overly complex for simulation, with many reagents and products. The existing LAMP model makes a simplification, based on observations from Liu *et. al.* 2014 regarding amplification dynamics, that circumvents the need for modelling the reaction itself. In Liu *et al.* 2014, a LAMP reaction was initiated within a reaction chamber that was connected to a microfluidic channel, as illustrated in Figure 3.1a. The channel contained reagents for amplification but none of the target DNA, which was only added to the reaction chamber. Liu *et al.* noted that the reaction moved down the microfluidic channel at a constant velocity, driven by both the replication of the DNA and its diffusion: a reaction-diffusion process.

Liu *et al.* developed a model that estimated the propagation front velocity as,

$$v_{front} = 2\sqrt{kD} \tag{3.1}$$

where D is the diffusivity of the molecule and k is a reaction constant for the LAMP reaction.



(a) (b)

Figure 3.1: (**a**) A schematic of the experiment in Liu *et al.* 2014 and (**b**) a graph of progress of the reaction front along the microfluidic channel, measured using fluorescence microscopy, against time, showing the constant velocity of DNA LAMP reaction-diffusion [3].

k is estimated through fitting a sigmoid of the form,

$$I(t) = \frac{I_0}{(1 - I_0)exp(-kt) + I_0} \tag{3.2}$$

to amplification curves of fluorescence intensity, I, obtained experimentally through benchtop thermal-cyclers, where I_0 is the initial fluorescence intensity. Liu *et al.* found the theoretical front velocity provided by Equation 3.1 of $1.8\,\mu m/s$ to be in good agreement with their experimental value of $1.73 \pm 0.15\,\mu m/s$. This speed was determined within a solution containing $0.04\,\%$ hexamethyldisilazane (HMDS) to limit diffusion of DNA molecules and ensure a sharp reaction-diffusion front for better optical detection.

Transferring these observations to the unrestricted 3D case, it is assumed that amplifying DNA forms spherical clusters that expand at a constant radial velocity. The origin of the spherical cluster is considered to be fixed at the position of the DNA upon initiation of amplification, as diffusion of DNA is already incorporated in the velocity of the propagation front. The radius of an amplifying DNA cluster at time, t, is given by,

$$r = v_{front}(t - t_{init}) + r_0 \tag{3.3}$$

where t_{init} is the time of amplification initiation for the DNA molecule and r_0 is the radius of the DNA cluster before amplification, which can be taken to be the radius of gyration of a DNA molecule. This is dependent on the length of the DNA molecule and is roughly $500\,nm$ for $45\,kbp$ λ-DNA [4].

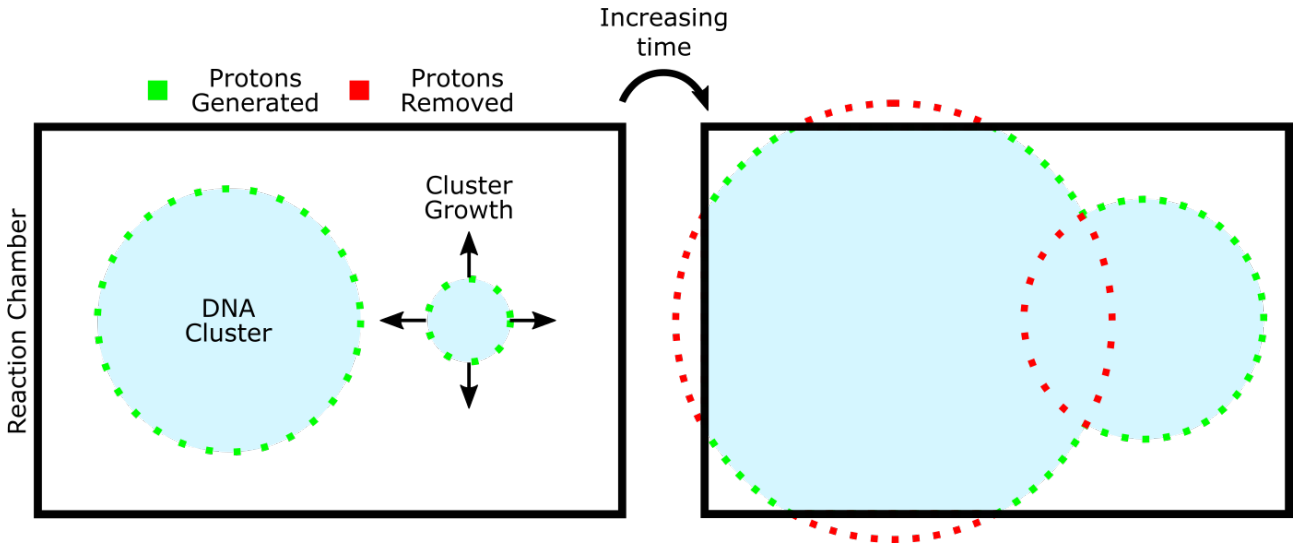


Figure 3.2: A schematic illustrating how protons are generated according to the LAMP model in [2].

This simplification obscures the mechanism by which amplification is initiated - the annealing of a primer with the target DNA. Thus, a probabilistic initiation time for each copy of the target DNA in the sample is required. The time of amplification initiation can be drawn from a normal distribution, whose mean and variance must be determined from a histogram of single-molecule amplification initiation times. Once the reaction is initiated, DNA will start to replicate and form expanding spheres of densely concentrated DNA.

3.2.2 Proton Production

As the propagation front expands radially, the amplification reaction will largely be confined to the surface of the DNA cluster, since it is these molecules that have ready access to reagents. The rate at which protons are produced at time, t, in $mols^{-1}$ for a single DNA cluster is thus assumed to be linearly proportional to the cluster's area, A,

$$\frac{dN}{dt} = \beta A(t) \tag{3.4}$$

where β is a constant of proportionality that represents a particle flux with dimensions $mols^{-1}m^{-2}$ and will be referred to as the proton flux.

The total cluster surface area is the sum of spherical surfaces areas, $A = 4\pi r^2$, of clusters that have begun amplifying. Thus, the rate of proton production is given by the equation,

$$\frac{dN}{dt} = 4\pi\beta \sum_{n=1}^{N_{clusters}} (v(t - t^n_{init}) + r_0)^2 H(t - t^n_{init}) \tag{3.5}$$

where $N_{clusters}$ is the total number of DNA clusters in the sample and $H(t-t^n_{init})$ is the Heaviside step function, which equals 0 for $t < t^n_{init}$ and 1 for $t \geq t^n_{init}$.

The total number of protons produced at a given time is the integral of Equation 3.5,

$$N(t) = \frac{4\pi\beta}{3v_r} \sum_{n=1}^{N_{clusters}} (v(t - t^n_{init}) + r_0)^3 \tag{3.6}$$

The surface area of the DNA cluster is defined as that not within another cluster, with a propagation front unable to progress through a cluster due to a lack of reagents, or outside of the bounds of the reaction chamber, as demonstrated by Figure 3.2. There is no trivial expression for the surface area of arbitrarily located and sized spheres intersecting with one another or with a cuboid. As such, out of the number of protons produced at a given time, according to Equation 3.6, protons that violate these criteria will need to be identified and removed from the simulation.

There will also be clusters that will not initiate amplification before they are enveloped by other clusters and will therefore not contribute to the production of protons. To reduce the computational burden, clusters that do not initiate before being enveloped are removed from the simulation. The full process of DNA amplification and proton generation is laid out in Routine 1.

Routine 1: Proton Generation Algorithm

1. Draw 3 uniform random variables, U, per initial DNA molecule to randomly distribute the origins of DNA clusters within the reaction chamber with dimensions $(x_{size} \times y_{size} \times z_{size})$,

$$0 \leq U_x \leq x_{size}$$

$$0 \leq U_y \leq y_{size}$$

$$0 \leq U_z \leq z_{size}$$

2. Draw amplification initiation times, t^i_{init}, for each cluster, i, from a normal distribution determined from empirical data.

3. Remove clusters that at their initiation time are within other, amplifying clusters.

4. Jump a time-step, t^r_{step}, in the reaction time, t^r.

5. The number of amplifying clusters is

$$N_{Amp} = \sum_{i=1}^{N_{clusters}} t^i_{init} \leq t^r$$

6. Calculate new radii for each amplifying cluster, j,

$$r^j_{new} = (v(t^r - t^j_{init}) + r_0)$$

.

7. Calculate the number of protons to release on each cluster, based on its radius at the previous time-step, r^j_{old},

$$N^j_{release} = \frac{4\pi\beta}{3v}(r^j_{new} - r^j_{old})^3$$

8. Create $N^j_{release}$ random points on the surface of sphere j in spherical coordinates,

$$0 \leq longitude \leq 2\pi$$

$$0 \leq latitude \leq \pi$$

$$a = cos(longitude)sin(latitude)$$

$$b = sin(longitude)sin(latitude)$$

9. Convert points from spherical to Cartesian coordinates,

$$x = r_{new}a + U_x$$

$$y = r_{new}b + U_y$$

$$z = r_{new}cos(latitude) + U_z$$

10. Remove points that are outside the reaction chamber or within other clusters.

11. Repeat Steps 4-10 until $t^r = t_{end}$ or a reaction step with no new protons produced occurs after the first cluster has begun amplifying, t^1_{init}.

3.3 Diffusion

Having been generated at the surface of the amplifying clusters, protons will start moving randomly due to diffusion. Diffusion, or Brownian motion, describes the random fluctuations in a particle's position over time due to particle-particle collisions. Einstein's theory on Brownian motion [5] deduced that in one dimension, the probability that a particle occupies the position $x + \Delta x$ at time $t + \Delta t$ is the Gaussian distribution,

$$P = \frac{1}{\sqrt{4\pi D\Delta t}} exp(-\frac{\Delta x^2}{4D\Delta t}) \tag{3.7}$$

Typically, the diffusion coefficient of a particle with radius, r, is given by the Stokes-Einstein relation,

$$D = \frac{k_b T}{6\pi\eta r} \tag{3.8}$$

where η is the viscosity of the solution. This relationship links particle diffusivity to medium viscosity, which, in the case of a LAMP reaction solution, is a function of DNA concentration and suggests that protons may diffuse more slowly in regions of high DNA concentration. Liu *et al* estimated a maximum concentration of DNA of $1.1 \times 10^{-13}\, M$ after the LAMP reaction had terminated, based on 1000 initial copies. This is at least $1000\times$ smaller than the concentrations used in studies of DNA solution viscosity in the literature [6][7], whilst the measured viscosities are only single digit factors larger, suggesting very little change in proton diffusivity [1]

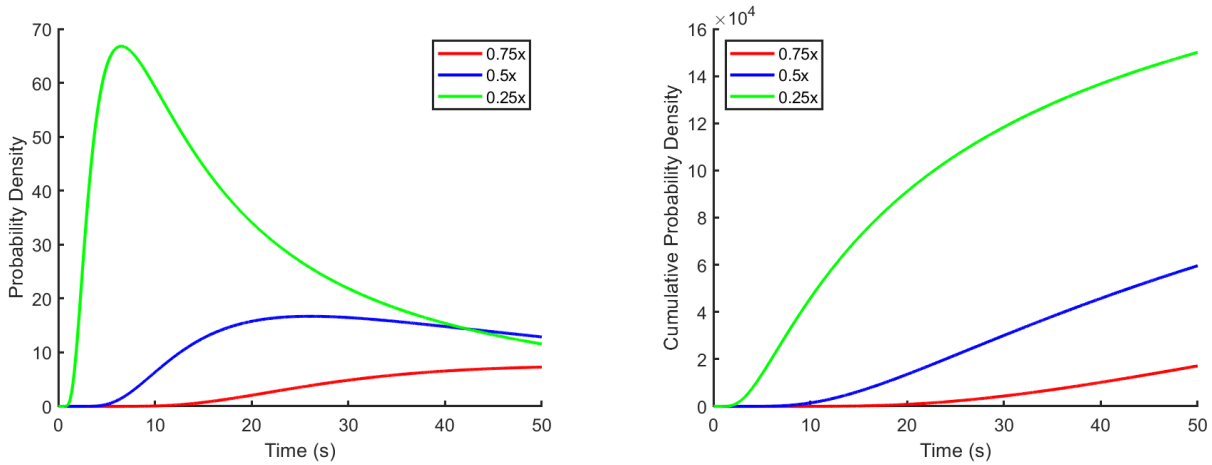
In 1D, given a starting point, x, the probability that a particle reaches a point, $x+\Delta x$, at time, t, is given by the first-passage distribution, which is a Fourier series [8]. A simplified expression is obtained for a semi-infinite boundary condition,

$$P_{FP} = \frac{\Delta z}{\sqrt{4\pi D t^{3/2}}} exp(-\frac{\Delta z^2}{4D\Delta t}) \tag{3.9}$$

with the upper limit in z set to infinity and an absorbing boundary at $z = 0$. An example of the first-passage probability density function (PDF) and cumulative density function (CDF) for protons in water is provided in Figure 3.3. Over a time-step, Δt, the displacement of a particle due to diffusion is given by the Smoluchowski equation,

$$\Delta x = \sqrt{2D\Delta t} N \tag{3.10}$$

[1] The validity of the Stokes-Einstein equation for protons travelling through water is questionable. In this case, proton transport occurs via the Grothuss mechanism, whereby they travel via the hydrogen bonds formed between water molecules, leading to faster diffusion times than would be expected. These fast diffusion times will lead to a greater computational burden for simulations tracking individual random walks.



(a) PDF (b) CDF

Figure 3.3: The PDF (**a**) and CDF (**b**) for the first-passage distribution of protons in water hitting the $z = 0$ plane, calculated for Δz values $0.25\times$, $0.5\times$, and $0.75\times$ the solution height used in experiments of $2.5\,mm$.

where N is a unit mean, unit variance normally distributed random number and Δt must be chosen such that Δx is significantly smaller than the boundaries of the system [9].

The characteristic mixing time is,

$$t_m = \frac{L^2}{4D} \tag{3.11}$$

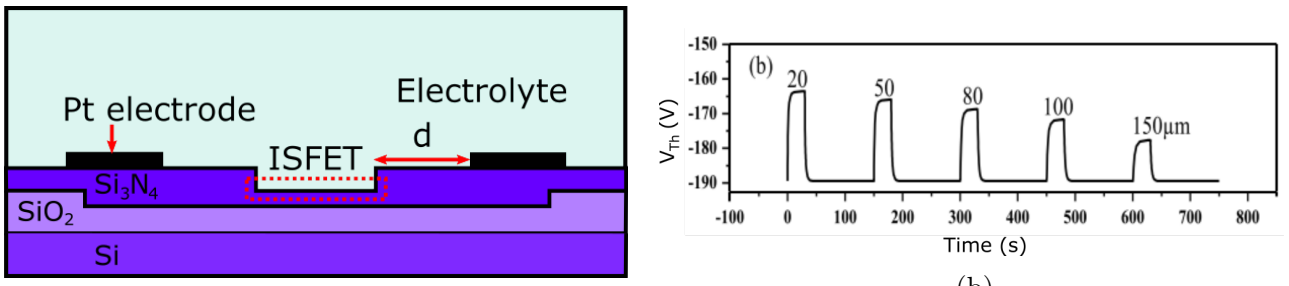
where L is the characteristic dimension of the chamber. A system evolving over a time longer than t_m is considered to be well-mixed and the concentration of particles to be uniform. With a diffusion coefficient of $D = 1 \times 10^{-8}\,m^2 s^{-1}$ [10], the mixing time for a proton within a reaction chamber with dimension $L = 2 \times 10^{-3}\,m$ is roughly $100\,s$. As ISFET arrays have frame rates on the order of $1\,s$ and below, the mixing time demonstrates the significance of spatial information in modelling ISFET-based DNA detection, as the solution cannot be treated as homogeneous.

3.4 Approaches to Simulating ISFETs with Spatio-Temporal Dependency

With the existing LAMP model outlined and the diffusive phenomena that need to be incorporated into it introduced, the most suitable approaches to simulating the model must be identified.

Year	Paper	Implementation	Application
1990	Luo *et al.* [11], W. Olthuis [12]	Pascal	Migration effect at ISFET-based coulometric sensor-actuator system
1992	Martinoia *et al.* [13][14]	H-SPICE	Macromodel for ISFET development
	Meixner *et al.* [15]	Turbo Pascal 5.5	ImmunoFETs – Protein detection
1997	Verzellesi *et al.* [16]	HFIELDS, box integration method (BIM) discretisation	Feed into TCAD simulations for ISFET process characterisation
2000	Kuhnhold *et al.* [17]	Mathematica	Investigate response of buried sites and surface oxidation on ISFET performance
2004	Janicki *et al.* [18]	Newton-Gauss parameter extraction (MATLAB), ISFET simulation in SPICE	ISFET characterisation with thermal effects
2005	Chung *et al.* [19]	H-Spice	H-SPICE micromodel with temporal drift
2009	Naimi *et al.* [20]	Genetic algorithm parameter extraction, least-squares fit optimisation	Model ISFET thermal drift
2010	Jarmin *et al.* [21]	P-SPICE	Characterisation of ISFET pre-fabrication
	Sundaram *et al.* [22]	C	Surface diffusion model of V_{Th} drift
2012	Uno *et al.* [23]	COMSOL	Lipid-bilayer detection
2014	Passeri *et al.* [24]	Synopsys Sentaurus TCAD	Study of ISFETs for biosensors
	Ma *et al.* [25]	Equivalent circuit, H-SPICE	Characterisation of extended gate ISFETs
2016	Abdolkader *et al.* [26]	Newton-Raphson algorithm (MATLAB)	Nanoscale ISFETs
	Aoun *et al.* [27]	COMSOL	Electrolysis detection
2017	Parizi *et al.* [28]	COMSOL	Study counterion size effect on ISFET sensitivity
2018	Mohammadi *et al.* [29]	TCAD	Characterisation
2019	Wrege *et al.* [30]	MATLAB algorithm	Characterisation of chip designed in Virtuoso
	Dinar *et al.* [31]	Silvaco TCAD	Technology specific simulation; Comparing GC/GCS models for pH sensitivity
2020	Mele *et al.* [32]	Linear equation system	Ion cross-sensitivity
2021	Grour *et al.* [33]	Verilog-A	TMD-ISFET
2022	Pandey *et al.* [34]	TCAD	Polarity controllable-ISFET sensitivity analysis
2023	Ghomi *et al.* [35]	Verilog-A, Newton-Raphson	Circuit-level simulations
	Dhar *et al.* [36]	Bisection	High-κ oxide effect on amino acid sensing
	Xie *et al.* [37]	Finite-element, artificial neural network	Ultra-fast ISFET simulation

Table 3.1: A table containing studies where ISFET simulation was a major part of the work and considered the insulator-electrolyte interface as part of pH detection.



(a) (b)

Figure 3.4: (**a**) A representation of the FEM geometry used in Aoun *et al.* 2016 and (**b**) a graph of ISFET threshold voltage against time, with varying distances between the Pt electrode and the ISFET, d, for a 30 s electrode polarisation time [27].

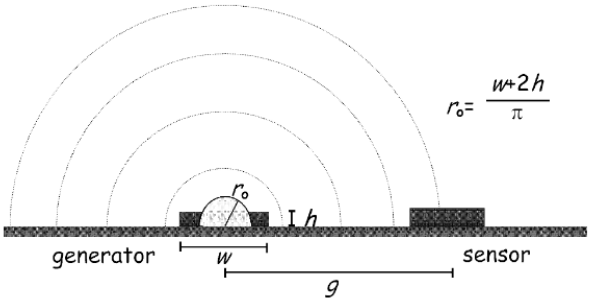
3.4.1 ISFET Simulations

A literature survey was conducted to find examples of simulations of ISFET sensing that explicitly considered the insulator-electrolyte interface, with Table 3.1 collecting the relevant studies. Simulations of ISFETs typically focus on the sensor-level to optimise designs for fabrication, through software such as Cadence or TCAD. The sensing front-end of the system needs to be incorporated to estimate the sensitivity of the readout. In its simplest form, this is done by approximating a pH change as a step voltage signal applied to the gate, typically the Nernstian sensitivity of $59\,mV/pH$. This can be taken a step further by adding an equivalent circuit model to represent the insulator-electrolyte interface, such as that seen in Figure 2.4 [25].

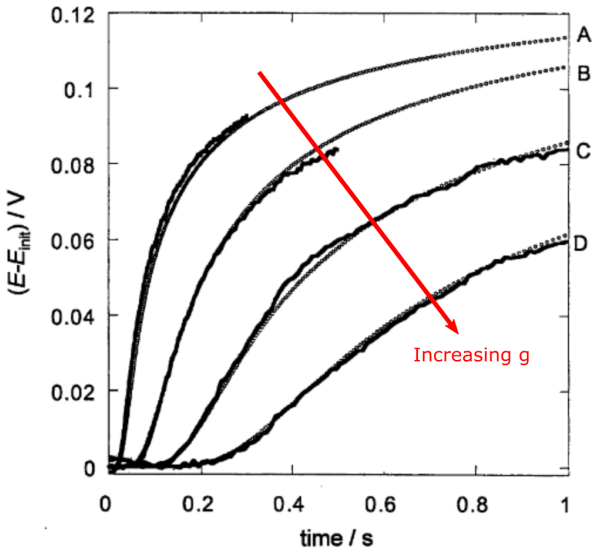
Many simulations use a workaround in SPICE [22, 25, 13, 14] or TCAD [29, 31] to replicate the electrolyte as a semiconductor element with pH-dependent characteristics. The Boltzmann relation is used to determine the surface charge of this element based on the pH of the bulk solution, which is treated as homogeneous [24, 31]. A time-dependent signal can then be obtained by varying the parameters of this electrolyte block in accordance with the pH change over time.

A good example of a spatio-temporal ISFET simulation can be found in Aoun *et al.* 2016, which describes ISFET detection of protons generated by hydrolysis at a platinum (Pt) electrode [27]. The FEM software COMSOL Multiphysics 4.3b is used. A FEM software will break a geometry created in its computer-aided design (CAD) interface into a mesh of elements. It will then solve sets of equations for the relevant physics and boundary conditions to give field values at each elemental node. ISFET threshold voltage was estimated as a linear function of surface proton concentration using Equation 2.2. The separation between the Pt electrode and the ISFET was then varied, with the signal becoming smaller and more delayed as the separation was increased, which demonstrates the spatial and temporal components of the model and can be seen in Figure 3.4.

One advantage of a FEM implementation is that the computational complexity would scale with



(a)



(b)

Figure 3.5: (**a**) A schematic of the generator-collector ETOF system used in Slowinska *et al.* 2003 and (**b**) a graph of change in collector electrode potential against time, with varying distances between the generator and collector [38]. The inter-electrode distance, g, increases from lines A to D. The solid line shows the experimental data, whilst the theoretical model is denoted with open circles.

the volume of the reaction solution instead of the number of protons being produced. FEM simulations could still take prohibitively long to execute when the sample solution is large, but the power of the software to incorporate complex geometries and a wide range of phenomena, such as equilibrium surface reactions, makes it an attractive approach for simulating ISFETs.

3.4.2 Other Electrochemical Simulations

After surveying examples of ISFET simulation, the scope of the search was broadened to other electrochemical sensing modalities to identify techniques that could be applicable to ISFETs. Electrochemical time-of-flight (ETOF) experiments provide interesting case studies of time and space-dependent measurement of particle diffusion [39, 38]. ETOF is used to measure diffusion rates of electrochemical species that are generated at one electrode and detected at another. The concentration of the generated species at the measuring electrode is a function of both the time after generation and the distance between the two electrodes, based on the first-passage distribution for diffusion of particles [40]. The diffusivity of the particle can then be estimated by fitting a theoretical model to graphs of collector electrode current or potential against time. An example of an ETOF experimental configuration and measurements from Slowinska *et al.* 2003 is supplied in Figure 3.5.

This is where the LAMP model becomes complex to simulate, as there is no analytical solution

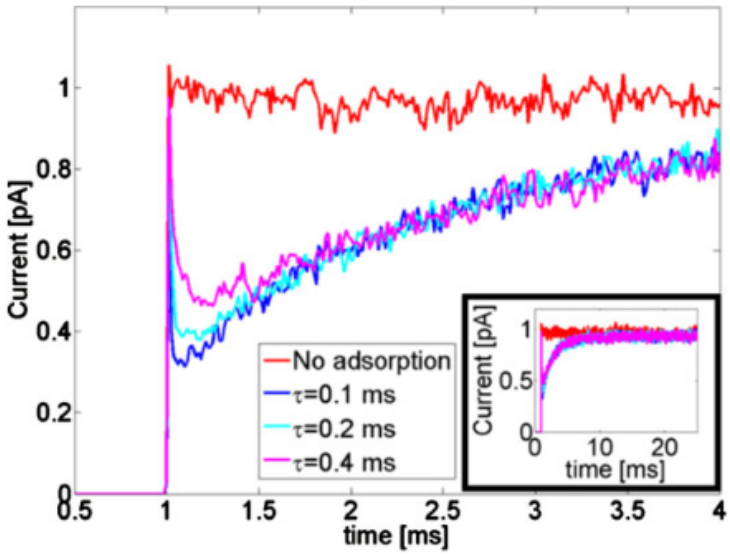


Figure 3.6: A graph of the time response of electrode current due to collision of molecular random walks with varying adsorption time, τ, from Krause *et al.* 2014 [41].

for the surface area of overlapping spheres with arbitrary radii and origins. Thus, there is no way to describe the initial concentration of protons as a function of space and time, nor subsequently the surface proton concentration. This prevents an analytical approach, such as that used for ETOF modelling, from being used for ISFET-based DNA detection. As such, numerical and Monte-Carlo approaches are the most feasible for implementation.

One such Monte-Carlo approach to the simulation of a collector-generator system was conducted in Cutress *et al.* 2011 by sampling the random walks of individual target particles using the Smoluchowski equation and tracking their location over small time-steps [42]. A similar approach was used in Krause *et al.* 2014 to model the transport of redox species to a set of interdigitated electrodes and estimate the current induced by electrochemical reactions [41]. The initial reaction solution is homogeneous, which would be aptly represented with steady-state models that give time-independent solutions. However, this study was looking specifically at the response time of the system - the time taken to reach the steady-state signal - as illustrated in Figure 3.6. Notably, Krause implemented a probabilistic absorption process of particles with the electrodes.

The random walk model is straightforward to implement, but is a computationally intensive simulation to run due to the quantity of random numbers to generate and calculations to perform in tracking individual random walks over many, small time steps. Taking inspiration from ETOF experiments, rather than simulating the full random walks, it may be possible to randomly sample the time it takes protons to reach the sensing surface from the first-passage distribution, therefore reducing the computational burden. This first-passage time can then subsequently be used to sample the protons' lateral displacement, creating a spatial dependence

of ISFET array signal.

3.5 Monte-Carlo Implementation

The first simulation approach to be considered is the Monte-Carlo first-passage, which is implemented in MATLAB. To validate this approach, a random walk simulation is also developed as a benchmark.

3.5.1 Random Walk Model

The most straightforward simulation of a proton's diffusive motion is to track its random walk after they are released. This requires randomly sampling the Smoluchowski equation (Equation 3.10) three times using unit mean, unit variance normal variables (N) with $\Delta t \ll t_m$ and updating the x, y, and z-coordinates of the proton. If a proton's updated coordinates are outside the boundaries of the reaction chamber, a wall collision will take place. For reflecting boundaries, the proton is moved to the intersection point of its diffusive trajectory with the wall. For absorbing boundaries, the proton is removed from the simulation, as if the proton has taken part in a surface reaction or formed part of the EDL and is no longer able to diffuse freely. When a proton meets the surface of a DNA cluster the most likely scenario is that proton diffusivity will not change significantly and protons will travel through DNA clusters relatively unimpeded, as suggested in Section 3.3.

The ISFET sensing region is commonly taken as a Debye's length from the insulating surface above the extended gate of the ISFET. Within this region, protons will influence the surface charge and contribute to the signal. Any protons finishing the time-step within a cuboid above the ISFET sensing area defined by the Debye length will be taken as 'detected', added to that sensor's proton count, and removed from the simulation. Protons hitting the surface outside sensing regions are similarly removed from the simulation. The full process of the random-walk simulation is provided in Routine 2.

One of the key drawbacks of this implementation of proton detection is that all protons will be absorbed given an infinite simulation time, which is not physical. Considering only the Si_3N_4 surface of the chip, at the pH range of interest, $7-9$, and with the solution pH only decreasing over the course of the reaction, the change in surface charge is dominated by transitions from SiO^- to $SiOH$, and transitions from $SiOH$ to $SiOH_2^+$ or $SiOH$ to SiO^- are rare. Thus, monotonic proton capture will provide a consistent net description of the sensing mechanism, up until the system reaches equilibrium after proton production has ceased.

Routine 2: Random Walk Algorithm

1. Generate Cartesian proton release points according to Routine 1.
2. Initialise the diffusion time, $t^D = t^r$.
3. Jump a time step, Δt^D, in the diffusion time, with $\Delta t^D \ll t_m$.
4. Generate 3 unit-mean, unit-variance normally distributed random variables, N, per proton and calculate diffusion displacements in x, y, and z dimensions,
$$\Delta x = \sqrt{2D\Delta t^D} N_x$$
$$\Delta y = \sqrt{2D\Delta t^D} N_y$$
$$\Delta z = \sqrt{2D\Delta t^D} N_z$$
5. Update the x, y, and z-coordinates of the proton,
$$x_{new} = x_{old} + \Delta x$$
$$y_{new} = y_{old} + \Delta y$$
$$z_{new} = z_{old} + \Delta z$$
6. For any proton positions outside the reaction chamber, either move them to the wall (reflecting boundary) or remove them from the simulation (absorbing).
7. If a proton hits the $z = 0$ plane, determine if it hits a sensor and if so, remove from the simulation and add to the proton count for that sensor. If it does not hit a sensor, remove from the simulation.
8. Repeat Steps 3 to 7 until $t^D = t^r + t^r_{step}$.
9. Repeat Steps 2 to 7 at the next reaction time.

3.5.2 First-Passage Model

To streamline the process of determining the time and location of proton detection compared to the random walk approach, the first-passage distribution can be sampled, based on the z-coordinate of a proton's origin. To randomly sample P_{FP}, the CDF is required, obtained by

integrating Equation 3.9 and rearranging to form,

$$\Delta t = (\frac{\Delta z}{erf^{-1}(-U)2\sqrt{D}})^2 \tag{3.12}$$

where U is a uniform random variable between 0-1 and erf^{-1} is the inverse error function.

Having obtained a time of detection for a proton, the x and y displacement over that period must be sampled from the CDF of Equation 3.7, given by,

$$C(x,t) = \frac{1}{2} + \frac{1}{2}erf(\frac{x}{\sqrt{4Dt}}) \tag{3.13}$$

where erf is the error function.

For absorbing boundaries, the random displacement is sampled using the equation,

$$x = erf^{-1}(2U-1)\sqrt{4D\Delta t} \tag{3.14}$$

and protons that fall outside the bounds of the reaction chamber are taken to be absorbed by the walls.

For reflecting boundaries, the CDFs must be truncated before being sampled, according to the distance from the reaction chamber walls in each direction. The lower limit, CDF_{LL}, is calculated for $x = -x_{proton}$ and the upper limit, CDF_{UL}, for $x = x_{size} - x_{proton}$, where x_{proton} is the starting coordinate of the proton. x_{size} is the size of the reaction chamber in the positive direction, given that the wall in the negative direction is at $x = 0$. The randomly sampled displacement is then obtained using,

$$x = erf^{-1}(2U((C_{UL} - C_{LL}) + C_{LL}) - 1)\sqrt{4D\Delta t} \tag{3.15}$$

The full process of the first-passage simulation is provided in routine 3.

Routine 3: First-Passage Algorithm

1. Generate Cartesian proton release points according to Routine 1.
2. Given the z-coordinate of the proton, calculate the time, Δt, taken for it to reach the ISFET array using Equation 3.9.
3. Using Δt, calculate both the x and y displacement in that time using Equation 3.15 for reflecting boundaries or Equation 3.14 for absorbing.

4. With the updated x and y coordinates of the proton, determine if the proton hits a sensor and add a count to the relevant sensor at the time-step $t^r + \Delta t$.

5. Repeat Steps 2-4 at the next reaction time.

3.5.3 ISFET Output Voltage

Both the random walk and first-passage simulations give the number of protons falling on each sensor as an output. To use this output in conjunction with Equation 2.9 to estimate the threshold voltage of an ISFET, the change in surface charge density is required. It is assumed that each proton that comes into contact with the chip surface takes part in the transition $SiO^- + H_s{}^+ \longrightarrow SiOH$ and the increase in surface charge over the simulation is therefore,

$$\Delta\sigma = \frac{eN_{detected}}{A}$$

where $N_{detected}$ is the number of protons falling on each sensor of area, A.

Since it is assumed that the reaction solution is well-mixed and at equilibrium initially, there is no initial variation in spatial ISFET output. The addition of sensor non-idealities, such as drift and trapped charge, is discounted at this stage, as the models will be compared to experimental datasets which have been compensated for these effects. The simulated voltage is the electric potential at the insulator-electrolyte interface. Yet, this differs from that output by the ISFET, due to attenuation, as described by Equation 2.12. Therefore, the final voltages must be scaled by the attenuation coefficient of the microchip, which has been experimentally measured as 0.48 [43].

3.5.4 Hardware

Simulations of the MATLAB script were conducted on a computing cluster, with 16 nodes, 32 CPUs, and 124 Gb of memory, allowing concurrent execution of up to 50 simulations.

3.6 Finite-Element Implementation

As decided in section 3.4, a FEM implementation of the LAMP model in COMSOL Multiphysics 5.5 was developed. The level-set method was chosen as the most suitable approach for FEM simulation of the LAMP model.

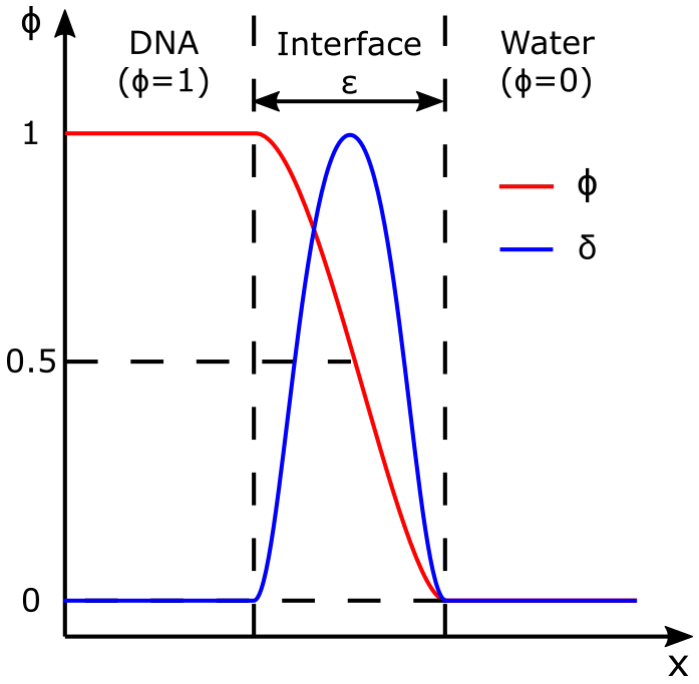


Figure 3.7: An illustrative graph of the level-set phase field (ϕ, **red**) and delta function (δ, **blue**) against distance, showing the two phases for DNA and water and the transition region that defines the interface, with the thickness parameter, ϵ.

3.6.1 Level-Set Method

The level set method treats the phase (ϕ) of the fluid as a scalar field, varying between 0 for the first phase (reaction solution) and 1 for the second (DNA cluster). The interface between the two phases is defined as the point at which the phase field equals 0.5, as demonstrated by Figure 3.7.

The distinction between the two phases is not abrupt. Instead, the phase field at the interface is a smooth step function and the transition zone can be represented by a delta function. This is a more physical representation of the reaction at cluster surfaces, where amplification occurs across a thickness of the DNA cluster that reagents can permeate. Proton production is then defined by a volume reaction rate that is multiplied by the delta function to ensure that the reaction is localised at cluster interfaces.

The growth of DNA clusters in the level-set model is controlled by the convection velocity, which in this case is defined as the radial velocity, v_{front}, in the direction normal to the initial DNA cluster sphere. The surface of the initial DNA cluster sphere, which is a part of the geometry, is defined as a fluid inlet. This inlet is set to release fluid with phase 0 until the cluster's amplification initiation time, and 1 after, using a Heaviside step function.

An array of rectangles on the bottom surface of the reaction solution was used to represent the ISFET array. The two-site binding model was implemented as a set of surface equilibrium

Parameter	Value
pH	8.88
pK(SiO^-)	7.5
pK($SiOH$)	-2.9
Temperature	336.15K
Cluster initial radius	$1.25 \times 10^{-6}\, m$
Surface site density	$5 \times 10^{18} m^{-2} (8.3056 \times 10^{-6}\, mol m^{-2})$
Proton diffusivity	$1 \times 10^{8}\, m^2 s^{-1}$
Surface site diffusivity	$0\, m^2 s^{-1}$
Time-dependent solver tolerance	1×10^{-3}
Minimum mesh element size	$2 \times 10^{-6}\, m$
Maximum mesh element size	$2 \times 10^{-5}\, m$
Reinitialisation parameter	v_{front}
Thickness parameter	$2 \times 10^{-5}\, m$

Table 3.2: A table collating the parameters used within the FEM simulation.

reactions on the bottom face of the reaction chamber. The concentration of each surface state, $[SiOH_2^+]$ and $[SiO^-]$ can be averaged over these rectangles and the surface charge, σ, calculated by the equation,

$$\sigma = e([SiOH_2^+] - [SiO^-]) \tag{3.16}$$

where the state $SiOH$ does not contribute to surface charge. Equation 2.9 can then be used to calculate the change in threshold voltage.

3.6.2 Simulation Parameters

For reliable results, it is vital that the size of the elements that make up the mesh are sufficiently small to capture the spatial gradients of simulated variables. The recommendation is for the minimum element size to be 10 % of the smallest droplet size [44]. Furthermore, the maximum and minimum mesh element sizes should be equal (isotropic mesh) to avoid the phase interface meeting mesh elements that are smaller than it and becoming unstable. For the same reason, it is recommended that the thickness parameter for the phase interface, ϵ, is set as the maximum mesh element size. Simulation results were found to be independent of the thickness parameter for values greater than the maximum mesh element size.

The reinitialisation parameter determines the amount that the phase fields are stabilised during simulation. It is recommended that it is set to the typical velocity of the phase field, in this case v_{front}. Simulation results were found to be independent of the reinitialisation parameter. The tolerance of the time-dependent study controls the allowed error in the integration between time steps. Simulation results were found to be independent of the tolerance for values under 0.001.

Whilst these parameters define the ideal set-up of the FEM simulation, the memory required to execute such a model was larger than the computational resources that were available. As such, the validity of numerical values estimated by COMSOL is questionable and the FEM model should be treated as a proof-of-concept. Future work could attempt to reduce the computational burden of the FEM simulations by using a 2D representation or performing deformed geometry simulations with remeshing of topology changes via COMSOL's MATLAB Livelink.

3.6.3 MATLAB Scripts

To simplify the construction of the model geometry, which contains thousands of entities each with physics defined on them, a MATLAB script was used to create the geometry, physics, mesh, and the studies through COMSOL's LiveLink for MATLAB interface. A separate script was also created to extract results from completed simulations, setting up and executing the surface averages on each ISFET, and extracting the surface concentrations of OH groups.

3.6.4 Surface Site Concentration: 1D Stationary Model

The initial values for the surface concentrations of each state can be obtained from a 1D stationary study. A stationary study finds steady-state (time-invariant) solutions to a system with set boundary conditions. Results from this simulation will provide equilibrium concentrations for a given starting pH, before the amplification reaction has started. The equilibrium surface concentrations in 1D can then be applied to a uniformly distributed 2D surface in the 3D model. These are vital in ensuring the stability of the time-dependent 3D system.

3.6.5 Hardware

Simulations were conducted on a Windows 10 PC with $64\,Gb$ ($4 \times 16\,Gb$) of RAM and an Intel Core i7 7700K ($4.20\,GHz$). Temporary files that COMSOL creates during execution, partly as virtual memory, were stored on a $894\,Gb$ SSD drive.

3.7 Results

Experimental data is taken from Malpartida Cardenas *et al.* 2019 [45], which used a microchip named Titanicks. Reactions were carried out with DNA copy numbers of 1×10^3, 1×10^5, and 1×10^7. pH measurements were taken before and after the reaction. Later simulations are run

Parameter	Value	
	Titanicks	Titan
# ISFETs x-dimension	64	204*
# ISFETs y-dimension	64	290*
ISFET width	$9.5\mu m$	$35\mu m$
ISFET length	$10.5\mu m$	$35\mu m$
ISFET separation	$2\mu m$	$2\mu m$
Solution height	$2.5mm$	$2.5mm$
Chamber width	$2.3mm$	$3.1mm$
Chamber length	$1.5mm$	$2.0mm$
Electrode width	n/a	$52.1\mu m$
Electrode thickness	n/a	$50nm$
Electrode-ISFET separation	n/a	$11.95\mu m$

Table 3.3: A table of parameters used to build the reaction chamber and sensing array for the two simulated microchips.* Only the set of ISFETs within the reaction chamber are simulated.

pH	Surface Site Concentration ($molm^{-2}$)		
	SiO^-	$SiOH$	$SiOH_2^+$
Initial - 8.88	1.657×10^{-7}	8.3049×10^{-6}	1.657×10^{-14}
Final - 7.75	1.4741×10^{-8}	8.2893×10^{-6}	1.8557×10^{-13}

Table 3.4: A table containing 1D stationary simulation results for OH site concentrations for the initial and final pH values from the 1×10^3 DNA copy experiments in Malpartida Cardenas *et al.* 2019 [45].

on an ISFET array named Titan, with design parameters for both of the simulated microchips contained in table 3.3.

3.7.1 Parameter Estimation

Before running simulations, there are multiple parameters that require estimation.

Surface Site Concentration

A 1D stationary study was run in COMSOL, to estimate OH state concentrations at both the initial and final solution pH for the 1×10^3 experiment in Malpartida Cardenas *et al.* 2019 [45]. Simulations were conducted using the PARDISO solver with a tolerance of 0.05. The initial results from Table 3.4 were entered into the 3D time-dependent study without the DNA reaction and the pH remained stable to 3 decimal places. The change in concentration of $SiOH_2^+$ is six orders of magnitude lower than that of SiO^-, which supports the previous assertion that the change in surface charge over the course of these DNA reactions is overwhelmingly dominated by protonation of SiO^- sites.

Amplification Initiation Time

The PDF for amplification initiation times was taken from Dr. Moniri's master's thesis [2], in which a normal distribution with a mean, μ, of $13\,mins$ and variance, σ^2, of $9\,mins$ was extracted from single-molecule amplification data. There was no such data for the experiments in Malpartida Cardenas *et al.* 2019, meaning that comparisons of the absolute times of the signals between simulations and experiments will not be valid.

Speed of Propagation Front

Fitting Equation 3.2 to fluorescent intensity curves obtained using a thermal-cycler for the 1×10^3 DNA copy reaction from Malpartida Cardenas *et al.* 2019 [45], a value of $k = 8.673 \times 10^{-3}\,s^{-1}$ was obtained. A r-squared value of 0.9964 supports the appropriateness of the fitting equation. Equation 3.1 then gave a value for v_{front} of $1.86 \times 10^{-6}\,ms^{-1}$, where the diffusivity of DNA was taken to be $1 \times 10^{-10}\,m^2s^{-1}$ [10]. This value is similar to the $1.8 \times 10^{-6}\,ms^{-1}$ and $1.73 \times 10^{-6}\,ms^{-1}$ theoretical and experimental values respectively, found in Liu *et. al* 2014 [3]. A faster front velocity is expected compared to Liu *et. al* due to the absence of HDMS.

Proton Flux Estimation

In accordance with Equation 3.6, the proton flux parameter, β, is linked to the total volume change of the clusters, in this case the volume of the reaction chamber, and the total number of protons produced during the amplification reaction. The pH of the solution will only account for the protons in the bulk solution. The surface protons must also be included using the simulated estimates in Table 3.4. There will also be protons produced during amplification that take part in buffer reactions and are thus removed from the solution. These removed protons can be disregarded, as they will not interact with the silicon surface nor be included in the pH measurement and thus do not influence the system.

An estimation of β can be obtained through the equation,

$$\beta = v_{front}(10^{-pH_f} - 10^{-pH_i} + (c^f_{SiOH} - c^i_{SiOH})A/V)N_A \tag{3.17}$$

where pH_i and pH_f are the initial and final reaction solution pH respectively, c^i_{SiOH} and c^f_{SiOH} are the initial and final surface concentrations of $SiOH$ from Table 3.4, A is the total silicon area exposed to the solution, V is the volume of the solution, and N_A is Avogadro's constant. For an $8.8\,\mu L$ reaction chamber, the propagation front velocity from Section 3.7.1, and initial and final pH of 8.88 and 7.73 respectively, $\beta = 1.80 \times 10^{13}\,m^{-2}s^{-1}$.

Model	Normal distribution parameters	
	μ	σ
Random walk	-3.0917×10^{-6}	1.0827×10^{-3}
First-passage	9.5273×10^{-7}	1.0823×10^{-3}

Table 3.5: A table showing the fitting parameters, the mean and variance respectively, for the normal distributions displayed in the right of Figure 3.8a.

3.7.2 Monte-Carlo First-Passage Model Validation

To test the validity and estimate the accuracy of the first-passage model, the random walk model was used as a 'ground truth'. Simulations were run with 1×10^5 protons released from a single point. The x, y, and z-coordinates and time of impact with the bottom plane was output. Simulations were run over $2400\,s$, to replicate the expected time window for experimental amplification data.

Without Boundary Conditions

Simulations were first run without any boundary conditions to test the equivalence of the first-passage and random walk models. Protons were released at $0.9\times$ the nominal ceiling height of $2.5\,mm$.

There is excellent agreement between the output of the two models, demonstrated by the reduced-χ^2 value of 1.25, which indicates that model implementation is correct.

The temporal signal is an integral of Equation 3.9. The release of protons from one point in space simultaneously is represented with a Heaviside step function, which changes the limit of the integral so that its final form is,

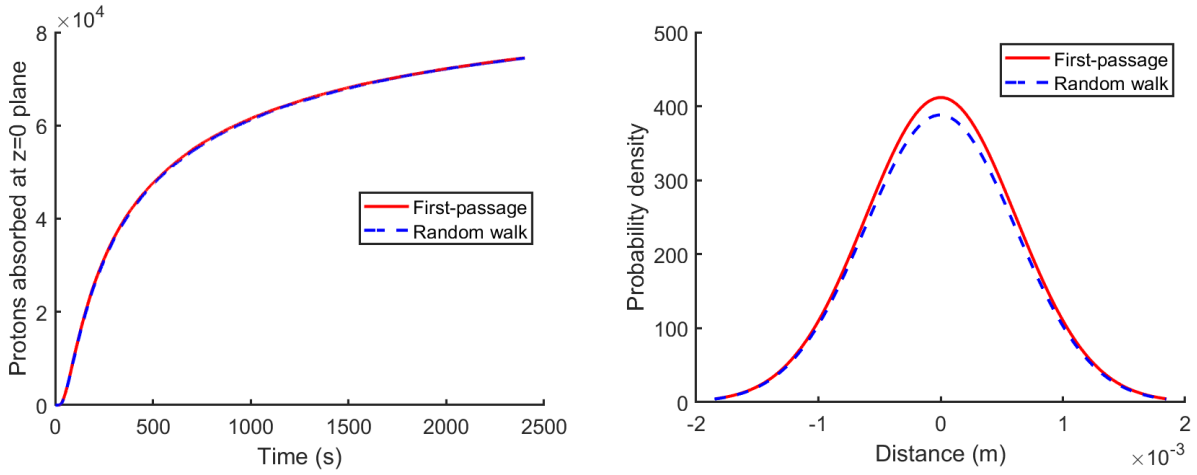
$$S(t) = \int_0^t dt\, exp(-\frac{z_0^2}{4\pi Dt})\frac{z_0}{\sqrt{4\pi Dt}^{\frac{3}{2}}} \tag{3.18}$$

This integral is the lower incomplete gamma function,

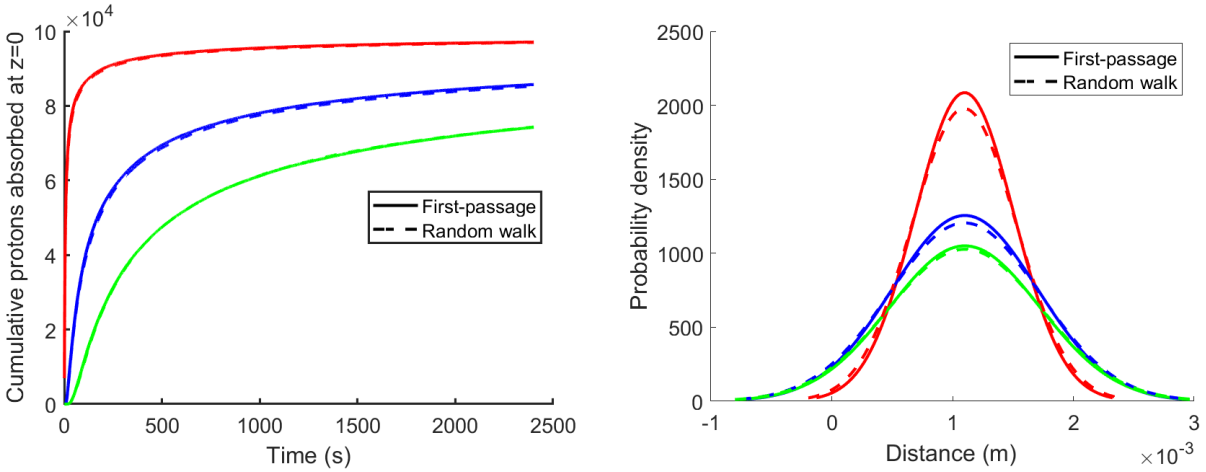
$$\Gamma(s,x) = \int_0^x y^{s-1}e^{-y}dt \tag{3.19}$$

which fits the shape of the simulated data.

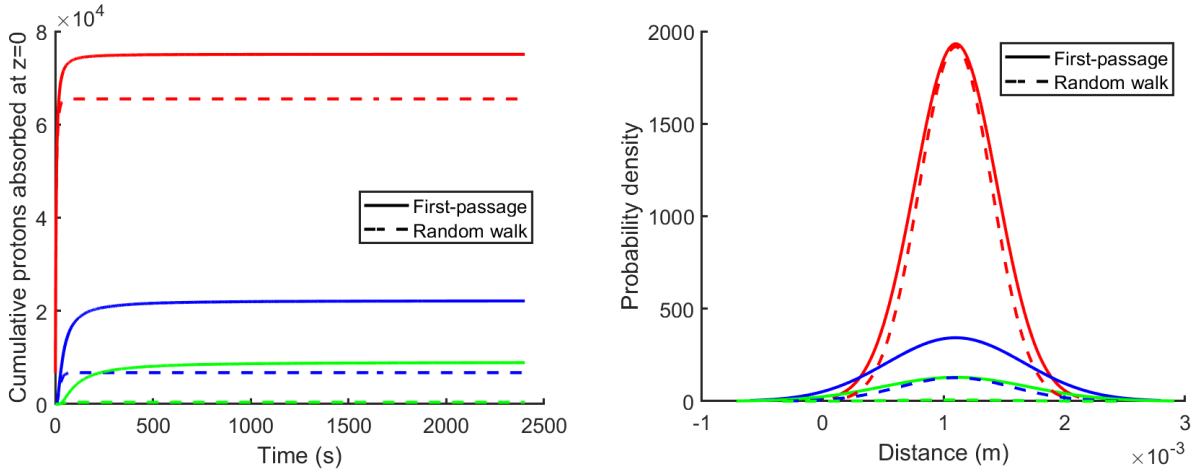
Moving from temporal to spatial output, the graph in the right of Figure 3.8a indicates further agreement between the two models in the spatial distribution of protons hitting the $z = 0$ plane and they both have the expected Gaussian profile, whose fitting parameters are provided in Table 3.5 to further demonstrate their agreement.



(a) No boundary conditions



(b) Reflecting boundary conditions (Semi-infinite)



(c) Absorbing boundary conditions (Semi-infinite)

Figure 3.8: A comparison of temporal (**left**) and spatial (**right**) results for protons absorbed at the $z = 0$ plane for the random walk (**dashed lines**) and first-passage (**solid lines**) simulations with no boundary conditions (**a**), reflecting boundary conditions (**b**), or absorbing boundary conditions (**c**). Where boundary conditions were applied, no ceiling was used so that the semi-infinite approximation held. 1×10^5 protons were released from $0.9\times$ the nominal chamber height of $2.5\,mm$ in all cases, and at $0.1\times$ and $0.5\times$ for the cases with boundary conditions. Boundary conditions were applied at x and y-coordinates of $2.2\,mm$ and $1.5\,mm$ respectively as well as at $x, y = 0$. Protons were released from the middle of these x and y dimensions. The lines in spatial graphs represent normal distributions fitted to histograms of the x-coordinate of protons absorbed at the $z = 0$ plane with 100 bins.

z-distance	reduced-χ^2	
	Reflecting	Absorbing
0.1×	0.987	1.352×10^3
0.5×	5.874	3.258×10^4
0.9×	1.125	1.596×10^5

Table 3.6: A table containing reduced-χ^2 values comparing first-passage and random walk simulation results for both reflecting and absorbing boundaries and at different heights from the sensing plane.

With Boundary Conditions: Semi-Infinite

z-distance	Reflecting				Absorbing			
	Random walk		First-passage		Random walk		First-passage	
	$\mu(m)$	$\sigma(m)$	$\mu(m)$	$\sigma(m)$	$\mu(m)$	$\sigma(m)$	$\mu(m)$	$\sigma(m)$
0.1×	1.096	0.757	1.100	0.719	1.099	0.527	1.101	0.599
0.5×	1.100	1.092	1.102	1.054	1.099	0.819	1.099	0.995
0.9×	1.103	1.116	1.101	1.091	1.085	0.835	1.099	1.062

Table 3.7: A table showing the fitting parameters, the mean and variance respectively, of the normal distributions displayed in the right of Figures 3.8b and 3.8c for reflecting and absorbing boundary conditions respectively.

Simulations were repeated, this time with boundary conditions applied in both positive and negative x and y directions, yet retaining the lack of a boundary condition in the positive z dimension to satisfy the semi-infinite assumption. This was done to verify the correct implementation of the boundary conditions and test their validity. Both reflecting and absorbing boundary conditions were applied at x and y-coordinates of $2.2\,mm$ and $1.5\,mm$ respectively, as well as at $0\,mm$ in both dimensions. The protons were again released from the centre of this rectangle, at heights of 0.1×, 0.5×, and 0.9× the nominal ceiling height of $2.5\,mm$.

The results for reflecting and absorbing boundaries are displayed in Figure 3.8b and 3.8c respectively. The reduced-χ^2 values comparing the first-passage and random walk simulation temporal results are presented in Table 3.6. The reduced-χ^2 values are close to one for reflecting boundaries, demonstrating the close agreement of the two models. In comparison, the absorbing boundaries have values between three and five orders of magnitude larger than one, which indicates poor agreement.

The parameters for the Gaussian histogram fits displayed in the right of Figures 3.8b and 3.8c are provided in Table 3.7. The means of the Gaussians would not be expected to vary significantly between simulations, as it should always be close to the point of proton release, which is $1.1\,mm$. The standard deviation of the models is more significant as it shows the spread of protons through diffusion. The reflecting boundary distributions have standard deviations that are up to 5% smaller than that of their random walk counterparts. In contrast, the

absorbing boundary distributions have standard deviations that are up to 25% larger.

The reason for the discrepancy with absorbing boundaries is an inherent flaw with the first-passage approach. When randomly sampling the lateral displacement of the proton, there is no information on the path the proton took. Therefore, a proton that hits the $z = 0$ plane within the bounds of the walls could have taken any number of paths that brought it into contact with a wall. With reflecting boundaries, this does not impact the total number of protons hitting the $z = 0$ plane. On the other hand, for the absorbing boundaries, there are protons being removed from the random walk simulation that hit the $z = 0$ plane in the first-passage simulation. Since the first-passage model fails to produce valid results with absorbing boundaries, reflecting boundaries should be used moving forwards. Following the same logic allowing for buffer reactions to be neglected, any protons absorbed at boundaries would not contribute to the measured pH or ISFET signal, making reflecting boundaries more suitable [2].

With Boundary Conditions: Finite

The semi-infinite assumption of the first-passage model will introduce errors when compared to experiments that contain a ceiling. To gauge this error, the random-walk simulations for reflecting sidewalls are repeated with a reflecting and an absorbing ceiling. The spatial distribution of protons on the $z = 0$ plane is not considered as it is not affected by the boundary conditions in the z-dimension beyond the error in the first-passage time sampling.

The results displayed in Figure 3.9 indicate that the closer protons are generated to the ceiling, the larger the discrepancy between the random walk and first-passage models. With a release point closer to the sensing plane, fewer protons are expected to interact with the upper boundary and thus the underlying differences in the models are less evident in the output. The signal at $2400\,s$ for reflecting ceiling varies between 3 % and 35 % larger than the first-passage model at $0.1\times$ and $0.9\times$ the solution height respectively. The same values are 8 % and 86 % for the absorbing ceiling. The error in the first-passage model increases as time progresses, as the protons are more likely to interact with the ceiling. The first-passage model performs well up until $100\,s$, which is the mixing time of the system, where discrepancy in the models varies between 0.59% for the $0.1\times$ case, up to 4.12% for the $0.9\times$ case.

3.7.3 First-Passage and FEM Model Comparison

To compare the first-passage and FEM simulation methods with reasonable simulation runtimes, a small representation of the full LAMP model was simulated. A 10×10 array of

[2] A comparison to experimental data for the first-passage model with both reflecting and absorbing boundaries can be seen in appendix C. The results further support the use of reflecting boundaries.

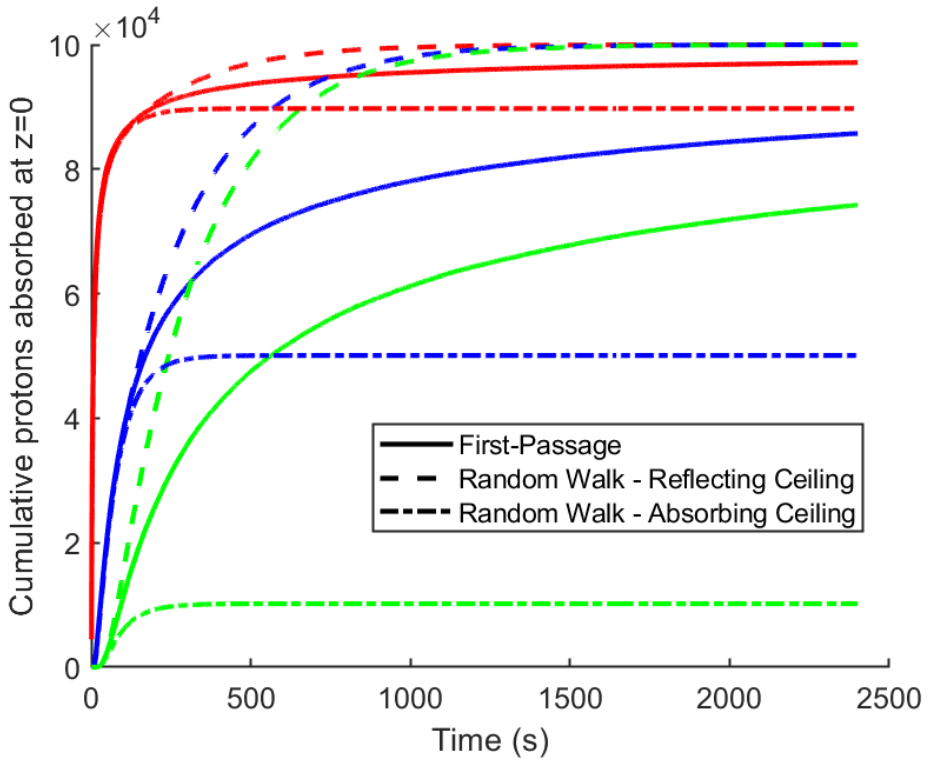


Figure 3.9: A comparison of temporal signals from random walk (**dashed lines**) and first-passage (**solid lines**) simulation of 1×10^5 protons released from $0.1\times$ (**red**), $0.5\times$ (**blue**), and $0.9\times$ (**green**) the chamber height of $2.5\,mm$. Reflecting boundary conditions were used on the side walls, with x and y chamber dimensions of $2.2\,mm$ and $1.5\,mm$. Protons were released from the middle of these x and y dimensions. Both reflecting (**dashed**) and absorbing (**dot-dashed**) boundary conditions were applied to the ceiling, in the positive z dimension.

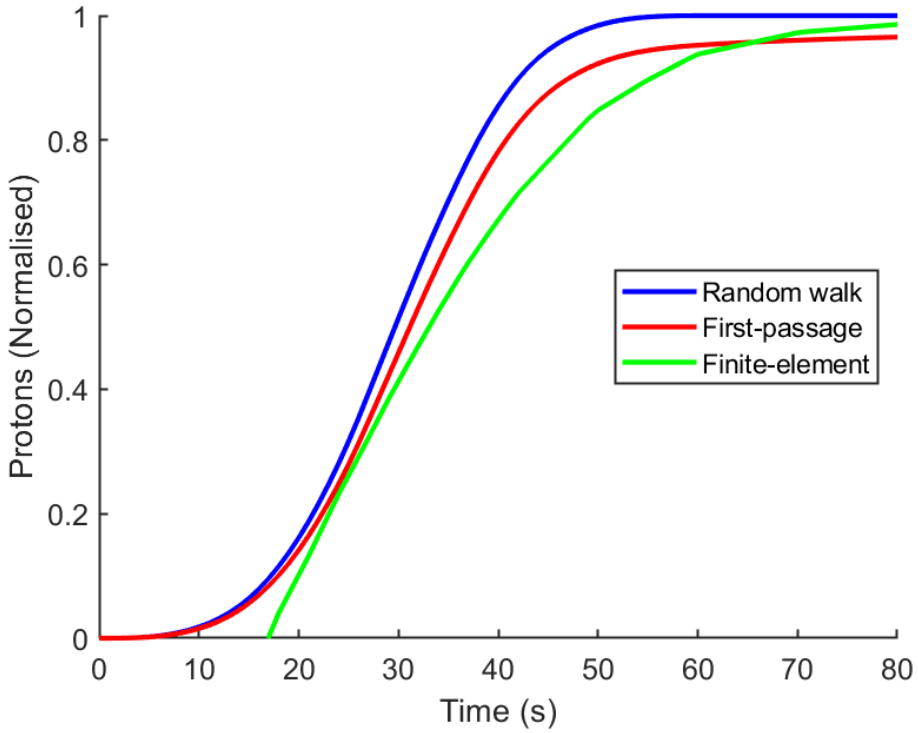


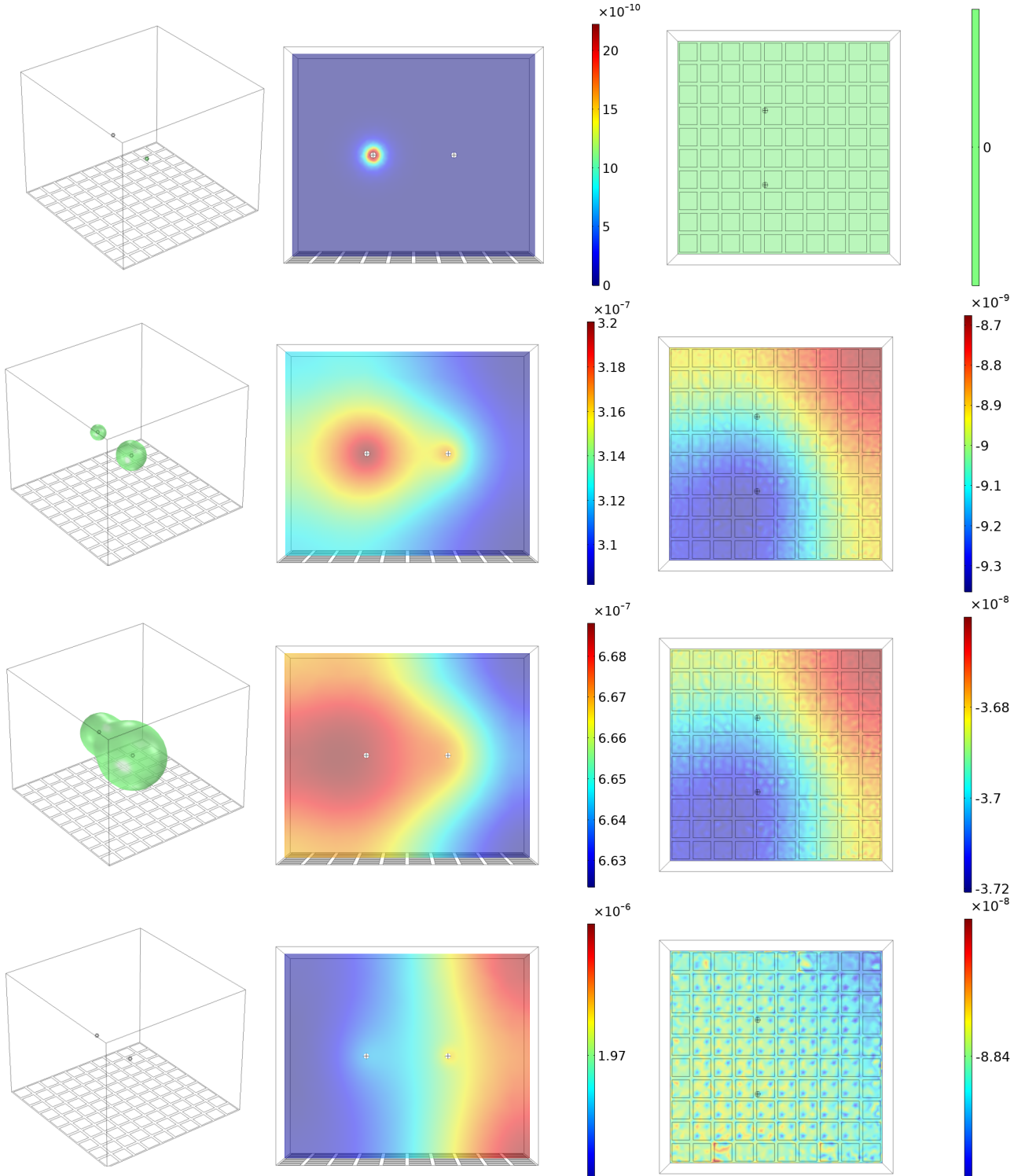
Figure 3.10: A graph of normalised number of protons against time comparing the random walk (**blue**), first-passage (**red**), and FEM (**green**) simulated output of two amplifying DNA clusters.

Model	Protons released	Protons detected	Detection probability
Random walk	1.29×10^7	8.61×10^6	0.667
First passage	1.37×10^7	9.54×10^6	0.696
FEM	7.78×10^8	5.39×10^8	0.693

Table 3.8: A table showing the values, as simulated by the different models, of final, cumulative number of protons released, the total number of protons detected by all sensors, and the corresponding detection probability.

$10\,\mu m \times 10\,\mu m$ sensors separated by $2\,\mu m$ was created within a reaction chamber of $120\,\mu m \times 120\,\mu m \times 100\,\mu m$. Two DNA clusters were initialised with origins ($40\,\mu m$, $50\,\mu m$, $50\,\mu m$) and ($80\,\mu m$, $50\,\mu m$, $50\,\mu m$). The clusters had initiation times of $0\,s$ and $10\,s$. Reflecting boundary conditions were chosen for all simulations.

There is good agreement temporally between all three simulations, as evidenced by Figure 3.10. Despite the temporal agreement, there are inconsistencies in the size of the signal produced. As can be seen in Table 3.8, the FEM simulation estimates over 15× greater proton release and detection than the random walk and first-passage models. The fraction of protons detected is similar between all approaches, with the proton detection probability for the first-passage and FEM models differing by close to 4 % from the value for the random walk simulation. This suggests that whilst the FEM simulation estimates a greater number of protons being produced,

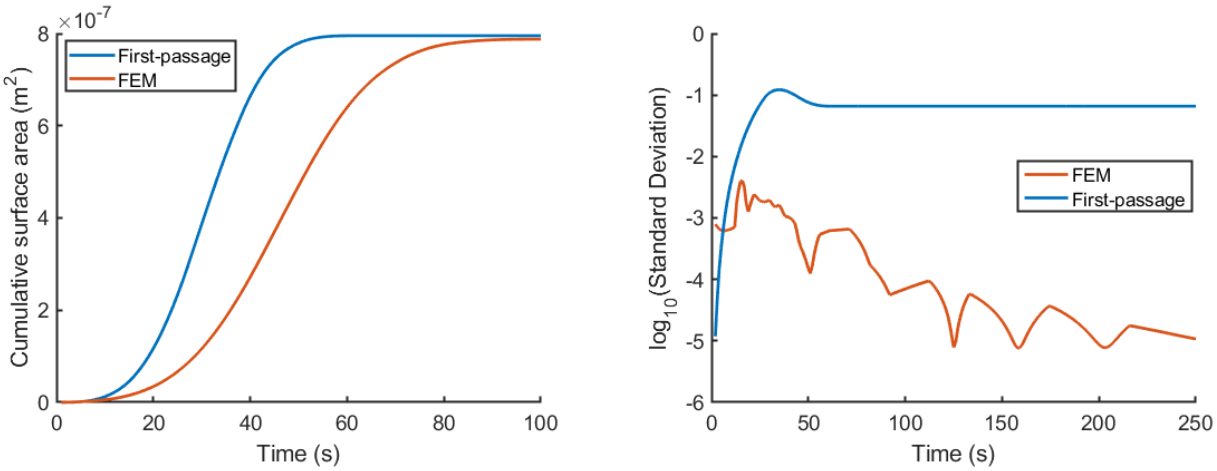


(a) Level set interface

(b) Proton concentration

(c) Surface SiO^- concentration

Figure 3.11: Plots from the FEM benchmarking simulation for: (**a**) the level set interface ($\phi = 0.5$), showing the surface of the DNA cluster; (**b**) the change in proton concentration from initial value in a vertical plane bisecting the two DNA clusters; and (**c**) the change in surface concentration of SiO^- from the initial value on the bottom plane of the reaction chamber. The times from top to bottom are: $0\,s$, $20\,s$ (before cluster overlap), $30\,s$ (after cluster overlap), $100\,s$ (after the reaction has ended). Where only a single number exists on the scale, the variation is negligibly small.



(a) Cluster surface area (b) Array V_{Th} standard deviation

Figure 3.12: (**a**) A graph of cumulative total cluster surface area against time as estimated by the first-passage and FEM models and (**b**) the standard deviation of the normalised signal over the sensing array for the FEM and first-passage simulations, plotted on a logarithmic y-axis.

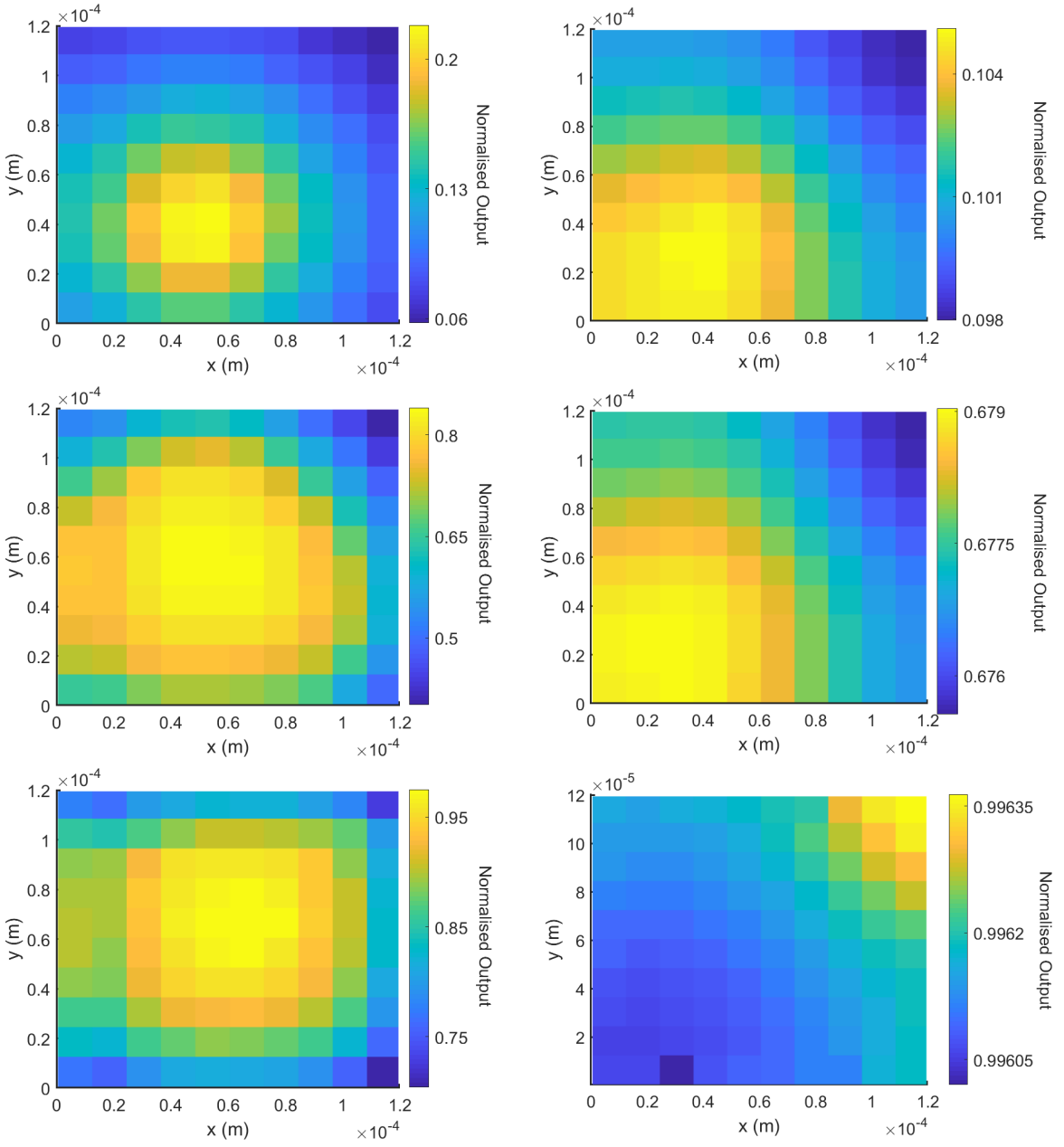
the net effect of proton diffusion and reaction is consistent.

To ascertain whether the FEM simulation generated more protons due to a larger cluster surface area, a volume integration of the delta function was computed. For the random walk and first-passage models, an estimate of total cluster surface area can be obtained by taking the proportion of total protons generated versus those removed, multiplied by the total surface area of all DNA cluster spheres. As seen in Figure 3.12a, there is under 1% difference between the two models for the final cumulative cluster surface area, although the FEM simulation predicts slower cluster growth.

The scaling of saturation threshold voltage with the proton flux was tested with values increasing in orders of magnitude from $1.8 \times 10^{13}\, m^{-2}s^{-1}$ to $1.8 \times 10^{16}\, m^{-2}s^{-1}$. The first-passage approach has almost perfect linearity between threshold voltage and proton flux, as demonstrated by a r^2 value of 1 to 9 decimal places. This allows a reduction in the number of protons generated at cluster surfaces by a factor to limit the computational burden of full-scale simulations, with the output then being re-scaled by this factor. On the other hand, The FEM simulations exhibit extreme non-linearity, due to the equilibrium processes involved.

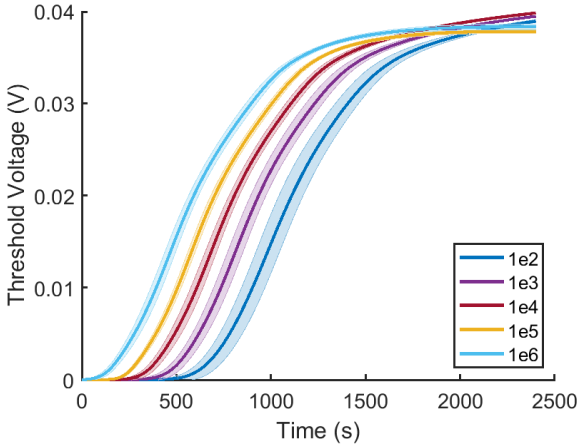
Moving attention to the spatial output from the simulations, an assortment of which is provided in Figure 3.13, key differences can be seen between the first-passage and FEM results. In both sets of data, regions of high signal can be seen in the areas directly underneath the leading edge of the amplifying clusters. However, the spatial distribution of signal differs near the boundaries, with the finite model predicting larger signals in these regions.

Another marked difference between the two models is the standard deviation across the array, shown in Figure 3.12b, which demonstrates the relative signal strength in regions of high activ-

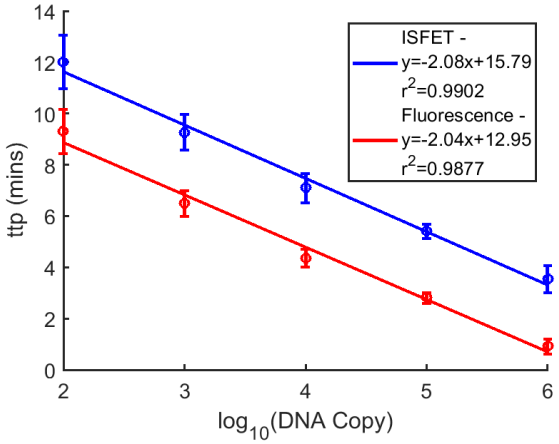


(a) First-passage (b) FEM

Figure 3.13: Surface plots of sensor output over the course of the reaction as simulated by the (**left**) first-passage and (**right**) FEM models. The times sampled, running from top to bottom, are: 20 s, 40 s, 100 s. All output is normalised to the maximum final value.



(a) Threshold voltage



(b) Ttp

Figure 3.14: (**a**) A graph of simulated threshold voltage change versus time curves for varying DNA copy number. The shaded regions indicate the standard deviation for each time point. (**b**) A graph of simulated ttp-log_{10}(DNA copy number) based on simulated fluorescence and ISFET threshold voltage. Linear fits were conducted for both sets of data points with fitting parameters and r^2 values provided in each case.

ity. The standard deviation in the first-passage simulation starts at 10^{-5} before rising quickly, peaking, and then plateauing around 10^{-1}, whereas for the FEM simulation the standard deviation starts at 10^{-3} and slowly decreases to 10^{-5}. This reflects the impact of the equilibrium processes incorporated in the FEM model, as the system will tend towards a uniform distribution over time.

The first-passage model was chosen over the FEM model moving forwards, due to its short run-times on full-scale simulations. Because of the size of the reaction chamber and the mesh requirements, the FEM model has a run-time in the order of months, whereas the first-passage simulation's is in the order of days.

3.7.4 Variation of ISFET Signal with DNA Copy Number

To demonstrate the ability of the first-passage model to replicate key features of experimental amplification data, simulations were run for 1×10^2, 1×10^3, 1×10^4, 1×10^5, and 1×10^6 DNA copies. Due to the stochastic nature of DNA spatial distribution and amplification initiation, 50 simulations were run at each copy number. The ttp is taken as the intercept of the point of maximum gradient of the mean sensor output with the line $y = 0$, as in Malpartida Cardenas *et al.* 2019.

As is expected from experimental observations, the simulated data shows ISFET signal shifting in the negative time direction for increasing DNA copy number, which is evident in Figure 3.14a. The threshold voltage change at saturation, whilst 3-4× greater than the experimental

Modality	Experimental		Simulated	
	m	c	m	c
Fluorescence	-1.99	22.69	-2.04 ± 0.34	12.95 ± 1.37
Voltage	-1.80	21.23	-2.08 ± 0.42	15.79 ± 1.67

Table 3.9: Fitting parameters of the form $y = mx + c$ for plots of ttp against log_{10}(DNA copy number), compared for experimental and simulated data. For experimental data, fluorescence is output from a thermal cycler, whereas for simulated data fluorescence is equated to the cumulative release of protons from clusters. In both experimental and simulated data, voltage refers to the mean threshold voltage change across the ISFET array. Experimental data is from Malpartida Cardenas *et al.* 2019 [45].

values, shows a similar independence from copy number. However, the number of protons detected by each sensor is at least three orders of magnitude lower than that estimated by the simulations in Table 3.4.

The model reproduces a linear relationship of ttp-copy number, as observed in experiments. The absolute values of ttp for the simulated data are roughly 2-6 $mins$ lower than their experimental counterparts. This can largely be attributed to the amplification initiation times for the simulation being for a different target than the one in the experimental data. The simulated gradient of the line-of-best-fit is within one standard deviation of the experimental value, as seen in Table 3.9, indicating consistency between the model and experiment.

The cumulative number of protons released at each timepoint is proportional to the total volume of DNA clusters in the reaction solution. This, in turn, is approximately proportional to the fluorescence data obtained for amplification reactions conducted in a thermal-cycler and provides another point of comparison between simulations and experiment. The ttp-copy number slope for the simulated fluorescence data is consistent with that of the experimental data. It also successfully predicts that there is no significant change in slope between the fluorescence and voltage signals. This makes sense as all points from the fluorescence signal are shifted by the same function.

However, the experimental data shows similar y-intercepts between fluorescence and voltage signals, indicating that there is no difference in the ttp of the two systems. This is not reflected in the simulated output. It would be assumed that since photons will be detected almost instantaneously relative to the transport of protons, that the ttp of the ISFET array would be larger than that from the thermal-cycler. Other transport phenomena, such as convection, and differences in the set-up and data processing between the two systems may obscure this delay.

3.7.5 Variation of ISFET Signal with DNA Trapping

To estimate the effect on the detected signal of positioning DNA near ISFET sensing regions before amplification, simulations were carried out with a proportion of DNA in the reaction being 'trapped' along electrode edges. The microchip chosen for simulation was Titan, whose design parameters can be found in Table 3.3. The electrodes were designed to span the width of two ISFET pixels, with a gap between the edge of the electrode and the neighbouring ISFETs. Two ISFET pixels were left completely uncovered within the gap between neighbouring electrodes.

To represent the trapping process, simulations were run both with no and all DNA trapped, as well as the lowest 25 %, 50 %, and 75 % percentile of z-coordinates. The DNA in the trapped proportion were randomly assigned a x-coordinate of one of the electrode edges, a random y-coordinate, and had their z-coordinate set to the electrode thickness, $50\,nm$. The lowest quartile of DNA would be those under roughly $0.6\,mm$, which represents a realistic range for DNA trapping by electrokinetic interactions. Simulations were run 50 times to account for the random variation of DNA positioning.

The resulting amplification curves, displayed in Figure 3.15, show that as trapping percentage increases, the saturation of the signal becomes more delayed. This can be explained by the volume of the reaction solution unoccupied by DNA, which must be expanded into by amplifying DNA to saturate the reaction. Focusing on the earlier stages of amplification, highlighted by the inset of Figure 3.15, an increase in signal with increasing trapping percentage can be observed. The values for tpp in Table 3.10 indicate a statistically significant decrease in ttp for the 100 % case of $96\,s$ compared to the 0 % case, whereas none of the intermediate trapping percentages saw a meaningful ttp change.

The evidence suggests that the trapped DNA has a limited influence on the size of the signal. For a single DNA molecule trapped on the sensing surface and amplifying at the centre of a $3.14\,mm \times 2\,mm$ well, the cluster will expand as a hemisphere and completely cover the sensing array in around $850\,s$. After that point, the propagation front will move upwards as one continuous surface. This can be seen in Figure 3.15, where there is an inflection of the 100 % curve at around $600\,s$. The maximum gradient of the curve comes before this point and is lower than the other curves, explaining the large difference in ttp. Compare this to the case of a DNA molecule amplifying within the bulk of the reaction solution. The protons that are generated must travel further and will take longer to be picked up by the sensing array. However, the available surface area of the cluster has been maximised and protons will be produced at a greater rate, leading to quicker signal growth. The competition of these two factors raises uncertainty over the efficacy of DNA trapping to improve ISFET-based detection.

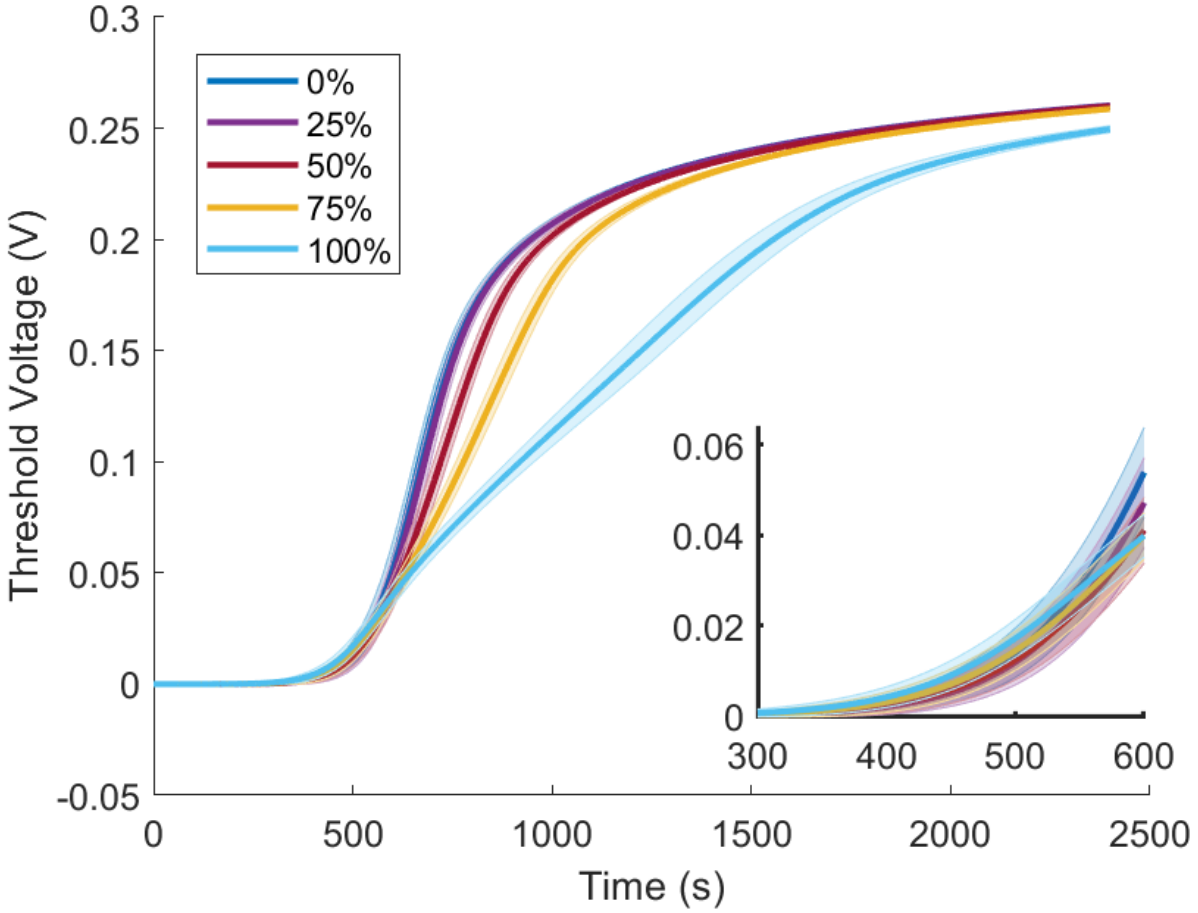


Figure 3.15: A graph of simulated threshold voltage against time with varying percentages of trapped DNA.

Trapping Percentage	**ttp** $(mins)$
0%	8.80 ± 0.32
25%	8.99 ± 0.34
50%	9.00 ± 0.32
75%	8.80 ± 0.30
100%	7.20 ± 0.32

Table 3.10: A table containing the average simulated ttp and associated standard deviation for various trapping percentages of DNA.

3.8 Discussion

3.8.1 Assessment of Models

Looking first at the original LAMP model developed by Dr. Moniri that forms the basis of these simulations, the main assumption is that the constant amplification front velocity observed in Liu *et al.* 2014 in 1D transfers to the 3D case. Experimental verification of spherical DNA cluster growth is necessary. It could be the case that v_{front} is dependent on the radius of the cluster, rather than a constant.

The two key divergences of the first-passage model from the random walk 'ground truth' come from the absorbing boundaries and the introduction of a ceiling. To eliminate the discrepancy stemming from the ceiling, the semi-infinite approximation would have to be replaced with a more complex Fourier series. This would increase the computational burden of the simulation and reduce the practicality of the first-passage approach.

Improving the performance of the absorbing boundaries would first require a survival probability for a proton diffusing in the x and y dimensions, based on the first-passage time of the proton hitting the $z = 0$ plane. A uniform random variable can then be generated to decide whether the proton survives to hit the sensing plane or not. Then, a new probability distribution is required for the x and y displacement that satisfies the absorbing boundary condition that the probability equals zero at the chamber walls.

However, neither fully absorbing nor reflecting boundaries comprehensively depict the physical reality, which is likely to be a blend of the two scenarios. This could be described by a probabilistic absorption of protons at walls, similar to that implemented in Krause *et al.* 2014 [41]. However, probabilistic absorption is not easily incorporated into the first-passage model, as it is unknown how many times a proton will interact with a boundary. An empirical approach could be used, where the probability is fitted to experimental output. Regardless, the first-passage model with reflecting boundaries demonstrated good agreement with the random walk 'ground truth' temporally and spatially.

In contrast, the FEM model estimated a larger number of protons hitting the sensors when compared to the first-passage model. For full-scale simulations, the first-passage model provided threshold voltage changes 3-4× higher than experimental results, despite the number of detected protons per sensor being over 3 orders of magnitude below that predicted by the stationary simulations in Table 3.4. This large discrepancy between the various models must be investigated. The 1D model could be further validated against ISFET output for a variety of pH changes.

Further to this, full-scale FEM simulations would allow comparison against experimental re-

sults, which would highlight if the pH change and the threshold voltage change were correct. Since the ratio of protons generated to protons detected shows consistency with the first-passage model, potential issues are more likely to stem from the DNA cluster interface, possibly due to the sub-optimal mesh used for the simulations, and the definition of the volume reaction rate, which may require normalisation.

Currently, the FEM approach is limited in its usefulness due to the long run-time of the full-scale simulations, but the proof-of-concept was successful. In the future, as hardware and software improve and reaction solutions tend towards smaller volumes, the full utility of the FEM approach introduced in this chapter can be realised.

3.8.2 Discussion of Results

The simulations run with varying numbers of initial DNA molecules demonstrated the ability of the model to capture key features and trends of experimental data, which is important for the validity of later results. The main differences were a systematic offset in ttp and larger total threshold voltage changes. As previously discussed, to improve the agreement between simulated and experimental ttps, single-molecule amplification data for the specific target is required to determine the correct probability distribution for amplification initiation times. Alternatively, following the previous logic that fluorescence measurements of LAMP reactions are proportional to the volume of DNA clusters, it may be possible to extract estimates for the distribution of initiation times from fluorescence curves through a Monte-Carlo simulation. Such an approach would provide a simpler experimental pathway.

Whilst not impacting the final results on DNA positioning, being able to accurately estimate the threshold voltage change is important for sensor design. The lack of equilibrium processes being incorporated in the first-passage simulations has been touched upon. Another potential source of error is from the equation for threshold voltage itself (Equation 2.10). For these simulations, the threshold voltage is dominated by the linear term, $V_{Th} = -\sigma/C_{Helm}$. The value of $0.2\,F/m^2$ was taken as it is the most commonly used in the literature, yet other studies have quoted alternative values of $0.8\,F/m^2$ or $1.6\,F/m^2$ [46], which would have a significant effect on the results. To have confidence in the simulated voltages, further investigations are required into the value of C_{Helm} for the surface of the microchips being tested.

Simulations suggest that trapping DNA at the sensing surface provides minor gains in the onset of detectable amplification at the expense of amplification efficiency at later stages of the reaction. However, the reality is that trapping 100 % of DNA within the reaction solution is highly improbable, and as such it will be difficult to realise the gains from this DNA positioning. It is possible that a larger signal could be obtained by having the trapping region slightly above

the sensing surface. In doing so, the cluster surface area available for proton generation can be increased and ISFET signal will accumulate at a greater rate.

3.9 Future Vision: Towards Detection of Amplification 'Hotspots' on ISFET Arrays

Over the course of this chapter, the main focus of the simulations has been on the temporal output of the ISFET array, averaged over all sensors. However, looking at the spatial output of the array holds much promise for improving the ttp through detection of amplification 'hotspots'.

It stands that if DNA amplification occurs in the growing clusters as modelled in this chapter, the projection of the protons being produced onto the ISFET array underneath will also exhibit a similar localisation. The largest signal will be from the sensors directly underneath the clusters as seen in Figure 3.13. If these hotspots can be identified and isolated, then a reaction can be more quickly classified as positive. Hotspots should be most evident during the initiation of the first few clusters, before the peak in standard deviation occurs in Figure 3.12b. As more clusters begin to amplify, the output of the ISFET array will become more spatially homogeneous and the appearance of hotspots will diminish.

The key to incorporating hotspot detection to the ISFET array is the development of efficient algorithms to segment areas of high activity. It is also vital that these algorithms are robust to the non-idealities of the ISFETs and compounding factors from the dynamics of the reaction. The first-passage model, as demonstrated in this chapter, can produce large numbers of training datasets on which algorithms can be trained. The addition of proton diffusion is an important test of the algorithms, as it smooths edges of the hotspots and makes the boundaries less well defined.

But it is the FEM model that has the most potential, as it is capable of simulating more phenomena. Further development of the level-set approach introduced in this chapter will provide more clues as to the feasibility of hotspot detection. Of particular interest is the inclusion of convective motion of fluid caused by heating of the reaction solution. Convection will establish vortices that will disrupt the formation of distinguishable hotspots on the array, and investigation of this effect is vital in confirming the viability of the hotspot approach.

3.10 Summary

Within this chapter, simulations have been developed to estimate the impact of DNA position on ISFET signal. A survey of ISFET simulations in the literature demonstrated that spatio-temporal variations in ISFET signal are rarely considered and identified some suitable approaches. The simulation methods selected for implementation were a level-set FEM model and a Monte-Carlo model based on the first-passage distribution. A random walk model was chosen to provide a 'ground-truth' against which to ascertain the validity of the other models.

The first-passage approach was found to be in good agreement with the random walk model when reflecting boundaries were used, and the discrepancies caused by the semi-infinite assumption were acceptable, with a 4 % difference in proton detection probability. The FEM model was temporally consistent with the other models, but estimated the threshold voltage change to be an order of magnitude larger and had prohibitively long run-times for full-scale simulations, though successfully demonstrated the level-set method concept.

The ability of the first-passage model to replicate key features and trends of experimental data was tested by conducting simulations with varying DNA copy number. The model displayed the expected linear relationship of decreasing ttp with increasing copy number and had gradients that were consistent with experimental values. Finally, by trapping all DNA within the reaction solution at the sensing surface, a statistically significant decrease in ttp of 96 s was observed when compared to the case with DNA randomly distributed throughout the reaction solution.

Bibliography

[1] K. Katarya. "Spatio-Temporal Modelling and Algorithms for Rapid Detection of Pathogenic DNA". MA thesis. Imperial College London, 2021.

[2] A. Moniri. "Novel Algorithms and Models for Sensing DNA through ISFET arrays". MA thesis. Imperial College London, 2017.

[3] C. Liu et al. "Nuclemeter: A Reaction-Diffusion Based Method for Quantifying Nucleic Acids Undergoing Enzymatic Amplification". In: *Scientific Reports* 4 (1 Dec. 2014), p. 7335. ISSN: 2045-2322. DOI: 10.1038/srep07335. URL: https://www.nature.com/articles/srep07335.

[4] H. Oana et al. "Folding transition of large DNA completely inhibits the action of a restriction endonuclease as revealed by single-chain observation". In: *FEBS Letters* 530.1 (2002), pp. 143–146. ISSN: 0014-5793.

[5] A. Einstein. "Über die von der molekularkinetischen Theorie der Wärme geforderte Bewegung von in ruhenden Flüssigkeiten suspendierten Teilchen". In: *Annalen der Physik* 322 (8 1905), pp. 549–560. ISSN: 15213889.

[6] E. L. Gilroy et al. "Viscosity of aqueous DNA solutions determined using dynamic light scattering". In: *Analyst* 136 (20 2011), pp. 4159–4163.

[7] A. Laesecke and J. Burger. "Viscosity Measurements of DNA Solutions with and without Condensing Agents". en. In: 51 (July 2014).

[8] S. Redner. *A Guide to First-Passage Processes*. Cambridge University Press, 2001.

[9] R. Erban, J. Chapman, and P. K. Maini. "A practical guide to stochastic simulations of reaction-diffusion processes". In: *arXiv: Subcellular Processes* (2007).

[10] S. H. Lee and J. C. Rasaiah. "Proton transfer and the mobilities of the H+ and OH ions from studies of a dissociating model for water". In: *The Journal of Chemical Physics* 135.12 (2011), p. 124505.

[11] J. Luo et al. "at an Modelling of the migration effect occurring ISFET-based coulometric sensor-actuator system". In: *Analytica Chimica Acta* (1990), p. 71.

[12] W. Olthuis et al. “Modelling of non-steady-state concentration profiles at ISFET-based coulometric sensor-actuator systems”. In: *Analytica Chimica Acta* 229 (C Jan. 1990), pp. 71–81. ISSN: 00032670.

[13] S. Martinoia, G. Massobrio, and M. Grattarola. “An ISFET model for CAD applications”. In: *Sensors and Actuators: B. Chemical* 8 (3 June 1992), pp. 261–265. ISSN: 09254005.

[14] S. Martinoia, M. Grattarola, and G. Massobrio. “Modelling non-ideal behaviours in H+-sensitive FETs with SPICE”. In: *Sensors and Actuators: B. Chemical* 7 (1-3 Mar. 1992), pp. 561–564. ISSN: 09254005.

[15] L. K. Meixner and S. Koch. “Simulation of ISFET operation based on the site-binding model”. In: *Sensors and Actuators: B. Chemical* 6 (1-3 Jan. 1992), pp. 315–318. ISSN: 09254005.

[16] G. Verzellesi et al. “Numerical analysis of ISFET and LAPS devices”. In: *Sensors and Actuators B: Chemical* 44 (1-3 Oct. 1997), pp. 402–408. ISSN: 0925-4005.

[17] R. Kühnhold and H. Ryssel. “Modeling the pH response of silicon nitride ISFET devices”. In: *Sensors and Actuators B: Chemical* 68.1 (2000), pp. 307–312. ISSN: 0925-4005.

[18] M. Janicki et al. “Ion sensitive field effect transistor modelling for multidomain simulation purposes”. In: *Microelectronics Journal* 35 (10 2004), pp. 831–840. ISSN: 00262692.

[19] W.-Y. Chung et al. *Drift Response Macromodel and Readout Circuit Development for ISFET and Its H + Sensing Applications*. 2005, pp. 29–34.

[20] S. E. Naimi et al. “Modeling of the pH-ISFET thermal drift”. In: *Proceedings of the International Conference on Microelectronics, ICM* (2009), pp. 288–291.

[21] R. R. Jarmin et al. “A new PSpice macro model for electrolyte insulator interface based Si3N4 Field Effect transistor responsive to H+ ion concentration for biomedical sensor”. In: *Proceedings of 2010 IEEE EMBS Conference on Biomedical Engineering and Sciences, IECBES 2010* (2010), pp. 505–508.

[22] S. Sundaram and N. N. Sharma. “Modeling interface diffusion as a mechanism for threshold voltage drift in pH sensors”. In: *Proceedings of IEEE Sensors* (2010), pp. 2547–2550.

[23] S. Uno. “Computer simulation of lipid bilayer detection using ion-sensitive field-effect transistors”. In: ed. by A. N. Cartwright and D. V. Nicolau. Vol. 8231. SPIE, Feb. 2012, pp. 82310V-82310V–6.

[24] D. Passeri et al. “Numerical simulation of ISFET structures for biosensing devices with TCAD tools”. In: *Bioinformatics and Biomedical Engineering* (2014).

[25] Y. Ma et al. “Compact modelling and simulation of extended-gate ion-sensitive field-effect-transistor”. In: IEEE, Oct. 2014, pp. 1–3. ISBN: 978-1-4799-3282-5.

[26] T. M. Abdolkader. "A numerical simulation tool for nanoscale ion-sensitive field-effect transistor". In: *International Journal of Numerical Modelling: Electronic Networks, Devices and Fields* 29 (6 Nov. 2016), pp. 1118–1128. ISSN: 08943370.

[27] N. Aoun et al. "Finite-Element Simulations of the pH-ElecFET Microsensors". In: *IEEE Sensors Journal* 16 (17 Sept. 2016), pp. 6519–6526. ISSN: 1530437X.

[28] K. B. Parizi et al. "ISFET pH Sensitivity: Counter-Ions Play a Key Role". In: *Scientific Reports* 7 (1 Feb. 2017), p. 41305. ISSN: 2045-2322. DOI: 10.1038/srep41305. URL: https://www.nature.com/articles/srep41305.

[29] E. Mohammadi and N. Manavizadeh. "An Accurate TCAD-Based Model for ISFET Simulation". In: *IEEE Transactions on Electron Devices* 65 (9 Sept. 2018), pp. 3950–3956. ISSN: 00189383.

[30] R. Wrege et al. "ISFETs: Theory, modeling and chip for characterization". In: *2019 IEEE 10th Latin American Symposium on Circuits and Systems, LASCAS 2019 - Proceedings* (Mar. 2019), pp. 109–112.

[31] A. M. Dinar et al. "Modeling and simulation of electrolyte pH change in conventional ISFET using commercial Silvaco TCAD". In: *IOP Conference Series: Materials Science and Engineering* 518 (4 May 2019), p. 042020. ISSN: 1757-8981.

[32] L. J. Mele, P. Palestri, and L. Selmi. "General Approach to Model the Surface Charge Induced by Multiple Surface Chemical Reactions in Potentiometric FET Sensors". In: *IEEE Transactions on Electron Devices* 67.3 (2020), pp. 1149–1156. DOI: 10.1109/TED.2020.2964062.

[33] T. E. Grour et al. "Compact Modeling of pH-Sensitive FETs Based on 2-D Semiconductors". In: *IEEE Transactions on Electron Devices* 68 (11 Nov. 2021), pp. 5916–5919.

[34] P. Pandey and H. Kaur. "Performance and Sensitivity Analysis of Polarity Controllable-Ion Sensitive FET for pH Sensing Applications". In: *Silicon 2022 14:14* 14 (14 Jan. 2022), pp. 8467–8474.

[35] A. Ghomi and M. Shalchian. "Design-Oriented Physical Model of Ion-Sensitive Field Effect Transistor for pH Sensing". In: *IEEE Sensors Journal* 23.3 (2023), pp. 2354–2363. DOI: 10.1109/JSEN.2022.3230849.

[36] R. Dhar et al. "Deriving a novel methodology for nano-BioFETs and analysing the effect of high-k oxides on the amino-acids sensing application". In: *Solid-State Electronics* 200 (Feb. 2023), p. 108525.

[37] J. Xie et al. "Efficient modeling approach for simulating multi-physics responses of an ion-sensitive field-effect transistor using artificial neural networks". In: *Journal of Computational Electronics* 22 (Nov. 2022), pp. 1–8.

[38] K. Slowinska, S. W. Feldberg, and M. Majda. "An electrochemical time-of-flight technique with galvanostatic generation and potentiometric sensing". In: *Journal of Electroanalytical Chemistry* 554-555 (2003). Special issue in memory of Professor M.J. Weaver, pp. 61–69. ISSN: 1572-6657.

[39] C. F. Monson and M. Majda. "Ion diffusion in channels containing random arrays of microspheres: An electrochemical time-of-flight method". In: *Analytical Chemistry* 79 (24 Dec. 2007), pp. 9315–9320. ISSN: 00032700.

[40] G. Nagy et al. "Electrochemical time of flight method for determination of diffusion coefficients of glucose in solutions and gels". In: *Analytical and Bioanalytical Chemistry* 394 (7 Aug. 2009), pp. 1955–1963. ISSN: 16182642.

[41] K. J. Krause et al. "Simulation of the impact of reversible adsorption on the response time of interdigitated electrode arrays". In: *physica status solidi (a)* 211.6 (2014), pp. 1352–1356.

[42] I. J. Cutress, E. J. Dickinson, and R. G. Compton. "Electrochemical random-walk theory: Probing voltammetry with small numbers of molecules: Stochastic versus statistical (Fickian) diffusion". In: *Journal of Electroanalytical Chemistry* 655.1 (2011), pp. 1–8. ISSN: 1572-6657.

[43] N. Miscourides and P. Georgiou. "ISFET Arrays in CMOS: A Head-to-Head Comparison Between Voltage and Current Mode". In: *IEEE Sensors Journal* 19.4 (2019), pp. 1224–1238.

[44] COMSOL. *Two-phase flow modeling guidelines*. `https://www.comsol.com/support/learning-center/article/Two-Phase-Flow-Modeling-Guidelines-59411`.

[45] K. Malpartida-Cardenas et al. "Quantitative and rapid Plasmodium falciparum malaria diagnosis and artemisinin-resistance detection using a CMOS Lab-on-Chip platform". In: *Biosensors and Bioelectronics* 145 (2019), p. 111678. ISSN: 0956-5663.

[46] T. Hiemstra and W. Van Riemsdijk. "Physical chemical interpretation of primary charging behaviour of metal (hydr) oxides". In: *Colloids and Surfaces* 59 (1991), pp. 7–25. ISSN: 0166-6622.

Chapter 4

Electrokinetic Manipulation of DNA to Enhance ISFET-based Detection

4.1 Introduction

The simulations conducted in Chapter 3 suggested an improvement in the ttp of ISFET-based DNA detection when the DNA is positioned at the sensing surface prior to amplification. To effect this improvement, a system to achieve DNA positioning must be selected and implemented on-chip.

There are many ways in which DNA can be spatially manipulated:

- **Hydrodynamic:** Microfluidic channels can be designed with side-channels, wells, or obstructions to trap particles at stagnation points [1].
- **Optical:** Optical tweezers can exert a highly-resolved trapping force via the refraction of photons from an tightly-focussed laser beam as they enter a particle [2].
- **Magnetic:** Through attachment to paramagnetic beads, particles can be spatially manipulated using magnetic fields [3].

Photolithography was carried out at the Centre for Bio-inspired Technology cleanroom. Thin-film deposition, FIB-SEM processing and characterisation, and fluorescence microscopy was conducted at the Hamlyn Centre, Imperial College London. Further thin-film deposition was carried out at the London Centre for Nanotechnology cleanroom, University College London, and the Royce Institute, Imperial College London. The Titan microchip used in this chapter was designed by Dr. Nicolas Moser. The Lacewing platform used for electrochemical testing of Titan was developed by Lei Kuang and others. Other contributions are explicitly stated.

- **Chemical:** By functionalising a surface with chemical groups, such as thiols, that will bond to the target, particles can be trapped in place with chemical bonds [4].

- **Electrokinetic:** Electric fields produced by electrodes can be leveraged to move and trap targets through a variety of electrokinetic interactions [5].

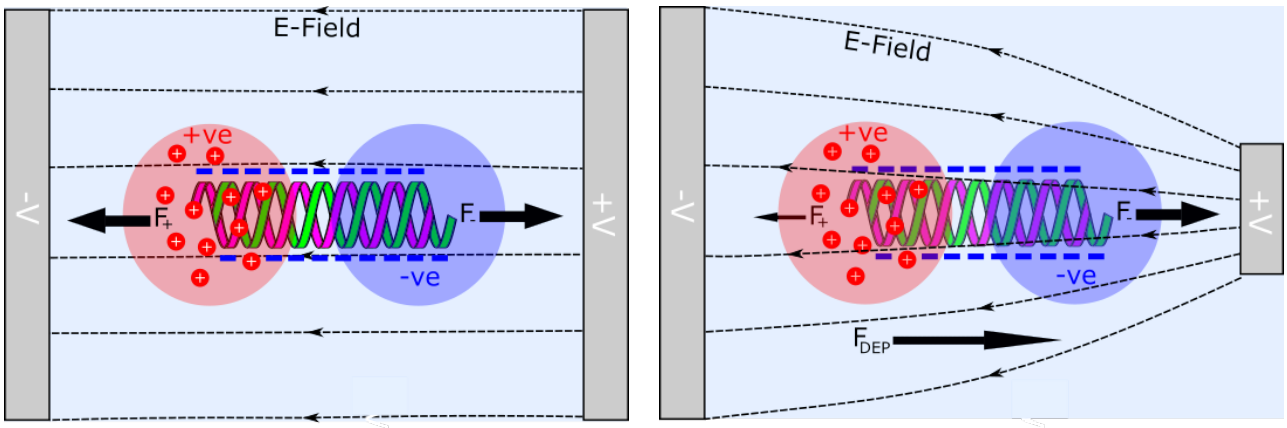
Hydrodynamic techniques can struggle to trap small molecules, such as DNA, and are more suited to cell trapping. Optical tweezers have a much higher trapping resolution, however the necessary optical apparatus and high-power beam make the technique suitable only for benchtop applications. Magnetic tweezers are simple to implement, but the paramagnetic beads to which the DNA must be tethered may inhibit amplification and block signal transduction. Whilst chemical bonding is capable of trapping DNA without the need for an external force, it still requires DNA to be positioned at the functionalised surface and may not be compatible with some amplification reactions.

In comparison, an electrode system that can use electric field interactions to manipulate DNA is ideally suited for on-chip implementation, due to the ease of integration and low power consumption. In particular, there is the opportunity to implement an electrode system as part of the CMOS IC, which would make the approach scalable for a mass-market device.

In this chapter, an electrode system will be designed and fabricated on-chip through photolithography. This electrode system will be used to trap DNA with electrokinetic interactions, aiming to improve ISFET-based detection of DNA amplification. Building on this work, electrodes will be fabricated as part of the top-metal of a commercial CMOS process and exposed through post-processing of the mircochip.

4.2 Electrokinetics

When DNA is subjected to an electric field, there are various interactions that can occur, both directly between DNA and electric field and also indirectly from fluidic motion induced by the field. All of these phenomena are collected by the umbrella term, electrokinetics. This can include electrophoretic, dielectrophoretic, electro-osmotic, and electrothermal motion. Electrokinetic motion is possible in both AC and DC fields, with the nature of the motion and the dominant phenomena changing with frequency and solution conductivity. The behaviour of the different electrokinetic phenomena are summarised in Table 4.1.



(a) Uniform fields (b) Non-uniform fields

Figure 4.1: A diagram outlining the electrostatic interactions of DNA and surrounding counterions in (**a**) uniform and (**b**) non-uniform electric fields . F_- and F_+ are the electrostatic forces on negative and positive charges respectively, with F_{DEP} indicating the direction of the pDEP force in case (**b**). Adapted from [8].

4.2.1 Electrophoresis

When an electric field is applied to charged particles, they will be attracted towards field regions of the opposite polarity in a motion known as electrophoresis. The force vector exerted on the particle is,

$$\vec{F} = Q\vec{E} \tag{4.1}$$

where $\vec{E}$ is the electric field vector and Q is the total electric charge of the particle, which has been reported as $0.08 - 0.63\,e$ per base pair (bp) for DNA [6]. Electrophoretic motion occurs in DC fields, and is used in gel assays to sort DNA strands by length. In AC fields, the net force averages to zero and particles will move in an oscillatory fashion with the reversing field, travelling further before changing direction with lower applied field frequency. The electrophoretic force on a particle will decrease with increasing solution conductivity due to increased Debye screening [7].

4.2.2 Dielectrophoresis

Within electric fields, polarisation of a particle will occur due to migration in opposite directions of the positive and negative charges that form it. This separation of opposite charge defines an electric dipole across the particle, whose moment vector is given by the product of electric charge and the vector from negative to positive charge. The polarisation vector, the dipole moment per unit volume, of a homogeneous material is,

$$\vec{P} = (\epsilon_r - 1)\epsilon_0\vec{E} \tag{4.2}$$

where ϵ_r and ϵ_0 are the relative dielectric permittivity of the particle and of free space respectively. Dielectric permittivity is a complex variable whose real part is a measure of a material's ability to store energy in response to an electric field. The imaginary part, ϵ'', represents energy losses within a material, and is linked to the electrical conductivity, σ, of the material by the equation,

$$\epsilon'' = \frac{\sigma}{2\pi f} \tag{4.3}$$

where f is the frequency of the external field. Dielectric permittivity decreases as frequency increases in a process known as dielectric relaxation, as electric dipoles cannot be created or orientate quickly enough before the polarity of the field reverses [9].

In a spatially non-uniform field, the two charges of a particle's electric dipole will experience unbalanced electrostatic forces, leading to acceleration of the particle. The subsequent motion is referred to as dielectrophoresis (DEP) and moves it towards electric field maxima or minima, known as positive DEP (pDEP) and negative DEP (nDEP) respectively. The direction of motion is independent of the polarity of the field, as the dipole will change orientation with the reversing field. The electrostatic forces on polarised DNA are compared with uniform and non-uniform fields in Figures 4.1a and 4.1b respectively.

The DEP force for a homogeneous particle is defined by the equation,

$$F_{DEP} \propto V\Re\{\epsilon_m K\}\nabla|\vec{E}|^2 \tag{4.4}$$

where ϵ_m is the dielectric permittivity of the surrounding medium, V is the volume of the particle, and $|\vec{E}|^2$ is the electric field intensity. Whether a molecule experiences pDEP or nDEP is dependent on the Clausius-Mossotti (CM) function, which for a sphere is given by,

$$K = \frac{\epsilon_p - \epsilon_m}{\epsilon_p + 2\epsilon_m} \tag{4.5}$$

and is used to relate the dielectric permittivity of a particle, ϵ_p, to that of the medium. The CM function is positive for pDEP and negative for nDEP. Since permittivity is a function of frequency, it is possible for the direction of motion to reverse as the field frequency is varied, if the CM function changes sign at a point known as the crossover frequency. Such behaviour is evident in Figure 4.2, which shows the CM function for DNA in solutions of different conductivity [1]. The electric dipole of individual particles can itself create a field gradient to which neighbouring particles are attracted. This creates 'pearl-chains' of polarised particles that are set up along electric field lines [11].

[1]The CM factor has been deemed by some as being insufficient to fully explain DEP of DNA. This is owing to the fact that DNA polarisation occurs due to external agents, in the form of counterions, instead of being solely due to DNA's fixed charges [10].

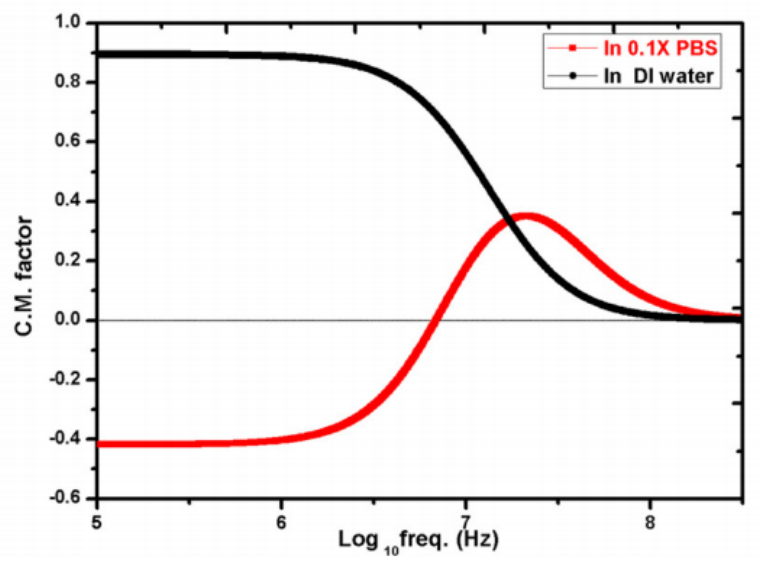


Figure 4.2: A graph plotting the CM function for DNA in deionised water (conductivity $2\,mSm^{-1}$) and 0.1× PBS ($160\,mSm^{-1}$) [13].

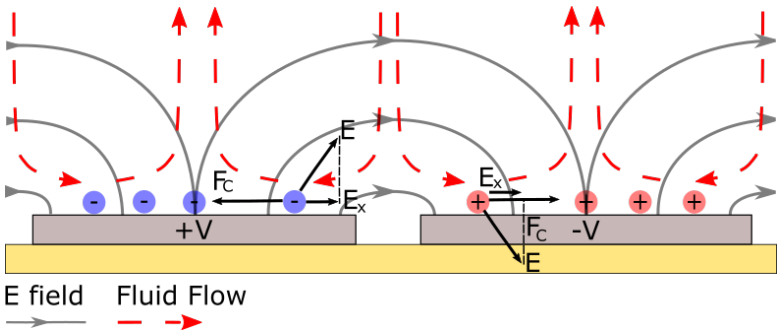


Figure 4.3: A diagram illustrating ACEO for a pair of oppositely polarised electrodes. E_X and F_C denote the electric field tangential to the electrode and electrostatic force respectively. Ions move in the direction of F_C and drag the surrounding fluid, causing fluid flow as shown in the figure. Adapted from [14].

DNA has a negligible permanent electric dipole due to the regular arrangement of nucleotides cancelling out their individual dipole moments. However, strong electric dipoles can be induced due to motion of the counterion cloud in response to an electric field. These counterions are positively charged ions that are attracted to the negatively charged DNA backbone, which are restricted from moving radially but are free to move along the length of the molecule. It is this movement of ions which dominates the dielectric spectrum of DNA up to applied field frequencies of $15\,MHz$ [12]. The high polarisability of DNA molecules means that the required field gradients for DEP actuation are small for a molecule of DNA's size, which is key to practical application of the technique.

Interaction	Relationship		
	Electric Field	Frequency	Conductivity
Electrophoresis	$\vec{E}$	DC	Decreases with increasing
Dielectrophoresis	$\nabla\|\vec{E}\|^2$	$<15\,MHz$	Decreases with increasing*
Electro-osmosis	$\vec{E_{tan}}$	$<100\,kHz$	$<100\,mSm^{-1}$
Electrothermal	$\|\vec{E}\|^4$	Increases with increasing	$>20\,mSm^{-1}$

Table 4.1: A table comparing the electrokinetic effects and their relationship with different variables. * The case for DNA.

4.2.3 Electro-osmosis

Electro-osmosis describes the fluid flow that is induced when an EDL is subjected to an electric field. In DC electro-osmosis, the tangential field exerts an electrophoretic force on the EDL that moves it along the surface and, in turn, induces a fluid flow due to hydrodynamic drag from the moving ions, as exemplified by Figure 4.3.

AC electro-osmosis (ACEO) can be observed in alternating fields applied to oppositely polarised electrode pairs. In this case, electric fields emanating from the electrodes contain a component that is tangential to the electrode surface. Once the polarisation of the electrode reverses, an EDL of the opposite charge forms, but the direction of motion remains the same. The velocity at which a particle moves under ACEO scales approximately with the square of the voltage applied to the electrodes [15].

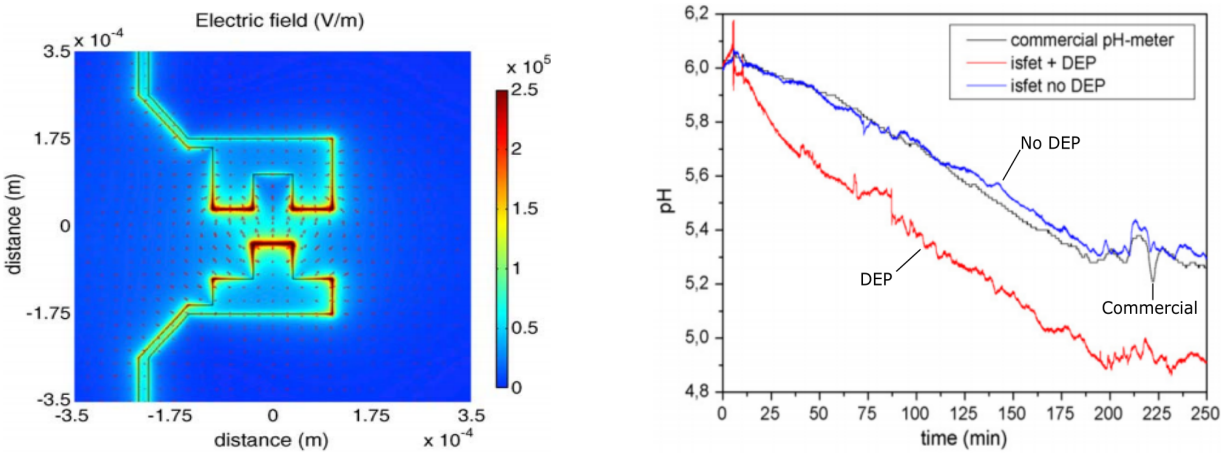
If the polarisation of the electrode switches before an EDL can form, then no fluid motion will occur. This defines the characteristic cut-off frequency for ACEO, which lies between 10-100 kHz, whereas the effect is maximised around $1\,kHz$ [6]. ACEO also becomes less effective in high conductivity solutions, above around $100\,mSm^{-1}$ [16], as the EDL becomes more compressed and imparts a weaker hydrodynamic drag on the surrounding fluid as it moves [17].

4.2.4 Electrothermal

Fluid flow can be induced in solutions by electric fields through Joule heating, which arises from particle interactions as ions move as part of an electrical current. The rate at which the fluid is heated is,

$$\frac{dq}{dt} = \sigma|\vec{E}^2| \tag{4.6}$$

For non-uniform electric fields, heating will be uneven, causing gradients in the dielectric permittivity and electrical conductivity of the solution. These gradients lead to the creation of space charge within the solution upon which a force is exerted by the electric field, resulting in a hydrodynamic flow that scales approximately with $|\vec{E}|^4$. Electrothermal motion predominates



(a) (b)

Figure 4.4: (**a**) A graph of FEM simulated electric field strength for the 'U' and 'T' shaped electrode pair used in Castellarnau *et al.* 2006 with an ISFET sensor in the trough of the 'U' electrode [20]; (**b**) A graph of pH against time as sensed by the ISFET with (**red**) and without (**blue**) a DEP field applied to the electrodes, with a commercial pH meter (**grey**) used as a reference. Edited from [21].

in solutions with conductivities over $20\,mSm^{-1}$, and increases slowly with frequency [18]. The temperature gradient also gives rise to natural convection of fluid from hot regions to cold due to the different fluid densities. However, this buoyancy force is an order of magnitude smaller than that exerted by the space-charge interaction over characteristic distances encountered in microfluidics [19].

4.3 Electrode Systems for Electrokinetic Manipulation of DNA

There have been a wide range of electrode designs applied for electrokinetic trapping in the literature, which must be explored to formulate a design to fabricate on-chip. Electrode systems in the literature that trap DNA will be surveyed, with specific studies involving non-DNA targets included where inspiration can be taken from the design.

4.3.1 Castellarnau *et al.* 2006: A Case study in ISFET-DEP Combination to Monitor Bacterial Digestion

There has been no example in the literature of ISFET-based DNA detection being enhanced by electrokinetic positioning. However, the combination of a DEP electrode system and an ISFET has been used by Castellarnau *et al.* in 2006 [21] to monitor the pH during anaerobic

digestion of glucose by *E. coli*. In their study, a pair of 'U' and 'T' shaped electrodes, shown in Figure 4.4a, were used to create an electric field minimum over the sensing region of the ISFET, to which *E. coli* was attracted under nDEP upon application of an $8\,V$ electric field at $10\,MHz$ across the electrodes. The ISFET experienced a larger decrease in pH when the DEP field was applied than when it was not, with a difference in pH change of 0.5 according to Figure 4.4b. Castellarnau attributes this observation to "local DEP positioning of bacteria cells on the ISFET gate which concentrates the acid production at the sensor surface before it is diluted by the solution medium" [21]. This provides strong support that DEP could be used to enhance DNA detection by an ISFET.

Castellarnau admitted that more experimental work was required to ascertain the mechanism causing the increased pH drop, as it could be caused by either the quicker onset or increased rate of anaerobic digestion due to the greater local concentration of *E. coli*. Also evident in this study, is that the addition of *E. coli* to the reaction solution caused a pH decrease as measured by the ISFET, potentially caused by electrostatic interaction, which could confound the detection of pH changes.

4.3.2 DEP Trapping Systems

Herbert Pohl, who was first to coin the term dielectrophoresis in 1951 [22], initially developed DEP for the separation of suspensions [23] and then dead and living cells [24] in the 1960s. The manipulation of smaller subjects was limited by the fabrication resolution of electrodes, as smaller features are required to provide a field gradient that can exert a sufficient DEP force. The first demonstration of DNA DEP trapping was conducted in 1990 by Washizu *et al.* [25].

To produce the non-uniform electric field required for DEP, either electrically floating electrodes that short fields around them [25] or insulators that expel field lines from their bulk [26] can be used. Whilst these methods allow the creation of small, densely packed structures without the need for electrical connection, high voltages are necessary, which rules them out for a portable, handheld device and they are not considered here. Instead, studies using integrated microelectrodes are sought.

pDEP Traps

The most simplistic electrode design for pDEP trapping is the line interdigitated electrode (IDE), first used on DNA in Asbury *et al.* 2002 [5]. $170\,\mu m$ wide IDEs were used with $30\,\mu m$ gaps. This enabled trapping of YOYO-1-stained, $45\,kbp$ λ-DNA with low voltages of 0.5-4 V_{pp} addressed to each electrode, compared to the $200\,V_{pp}$ required for the floating electrode version of this system in their 1998 paper [27]. The electric field strength was estimated to be $25\,kV/m$

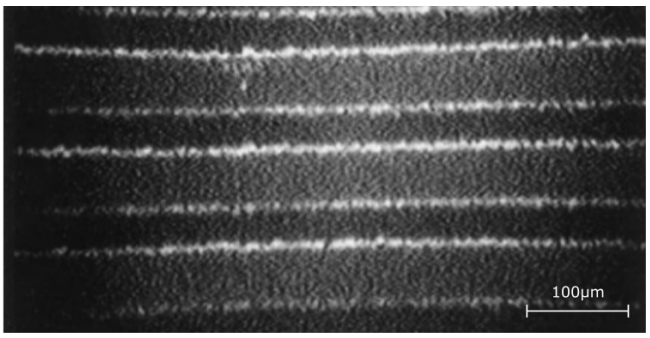


Figure 4.5: A fluorescence microscope image of YOYO1-stained, 45 *kbp* λ-DNA during DEP trapping in Asbury *et al.* 2002 [5].

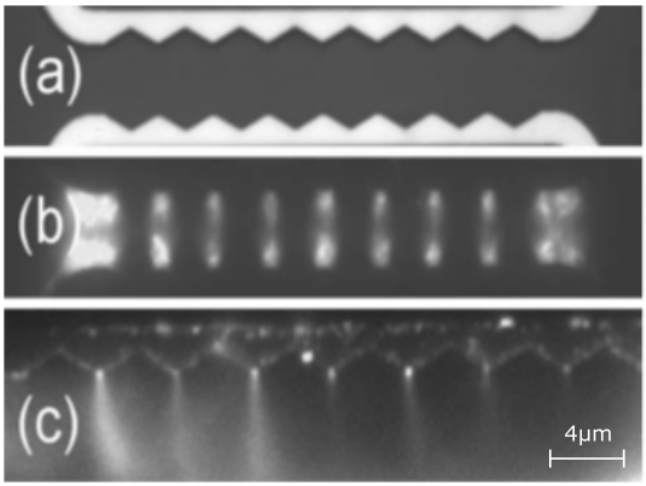


Figure 4.6: (**a**) An optical microscope image of the sawtooth electrodes used in Dewarrat *et al.* 2002 and (**b**) a fluorescence microscope image of YOYO-dyed 48.5 *kbp* λ-phage DNA; (**c**) is a close-up image of (**b**) [28].

at 1 μm from the electrode edge with 1 V applied. The electrodes were fabricated using Au to avoid the DNA-electrode bonding that was evident with the aluminium (Al) electrodes used in Washizu *et al.* 1990 [25].

Once the voltage was applied, DNA was instantaneously attracted to the edges of the line electrodes, as evident in Figure 4.5. After turning off the electric field, a spike of fluorescence indicated that the concentration of DNA had been increased almost 16× from the initial solution, with concentration up to 64× also reported. Asbury observed a decrease in trapping efficiency with increased field frequency, due to a decrease in DNA's CM factor. The CM factor was also reduced with increased solution conductivity, which explains observations in Asbury *et al.* 1998.

For a given applied voltage, greater electric field strengths can be obtained by using smaller electrode features. Thus the trapping performance of a line electrode can be improved by adding castellations. Dewarrat *et al.* 2002, attempted this by using a pair of Au sawtooth (triangular castellated) electrodes across a microfluidic channel [28]. 4 V applied over the 4 μm

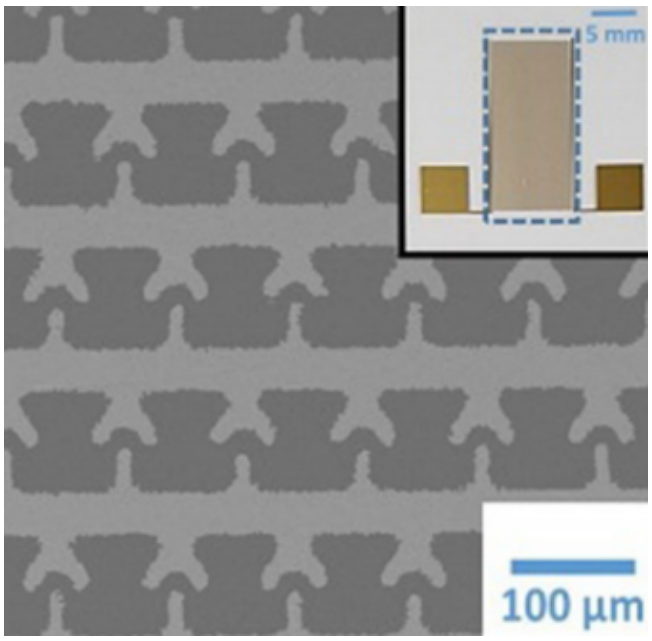


Figure 4.7: A SEM image of the electrode array used in Velmanickam *et al.* 2018, showing the opposing thin rectangular and curved castellations used to maximise field gradients [31].

gap between opposing tips produced electric field strengths of $10^6\,Vm^{-1}$ and resulted in pDEP trapping of DNA in a $7\,mSm^{-1}$ buffer at a field frequency of $1\,MHz$.

The fluorescence microscope images in Figure 4.6 demonstrate the formation of pearl-chains of DNA across the microfluidic channel. Another phenomenon that can potentially be seen in Figure 4.6 is the elongation of DNA strands from their compact, spherical equilibrium state. This was also observed in Washizu *et al.* 1990 and has since been attributed to the combination of hydrodynamic drag from migrating counterions and electrophoresis exerted on the DNA backbone [29]. Further experiments observed DNA collapsing into a condensed configuration in low frequency fields [30].

Other castellation shapes have been used in the literature. Trapezoid castellations were utilised to trap DNA in Kawabata *et al.* 2001 [32]. Square castellations, like those used in Pethig *et al.* 1992 [33] on yeast cells, are also a suitable candidate, and can be used for pDEP and nDEP trapping, as an electric field minimum exists within the troughs of castellations.

The common castellated IDE design used in the literature for DEP applications has identical castellations on both sides. However, this does not maximise the gradients of the electric field. A good example of a high-gradient electrode design was used in Velmanickam *et al.* 2018 [31] to trap RNA and DNA, where thin, rectangular castellations opposed curved extensions, as seen in Figure 4.7. Velmanickam estimated the gradients to be in the order of $10^{18}\,V^2m^{-3}$, which is quoted as being larger than those produced by traditional IDEs. Furthermore, Velmanickam utilised low-resolution photolithographic methods and an under-exposing of the photoresist to produce electrodes with rough surfaces that contained hotspots of high electric field gradient

to which molecules were attracted.

It is interesting that electrode designs akin to that used by Velmanickam *et al.* are not used more frequently for DEP applications. In high conductivity solutions where significant Debye screening occurs, the electric fields from opposing electrodes will have a limited interaction. In this case, the benefits from having a high-gradient electrode design are negated. Another potential means of increasing field gradients in castellated IDEs is to align the castellations of one electrode with the gaps between castellations of adjacent electrodes, as opposed to aligning castellations with each other, as was done in Pethig *et al.* 1992 [33].

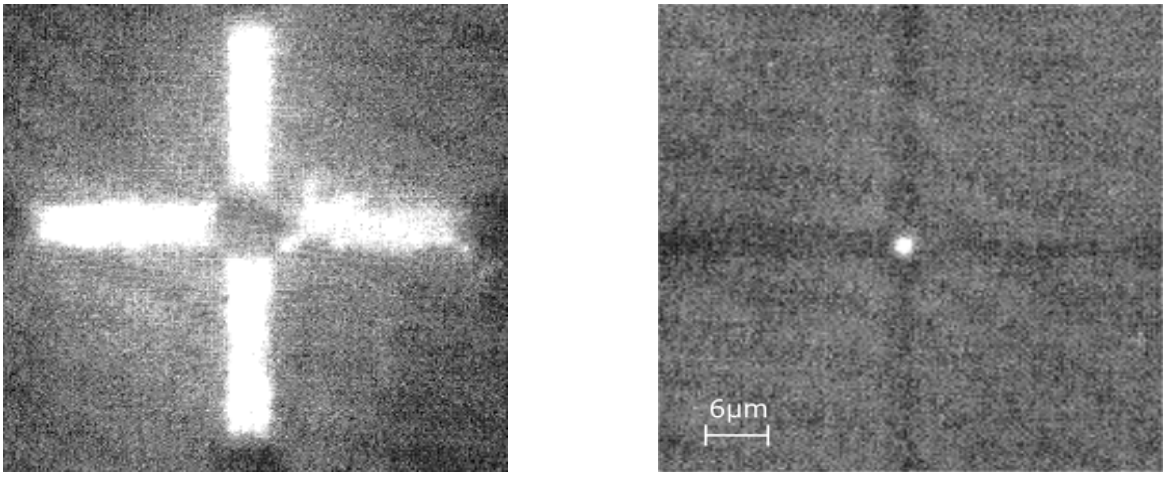
nDEP

Whilst pDEP traps are strong, the high electric field strengths that DNA is exposed to could lead to strand breakage, as well as DNA bonding to the electrode surface. Traps based on nDEP are able to hold subjects away from electrode surfaces and could be used to hold DNA directly over ISFET sensing regions for improved signal.

The predominant form of nDEP trapping is with electric quadrupoles, first used on DNA by Bakewell *et al.* in 1998 [34]. They tested a quadrupole system consisting of four Au electrodes which had polynomial profiles to allow accurate determination of the electric potential. The system was designed to be capable of both pDEP in the $2\,\mu m$ gap between adjacent electrodes and nDEP in the $6\,\mu m$ central gap, as demonstrated in Figure 4.8. However, whilst conducting trapping in a TE buffer with a high conductivity of $80\,mSm^{-1}$ and applying $4\,V_{pp}$ with alternating polarities between neighbouring electrodes, only nDEP was observed for DNA at field frequencies between 1-20 MHz. Zheng *et al.* achieved pDEP trapping of DNA in a similar quadrupole in their 2003 paper, using a $1\,MHz$, $1\,V_{pp}$ signal [36].

The polynomial quadrupoles used by Bakewell *et al.* and Zheng *et al.* could not be scaled into array form, whereas Krishnan *et al.* used circular electrodes to form a quadrupole array in their 2008 paper [35]. When a checkerboard polarity was applied to the electrode system at $10\,V_{pp}$ and $10\,kHz$ in a solution conductivity of $1.82\,mSm^{-1}$, DNA and cells moved under pDEP and nDEP respectively, as demonstrated by Figure 4.10. The fact that the electrodes require alternate polarities means that integration and fabrication of such a system is relatively complex. Buried interconnects are required with the electrodes, which could be implemented as part of CMOS IC.

A major drawback of planar quadrupole electrodes is their weakness, as the DEP force they exert always acts upwards. Gravitation is relied upon to overcome this upwards force and trap particles, as illustrated by Figure 4.9, which for light and highly polarisable molecules like DNA may be insufficient. An improved nDEP trap design is the square ring developed in Rosenthal



(a) nDEP (b) pDEP

Figure 4.8: Fluorescence microscope images from Bakewell et. al 1998 [34] showing avidin trapped under (**a**) pDEP and (**b**) nDEP between adjacent polynomial quadrupole electrodes.

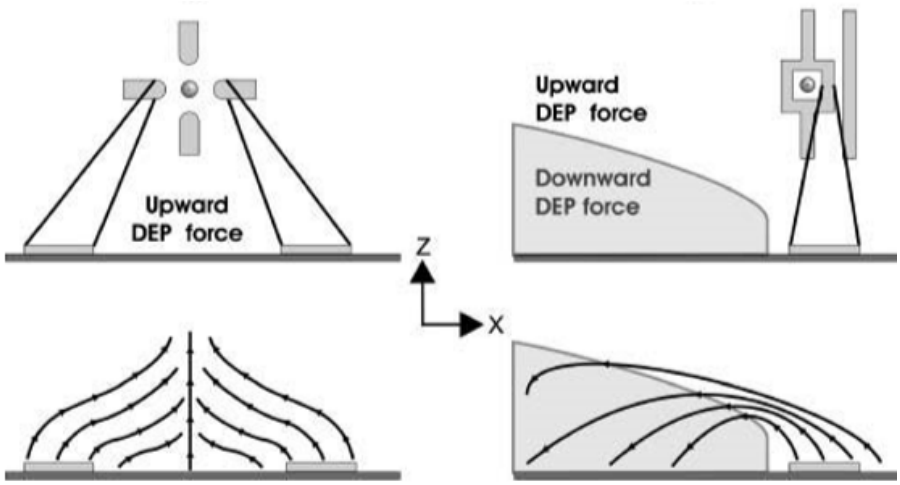
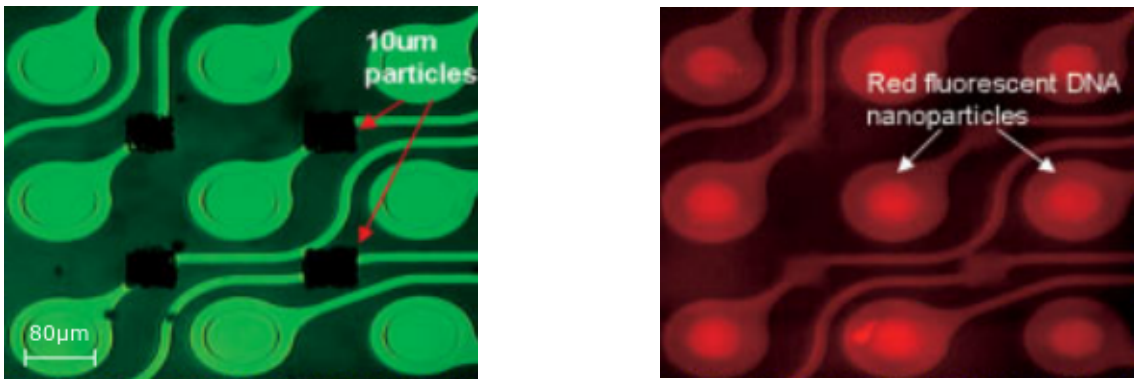


Figure 4.9: A comparison of the DEP force direction for (**left**) quadropoles and (**right**) square-ring traps [8].



(a) nDEP (b) pDEP

Figure 4.10: Fluorescence microscope images from Krishnan *et al.* 2008 showing (**a**) nanoparticles trapped under nDEP at the centre of circular quadrupoles and (**b**) DNA trapped under pDEP at the edges of circular electrodes [35].

et al. 2005 for use in single cell patterning, which is able to force particles downwards under DEP, producing a significantly stronger trap with an increased range [8]. Each square ring is interconnected along a line which eases integration. However, the trapping range of nDEP traps remains significantly lower than that of a pDEP trap.

Carbon Electrodes

As an improvement to planar electrodes, the electrodes can be extended to form 3D pillars and increase trap capacity, which is determined by the total volume surrounding the electrodes where the electric fields are intense enough to trap DNA. In Martinez Duarte *et al.* 2013, pillar electrodes were fabricated by creating a precursor structure out of SU-8 which was carbonised at $900°C$ [37]. These high temperatures make this fabrication method incompatible with a CMOS-based ISFET device.

The carbon structures sat upon metallic IDEs, so that each row of pillars had the same polarity. This approach was therefore was unable to produce the checkerboard polarity required for quadrupoles, instead observing nDEP to the regions between pillars along with pDEP towards pillar surfaces. The main advantage of using carbon electrodes is that they have a high electrochemical stability, which means that larger voltages can be applied and at lower frequencies without causing electrolytic reactions. As such, Martinez Duarte was able to use a $14\,V_{pp}$, $10kHz$ signal that was capable of trapping $48.5\,kbp$ λ-phage DNA in a $18.7\,mSm^{-1}$ solution under pDEP up to a crossover frequency of around $75\,kHz$, with simulated electric field strengths shown in Figure 4.11.

The superior characteristics of carbon-based electrodes have also been seen in the emergence of graphene and carbon nanotubes as electrode materials. In 2006, Tuukkanen *et al.* were able to set up metallic contacts across a carbon nanotube deposited on a silicon (Si) substrate [38]. Even at a modest voltage of $1.6\,V_{rms}$ across it, the nanotube was able to produce extremely high electric field gradients due to its small geometry, which is compared in Figure 4.12 against the electrode without a nanotube.

Graphene can also create large electric field gradients due to its atomic thickness. Barik *et al.* transferred graphene onto a Si substrate and integrated it into an electrode system for DEP manipulation of DNA in their 2017 paper [39]. The sheet of graphene formed a parallel plate with a platinum (Pt) electrode on the bottom of the substrate, between which $1\,V$ was applied. As seen in Figure 4.13, this produced large field gradients on the edge of the graphene.

For both nanotubes and graphene, expense and currently imperfect fabrication methods mean that these materials are not suitable for a low-cost, mass-produced diagnostic device. However, in the future, as methods involving these materials improve and costs go down, graphene and

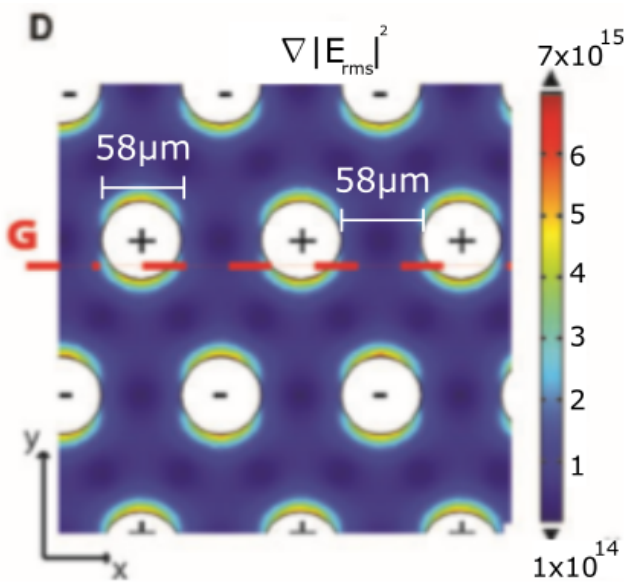


Figure 4.11: A diagram showing the polarisation of the carbon pillar electrodes from Martinez-Duarte *et al.* 2013 and the simulated electric field strength gradients ($\nabla|E|^2$) they produce [37].

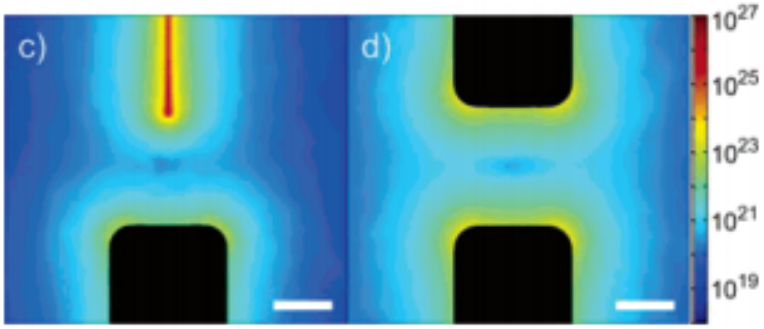
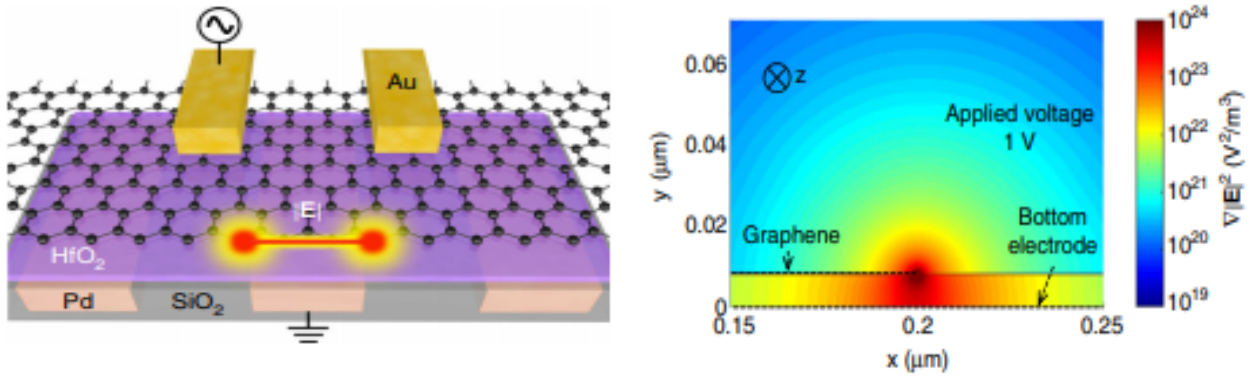


Figure 4.12: The simulated electric field strength gradients produced in Tuukkanen *et al.* 2006 both with and without the carbon nanotube. The gap between the nanotube and the opposing electrode is 100 nm and the white scale bars represent 50 nm [38].



(a) (b)

Figure 4.13: (**a**) A schematic of the parallel plate set-up including graphene and an electrode used in Barik *et al.* 2017 and (**b**) the electric field strength gradients produced by the graphene sheet [39].

Year	Paper	Application	Electrode Design	Electrode Material	Frequency	Voltage	σ (mSm^{-1})
1998	Bakewell *et al.* [34]	Trapping	Polynomial quadrupole	*Au*	nDEP<1 MHz	4 V_{pp}	80
2001	Kawabata *et al.* [32]	Separation	Trapezoid castellated IDE	*Al*	1 MHz	7 V	2
	Tsukahara [40]	Trapping	quadrupole	-	1 kHz	1.2 − 7.1 V	4
2002	Asbury *et al.* [5]	Trapping	Interdigitated line	*Au*	5 − 2000 Hz	0.5-4V_{pp}	-
2002	Dewarrat *et al.* [28]	Trapping	Sawtooth	*Au*	1 MHz	4 V	7
	Hölzel *et al.* [41]	Trapping	Interdigitate line	*Al*	1 MHz	2.5	0.2 [1]
	Namasivayam *et al.* [42]	Stretching	Line	*Au*	1 MHz	12 V	-
2003	Zheng *et al.* [36]	Trapping	quadrupole	*Au*	pDEP<500 kHz	<10 V	0.2 [1]
2005	Lao *et al.* [43]	Size separation	Lines and plate	*ITO*	100 Hz	1.7 V	0.2 [1]
	Tuukkanen *et al.* [44]	Trapping	Square tips	*Au*	750 kHz	10^7 Vm^{-1}	-
2006	Bakewell *et al.* [45]	Trapping	Interdigitated line	*Au*	100 kHz	4.5 V	8.5
	Bown *et al.* [46]	ACEO concentration	Concentric circles	*Au*	1 kHz	4 V_{pp}	5.5
	Sung *et al.* [47]	Stretching	Tip and plate	*Au*	1 kHz collect 1 MHz stretch	7 V_{pp} collect 23 V_{pp} stretch	0.02
	Tuukkanen *et al.* [38]	Trapping	Nanotube	*C*	0.2 MHz	7-8 V	2
2007	Kumemura *et al.* [48]	Trapping	Square pillars	*Al*	900 kHz	10 V	0.2 [1]
	Pham *et al.* [49]	Trapping	Pyramidal	*Au*	>200 kHz	15 − 40 V	0.2 [1]
	Walti *et al.* [50]	Stretching	Interdigitated line	*Au*	250 kHz	<12 V	0.2
2008	Du *et al.* [51]	Trapping	Asymmetric T-quadrupoles	*Au*	1 kHz	5 − 20 V_{pp}	15
	Yamahata *et al.* [52]	Mechanical analysis	Nanotweezer	*Al*	2.6 kHz	40V_{pp}	0.2
	Vedala *et al.* [53]	Trapping	Nanotube	*C*	1 MHz	1V_{pp}	-
2009	Agastin *et al.* [54]	Separation	Coplanar lines	*Al*	100 kHz	340V_{rms}	0.95
	Dalir *et al.* [55]	Stretching	Sawtooth with diamonds in gap	*Al*	100 kHz	28V_{pp}	0.02
	Leitherer *et al.* [56]	Trapping	Triangular tips	*Au*	100 kHz	5V_{pp}	100
	Yeo *et al.* [57]	Size specific concentration	Nanotip	*SiC*	5 MHz	20V_{pp}	0.2 [1]
2010	Cheng *et al.* [58]	Trapping	Cusp shaped	*Au*	0.8 − 1.2 MHz	<10^7 Vm^{-1}	-
	Yokokawa *et al.* [6]	ACEO concentration	Concentric circles	ITO	1 kHz	2.5 V	2
2011	Kumemura *et al.* [59]	Single DNA trapping	Nanotweezer	*Al*	1 MHz	15 V	0.11
	Martinez-Duarte *et al.* [60]	Concentration	Circular posts	*C*	nDEP<75 kHz	16V_{pp}	0.187
2012	Kalyanasundram *et al.* [61]	Trapping	Nanotips	*Au*	100 Hz	20V_{pp}	-
	Sonnenberg *et al.* [62]	Particle isolation	Circular quadrupole array	*Pt*	10 kHz	20V_{pp}	740-1150
2014	Mohamad *et al.* [63]	Conductivity analysis	quadrupole	*Au*	3 − 12 MHz	5 − 10 V_{pp}	1-1000
2015	Li *et al.* [64]	Impedance sensing	Interdigitated line	*Al*	100 kHz/300 kHz for λ/pUC18	10 V_{pp}	-
	Zhou *et al.* [30]	DNA collapse	Parallel wires	*Pt*	100 − 800 Hz	-	-
2017	Barik *et al.* [39]	Trapping	Sheet	*Gr* [2]	1 MHz	<3 V	1.2
	Cheng *et al.* [65]	Hybridisation	Parallel Plates	*Al*	100 kHz	3V_{rms}	1000
2018	Hung *et al.* [66]	Trapping	Square with line array in gaps	*Al*	1 MHz	48 V	-
	Velmanickam *et al.* [67]	Concentration	Curved-T array	*Au*	1 MHz	10V_{pp}	0.5
2019	P. Pungetmongkol *et al.* [68]	Trapping (Impedance spectroscopy)	Nanogap	*Au*	< 1.5 V (0.5 MV/m)	10 kHz − 1 MHz	-
2022	Q. Zhao *et al.* [69]	Concentration & Separation	Nanogap	*Au*	1 − 50 MHz	5 − 10 V	1

Table 4.2: Electrode systems used for electrokinetic manipulation of DNA free in solution. Systems manipulating of DNA origami, DNA nanoparticles, or DNA bonded to microspheres, nanotubes, or surfaces have not been considered. Systems involving nanotweezers or nanopipettes have also been excluded. [1] Estimation based on deionised water. [2] Graphene.

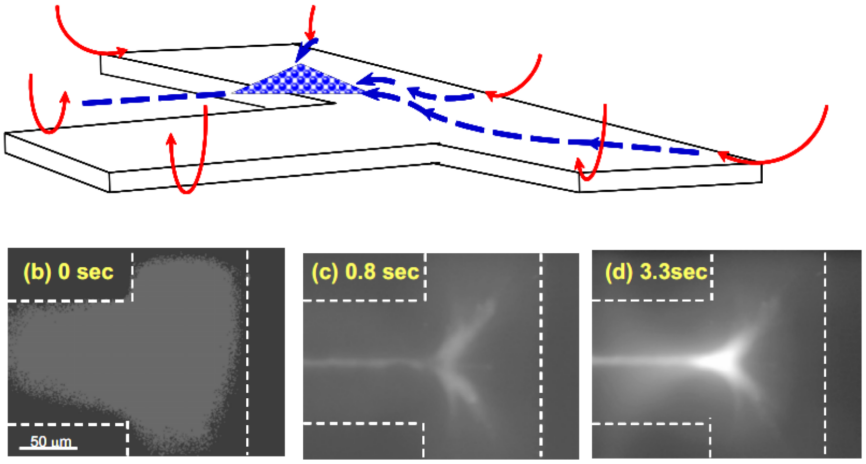


Figure 4.14: Figures from Du *et al.* 2008 showing (**top**) the direction of vortices created via ACEO on the 'T'-shaped quadropoles and (**bottom**) the subsequent trapping of $T4$-DNA [51].

carbon nanotubes should become the predominant materials for DEP applications.

4.3.3 Other Electrokinetic Trapping Systems

One major limitation of DEP is that it has a limited range of trapping, at least when using microelectrodes restricted to low applied voltages. Alternatively, the fluidic vortices generated by ACEO and electrothermal effects can extend much further into the test solution and bring DNA down to trapping regions at electrodes.

In Park *et al.* 2009 [70], an array of square ring traps was able to utilise electrothermal vortices to move latex beads at a long range down to the electrodes where they were trapped. Trapping was achieved in high conductivity solutions of $1 \times 10^{-5}\, S/m$, $0.05\, S/m$, and $0.224\, S/m$ and with a $10\, V_{pp}$, $10\, MHz$ voltage applied to the electrodes.

In low conductivity solutions, $< 20\, mSm^{-1}$, and at low field frequencies, $< 100\, kHz$, ACEO motion is stronger than electrothermal. In such conditions, ACEO trapping can be conducted, as is presented in Du *et al.* 2008 for an asymmetric 'T'-shaped quadrupole [51]. Du used a frequency of $1\, kHz$ for optimal vortex creation in a solution with a conductivity of $150 \times 10^{-6}\, S/m$, and DNA was collected within a stagnation point above the electrodes, as seen in Figure 4.14, held there by pDEP. With a fluid velocity of $10\, \mu ms^{-1}$, vortex assisted trapping can be faster than that of DEP and could provide a means of concentrating amplification reagents, which would experience weak DEP forces, at trapping regions.

4.3.4 Challenges in ISFET-DEP Combination for DNA Detection

Having considered the electrode designs applied to electrokinetic trapping of DNA in the literature and noting the observations on trapping dynamics, many challenges that will be faced in implementing an electrode-based DNA trap on an ISFET array have been made apparent.

Electrostatic interference

DNA drawn to the ISFET surface will electrostatically interact with the ISFET due to its negative charge. This would cause variations in the ISFET threshold voltage, as previously shown in Castellarnau *et al.* 2006, and inhibit detection of pH changes. DNA's negative charge would have the opposite effect on ISFET threshold voltage as that of positively charged protons and this signal suppression could lead to lower sensitivity and a higher ttp. Therefore, DNA trapping regions should be significantly over a Debye length from ISFET sensing regions to avoid electrostatic interaction.

DNA amplification

If many DNA strands are packed tightly into a small volume, as is possible with DEP trapping, then amplification reagents may be unable to reach target DNA. The result of this would be to render DNA strands at the centre of DEP trapping regions or dense pearl-chains undetectable, causing false-negatives to potentially be recorded by the device. Higher field frequencies can be used to reduce DNA polarisation and avoid excessive coalescence of neighbouring strands, possibly at the expense of DEP strength.

To maximise the signal enhancement from surface localised DNA, amplification reactions should be initiated whilst the DNA is trapped by the electrodes. However, without the ability to concentrate amplification reagents at DEP trapping regions, reactions will not progress efficiently. Primers and enzymes will prove difficult to influence under DEP due to low molecular polarisation. This suggests that alternative means of concentrating amplification reagents is required, such as using ACEO [51], electrothermal [46], or chaotic vortices [71]. If amplification reagents can be concentrated at electrode edges, then the high concentration of DNA could lead to improved reaction kinetics. The elongation of DNA strands in electric fields, as observed in Washizu *et al.* 1990 [25], will also improve reaction efficiency as primers will be better able to bind to target DNA.

The thermal regulation required for the amplification reactions could confound DEP trapping by creating convective vortices that release DNA from traps. One advantage of using LAMP as the reaction, as opposed to PCR, is that using a constant temperature throughout will reduce

thermal gradients within the reaction solution. Yet, convection remains unavoidable and higher voltages may be required to overcome it.

High Electrolyte Conductivity

With the high solution conductivity anticipated for LAMP reaction solutions, electrode reactions, catalysed by the applied voltage, are a strong possibility. These reactions will quickly degrade an electrode, cause large currents to flow through the system, and generate bubbles, making reliable sensing impossible. It is key that electrochemically stable metals, such as Au and Pt, are used to construct the electrode. Alternatively, passivation over metal electrodes would limit electrolytic reactions at the expense of electric field strength and thus trap efficiency.

A further challenge posed by high electrolyte conductivities is a lower CM factor of DNA and subsequently a weaker DEP force. This may necessitate the use of higher voltages, which in turn increases the risk of electrode spoiling and bubble formation. As demonstrated by the experimental observations of Tao *et al.*, higher field frequencies may produce the most effective DEP trapping in high conductivity solutions [13].

Electrode-ISFET Interaction

The introduction of electrodes on the surface of the ISFET array may cause undesirable side-effects. The fabrication process will introduce trapped charges that will offset the ISFET output. The electric fields from the electrodes themselves could contribute to noise on the signal observed by the ISFET. Field frequencies that are much higher than the ISFET array frame rate will have little direct effect, but non-linear interactions could occur. The surface electrodes could also interfere with ISFET biasing via the reference electrode. The reference potential, if large, could catalyse reactions on the electrode surface.

4.3.5 Electrode System Design

Taking into account all of the evidence, it is clear that pDEP should be favoured to trap DNA due to the stronger forces it can exert. IDEs with some form of castellation offer high electric field strengths with easy integration and fabrication. A sawtooth electrode opposing a line electrode would provide high-gradient fields and a strong DEP force. Au or Pt are the most practical choices for electrode materials to minimise DNA bonding and electrolytic reactions.

The characteristic dimensions of the electrode should generally all be as small as possible, to maximise electric field gradients and thus the DEP force that can be exerted. Electrodes with

a width and separation in the order of $10\,\mu m$ have shown to be capable of DEP manipulation of DNA. Electrode thickness should be as small as possible to produce high intesnity fields, with typical thicknesses of 10-100 nm in the literature. The electrodes should have at least a Debye length separation from ISFET sensing regions to avoid electrostatic interference of trapped DNA, for which a separation in the order of $1\,\mu m$ would suffice.

The voltage applied to the electrode must achieve the target electric field strength of $1.9 \times 10^5\,Vm^{-1}$ to trap DNA, which electric field simulations can help to verify. The optimum field frequency is subject to various factors, namely the conductivity of the solution in which the DNA is suspended. However, over $10\,kHz$ offers a frequency where DNA is likely to experience strong pDEP whilst avoiding strong electro-osmosis and electrode spoiling.

4.4 Photolithographically Fabricated On-CMOS Electrodes

The most suitable approach to producing on-CMOS electrodes capable of DEP manipulation of DNA is to use photolithography. Photolithography is the process of creating topological patterns in photo-sensitive compounds known as photoresists, which then allows selective post-processing.

4.4.1 Design and Simulation

The microchip selected for on-chip electrode fabrication was Titan, which is a $12\,mm \times 8\,mm$ microchip fabricated in $0.18\,\mu m$ CMOS by Taiwan Semiconductor Manufacturing Company (TSMC), that contains a 204×290 array of ISFETs. The ISFET pixels conduct pH-time conversion, so the output voltage varies in the same direction as pH, instead of the opposite direction as is the case when threshold voltage is used as an output.

An IDE array was designed with an electrode width and separation that fits either one or two sensors between each interdigitation, allowing extra space for manufacturing tolerances. Arrays were designed to occupy only half of the short dimension of the array, providing space to incorporate an $Ag/AgCl$ wire RE. Line IDEs were designed to form a benchmark, with one-sided sawtooth IDEs also produced. The triangular castellations of the sawtooth IDEs were arranged such that there was one castellation adjacent to each pixel between the electrodes. The dimensions of the IDEs are provided in Figure 4.15.

Both electrode systems were simulated in COMSOL Multiphysics 5.4 to estimate electric field strengths and intensity gradients, including a line IDE with one ISFET separation between electrodes and a two-sided sawtooth to act as comparisons. Estimates were made at the mid-point of electrode edges, which for the sawtooth electrodes is the tip of the middle triangular

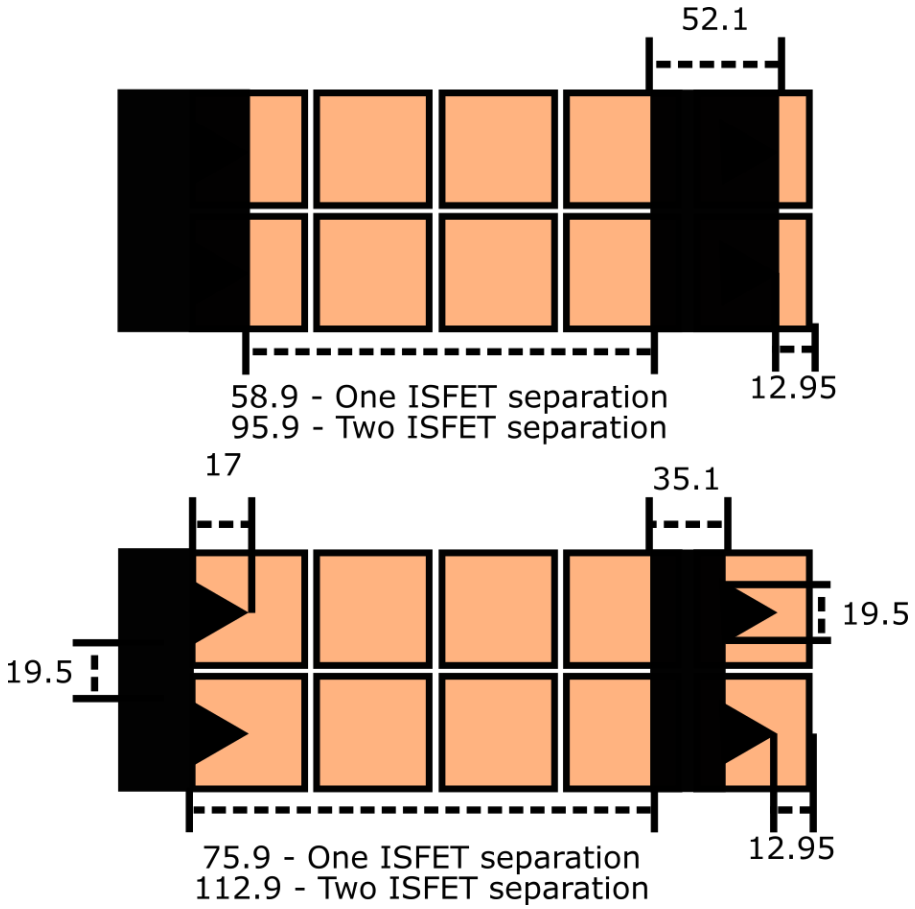


Figure 4.15: A schematic detailing the design features of the (**top**) line and (**bottom**) one-sided sawtooth electrode arrays. Values are given in micrometres. ISFETs are represented by orange squares and electrode separations are provided for designs with one and two ISFETs between neighbouring electrodes.

Electrode Design	$\|\boldsymbol{E}\|$ (V/m)	$\boldsymbol{\nabla}\|\boldsymbol{E^2}\|$	Trapping Voltage (V)
Line - One ISFET Separation	4.10×10^6	1.63×10^{20}	0.10
Line - Two ISFET Separation	3.40×10^5	3.10×10^{17}	1.20
One-sided Sawtooth - Two ISFET Separation	2.84×10^6	6.23×10^{19}	0.13
Two-sided Sawtooth - Two ISFET Separation	2.51×10^6	4.03×10^{19}	0.15

Table 4.3: A summary of FEM simulation estimates of electric field variables for the designed electrodes.

castellation. An electrode thickness of $100\,nm$ was assumed and a mesh size of $50\,nm$ was found to be sufficient to make results mesh-invariant. Results were simulated for applied voltages of 0.1-2 V in $0.1\,V$ increments, with the outer electrodes of a three electrode system given positive polarities and the middle electrode given a negative polarity. The electric fields were simulated with water on top of the electrodes, which themselves were Au, whilst the chip surface was set as SiO_2. The trapping voltage is the smallest voltage for which electric field strengths over $1.9 \times 10^5\,V/m$ are obtained, in accordance with the observations in Asbury *et al.* 1998 [27].

The results of the simulations, compiled in Table 4.3, show that all electrodes are capable of trapping DNA with low voltages applied. The sawtooth electrodes produce stronger fields and gradients than the line electrodes, with the one-sided sawtooth outperforming the two-sided sawtooth, as expected.

4.4.2 Method and Materials

Electrode Fabrication Process

There are typically two main approaches to producing metallic patterns on a substrate: etching or lift-off, both of which are illustrated in Figure 4.16. With etching, the substrate is coated with a metal, a photopattern is produced on top, and then chemical or physical etching is conducted to remove metal in the desired areas. By instead coating the metal on top of the photopattern and then 'lifting off' the underlying resist, an electrode design can be transferred to the substrate. Lift-off is the more desirable approach as it has fewer processing steps and better protects the underlying substrate.

Lift off processes require a photoresist capable of producing an undercut sidewall, to avoid deposited metal forming a continuous layer. This necessitates the use of resists capable of working in negative mode, where it is the exposed areas that are removed during development. Image reversal resists can operate in negative mode, with extra processing steps, as illustrated in Figure 4.17. After the first exposure, the resist is baked, causing exposed areas to lose their solubility [72]. Then, during a second, 'flood' exposure, the previously unexposed areas,

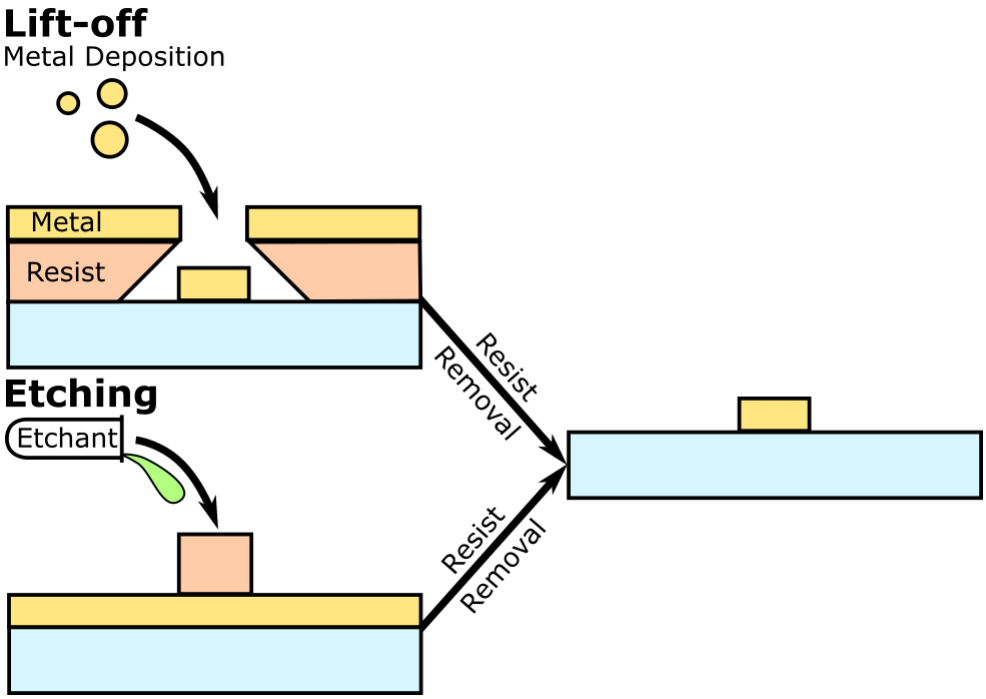


Figure 4.16: A schematic illustrating the lift-off and etching approaches to producing patterned metal.

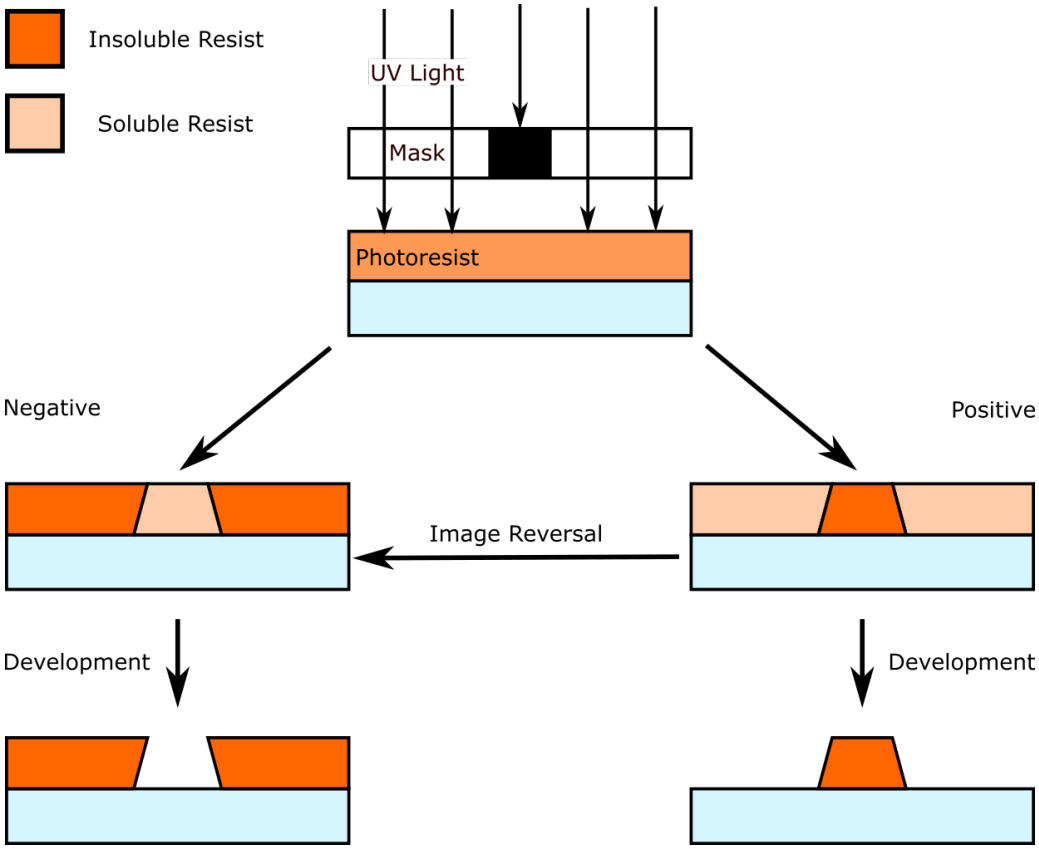


Figure 4.17: A schematic depicting the creation of photopatterns with different types of photoresists.

which remain photoactive, become soluble and will be removed upon development. These image reversal resists can produce patterns with greater resolution and with better lift-off performance than negative resists, but require an extra, carefully optimised thermal processing step.

Electrodes were initially fabricated on $0.17\,\mu m$ thick glass coverslips (Fisher) to verify their ability to trap DNA, before moving production on to microchips. Photopatterning on individual microchip dies is a more complex process than if conducted on an entire wafer. This is due to the resist coating process, where surface tension and solvent evaporation create regions of large resist thickness around the substrate, known as edge-beads. Fortunately, the impact of these edge-beads has been significantly reduced by using Titan, due to its large, $12\,mm \times 8\,mm$ dimensions.

Having produced the photopattern in the image-reversal resist, the chip was cleaned in an oxygen (O_2) plasma cleaner (Diener Asher), to remove residues left on the surface and avoid poor adhesion of deposited metal. Then, $10\,nm$ of chromium (Cr) or titanium (Ti) was deposited as an adhesion layer, either through evaporation or sputtering, after which $50\,nm$ of Au or Pt was deposited immediately via sputtering (HEX or PVD75).

After conducting lift-off of the resist using acetone (Sigma) and mild sonication (USC 300 THD), the chip was glued to a PCB using a Ag epoxy (Epotek) and then wirebonded using a F&S wedge bonder with $25\,\mu m$ Al wire. These bonds were then encapsulated in black epoxy (Epotek), with electrical contact made to the electrodes via Ag epoxy to wires.

Fabrication Process

1. Clean the substrate with ultrasonication for 10mins in acetone, isopropanol (ThermoFisher), and deionised (DI) water before drying with a nitrogen (N_2) gun.
2. Heat at $150°C$ to break hydroxyl bonds on the substrate and improve resist adhesion.
3. Spincoat (CEE Apogee Spinner) AZ 5214E (Microchemicals) image-reversal photoresist onto the substrate at $4000\,rpm$ for $30\,s$, giving $1.4\,\mu m$ coating thickness, before a ramp up to $6000\,rpm$ for $10\,s$ to reduce edge-beading.
4. Softbake the photoresist at $110°C$ for $50\,s$ to evaporate solvents and improve surface adhesion.
5. Rest the substrate for $10\,mins$ to rehydrate.
6. Carry out the first exposure with a mask, at a target dose of $120\,mJcm^{-1}$.

7. Rest the substrate for 10 $mins$ to allow N_2 to degas.
8. Carry out the image reversal bake at 120°C for 2 $mins$.
9. Carry out the flood exposure without a mask, at a target dose of 540 $mJcm^{-1}$.
10. Develop the photopattern in a bath of AZ 326 MIF developer (Microchemicals) for 78 s. This development time is longer than usual to allow sufficient overhang of resist sidewalls.
11. Treat the substrate in O_2 plasma at 0.4 $mTorr$ and 300 W for 10 $mins$ to remove surface residue.
12. Deposit a 10 nm Cr adhesion layer via e-beam evaporation or sputtering.
13. Deposit a 50 nm Au layer via sputering.
14. Lift-off the resist using an acetone bath and mild sonication.

Testing

45 kbp λ-DNA was fluorescently dyed with YOYO-1 at a ratio of 10 bp to 1 molecule of dye (both Fisher Scientific). Concentrations of 400 pM and 40 pM were used, as seen in the literature. DNA trapping was conducted in both DI water and LAMP reaction solutions. The constituents of the LAMP reaction solution at final concentrations are: 1× isothermal buffer ($Tris - NH_4SO_2$), 6 mM $MgSO_4$, 1.4 mM dNTP mix, 1.2 mg/mL BSA, 0.8 M Betaine, 1× LAMP primer mix, and 0.5 $U/\mu L$ Bst 2.0 DNA polymerase (All Biolabs). For electrochemical testing, pH buffers consisting of 1 M potassium chloride (KCl, Scientific Laboratory Supplies) and 1 M Tricene (Sigma) were used. The final pH of the buffers was determined by the addition of 1 M hydrochloric acid (HCl) or 1 M sodium hydroxide ($NaOH$, both Sigma) whilst measuring pH with a probe (Sentron). The conductivity of all solutions was tested using a conductivity meter (Extech Instruments).

Fluorescence microscopy was conducted on a Carl Zeiss Axio Zoom V.16 upright microscope. Because of the opacity of the microchip, it is not possible to use inverted or confocal fluorescence microscopes. The microscope was equipped with ApoZ 1× and 1.5× objective lenses that had ultra-long working distances. This allows the imaging of DNA at electrode surfaces through thick samples in the order of mm.

An Agilent 33522A function generator with two channels was used to provide the excitation to the electrodes. One channel was sent to each of the two sets of interdigitations, with a 180^o

phase shift between the sinusoidal signals. For electrochemical testing, the Lacewing platform was used to handle sensor calibration and readout [73]. An $Ag/AgCl$ RE was fabricated by anodising a Ag wire in $3\,M\ KCl$ for $10\,mins$.

4.4.3 Results

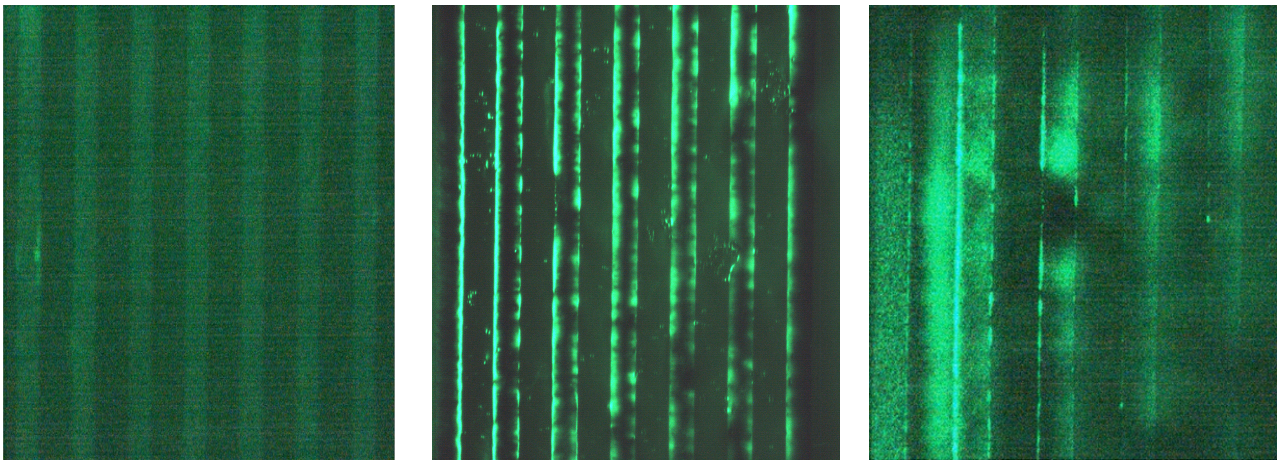
Glass Coverslips

Successful DEP trapping of DNA was conducted with the glass coverslip-based electrodes, as illustrated in Figure 4.18, using a $4\,V$, $500\,Hz$ excitation and $400\,pM$ DNA. In Figure 4.18a, the electrode surface can be seen, with a low, uniform fluorescence given off by the DNA. Then, in Figure 4.18b, strong concentrations of DNA can be seen along the edges of the electrodes almost instantaneously after the voltage was applied, consistent with DEP trapping. However, with the low frequency being used electric fields will decay due to Debye screening over a short distance in the order of $10nm$. This means that the observed concentration of DNA at electrode edges is likely caused by DNA-DNA interactions rather than DEP. Trapping was not observed that could be attributed to DEP at any frequency up to $1\,MHz$.

Once the voltage was removed, DNA slowly drifted away from the electrode edges over the period of $1\,min$, as seen in Figure 4.18c, with an exponential decay in fluorescence, as also seen in Asbury *et al.* 1998 [27]. In regions along the edges of electrodes, DNA remained after the voltage was removed, suggesting DNA-electrode bonding. This bonding may occur due to imperfections in the Au coating exposing the Cr underneath, which are more likely at electrode edges due to the lift-off procedure.

Increasing the frequency of the voltage to $10\,kHz$, DNA concentration moved to the centre of the electrodes rather than at the edges, as can be seen in Figure 4.19, suggesting ACEO trapping. Both $500\,Hz$ and $10\,kHz$ lie on the border of strongest expected ACEO activity. Therefore, rather than $10\,kHz$ demonstrating stronger ACEO, it may be a consequence of weaker DEP. This is backed up by the observation of centrally trapped DNA with a $1.8\,V$, $500\,Hz$ voltage[2]. ACEO DNA trapping is also demonstrated with $900\,mV_{pp}$ and a $900\,mV$ offset - oscillating between $0 - 1.8\,V$ limits. This is significant as these are the notional voltage limits of a TSMC $0.18\,\mu m$ microchip.

[2]Fluorescence microscope images that show this trapping behaviour, and that of the $900\,mV_{pp}$, $900\,mV$ offset case, can be found in Appendix D. They are not provided here because of their close similarity to Figure 4.19.



(a) Before (b) During (c) After

Figure 4.18: Fluorescence microscope image of line electrodes with a $4\,V$, $500\,Hz$ electric field applied, trapping $400\,pM$ YOYO-1-dyed λ-DNA. The images show the electrodes (**a**) before, (**b**) during, and (**c**) just after the electric field is applied.

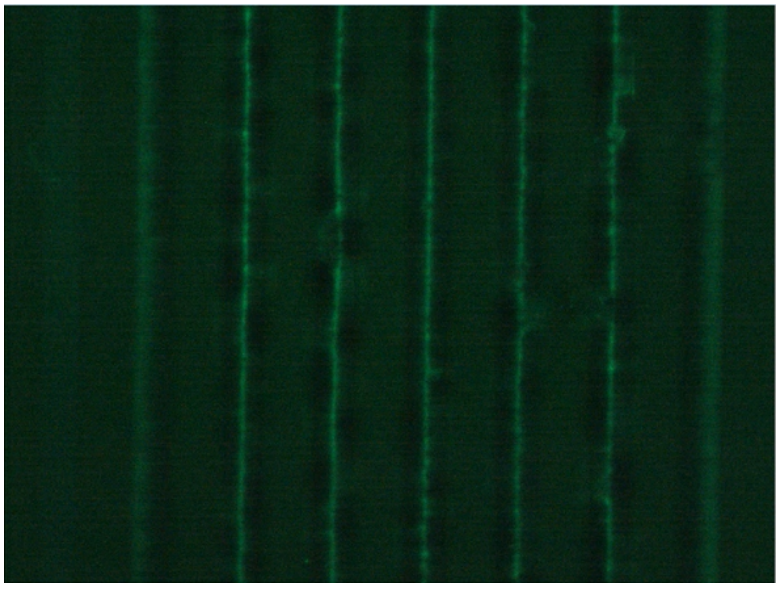


Figure 4.19: Fluorescence microscope image of line electrodes with a $4\,V$, $10\,kHz$ electric field applied, trapping $400\,pM$ YOYO-1-dyed λ-DNA.

Titan

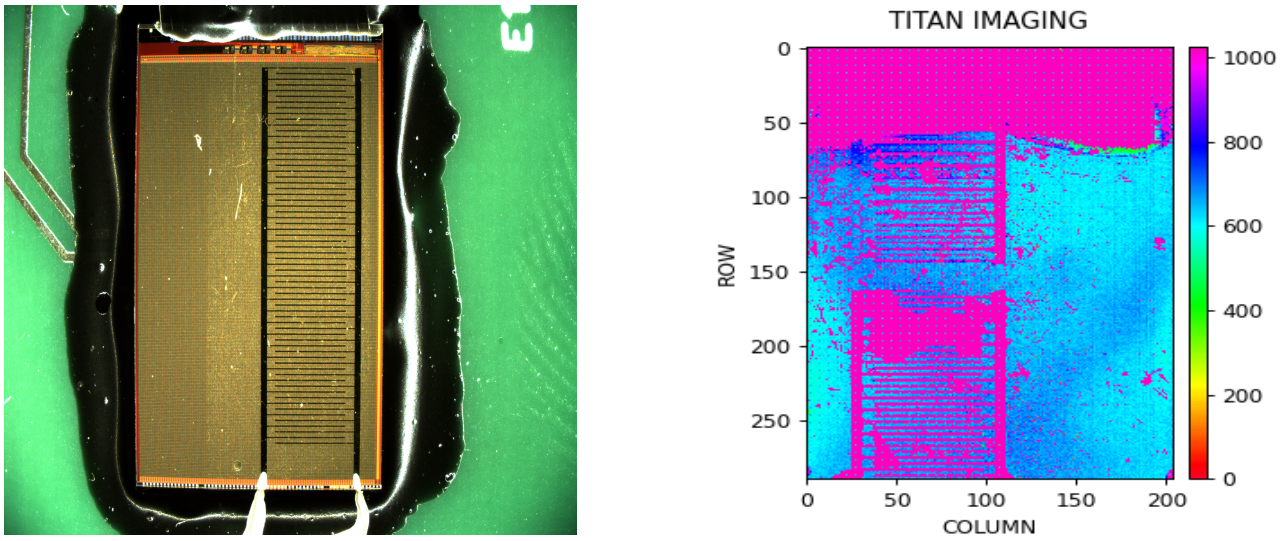
After moving the electrode designs onto the microchip surface, electrochemical testing was carried out to ensure that the microchip still remained electrically active. The ISFET array output, seen in Figure 4.20b, for a Titan microchip with surface electrodes and covered by a pH 7 buffer shows that the chip survived the fabrication process. Pixels underneath electrodes were out of range due to the trapped charge introduced by metal deposition, shown by the purple regions of Figure 4.20b. There were also a large proportion of out of range pixels in areas around the electrodes, which is made apparent when comparing the left side of the array in Figure 4.20b that metal was deposited on, to the right side of the array that was covered during deposition. This is likely caused by pin imperfections in the photoresist causing small points of metal to be deposited on the surface.

Upon application of a $2\,V$, $500\,Hz$ voltage to the electrodes, the mean output of the ISFET array increases by roughly $250\,mV$, as shown in Figure 4.21a. Despite this, when HCl is added to the solution to decrease its pH, a corresponding decrease of around $200\,mV$ in output voltage is seen, demonstrating the electrochemical activity of the chip.

The variation of ISFET output with an applied AC electric field was also observed in Castellarnau *et al.* 2006 [21]. The effect was attributed to disruption of the EDL on the surface of the ISFET sensing region. The impact on array readout can be seen in Figure 4.22, with spatial patterns forming due to the finite frame rate capturing the oscillating voltage - reminiscent of the rolling shutter effect. These patterns are less prominent with higher field frequencies, which should be used if 2D array output is required during trapping. Alternatively, the DEP trapping system could be turned off during readout at the expense of frame rate and trap effectiveness.

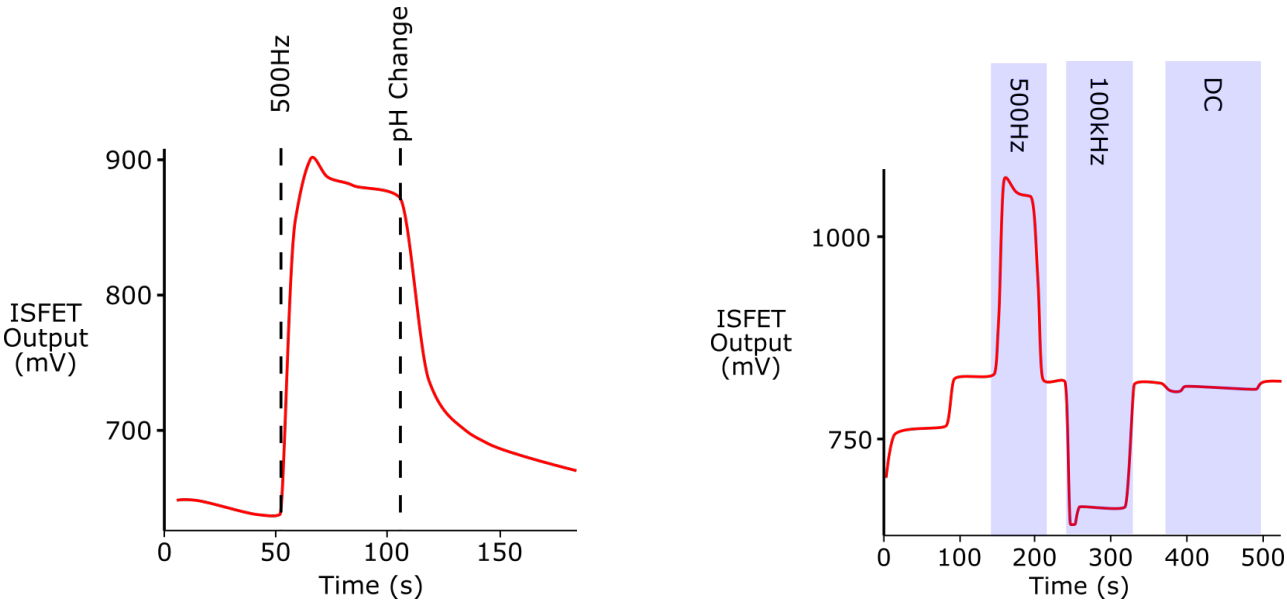
DEP trapping was successfully conducted with the on-chip line IDEs, as demonstrated by Figure 4.23. Experiments were also carried out on one-sided sawtooth electrodes. As can be seen in Figure 4.24a, with a $2\,V$, $500\,Hz$ voltage applied in a $400\,pM$ DNA solution, rather than DNA concentrating at the tips of the saw, where electric field strength is greatest, DNA is trapped along the entire edge of the electrode. Moving down to a DNA concentration of $40\,pM$ in Figure 4.24b, strong ACEO vortices can be seen and a magnified image of the sawtooth tips in Figure 4.24c shows DNA trapping at the centre of the triangular castellations. The reason for reduced ACEO motion in the $400\,pM$ case could be due to increased charge screening or physical impediment from the high concentration of DNA hindering movement of the EDL.

The measured fluorescence intensity profiles across the line and sawtooth electrodes are compared in Figure 4.25, normalised to the background intensity (taken as the first reading). The sawtooth achieves a peak intensity over double that of the line electrode, demonstrating superior DNA trapping.



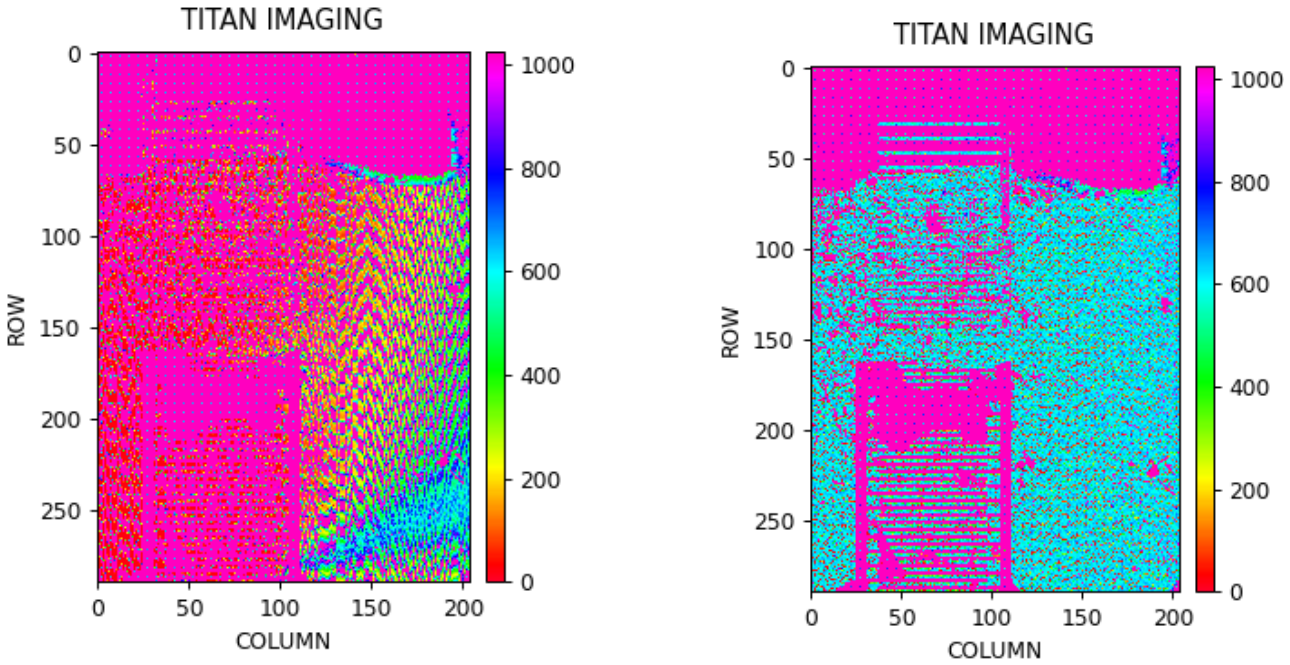
(a) (b)

Figure 4.20: (**a**) Brightfield image of a gold electrode array on a TITAN microchip. (**b**) A plot of ISFET output voltage in mV for an array with surface electrodes.



(a) pH response (b) Frequency response

Figure 4.21: Plots of average ISFET output voltage against time. (**a**) shows how ISFET output voltage changes with the application of a 500 Hz voltage to the electrodes and then the addition of HCl to reduce the pH of the solution. (**b**) shows how varying frequency of the signal applied to the electrodes affects mean ISFET output.



(a) 500Hz (b) 100kHz

Figure 4.22: Plots of ISFET output voltage in mV for an array with surface electrodes after DEP trapping, whilst (**a**) a $500\,Hz$ and (**b**) a $100\,kHz$ voltage is being applied to the electrodes.

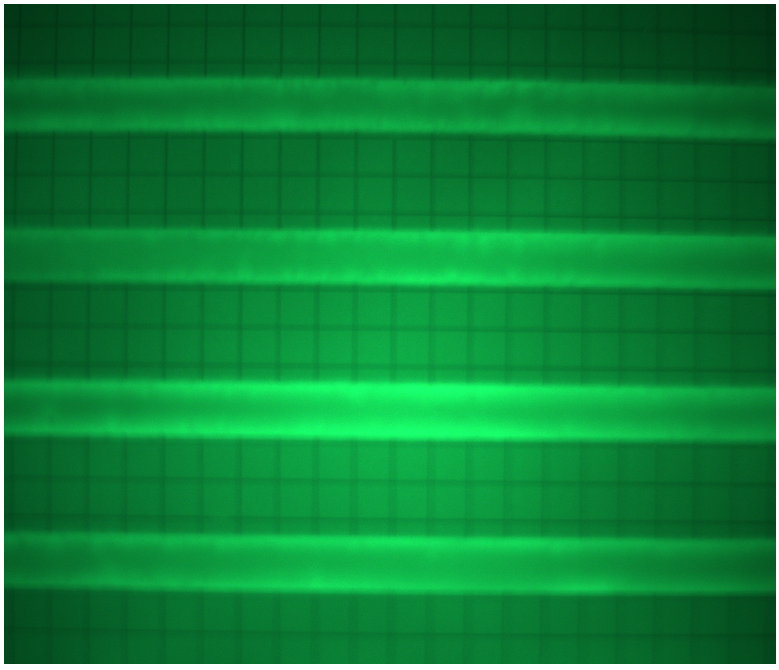
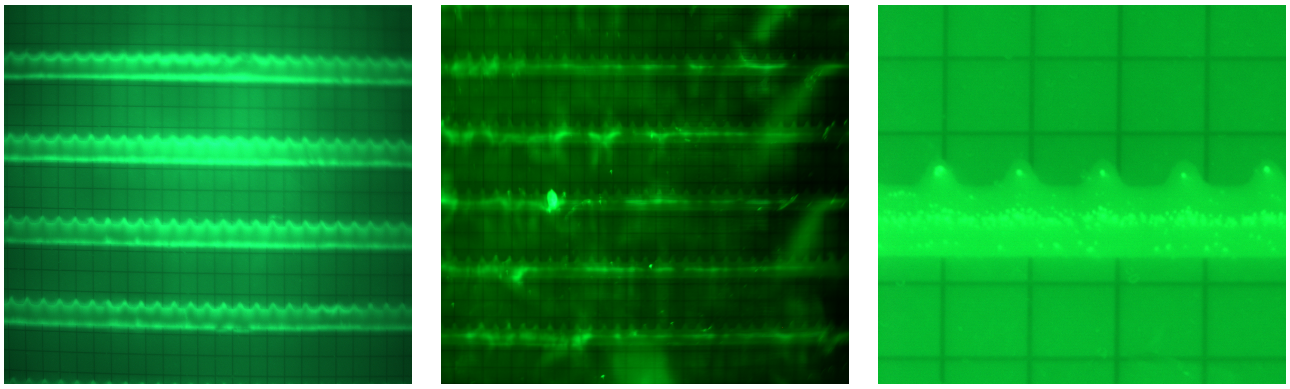


Figure 4.23: A fluorescence microscope image of the photolithographic, on-chip line IDEs with a $2\,V$, $500\,Hz$ electric field applied, trapping $400\,pM$ YOYO-1-dyed λ-DNA.



(a) 400 pM DNA (b) 40 pM DNA (c) 40 pM DNA: Close-up

Figure 4.24: Fluorescence microscope images of photolithographic one-sided sawtooth IDEs with a 2 V, 500 Hz electric field applied, trapping YOYO-dyed λ-DNA. (**a**) shows trapping of 400 pM DNA with (**b**) and (**c**) using 40 pM DNA. (**c**) is a close-up of (**b**).

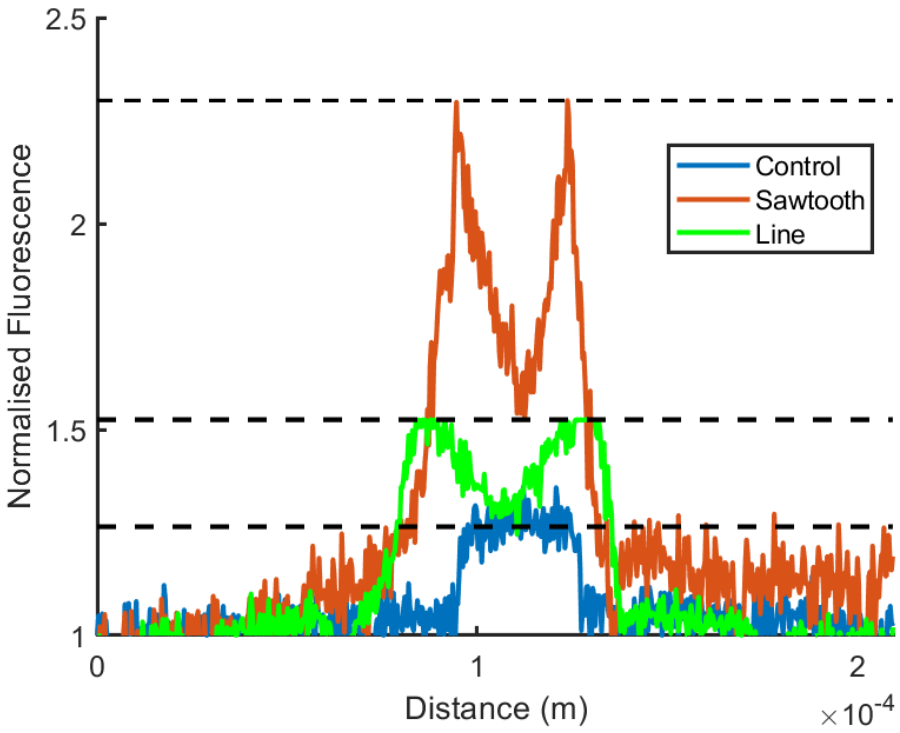


Figure 4.25: A graph containing fluorescence profiles of a control with (**blue**) no electric field applied and the photolithographic, on-chip (**red**) one-sided sawtooth and (**green**) line IDEs 3 $mins$ after the electric field has been applied. A 2 V, 500 Hz voltage is used to trap 400 pM λ-DNA stained with YOYO-1. The data is normalised to the background, which is taken as the first reading.

Solution	Conductivity (mSm^{-1})
DI water	0.7
LAMP	500
Reduced LAMP	236
pH buffer	1724

Table 4.4: A table showing the conductivity of the solutions used for experiments.

DEP trapping was then tested with DNA in the LAMP reaction solution. No DEP was observed at any frequency with voltages up to $4\,V$. Beyond $4\,V$, significant electrode dissolution and bubble generation was observed. A major contributor to this is the high conductivity of the LAMP solutions, which was measured and can be seen in Table 4.4. In an attempt to overcome this, a reduced LAMP solution was tested, with betaine, BSA, and the isothermal buffer omitted. This halved the conductivity of the solution and whilst the rate of electrode dissolution was significantly reduced, allowing the application of voltages up to $10\,V$, DEP trapping was still not observed. Further electrode designs were tested with reduced electrode separations of $59.9\,\mu m$ (one ISFET separation) and $10\mu m$, and Pt used as an electrode material to avoid electrolysis and allow the application of higher voltages. None of them demonstrated electrokinetic trapping of DNA in either LAMP reaction solution.

4.4.4 Discussion

The inability to conduct electrokinetic trapping of DNA in the LAMP reaction solutions with up to $10\,V_{pp}$ applied to the electrodes is concerning for the feasibility of enhancing ISFET-based DNA detection. The LAMP solutions' conductivities were measured to be 2-4× lower than than the highest values in Table 4.2, therefore it should be possible to trap DNA under DEP in LAMP solutions. Further experiments could be carried out with DNA trapped initially in low conductivity solutions and then adding LAMP regents individually. In doing so, it may be possible to identify methods or means of altering conditions to electrokinetically trap DNA in LAMP solutions.

Higher voltages can be applied to increase the DEP force on the DNA. However, as discussed previously, the use of large voltages in high conductivity solutions will quickly spoil the electrodes and generate bubbles. Carbon electrodes could provide a more electrochemically stable electrode if they can be successfully fabricated on CMOS. Other means of preventing electrolysis is the use of an electrode coating, such as a hydrogel [35] or an oxide layer. pH-sensitive hydrogels, such as acrylamide, and thin oxide layers can coat ISFETs without impacting the sensing mechanism, allowing deposition on the entire chip. If the electrode coating is not compatible with the ISFETs, selective patterning must be performed. For oxides deposited by physical or chemical vapour deposition, this can be achieved with photolithography, whereas

accurately patterning hydrogels on the chip would be more complex.

The design of the electrode system can also be reconsidered to create higher field gradients. The current approach of placing ISFETs between IDEs is reasonable from a sensing viewpoint, but increases the separation between the electrodes. An alternative approach could see pairs of electrodes fabricated with separations in the order of $100\,nm$-$1\,\mu m$ to increase DEP forces, with ISFETs placed outside the electrodes [69]. Moving the DEP trapping region away from the sensors will likely only cause a slight increase in the ttp.

4.5 Commercial CMOS Top-Metal Electrodes: The FRY Microchip

The trapping of DNA through electrokinetics has been successfully demonstrated in low conductivity solutions with electrodes deposited on the chip surface in the previous section. The next step, for greater ease of application, is to integrate the electrode system as part of the CMOS fabrication process. To this end, the FRY microchip was designed with electrodes as part of the top-metal and exposed through post-processing from underneath the passivation layer.

4.5.1 Design and Simulation

A prototype $800\,\mu m \times 400\,\mu m$ microchip, named FRY and fabricated by TSMC, was developed in $0.18\,\mu m$ CMOS technology to investigate the efficacy of using CMOS top-metal for DEP trapping of DNA. The chip contains three 5×2 arrays of ISFETs with a $20\,\mu m \times 20\,\mu m$ pixel area and extended gate configuration, designed by Dr. Nicolas Moser. The ISFETs are source-followers, with the drain tied to a $1.8\,V$ voltage, the source tied to ground, and the voltage measured at the source as the output. The layout of FRY was conducted in Cadence Virtuoso. The ISFET pixel's pH-sensitivity was estimated to be $21\,mV/pH$ by simulations in ADE XL using a $30\,mV$ change in gate voltage to represent a pH change of 1. The linear region of ISFET operation was predicted to occur between gate voltages of 0-2 V, and is seen compared to experimental performance in Figure 4.32a. Three electrode designs were tested: Line, wide castellated, and thin castellated. For each set of three electrodes, the outer two can be connected to an external voltage source, limited to $0 - 1.8\,V$, and the middle connected to ground. A 16-bit decoder is used to select electrodes to connect to the voltage source, as well as the row and column of an ISFET for output of data via a serial peripheral interface (SPI). The ISFETs are placed in line with the castellations so that they are adjacent to DEP trapping regions. A schematic of the top-level system architecture can be seen in Figure 4.27.

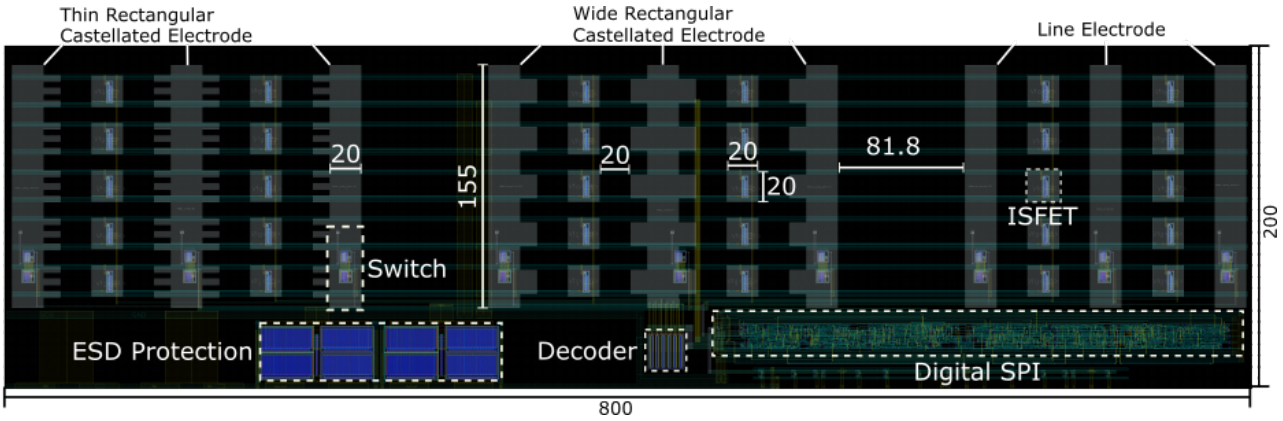


Figure 4.26: The Cadence layout of the FRY microchip, consisting of three 5×2 arrays of extended gate configuration ISFETs situated between IDEs, two of which contain wide and thin rectangular castellations. All dimensions are quoted in μm. The pad regions of the $800\,\mu m \times 400\,\mu m$ chip are omitted from this Figure.

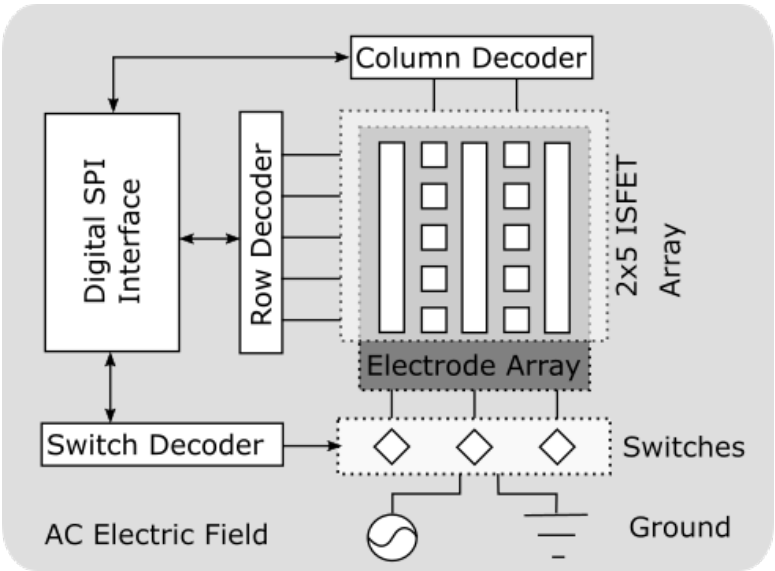


Figure 4.27: A schematic showing the top level system architecture for the FRY microchip.

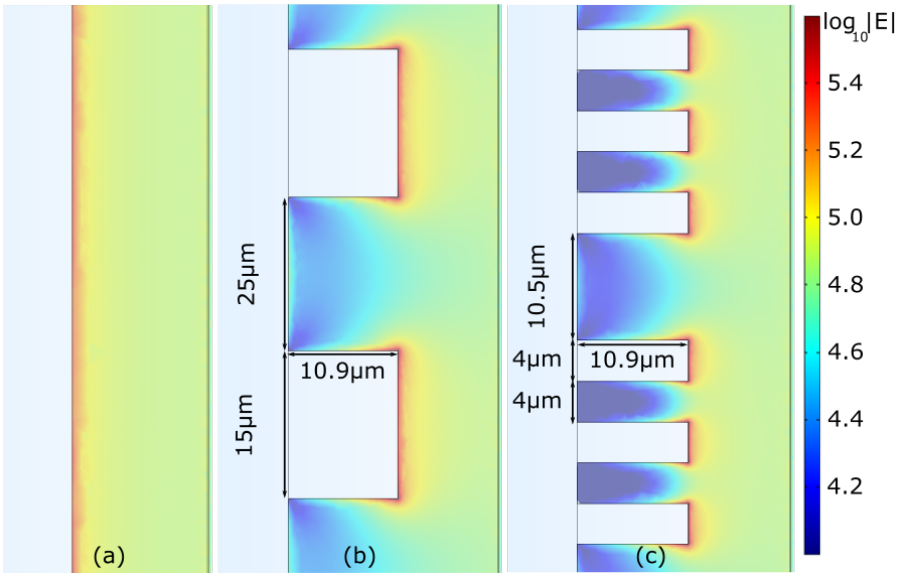


Figure 4.28: Plots of electric field strength as simulated in COMSOL for the (**a**) line electrode, (**b**) wide rectangular castellated electrode, and (**c**) thin rectangular castellated electrode. A logarithmic scale is used and grey areas denote the electrodes.

The electrodes were simulated using the FEM simulation software COMSOL Multiphysics 5.4. A minimum mesh element size of $0.08\,\mu m$, which is the thickness of the electrodes, was sufficiently small for mesh-invariant results. Simulations were carried out with the $2\,\mu m$ passivation layer above the electrodes removed. Figure 4.28 shows plots of electric field strength for the three sets of electrodes with the maximum chip input of $1.8\,V$ applied to the outside electrodes and the inside electrode grounded.

Table 4.5 summarises electric field values. Electric field strength, $|\vec{E}|$, and intensity gradient, $\nabla|\vec{E}|^2$, were averaged along the top edge for the line electrode and over all protruding corners of the castellations. The uncertainties are represented by the standard deviation of the population.

For all electrodes, electric field strengths higher than $1.9 \times 10^5\,Vm^{-1}$ are achieved, which is quoted in Asbury *et al.* 1998 as being capable of trapping DNA [27]. In Velmanickam *et al.* 2018 , an electric field intensity gradient of $10^{18}V^2m^{-3}$ is quoted [31]. Both castellated designs produce similar or stronger gradients than this value. As anticipated, the castellated designs produce stronger electric fields and gradients than the line IDEs. Low trapping voltages are

Electrode Type	$\|\vec{E}\|$ (Vm^{-1})	$\nabla\|\vec{E}\|^2$ (V^2m^{-3})	**Trapping Voltage** (V)
Line	$(2.58 \pm 0.08) \times 10^5$	$(8.04 \pm 1.22) \times 10^{17}$	1.40 ± 0.05
Wide Rectangle	$(4.57 \pm 0.52) \times 10^5$	$(1.15 \pm 0.54) \times 10^{19}$	0.80 ± 0.05
Thin Rectangle	$(7.70 \pm 0.76) \times 10^5$	$(7.63 \pm 3.30) \times 10^{18}$	0.50 ± 0.05

Table 4.5: A summary of electrode system FEM simulation results.

Parameter	Value
CMOS process	$0.18\,\mu m$ TSMC
Chip dimensions	$800\,\mu m \times 400\,\mu m$
ISFET pixel dimensions	$20\,\mu m \times 20\,\mu m$
ISFET array size	3 sets of 5×2
ISFET sensitivity	$21\,mVpH^{-1}$ ($30\,mVpH^{-1}$ intrinsic sensitivity assumed)
supply voltage	$1.8\,V$
Maximum electric Field strength	$7.70 \times 10^5\,Vm^{-1}$
Maximum electric field intensity Gradient	$1.15 \times 10^{19}\,V^2m^{-3}$

Table 4.6: Summary of FRY microchip specifications

achieved by all electrodes.

It would be beneficial to conduct DEP manipulation of DNA without removing the passivation layer over the electrodes completely and exposing the electrodes to the electrolyte, to avoid electrode spoiling. Simulations varying the thickness of the passivation layer above the electrode estimated that DNA could be trapped under pDEP with $0.6\,\mu m$ of passivation covering the electrodes.

4.5.2 Methods and Materials

Passivation Removal by Focussed Ion Beam Milling

Removal of the passivation layer above electrodes was conducted using focussed ion beam (FIB) milling. FIB milling uses a beam of ions, typically from a liquid metal ion source such as gallium (Ga), to physically etch materials as ions strike the surface. The main advantage of using a FIB is that precise etching can be achieved at the single-die level without a mask, as is required for reactive ion etching (RIE) [74].

A Tescan Lyra3 GM combined FIB-scanning electron microscope (SEM) tool was used to perform FIB milling. A Bruker Quantax energy dispersive X-ray (EDX) spectroscope was used to identify the elements present on the microchip surface from the X-rays produced upon atomic interaction with the electron beam. EDX allows in-situ determination of when the layers of passivation have been removed. EDX required a $10\,kV$ beam voltage, whereas SEM imaging was conducted at $2\,kV$ to avoid charging effects, which were further reduced by using carbon tape to ground the chip. FIB milling was carried out with a $10\,nA$ or $40\,nA$, $30\,keV$ beam. The electron beam was run concurrently with FIB milling to neutralise charge and increase FIB accuracy [75].

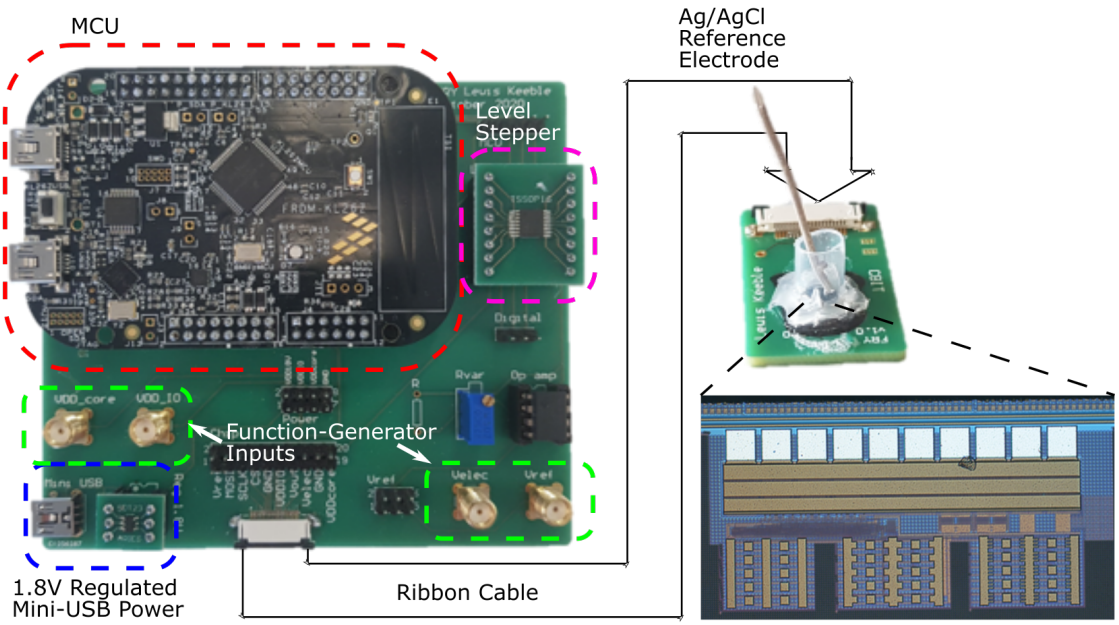


Figure 4.29: An annotated image of the motherboard and cartridge set-up used for testing FRY. A microphotograph of the fabricated microchip is provided in the bottom-right.

Test Platform

The microchip was glued to a printed circuit board (PCB) cartridge[3], using Ag epoxy (Epotek) to ensure good thermal and electrical connection to the ground plane underneath. A $1.5\,mL$ Eppendorf tube was cut and glued on top of the chip to provide encapsulation for test electrolytes. The smaller PCB cartridge connects to a motherboard via a ribbon cable. The board contains a FRDM-KL26Z microcontroller (MCU) to control the input to and output from the microchip. The MCU provides a $1.5\,MHz$ clock and accesses the serial peripheral interface (SPI) at $10\,MHz$. A regulated $1.8\,V$ mini-USB connection provides power to the chip's core.

Characterisation and Testing

Characterisation of the ISFETs was conducted using a Keithley 4200A-SCS Parameter Analyser. A current of $10\,\mu A$ was applied at the drain, with the voltage measured. The reference voltage was varied whilst measuring the change in output voltage. Buffer solutions and $Ag/AgCl$ REs were produced using the same methods as in section 4.4.2. The fluorescence microscopy set-up to test the DEP trapping system is also the same as in section 4.4.2. In some experiments, an indium tin oxide (ITO)-coated microscope slide is used to provide the electric field. Where an ITO slide was used, the electrodes were connected to ground and an Agilent 33522A function generator applied a DC voltage of up to $10\,V$ to the ITO slide via a

[3]All PCB design was conducted by Dr. Nicolas Moser

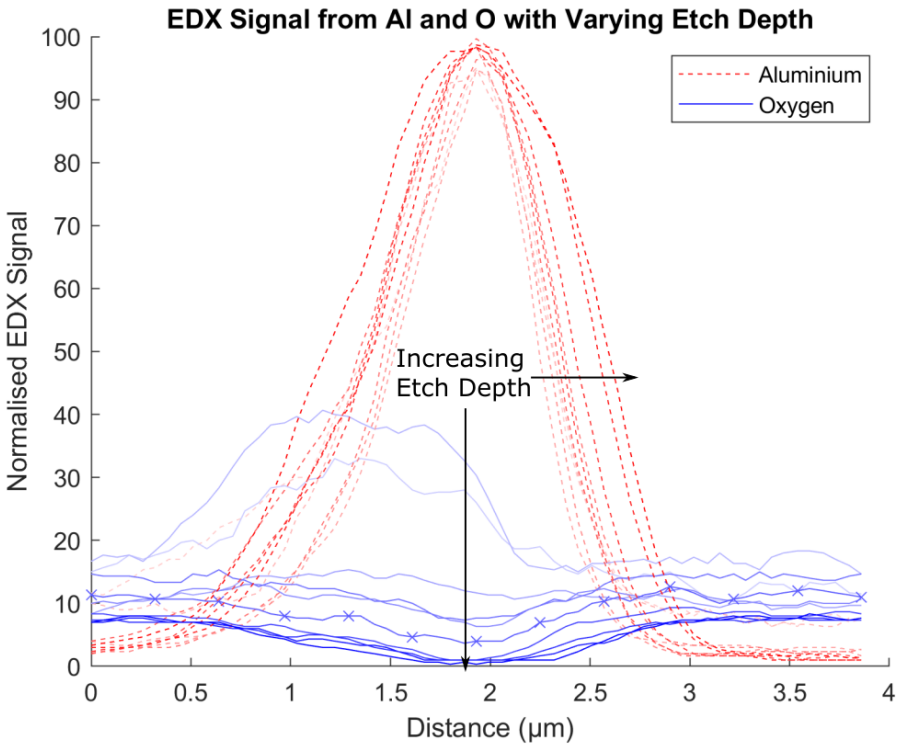


Figure 4.30: EDX signal intensity for (**red**) Al and (**blue**) O with increasing FIB milling depth. The lines get darker for increasing etch depth. The line marked with crosses denotes the etch depth chosen for electrodes that have a thin SiO_2 layer still covering them, which is $1\,\mu m$.

Ag epoxy-adhered wire. $40\,pM$, $45\,kbp$ λ-DNA dyed with YOYO-1 was used as a test subject for trapping.

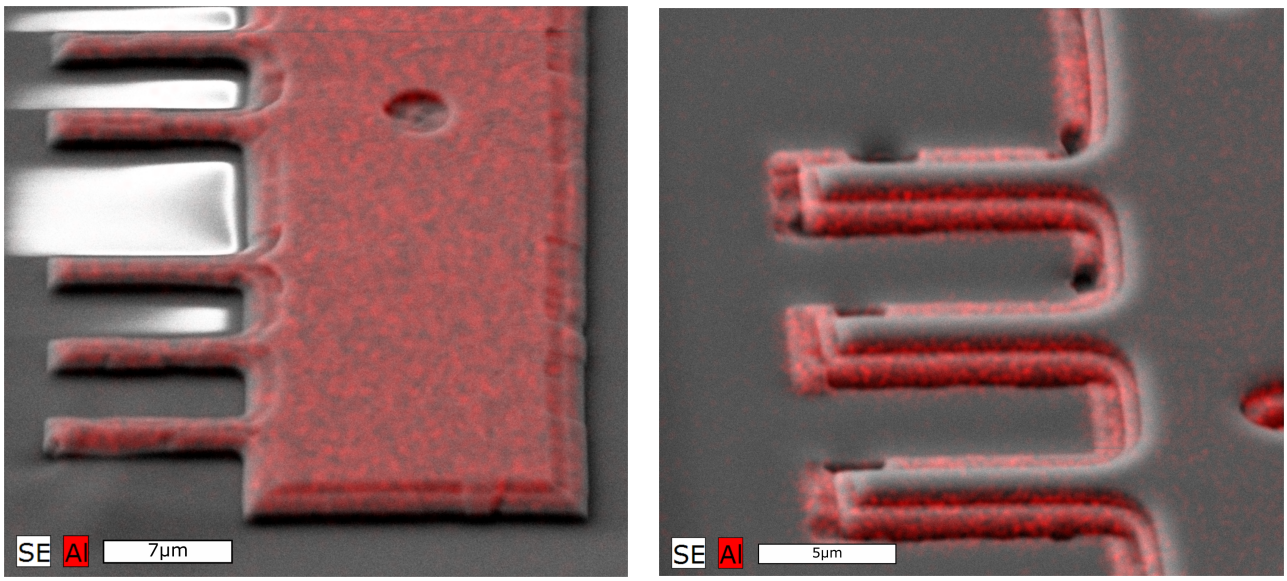
4.5.3 Results

Passivation Removal by Focussed Ion Beam Milling

The passivation was initially removed in increments and analysed using EDX, to determine the optimum etching depth. It was found that the edges of the electrodes were exposed first when using the $40\,nA$ beam current, compared to the $10\,nA$ current that more uniformly etched the passivation. Since electric field intensity maxima occur at electrode edges, the inner regions of the electrode remaining covered by passivation is beneficial as it reduces electrode spoiling, and thus $40\,nA$ is chosen as the beam current.

ISFET Characterisation

To characterise ISFET performance, firstly, the gate voltage supplied by the $Ag/AgCl$ reference electrode was swept from 0-6 V and the source voltage measured. As can be seen in Figure



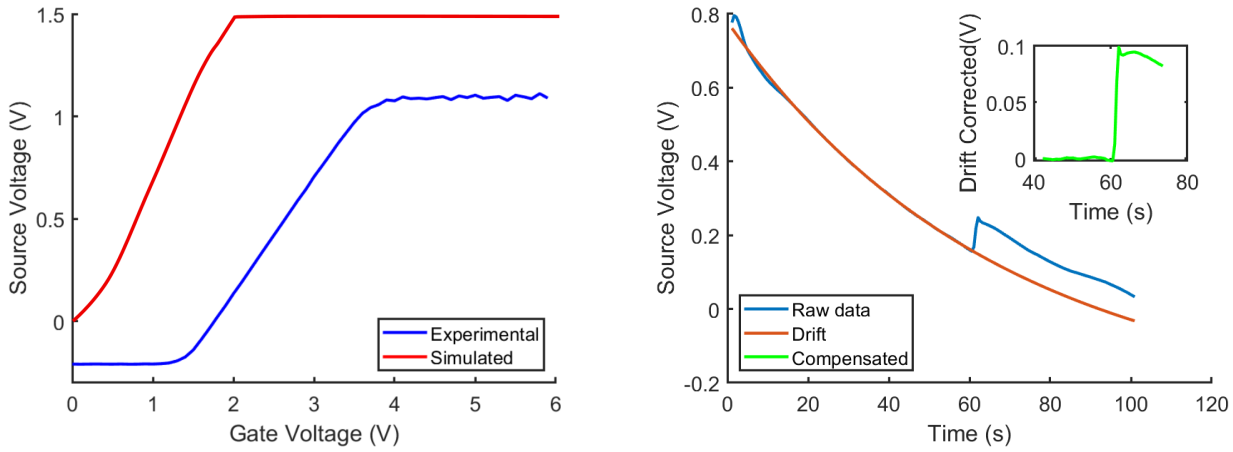
(a) 10nA (b) 40nA

Figure 4.31: Scanning electron microscope images with EDX analysis overlaid, showing the exposure of *Al* top metal with FIB etching currents of (**a**) $10\,nA$ to $3\,\mu m$ depth and (**b**) $40\,nA$ to $1.5\,\mu m$ depth.

4.32a, the linear region occurs between gate voltages of 1-4 V, which is roughly $1\,V$ wider and higher than was predicted by simulations. The temporal output, contained in Figure 4.32b, demonstrates the large drift that was encountered with all chips. The characteristic drift time, τ in equation 2.11, as fitted to experimental data was estimated as $66.9\,s$, which is two orders of magnitude smaller than the drift observed in Malpartida Cardenas *et al.* 2019 [76]. Such a high drift rate makes the chip unusable for detection of pH changes from DNA amplification reactions, as the ISFETs will drift out of range before the LAMP reaction has occurred. A $10\,\mu L$ drop of $1\,M$ HCl was added to the pH 8.1 solution at $60\,s$ to cause a step-change in pH of 7.4 down to 0.7. Using HCl at the same molarity as the KCl in the initial buffer ensures no variation of the reference potential. A change in source voltage of $99\,mV$ was observed, after the drift was subtracted from the output. This equates to a sensitivity of $13.4\,mV/pH$, which is significantly lower than the $22\,mV/pH$ predicted by the simulations. It is possible that capacitive attenuation is greater than expected for this microchip or that the large pH change or drift has moved the ISFET out of its linear range.

DNA Trapping

No DNA trapping was observed when applying voltages solely to the top-metal electrodes, both with electrodes exposed and with a thin layer of passivation remaining. When connecting all electrodes to ground and applying $10\,V$ across the test solution using the ITO-coated slide, it is possible that DEP trapping of DNA was observed. The fluorescence microscopy image



(a) (b)

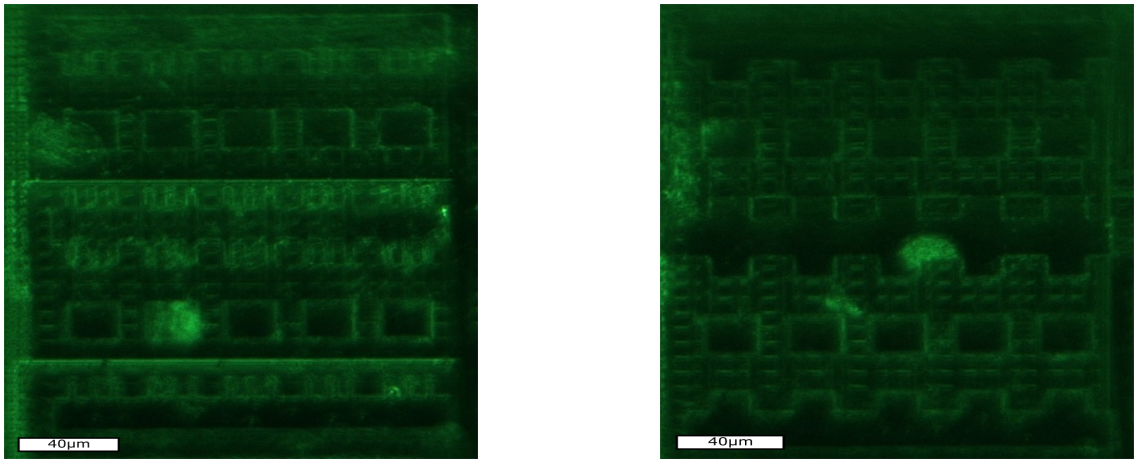
Figure 4.32: Characterisation of a FRY microchip. (**a**) shows a graph of source voltage against gate voltage, with a pH 7 buffer. (**b**) shows a graph of source voltage against time, exhibiting sensor drift that was fitted (**red**). The inset shows the drift corrected signal (**green**), with a pH change from 8.1 to 0.75.

shown in Figure 4.33a shows a high intensity at the tips of exposed thin-castellated electrodes. Comparison can be made to the unexposed, wide-castellated electrodes on the same chip in Figure 4.33b, where there are lower fluorescence intensities. Further repeats of testing, including controls, would be necessary to verify these observations. However, as shown in Figure 4.34, the electrodes dissolved as the electric field was applied, making repeated testing difficult.

4.5.4 Discussion

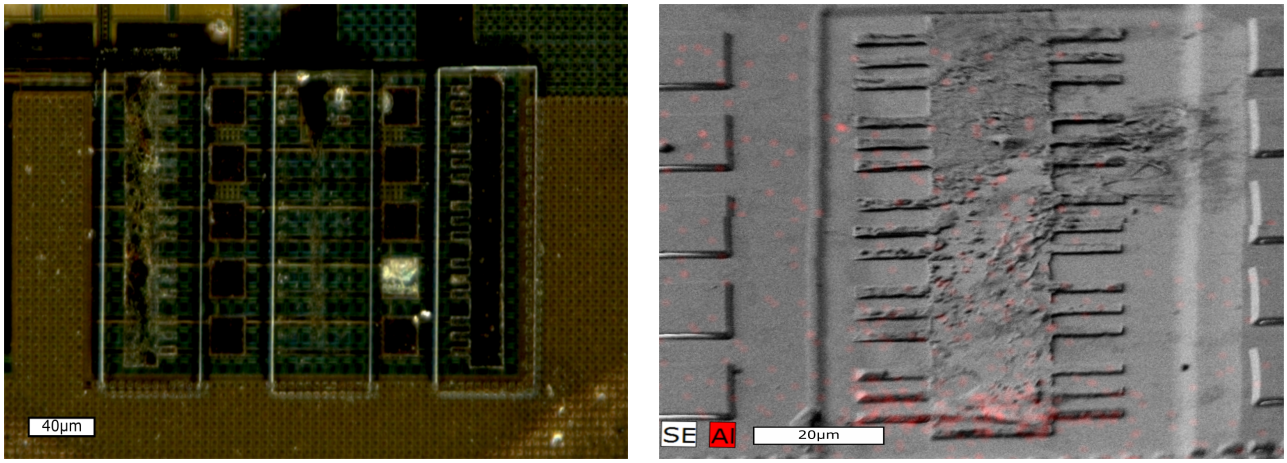
The evidence is insufficient to conclude that DNA trapping was observed with the $10\,V$ voltage applied to the ITO slide. If it could be confirmed, this would be the first demonstration of DEP trapping of DNA using CMOS top-metal electrodes. However, this point is largely moot, due to the failure of the system to trap DNA solely with voltages applied to the top-metal electrodes. It is clear that a different approach is required.

Firstly, using FIB milling to expose the electrodes from underneath the passivation layer is a fraught process. RIE could be used with either a photopattern protecting the ISFET extended gates or with the DEP electrodes placed in a metal layer above them. However, it would be significantly more straightforward to use pad-openings, which are regions of the chip where passivation is removed as part of the native CMOS process, to have top-metal exposed to the electrolyte without any additional post-processing. The shape and size of the electrodes that can be created is then limited to what conforms to the chip manufacturer's design rules or can be agreed with them as an exception. That notwithstanding, it is likely that a DEP trapping system could be designed out of standard bond-pads that use passivation openings



(a) Exposed (b) Unexposed

Figure 4.33: Florescence microscopy of $40\,pM$, $45\,kbp$ λ-DNA with (**a**) exposed and (**b**) unexposed sets of electrodes on FRY. A $10\,V$ DC voltage was applied to an ITO-coated slide held just above the chip surface and the electrodes were held at ground.



(a) Microscope (b) SEM

Figure 4.34: Images of a FRY microchip with exposed top-metal, after a DEP trapping voltage has been applied and significant dissolution of the metal has occurred. (**a**) shows a microscope image of the electrodes and (**b**) a SEM image with EDX analysis overlaid, showing a lack of aluminium signal.

with dimensions in the order of $10\,\mu m$.

Next, the limitations on the voltage applied to the electrodes, between 0-1.8 V, must be overcome. Whilst a $900\,mV_{pp}$ voltage with $900\,mV$ offset was shown to be capable of trapping DNA in section 4.4.3, practical application of CMOS-based DEP requires larger voltages. CMOS microchip voltage limits are typically related to transistor tolerances and not to the breakdown of the substrate itself. Therefore, an electrode system that does not include transistors will be able to sustain higher voltages. Such a system will need to have 'hard-wired' connections to input pads.

Finally, the *Al* used for metallisation in the TSMC $0.18\,\mu m$ process is inadequate for conducting DEP when in contact with the electrolyte. The top-metal surface must be post-processed to ensure electrochemical stability during DEP trapping. Metal deposition through photolithography is viable, yet having made a photopattern on the substrate, then electrodes could be fabricated as in section 4.4 without involving CMOS top-metal. Alternatively, electroplating could offer an avenue for selective metal deposition on exposed top-metal with minimal post-processing and high scalability.

Such an approach would be similar to that used in Bonanno *et al.* 2016, where electroless nickel, immersion gold (ENIG) plating was conducted on CMOS top-metal exposed through RIE of the passivation. Interestingly, the use of pad openings was rejected on the basis that passivation would remain between the top-metal electrodes, impeding DEP, despite the fact that the ENIG process can be used to plate metal above the level of the passivation. Thus, the use of CMOS top-metal combined with standard manufacturer pad openings is yet to be leveraged to create a DEP manipulation system and is a promising avenue for research.

4.6 Future Vision: An Electrokinetic System Utilising Bond-pads Towards a Lab-on-CMOS Diagnostic Device

The use of DEP trapping to enhance ISFET-based detection of DNA is yet to be achieved and progress in this area must overcome significant obstacles. The practical difficulties involved in DEP of DNA is reflected in the steady decline of the field since its peak in 2007, in terms of papers published per year[4]. In comparison, DEP of cells appears to only just be reaching its peak. This is not to say that the technique of electrokinetic DNA trapping will become defunct, but instead its abilities in sample preparation will come to the foreground for diagnostic applications. Electrokinetic manipulation of DNA has proved capable of a plethora of

[4]Data obtained from SCOPUS document searches.

sample preparation applications, such as: cellular lysis [77], sample concentration [5], sample purification [62], sample mixing [78], and sample transport [79]. All of these functions can be conducted by a CMOS-based microelectrode system within a small area on-chip to create a truly sample-to-result diagnostic device.

Sample-to-result LoC diagnostic devices typically exist as a microfluidic chip that may include CMOS microchips for sensing, sample manipulation, or added functionality [80]. But when the full process, from sample preparation to target detection, is conducted entirely within the confines of a CMOS microchip, the device can be described as a Lab-on-CMOS [81]. As devices continue to scale down in size, lab-on-CMOS appears to be the natural direction of the field.

Whereas most electrokinetic LoC systems have multiple, separate electrode systems, each specialised for one stage of sample preparation, the spatial limitations for a lab-on-CMOS necessitate an all-in-one electrode system able to conduct each stage of sample preparation. An array of ENIG-plated bond-pads interspersed amongst an ISFET sensing array could be the ideal platform on which to create an electrokinetic lab-on-CMOS sample-to-result diagnostic device.

This concept will be expanded on in Chapter 6, but first, surface treatment of the Al bond-pads to produce a more electrochemically stable, Au electrode must be conducted. This process opens up further opportunities for on-chip functionality, by producing an electroplated $Ag/AgCl$ reference electrode on a bond-pad. The fabrication of such a reference electrode will be covered in the next chapter whilst also developing the process for ENIG-plating bond-pads for electrokinetic applications.

4.7 Summary

This chapter has attempted to implement an on-chip electrokinetic trapping system to enhance ISFET-based DNA detection by positioning DNA at the sensing surface prior to amplification. The literature was surveyed to determine the optimum system design. Photolithographic electrodes were then produced on-chip that demonstrated successful pDEP and ACEO trapping of DNA at low voltages in low conductivity solutions. When moving to high conductivity LAMP reaction solutions, the electrode system proved unable to trap DNA. To fully integrate an electrokinetic electrode system as part of the CMOS IC design, the FRY microchip attempted to use CMOS top-metal as an electrode. Whilst this approach was not immediately successful, it provided inspiration for how top-metal integration could be achieved with electroplated bond-pads.

Bibliography

[1] Y. Jiang et al. "Stretching DNA to twice the normal length with single-molecule hydrodynamic trapping". In: *Lab on a Chip* 20 (10 2020), pp. 1780–1791.

[2] M. Soltani et al. "Nanophotonic trapping for precise manipulation of biomolecular arrays". In: *Nature Nanotechnology* 9 (6 2014), pp. 448–452. ISSN: 17483395.

[3] J. Yan, D. Skoko, and J. F. Marko. "Near-field-magnetic-tweezer manipulation of single DNA molecules". In: *Physical Review E - Statistical Physics, Plasmas, Fluids, and Related Interdisciplinary Topics* 70 (1 July 2004), p. 5. ISSN: 1063651X.

[4] S. Huang et al. "An electrochemical biosensor based on single-stranded DNA modified gold electrode for acrylamide determination". In: *Sensors and Actuators, B: Chemical* 224 (Mar. 2016), pp. 22–30. ISSN: 09254005.

[5] C. L. Asbury, A. H. Diercks, and G. van den Engh. "Trapping of DNA by dielectrophoresis". In: *Electrophoresis* 23.16 (2002), pp. 2658–2666.

[6] R. Yokokawa et al. "Individual evaluation of DEP, EP and AC-EOF effects on lambda-DNA molecules in a DNA concentrator". In: *Sensors and Actuators B: Chemical* 143.2 (2010), pp. 769–775. ISSN: 0925-4005.

[7] E. Stellwagen and N. C. Stellwagen. "Probing the Electrostatic Shielding of DNA with Capillary Electrophoresis". In: *Biophysical Journal* 84.3 (2003), pp. 1855–1866. ISSN: 0006-3495.

[8] A. D. Rosenthal and J. Voldman. "Dielectrophoretic traps for single-particle patterning." In: *Biophysical Journal* 88 3 (2005), pp. 2193–205.

[9] H. A. Pohl. *Dielectrophoresis : the behavior of neutral matter in nonuniform electric fields*. eng. Cambridge monographs on physics. Cambridge: Cambridge University Press, 1978. ISBN: 0521216575.

[10] R. Pethig. "Limitations of the Clausius-Mossotti function used in dielectrophoresis and electrical impedance studies of biomacromolecules". In: *Electrophoresis* 40.18-19 (2019), pp. 2575–2583. ISSN: 0173-0835.

[11] T. B. Jones. *Electromechanics of particles*. eng. Cambridge: Cambridge University Press, 1995. ISBN: 0521431964.

[12] S. Tomi ć et al. “Dielectric relaxation of DNA aqueous solutions”. In: *Physical Review. E, Statistical, Nonlinear, and Soft Matter Physics* 75 (2 2007), p. 021905.

[13] Y. Tao and H. Kumar Wickramasinghe. “Coaxial atomic force microscope probes for dielectrophoresis of DNA under different buffer conditions”. In: *Applied Physics Letters* 110.7 (2017), p. 073701.

[14] N. Green et al. “Fluid flow induced by non-uniform AC electric fields in electrolytes on microelectrodes III: Observation of streamlines and numerical simulation”. In: *Physical Review. E, Statistical, Nonlinear, and Soft Matter Physics* 66 (2002), p. 026305.

[15] A. Ramos et al. “AC Electric-Field-Induced Fluid Flow in Microelectrodes”. In: *Journal of Colloid and Interface Science* 217.2 (1999), pp. 420–422. ISSN: 0021-9797.

[16] V. Studer et al. “An integrated AC electrokinetic pump in a microfluidic loop for fast and tunable flow control”. In: *Analyst* 129 (10 2004), pp. 944–949.

[17] J. Wu, M. Lian, and K. Yang. “Micropumping of biofluids by alternating current electrothermal effects”. In: *Applied Physics Letters* 90.23 (2007), p. 234103.

[18] Y. Lu et al. “Long-range electrothermal fluid motion in microfluidic systems”. In: *International Journal of Heat and Mass Transfer* 98 (2016), pp. 341–349.

[19] A. Ramos et al. “Ac electrokinetics: a review of forces in microelectrode structures”. In: *Journal of Physics D: Applied Physics* 31.18 (1998), pp. 2338–2353.

[20] M. Castellarnau et al. “Integrated microanalytical system based on electrochemical detection and cell positioning”. In: *Materials Science and Engineering: C* 26.2 (2006), pp. 405–410. ISSN: 0928-4931.

[21] M. Castellarnau et al. “Integrated cell positioning and cell-based ISFET biosensors”. In: *Sensors and Actuators B: Chemical* 120.2 (2007), pp. 615–620. ISSN: 0925-4005.

[22] H. A. Pohl. “The Motion and Precipitation of Suspensoids in Divergent Electric Fields”. In: *Journal of Applied Physics* 22.7 (1951), pp. 869–871.

[23] H. A. Pohl and C. E. Plymale. “Continuous Separations of Suspensions by Nonuniform Electric Fields in Liquid Dielectrics”. In: *Journal of The Electrochemical Society* 107.5 (1960), pp. 390–396.

[24] H. A. Pohl and I. Hawk. “Separation of Living and Dead Cells by Dielectrophoresis”. In: *Science* 152.3722 (1966), pp. 647–649. ISSN: 0036-8075.

[25] M. Washizu and O. Kurosawa. “Electrostatic manipulation of DNA in microfabricated structures”. In: *IEEE Transactions on Industry Applications* 26.6 (1990), pp. 1165–1172. ISSN: 0093-9994.

[26] C.-F. Chou et al. “Electrodeless Dielectrophoresis of Single- and Double-Stranded DNA”. In: *Biophysical Journal* 83.4 (2002), pp. 2170–2179. ISSN: 0006-3495.

[27] C. L. Asbury and G. van den Engh. "Trapping of DNA in Nonuniform Oscillating Electric Fields". In: *Biophysical Journal* 74.2 (1998), pp. 1024–1030. ISSN: 0006-3495.

[28] F. Dewarrat, M. Calame, and C. Schönenberger. "Orientation and Positioning of DNA Molecules with an Electric Field Technique". In: *Single Molecules* 3.4 (2002), pp. 189–193.

[29] H. Zhao. "Role of hydrodynamic behavior of DNA molecules in dielectrophoretic polarization under the action of an electric field". In: *Physical Review. E, Statistical, Nonlinear, and Soft Matter Physics* 84 (2 2011), p. 021910.

[30] C. Zhou and R. Riehn. "Collapse of DNA under Alternating Electric Fields". In: *Physical Review. E, Statistical, Nonlinear, and Soft Matter Physics* 92 (2015), p. 012714.

[31] L. Velmanickam et al. "iLluminate-miRNA: Paradigm for high-throughput, low-cost, and sensitive miRNA detection in serum samples at point-of-care". In: *Journal of Physics D: Applied Physics* 52.5 (Nov. 2018), p. 055401.

[32] T. Kawabata and M. Washizu. "Dielectrophoretic detection of molecular bindings". In: *IEEE Transactions on Industry Applications* 37.6 (2001), pp. 1625–1633. ISSN: 0093-9994.

[33] R. Pethig et al. "Positive and negative dielectrophoretic collection of colloidal particles using interdigitated castellated microelectrodes". In: *Journal of Physics D: Applied Physics* 25.5 (1992), p. 881.

[34] D. J. G. Bakewell et al. "Dielectrophoretic manipulation of avidin and DNA". In: *Proceedings of the 20th Annual International Conference of the IEEE Engineering in Medicine and Biology Society. Vol.20 Biomedical Engineering Towards the Year 2000 and Beyond (Cat. No.98CH36286)*. Vol. 2. 1998, 1079–1082 vol.2.

[35] R. Krishnan et al. "Alternating current electrokinetic separation and detection of DNA nanoparticles in high-conductance solutions". In: *Electrophoresis* 29.9 (2008), pp. 1765–1774.

[36] L. Zheng, J. P. Brody, and P. J. Burke. "Electronic manipulation of DNA, proteins, and nanoparticles for potential circuit assembly". In: *Biosensors and Bioelectronics* 20.3 (2004), pp. 606–619. ISSN: 0956-5663.

[37] R. Martinez-Duarte et al. "Dielectrophoresis of lambda-DNA using 3D carbon electrodes". In: *Electrophoresis* 34.7 (2013), pp. 1113–1122.

[38] S. Tuukkanen et al. "Carbon Nanotubes as Electrodes for Dielectrophoresis of DNA". In: *Nano Letters* 6 (Aug. 2006), pp. 1339–43.

[39] A. Barik et al. "Graphene-edge dielectrophoretic tweezers for trapping of biomolecules". In: *Nature Communications* 8.1 (2017).

[40] S. Tsukahara, K. Yamanaka, and H. Watarai. "Dielectrophoretic Behavior of Single DNA in Planar and Capillary Quadrupole Microelectrodes". In: *Chemistry Letters* 30.3 (2001), pp. 250–251.

[41] R. Holzel. "Single particle characterization and manipulation by opposite field dielectrophoresis". In: *Journal of Electrostatics* 56.4 (2002), pp. 435–447. ISSN: 0304-3886.

[42] V. Namasivayam et al. "Electrostretching DNA Molecules Using Polymer- Enhanced Media within Microfabricated Devices". In: *Analytical Chemistry* 74.14 (2002), pp. 3378–3385.

[43] A. Ieng Kin Lao and I.-M. Hsing. "Flow-based and sieving matrix-free DNA differentiation by a miniaturized field flow fractionation device". In: *Lab Chip* 5 (6 2005), pp. 687–690.

[44] S. Tuukkanen et al. "Dielectrophoresis as a tool for nanoscale DNA manipulation". In: *International Journal of Nanotechnology* 2 (2005), p. 280.

[45] D. J. Bakewell and H. Morgan. "Dielectrophoresis of DNA: time- and frequency-dependent collections on microelectrodes". In: *IEEE Transactions on NanoBioscience* 5.1 (2006), pp. 1–8. ISSN: 1536-1241.

[46] M. R. Bown and C. D. Meinhart. "AC electroosmotic flow in a DNA concentrator". In: *Microfluidics and Nanofluidics* 2.6 (2006), pp. 513–523. ISSN: 1613-4990.

[47] K. E. Sung and M. A. Burns. "Optimization of Dielectrophoretic DNA Stretching in Microfabricated Devices". In: *Analytical Chemistry* 78.9 (2006), pp. 2939–2947.

[48] M. Kumemura et al. "Single DNA Molecule Isolation and Trapping in a Microfluidic Device". In: *ChemPhysChem* 8.12 (2007), pp. 1875–1880.

[49] P. Pham et al. "Numerical design of a 3-D microsystem for bioparticle dielectrophoresis: The Pyramidal Microdevice". In: *Journal of Electrostatics* 65.8 (2007), pp. 511–520. ISSN: 0304-3886.

[50] C. Walti et al. "AC electrokinetic manipulation of DNA". In: *Journal of Physics D: Applied Physics* 40.1 (2007), p. 114.

[51] J.-R. Du et al. "Long-range and superfast trapping of DNA molecules in an ac electrokinetic funnel". In: *Biomicrofluidics* 2.4 (2008), p. 044103.

[52] C. Yamahata et al. "Silicon Nanotweezers With Subnanometer Resolution for the Micromanipulation of Biomolecules". In: *Journal of Microelectromechanical Systems* 17.3 (June 2008), pp. 623–631. ISSN: 1057-7157.

[53] H. Vedala et al. "The effect of environmental factors on the electrical conductivity of a single oligo-DNA molecule measured using single-walled carbon nanotube nanoelectrodes". In: *Nanotechnology* 19.26 (2008), p. 265704.

[54] S. Agastin, M. R. King, and T. B. Jones. "Rapid enrichment of biomolecules using simultaneous liquid and particulate dielectrophoresis". In: *Lab Chip* 9 (16 2009), pp. 2319–2325.

[55] H. Dalir, Y. Yanagida, and T. Hatsuzawa. "Probing DNA mechanical characteristics by dielectrophoresis". In: *Sensors and Actuators B: Chemical* 136.2 (2009), pp. 472–478. ISSN: 0925-4005.

[56] C. Leiterer et al. "Integration of DNA molecules in microelectronic environment using dielectrophoresis". In: vol. 7397. Proceedings SPIE Nanoscience and Engineering, 2009, pp. 7397 - 7397 –7.

[57] W.-H. Yeo et al. "Size-Specific Concentration of DNA to a Nanostructured Tip Using Dielectrophoresis and Capillary Action". In: *The Journal of Physical Chemistry B* 113.31 (2009), pp. 10849–10858.

[58] I.-F. Cheng et al. "A rapid field-use assay for mismatch number and location of hybridized DNAs". In: *Lab Chip* 10 (7 2010), pp. 828–831.

[59] M. Kumemura et al. "Single-DNA-molecule trapping with silicon nanotweezers using pulsed dielectrophoresis". In: *Journal of Micromechanics and Microengineering* 21.5 (2011), p. 054020.

[60] R. Martinez-Duarte, P. Renaud, and M. J. Madou. "A novel approach to dielectrophoresis using carbon electrodes". In: *Electrophoresis* 32.17 (2011), pp. 2385–2392.

[61] D. Kalyanasundaram et al. "Electric field-induced concentration and capture of DNA onto microtips". In: *Microfluidics and Nanofluidics* 13.2 (2012), pp. 217–225. ISSN: 1613-4990.

[62] A. Sonnenberg et al. "Dielectrophoretic isolation of DNA and nanoparticles from blood". In: *Electrophoresis* 33.16 (2012), pp. 2482–2490.

[63] A. S. Mohamad, J. C. G. Jeynes, and M. P. Hughes*. "Dielectrophoretic Response of DNA Shows Different Conduction Mechanisms for Poly(dG)-Poly(dC) and Poly(dA)-Poly(dT) in Solution". In: *IEEE Transactions on NanoBioscience* 13.1 (2014), pp. 51–54. ISSN: 1536-1241.

[64] S. Li et al. "On-chip DNA preconcentration in different media conductivities by electrodeless dielectrophoresis". In: *Biomicrofluidics* 9 (5 2015).

[65] C. Cheng et al. "Capacitive DNA sensor for rapid and sensitive detection of whole genome human herpesvirus-1 dsDNA in serum". In: *Electrophoresis* 38.12 (2017), pp. 1617–1623.

[66] M. Hung and C. Chen. "Laser-induced heating for in situ DNA replication and detection in microchannels". In: *IET Nanobiotechnology* 12.6 (2018), pp. 841–845. ISSN: 1751-8741.

[67] L. Velmanickam, I. T. Lima, and D. Nawarathna. "High Throughput and Low-Cost Detection of Short Nucleic Acid Biomarkers in Serum using Dielectrophoretic Biosensor". In: *2018 IEEE Research and Applications of Photonics In Defense Conference (RAPID)*. 2018, pp. 1–3.

[68] P. Pungetmongkol and T. Yamamoto. "Single-Molecule Detection of DNA in a Nanochannel by High-Field Strength-Assisted Electrical Impedance Spectroscopy". In: *Micromachines 2019, Vol. 10, Page 189* 10 (3 Mar. 2019), p. 189. ISSN: 2072-666X.

[69] Q. Zhao et al. "Nanogap Electrode-Enabled Versatile Electrokinetic Manipulation of Nanometric Species in Fluids". In: *Biosensors* 12 (7 July 2022).

[70] S. Park, M. Koklu, and A. Beskok. "Particle Trapping in High-Conductivity Media with Electrothermally Enhanced Negative Dielectrophoresis". In: *Analytical Chemistry* 81.6 (2009), pp. 2303–2310.

[71] H.-Y. Lee and J. Voldman. "Optimizing Micromixer Design for Enhancing Dielectrophoretic Microconcentrator Performance". In: *Analytical Chemistry* 79.5 (2007), pp. 1833–1839.

[72] C. Koch and T. Rinke. *Photolithography: Basics of Microstructuring*. MicroChemicals GmbH, 2017. ISBN: 9783981878219.

[73] N. Moser, J. Rodriguez-Manzano, and P. Georgiou. "ProtonDx: Accurate, Rapid and Lab-Free Detection of SARS-CoV-2 and Other Respiratory Pathogens [Society News]". In: *IEEE Circuits and Systems Magazine* 21 (3 July 2021), pp. 84–88. ISSN: 15580830.

[74] N. Moser et al. "ISFET Arrays for Lab-on-Chip Technology: A Review". In: *2019 26th IEEE International Conference on Electronics, Circuits and Systems (ICECS)*. 2019, pp. 57–60.

[75] H. LUO et al. "Improvement of fabrication precision of focused ion beam by introducing simultaneous electron beam". In: *Progress in Natural Science: Materials International* 20 (2010), pp. 111–115. ISSN: 1002-0071.

[76] K. Malpartida-Cardenas et al. "Quantitative and rapid Plasmodium falciparum malaria diagnosis and artemisinin-resistance detection using a CMOS Lab-on-Chip platform". In: *Biosensors and Bioelectronics* 145 (2019), p. 111678. ISSN: 0956-5663.

[77] J. Cheng et al. "Preparation and hybridization analysis of DNA/RNA from E. coli on microfabricated bioelectronic chips". In: *Nature Biotechnology* 16 (1998), pp. 541–6.

[78] W. Y. Ng et al. "DC-biased AC-electroosmotic and AC-electrothermal flow mixing in microchannels". In: *Lab on a Chip* 9 (6 Mar. 2009), pp. 802–809. ISSN: 1473-0189.

[79] N. Loucaides, A. Ramos, and G. E. Georghiou. "Configurable AC electroosmotic pumping and mixing". In: *Microelectronic Engineering* 90 (Feb. 2012), pp. 47–50. ISSN: 01679317.

[80] C. Zhu, J. Maldonado, and K. Sengupta. "CMOS-Based Electrokinetic Microfluidics With Multi-Modal Cellular and Bio-Molecular Sensing for End-to-End Point-of-Care System". In: *IEEE Transactions on Biomedical Circuits and Systems* 15.6 (2021), pp. 1250–1267.

[81] Y. Huang and A. J. Mason. "Lab-on-CMOS integration of microfluidics and electrochemical sensors". In: *Lab Chip* 13 (19 2013), pp. 3929–3934.

Chapter 5

An Electroplated *Ag/AgCl* Reference Electrode based on CMOS Top-Metal

5.1 Introduction

To detect the pH-induced changes in surface charge from DNA amplification, an ISFET needs to be biased with a reference potential. A RE must be able to produce a stable reference potential for long durations, whatever environmental changes may occur, such as varying ion concentrations. Any fluctuations or drift in reference potential will obscure the signal from DNA amplification and could reduce the sensitivity of the diagnostic device.

The most popular RE, particularly in electrochemical sensing applications, is $Ag/AgCl$, due to its stability, robustness, and relatively simple and inexpensive construction. The chemical reaction that defines the behaviour of the $Ag/AgCl$ RE is,

$$AgCl(s) + e- \rightleftharpoons Ag(s) + Cl - (aq) \tag{5.1}$$

The potential of the electrode is governed by the Nernst equation,

$$E = E_0 - \frac{RT}{F} ln(a_{Cl^-}) \tag{5.2}$$

The optimisation of the ENIG process was carried out jointly with Arthur Jaccottet as part of their master's project [1]. ENIG plating was conducted at the Bionanofabrication cleanroom, Department of Bioengineering, Imperial College London under the guidance of Dr. Florent Seichepine. *Ag* plating and electrochemical characterisation was conducted at the Centre for Bio-inspired Technology cleanroom. SEM characterisation was conducted at the Hamlyn Centre, Imperial College London.

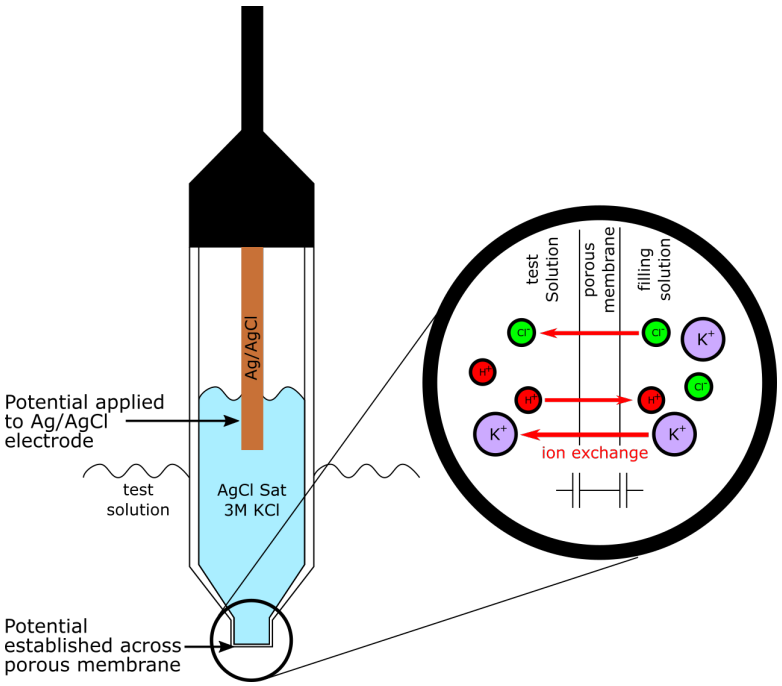


Figure 5.1: An illustration of a basic $Ag/AgCl$ glass RE, with the reference potential applied by the $Ag/AgCl$ electrode and established across the porous membrane due to ion exchange.

where E_0 is the standard potential, R is the universal gas constant, F is Faraday's constant, and a_{Cl^-} is the activity[1] of chlorine (Cl) ions [1].

In applications with large sample volumes, a glass electrode can be used, which uses a porous glass or ceramic membrane to divide the sample solution from the internal filling solution, typically $AgCl$ saturated KCl, that the $Ag/AgCl$ electrode is placed in. This ensures stability of Cl ion concentration, and thus the potential of the electrode. Ion exchange between the two solutions then establishes a potential across the membrane, as demonstrated by Figure 5.1. A simplification of the glass $Ag/AgCl$ RE is a quasi-RE (QRE), where the electrode, for example a chlorinated Ag wire, is placed directly into the test solution. A half-cell exists between electrode and sample solution, but there is no control of ion concentration and as such RE performance is less dependable[2].

As diagnostic testing is scaled down to a portable, handheld format and microfluidic approaches are applied to sample handling, ISFETs are being housed within ever smaller test volumes. This presents an obstacle to integration of conventional REs, such as glass electrodes or wires. Over the past two decades, great effort has been put into miniaturising REs to the microscale. These fall into three main categories:

- **Thin-Film:** The development of photo-patterns on a substrate combined with deposition

[1] Activity is the effective concentration of a species in a non-ideal solution.

[2] Pseudo-REs (PRE) also exist, where there is no half-cell and significant potential drift is expected, which is then calibrated for. Note that there is inconsistent use of the terms pseudo- and quasi-RE in the literature.

of metal through sputtering or evaporation. Further deposition on these metal surfaces can be achieved through electrochemical reactions in a process referred to as electroplating [2].

- **Inkjet printing:** Deposition of metallic inks, often nanoparticle suspensions, through specialised printing equipment [3, 4, 5].
- **Screen printing:** Deposition of metallic pastes that are pushed through a patterned mesh [6, 7].

Screen printing, whilst cheap and straightforward, lacks resolution in its metal deposition. Inkjet printing allows fast and scalable electrode production, yet also suffers from poor deposition resolution and requires expensive equipment and materials. Thin-film approaches to QRE fabrication offer the best resolution in metal deposition, but require more processing, expensive equipment, and a controlled environment. Furthermore, sputtering and evaporation are ill-suited to deposit thick layers of silver (Ag) in the order of microns.

The thickness of the Ag layer will determine the amount of $AgCl$ available after chlorination of the surface. This, in turn, is the limiting factor in a QRE's lifetime, as it will not be able to hold a stable potential after all $AgCl$ has dissolved. Some studies use a dissolution-limiting coating over a QRE to extend its lifetime [8, 9, 10], but this is not necessary if the $AgCl$ layer is sufficiently thick.

Electroplating is ideal for producing thick layers of metals through electrochemical reactions and requires little in the way of set-up. This is particularly the case for electroless plating, which occurs without an applied current and can be conducted at scale. However, Electroplating on its own can not produce a QRE - A metallic base is required upon which to electroplate, which is most commonly achieved via sputtering or evaporation.

Alternatively, the aluminium (Al) top-metal of commercial CMOS processes can be exposed through pad-openings in the passivation. These bond-pads can be used as a base for electroplating an on-chip $Ag/AgCl$ QRE, instead of sputtering additional layers. Electrical connections to the QRE can be buried under the CMOS passivation as part of the integrated circuitry, which makes subsequent encapsulation of the sensing system more straightforward. Furthermore, the fabrication process consists of simple steps, requires little in the way of equipment, and can be manufactured at scale. This contributes to the accessibility and commercial viability of CMOS-based electrochemical sensing devices.

In this chapter, the fabrication of the first $Ag/AgCl$ QRE that is electroplated on CMOS top-metal will be carried out and its performance characterised versus other thin-film QREs in the literature. A major component of this bond-pad QRE is an ENIG-plated layer on the Al

top-metal. Following on from Chapter 4, this layer is produced with a view to achieving DEP trapping of DNA with CMOS top-metal electrodes in Chapter 6.

5.2 Thin-film fabrication approaches for *Ag/AgCl* reference electrodes

In the overwhelming majority of cases, fabrication of thin-film $Ag/AgCl$ REs begins with the sputtering or evaporation of a base metal, as can be seen in Table 5.1. Cr or Ti are commonly used in this role due to their good adhesive properties, with Ag then be deposited on top. One drawback of sputtering and evaporation is that these techniques are not well-suited to producing thick layers of Ag in the order of μm. The thickness of the Ag layer will determine the amount of $AgCl$ available after chlorination. This, in turn, is the limiting factor in a RE's lifetime, as it will not be able to hold a stable potential after all $AgCl$ has dissolved. Electroplating, on the other hand, can readily form thick layers of Ag on a metal base.

An electroplated bond-pad RE will use Al top-metal as a base. Electroplating directly onto Al is prohibited by the native aluminium oxide (Al_2O_3) layer that displays poor adhesion with electrodeposited metal. Al oxidises so readily, that even if this oxide layer was etched away, it would reform before any subsequent plating could occur [42]. Therefore, it is common practice to immediately replace the surface Al with a metal that is more resistant to oxidation. Zincate is the most popular treatment, whereby the oxide layer is etched and surface Al atoms are immediately replaced with zinc (Zn) ions as part of the same chemical bath. Zincation is chosen for this study because the process is well-established. It is also possible to use nickel (Ni) to replace Al, but this requires non-standard plating solutions [43].

Ag is most commonly electroplated onto Ni or copper (Cu). However, in Polk *et al.* 2006 gold (Au) was used as an intermediary layer to form a barrier against the diffusion of metal oxides in to the Ag layer [2]. These metal oxides could change the potential of the RE if they migrate towards the surface. ENIG is a process used to create Au bump-pads on CMOS dies [44] and form solder pads on PCBs. The electroless Ni is an autocatalytic plating process, in which the Ni layer grows continually. The immersion process for Au is a displacement reaction through which Au atoms replace surface Ni atoms and, as such, a thin Au layer is formed with a maximum thickness in the order of $10\,nm$. ENIG is chosen as the intermediary layer before Ag plating in this study because it is an industry-standard process that has been applied to CMOS previously and can also produce a CMOS top-metal electrode capable of DEP trapping of DNA. Alternative intermediary layers include electroless Cu, which could be plated onto the Zn layer.

For Ag deposition on the immersion Au surface, there is currently no commercially available

Year	Paper	Application	Substrate	Base	Coating	Method	Drift
1986	L. Bousse et al.	-	Si	-	-	Ev	-
1998	H. Suzuki et al.[11]	-	Si-SiO_2	Au	-	S	$1\,mV/24hr$
1999	H. Suzuki et al. [12]	Glucose sensing	Glass	Pt	-	S	-
2001	H. Suzuki et al. [13]	-	Glass	Au	polyHEMA/ENT-2000	S	$8\,\mu V/hr$
	A. Hiratsuka et al. [14]	Amperometric sensing	Glass	Pt	-	S	-
2002	T. Matsumoto et al. [15]	Glucose sensing	Quartz	Ti	APTES/PFCP	S	0.034-$0.6\,mV/hr$
2003	I. Huang et al. [16]	ISFET sensing	SiO_2-Si_3N_4	Pd	Agarose/KCl	S	8.5-$27\,mV/hr$
	S. Park et al. [17]	Glucose sensing	Si-SiO_2	-	-	Ev	$13\,mV/5hr$
2004	H. Kim et al. [18]	-	Si-SiO_2	Ti/Ni-Ti	-	S	-
2006	R. Maminska et al.	-	PCB	Cu	PVC/Ionic Liquid	El	0.25-$0.45\,mV/hr$
	B. Polk et al. [2]	Microfluidics	Si	Au-Cr	-	S & El	$2\,mV/1000min$
2009	F. Almeida et al. [19]	-	-	Au-Pt	Nafion	El	$76.8\,\mu V/hr$
2010	J. Zhou et al. [20]	Disposable electrochemical systems	Glass	Pt	-	S & El	$5\,mV/8hr$
2013	J. Schnitker et al.[21]	Ionic current measurement	p-Si	Pt-Cr	-	Ev & El (Pulse)	$1.48\,mV/hr$
	A. Baraket et al. [22]	Cytokine detection	PI	Au	-	S & El (CV)	$0.6\,mV/hr$
2014	Y. Abbas et al. [23]	Chloride ion measurement	Glass	Pd	-	S	$59\,\mu M/24hr$
2015	T. Kim et al. [24]	pH measurement	Glass	-	Graphene Oxide	S	$< 2\,mV/26days$
	T. Monteiro et al. [25]	PDMS encapsulation	Glass/p-Si	Al	-	S	-
	S. Wu et al. [26]	ISFET sensing	PET	-	-	S	-
2016	E. Cordero et al. [27]	ISFET sensing	PSA	-	-	S	-
2017	N. Wang et al. [28]	Disposable electrochemical systems	Si	Au	-	S	-
	T. Rahman et al. [29]	Biosensing	Glass	Au	SAM	S	$0.2\,mV/hr$
	Q. Li et al. [9]	ISFET sensing	PEN	Au	PVB	Ev	$< 1.7\,mV/hr$
2018	L. Hoa [30]	Glutamate sensing	$SiO2$	Pt	Nafion	S & El	$0.1\,mV/hr$
	B. Bao et al. [31]	Neural prosthesis	PI	Au	-	S & El	-
2019	N. Wang et al. [32]	Disposable electrochemical systems	LCP	Au	-	S	$0.457\,mV/hr$
	T. Huynh et al. [33]	pH measurement	Si	-	-	Ev	-
	A. Rosli et al. [34]	pH measurement	Glass	ITO	-	Ev	-
	J. Yin et al. [35]	Nitrite sensing	Glass	-	-	S	-
	K. Tjon et al. [36]	Biosensing	Quartz	Au	-	S	-
	Z. Zhang et al.	Chemical oxygen demand	Glass	-	-	S	-
2020	H. Lim et al. [8]	Glucose sensing	Si	-	Nafion	Ev	$0.09\,mV/hr$
	K. Xu et al. [37]	-	PCB	-	Graphene-chitosan	S	-
2021	J. Dai *et al.* [38]	Pb(II) measurement	Glass	-	Liquid junction	S	$0.6\,mV/hr$
	L. Wang *et al.* [39]	Neural recording	Si	Au	-	S & El	-
2022	V. Torres González *et al.* [40]	Disposable electrochemical systems	Acetate	Ti	PDMS + salt	Ev	$0.02mV/70hr$
	P. Tirado *et al.* [41]	-	PI	Ti	SU-8 + KCl	Ev	-

Table 5.1: A table of thin-film $Ag/AgCl$ quasi-REs in the literature. These are papers where the fabrication of the RE is a focus of the study. S = Sputtering, Ev = Evaporation, El = Electroplating.

autocatalytic process. The remaining choices are an immersion Ag solution or a current-driven (electrolytic) approach. Since immersion finishes are inherently limited in the thicknesses they can provide, they may not deposit sufficient Ag to create a RE with a realistically usable lifetime. Most immersion Ag solutions can deposit thicknesses in the order of $100\,nm$ to Ni or Cu, rather than over $1\,\mu m$ as desired [45, 46]. Consequently, current-driven Ag plating will be conducted for this proof-of-concept to ensure a sufficiently thick Ag layer.

As opposed to having the plating current applied constantly, it is possible to get more uniform Ag coverage by pulsing the current [47]. When the current is active, Ag ions will be removed from the solution as they are deposited on the metal surface, leading to its depletion. By having periods during which the current is not applied, Ag ions are given time to diffuse from the bulk solution and evenly distribute across the metal surface. This leads to smoother plating with smaller Ag grain sizes. However, it is possible that a non-uniform, high-porosity Ag surface, may be beneficial to RE performance [48]. By having a larger surface area in contact with the electrolyte, the exchange of Cl ions can occur at a greater rate, allowing the RE to react more quickly to changes in local Cl ion concentration and thus keep a more stable potential. However, for increased reliability of Ag deposition, pulsed-current electroplating is conducted.

To complete the $Ag/AgCl$ RE, the Ag layer must be chlorinated. There are two main approaches to the chlorination of Ag: Chemical oxidation and electro-chemical anodisation. Common oxidisers used for Ag chlorination are sodium hypochlorite ($NaClO$) and iron (III) chloride ($FeCl_3$). The electrochemical approach applies a current through Ag acting as an anode in an aqueous solution of a chloride salt, such as KCl. Both methods have been found to produce equally stable REs [2]. For the purpose of wafer-level fabrication, chemical oxidation is preferential because it does not require an electrical connection.

Many studies apply a coating over the $AgCl$ layer to limit dissolution and prolong the lifetime of the electrode [8, 9, 10]. It is also possible to use this layer to control the local concentration of Cl ions by saturating it with a Cl-containing salt [16]. This can greatly reduce RE drift and transform it from a QRE to a full RE. Despite their advantages, these coatings add complexities to manufacturing and, as a result, are not considered for fabrication as part of this proof-of-concept, but are worth investigating for future iterations.

5.3 Materials and Methods

5.3.1 CMOS Test Platform

A CMOS microchip fabricated in $0.18\mu m$ TSMC was used as a test platform for the $Ag/AgCl$ bond-pad QRE fabrication process [49]. The chip contains seven Al bond-pads within the inte-

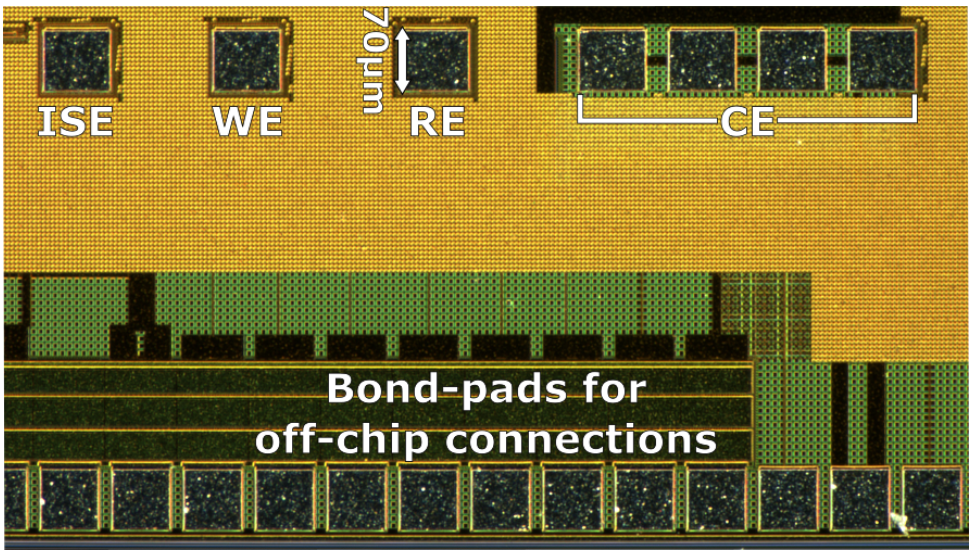


Figure 5.2: Micrograph of the $0.18\,\mu m$ TSMC microchip used as a test platform in this study. The pads for the ISE, WE, RE, and CE are highlighted.

rior of the chip as part of a four-electrode voltammetry-amperometry sensing system, consisting of: an ion-sensitive electrode (ISE), a RE, a WE, and a counter electrode (CE, four connected pads), as seen in figure 5.2. These are connected as part of the IC to bond-pads on the edge of the chip to allow external connection.

Prior to electroplating, the dies were glued to a PCB with silver epoxy (*Epotek*), wirebonded using a wedge wirebonder (*F&S 53*), and the wires covered in black epoxy (*Epotek*). The PCB was also coated in black epoxy to protect the tracks and vias from the plating baths.

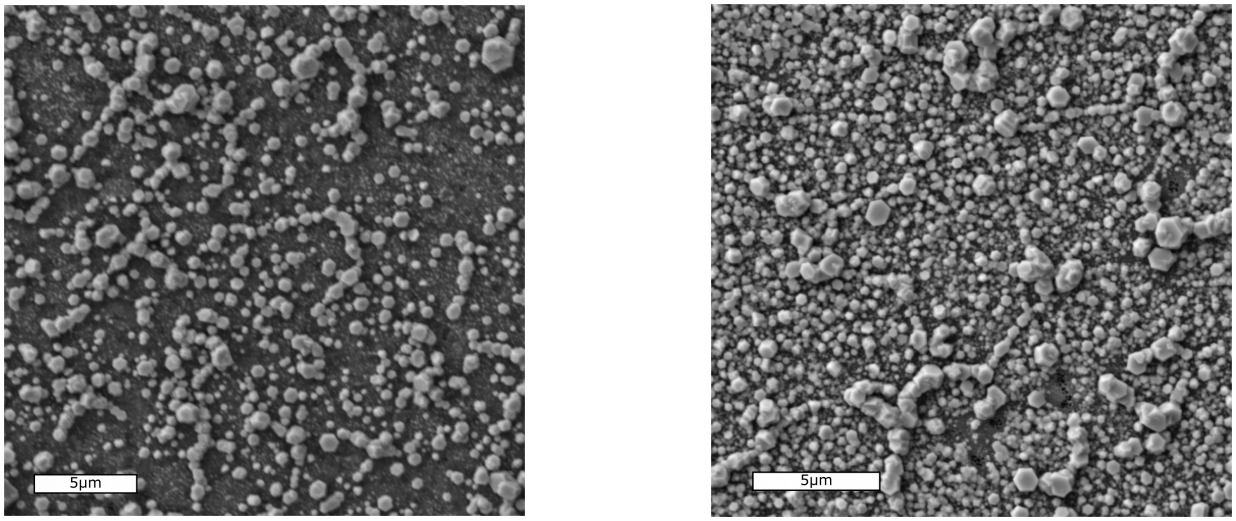
5.3.2 Fabrication Process

Zincation

The Al_2O_3 layer is etched using $NaOH$ (Sigma). The Cu within the etched Al can form precipitates which will affect the adhesion of subsequently deposited metal layers. This Cu 'smut' is removed by etching in nitric acid (HNO_3, Sigma) and the zincate solution is then applied immediately. The zincate solution that was used in this study, Techni Zincate (Technic UK), consists of zinc oxide (ZnO) dissolved in $NaOH$, to etch any reformed Al_2O_3. Trace amounts of $FeCl_3$ are added to make the Zn layer more compact and smooth [50]. The oxidation reaction that occurs is,

$$\mathrm{Al_{(s)} + 2\,H_2O \longrightarrow AlO_2^- + 4\,H^+ + 3\,e^-}$$

and the reduction reaction that occurs is,



(a) Single Zincation (b) Double Zincation

Figure 5.3: SEM images of CMOS bond-pads after (**a**) first zincation for 150 s with a 5 s etch in both $NaOH$ and NHO_3 and (**b**) second zincation for 50 s with a 5 s etch in NHO_3. SEM images were obtained with a 10 kV beam energy.

$$\mathrm{Zn(OH)_4}^{2-} + 2\,\mathrm{e}^- \longrightarrow \mathrm{Zn_{(s)}} + 4\,\mathrm{OH}^-$$

where subscript (s) represents solid species and $Zn(OH)_4^{2-}$ is produced by a reaction between ZnO and $NaOH$ [51].

A double zincation process is used, whereby the first Zn layer is stripped away with HNO_3, after which another Zn layer is applied that achieves greater coverage to the first [42] and results in greater smoothness for subsequently deposited layers. A comparison of single versus double zincation is provided in Figure 5.3, where an increase in Zn surface coverage from around 50% for single zincation to over 80% for double zincation.

Techni Zincate was used diluted 1:3 with DI water (MilliQ Ultrapure system). A 150 s first zincation time was carried out after etching in 5 % $NaOH$ and 50 % NHO_3 for 5 s each. These short etching times were used to avoid complete removal of the Al pads. The second zincation step was 50 s long after etching of the first Zn layer in 50 % NHO_3 for 3 s.

Electroless Nickel

The electroless Ni process used was Techni EN AT 5600 (Technic UK). This is a three-part, cyanide-free electroless Ni plating solution: Part A is used for Ni replenishment in-situ, part B provides the initial source of Ni and the reducing agent hypophosphite ($H_2PO_2^-$), and part C is a secondary source of $H_2PO_2^-$ and other components that is only needed for replenishment. Other stabilisers will be present in the solution to prevent the Ni spontaneously and non-selectively plating all surfaces [52].

The oxidation reactions that take place are,

$$\mathrm{Zn_{(s)}} \longrightarrow \mathrm{Zn^{2+}} + 2\,\mathrm{e^-}$$

$$\mathrm{H_2PO_2^-} + \mathrm{H_2O} \longrightarrow \mathrm{H_2PO_3^-} + 2\,\mathrm{H^+} + \mathrm{e^-}$$

and the reduction reaction taking place is,

$$\mathrm{Ni^{2+}} + 2\,\mathrm{e^-} \longrightarrow \mathrm{Ni_{(s)}}$$

with Ni replacing the Zn and then growing in thickness as the autocatalytic reaction takes place.

The plating solution is made up of 1.2 % part A, 25 % part B, and 73.8 % DI water. The plating solution is heated to 85^oC (82-87^oC limits) with mild stirring provided by a magnetic stirrer at $350\,rpm$ (CRS 22H hotplate). The plating is conducted for up to $18\,mins$, with a predicted plating rate of 10-15 $\mu m/hr$.

Immersion Gold

The immersion Au solution used in this study was the ready-to-use, cyanide-free Supermex 250 (Metalor). It contains an Au salt along with chelating agents and other stabilisers. The oxidation reaction that takes place is,

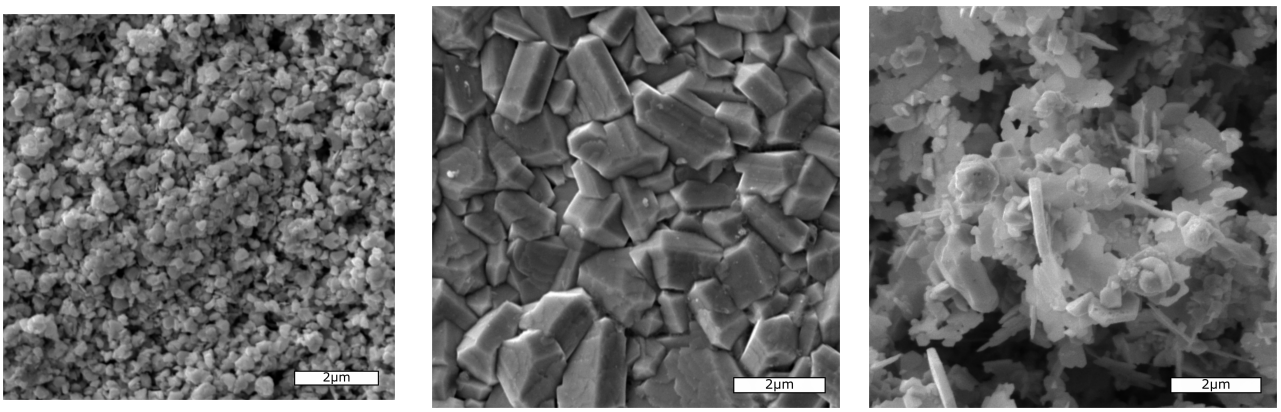
$$\mathrm{Ni_{(s)}} \longrightarrow \mathrm{Ni^{2+}} + 2\,\mathrm{e^-}$$

and the reduction reaction that takes place is,

$$\mathrm{Au^+} + \mathrm{e^-} \longrightarrow \mathrm{Au_{(s)}}$$

with the reaction terminating once all surface Ni has been replaced with Au.

The plating solution is heated to 65^oC (55-75^oC limits) with mild stirring provided by a magnetic stirrer at $200\,rpm$. Plating is conducted for up to $25\,mins$, providing a maximum thickness of 0.1 μm.



(a) Pulsed current (b) Constant current (c) Constant current: Repeat

Figure 5.4: SEM images of Au coated microscope slides electroplated with Ag in a $1\,M$ NH_3 and $0.3\,M$ $AgNO_3$ bath and a (**a**) pulsed ($2\,s$ on, $20\,s$ off) or (**b,c**) constant $13\,mAcm^{-2}$ current applied. (**b**) and (**c**) show repeats of plating with a constant current, demonstrating the lower reliability of the process. SEM images were obtained with a $10\,kV$ beam energy.

Electroplated Silver

The Ag plating solution used in this study was a mixture of $0.3\,M$ silver nitrate ($AgNO_3$, ThermoFisher) dissolved in $1\,M$ ammonium hydroxide (NH_4OH, Sigma). An Ag wire is used as a RE as it creates a half-cell with the plating bath [47]. An $Ag/AgCl$ RE would leach Cl ions into the bath and cause precipitation of $AgCl$. A platinised titanium mesh was used as a counter electrode, with the three-electrode system run using a VersaStat 3 electrochemical workstation. Prior to electroplating, the chip is cleaned with acetone (Sigma) and isopropanol (ThermoFisher) in an ultrasonic bath and the surface is activated using $1\,M$ HCl (Sigma).

A pulsed current of $13\,mA/cm^2$ ($2\,s$ on, $20\,s$ off) is used, as it provides a more reproducible, smooth electrode than a constantly applied pulse. A comparison of surface morphology between the pulsed and constant-current plating approaches is shown in Figure 5.4 for Ag plating on Au-coated slides. The pulsed current is applied for $10\,mins$ of total 'on' time, with an estimated plating rate of $0.5\,\mu m/min$ [2].

Silver Chlorination

$FeCl_3$ (Sigma) was chosen as the chemical oxidiser and an immersion time of $60\,s$ in a solution with a concentration of $50\,mM$ was used [2]. Subsequently produced Ag^+ reacts with Cl^- chloride ions to produce $AgCl$.

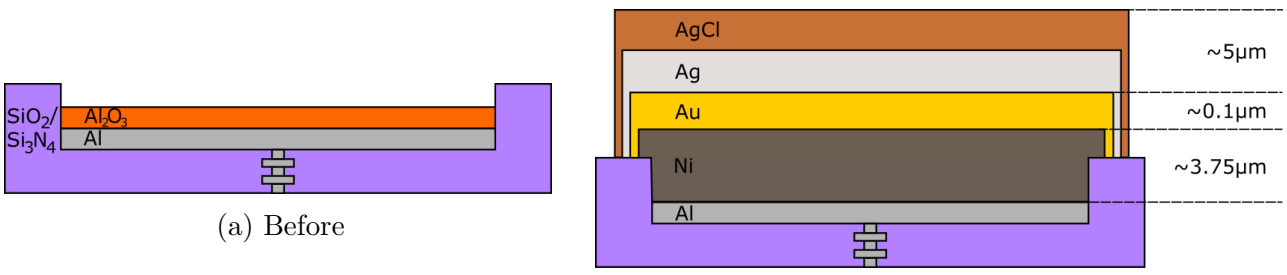
$$\mathrm{Ag} \longrightarrow \mathrm{Ag^+} + \mathrm{e^-}$$

$$\mathrm{Ag^+} + \mathrm{Cl^-} \longrightarrow \mathrm{AgCl}$$

The planned RE design, including anticipated layer thicknesses, is illustrated in Figure 5.5.

RE Fabrication Process

1. Clean the dies for 10 $mins$ in both acetone and isopropanol in an ultrasonic cleaner. All steps carried out at room temperature unless otherwise stated.
2. Etch the Al_2O_3 layer for 5 s in 5 % $NaOH$.
3. De-smut the dies with a 5 s immersion in 50 % NHO_3.
4. Apply the first Zn layer by immersing the dies for 150 s in the Zn plating solution.
5. Remove the first Zn layer with a 3 s immersion in 50 % NHO_3.
6. Apply the second Zn layer by immersing the dies for 50 s in the Zn plating solution.
7. Apply the Ni layer by immersing the dies in the Ni plating solution for 6-30 $mins$, which is heated to 85-89^oC and has magnetic stirring at 350 rpm.
8. Apply the Au layer by immersing the dies in the Au plating solution for 25 $mins$, which is heated to 60-70^oC and has magnetic stirring at 200 rpm.
9. Clean the dies for 10 $mins$ in both acetone and isopropanol in an ultrasonic cleaner and then activate the surface with a 10 min immersion in 1 M HCl.
10. Electroplate the Ag layer in a bath of 1 M NH_3 and 0.3 M $AgNO_3$ at a current of 13 $mAcm^{-2}$ for 300 cycles of 2 s on, 20 s off (10 $mins$ total on) with an Ag wire RE, Pt mesh counter electrode, and mixing from a magnetic stirrer at 350 rpm.
11. Immediately chlorinate the Ag with a 60 s immersion in 50 mM $FeCl_3$.



(a) Before

(b) After

Figure 5.5: A schematic showing the composition of the pad (**a**) before and (**b**) after post-processing, with the approximate thicknesses of the electroplated layers provided.

5.3.3 Characterisation

Microscopy

Brightfield microscopy was conducted with a Nikon Eclipse LV100 equipped with 5×, 10×, 20×, and 50× objective lenses. SEM was carried out using a Lyra Tescan G3, with concurrent EDX analysis.

Adhesion Tests

Tape tests were run on both ENIG and *Ag*-plated electrodes by applying and removing Kapton adhesive tape to the microchip surface. Microscopy was then used to determine whether delamination had occurred and which layer had failed. A second adhesion test used a F&S 53 wedge wire-bonder to attempt to make wirebonds to the ENIG-plated electrodes. Where bonds were successfully made, the wires were then pulled to cause failure and the failure mode was confirmed via microscopy. Both adhesion tests are purely qualitative and can only give an indication of layer adhesion.

Profilometry

A Dektak 6M Veeco stylus profilometer was used to provide surface profiles of bare, ENIG-plated, and *Ag*-plated bondpads. This allowed estimation of layer thicknesses.

Open Circuit Potential

The open circuit potential (OCP) of an electrochemical system is the potential when no external load is applied and no current flows. A two-electrode set-up is used, with the potential of the WE measured relative to the RE. The measured potential will be determined by the electrolytic activity at the WE, with a constant OCP indicating thermodynamic stability. OCP is a useful measure of the lifetime of a RE, as the electrode corrodes during measurement. Once all $AgCl$ has dissolved from the electrode, the OCP will display a large change. The OCP can also provide the drift rate of the electrode.

OCP was measured in $100\,mM\ KCl$ (Scientific Laboratory Systems), with the electroplated $Ag/AgCl$ pad as the working electrode and a commercial, glass RE (Sigma). Measurements were made with a VersaStat 3 potentiostat.

Cyclic Voltammetry

Cyclic voltammetry (CV) is used to characterise electron transfer processes. The technique involves applying a voltage to the cathode that increases up to a switchover voltage, V_{switch}, before then decreasing, whilst measuring the current. As the anode potential increases, oxidation events will occur and a positive current will flow, as seen in Figure 5.6[3]. This current will grow with anode potential up to a maximum, after which the rate of diffusion of the oxidised molecule from the bulk solution to the electrode surface limits the reaction and a decrease is observed.

When the direction of the voltage scan switches, a similar shape of the I-V curve is observed, but with a negative current due to reduction reactions. There is also hysteresis within the measurement because at switchover there is a higher concentration of the reduced species at the electrode surface than was present at the start of the experiment and thus it takes longer to become depleted. The peak value of current, i_p, is related to the scanning rate, v, at which the applied potential is increased or decreased, by the Randles-Cevcik equation,

$$i_p = 0.446nFAc_0\sqrt{\frac{nFvD_o}{RT}} \tag{5.3}$$

where F is the Faraday constant, n is the number of electrons involved in reduction, D_o is the diffusivity of the oxidised molecule, c_0 is the bulk analyte concentration, and T is the temperature of the system. By varying the scan rate of the CV curves and plotting peak current against the square root of scan rate, a linear relationship will indicate that the reaction is diffusion-limited and electron transfer at the electrode surface is fast, an important feature for a reliable RE. Slow electron transfer could result in electrode polarisation.

Another important feature in interpreting CV curves is the peak-to-peak separation of the anodic (i_p^a) and cathodic (i_p^c) peaks. For perfectly fast electron transfer, the peak-to-peak separation is $57\,mV$ [53]. The ratio of anodic to cathodic peak current should be 1. However, measurement of the peak ratio is complicated by the inherent hysteresis. V_{switch} influences the value of the anodic peak, and as such its raw value cannot be used. An empirical model for peak ratio,

$$R = \frac{i_p^c}{i_p^a} + 0.48\frac{i_\lambda}{i_p^a} + 0.086$$

where i_λ is the current at the switching voltage, was determined by Nicholson *et al.* [54].

CV was conducted in a solution of $0.1\,M\ KCl$, $0.1mM\ K_3FeCN_6$ (Sigma), and $1mM\ K_4FeCN_6$ (Sigma). The electrochemical reaction that occurs between the ferricyanide and ferrocyanide

[3]It is worth noting that anodic and cathodic peaks can switch positions on a CV graph depending on what convention is followed. The direction of the scan is indicated on the graph.

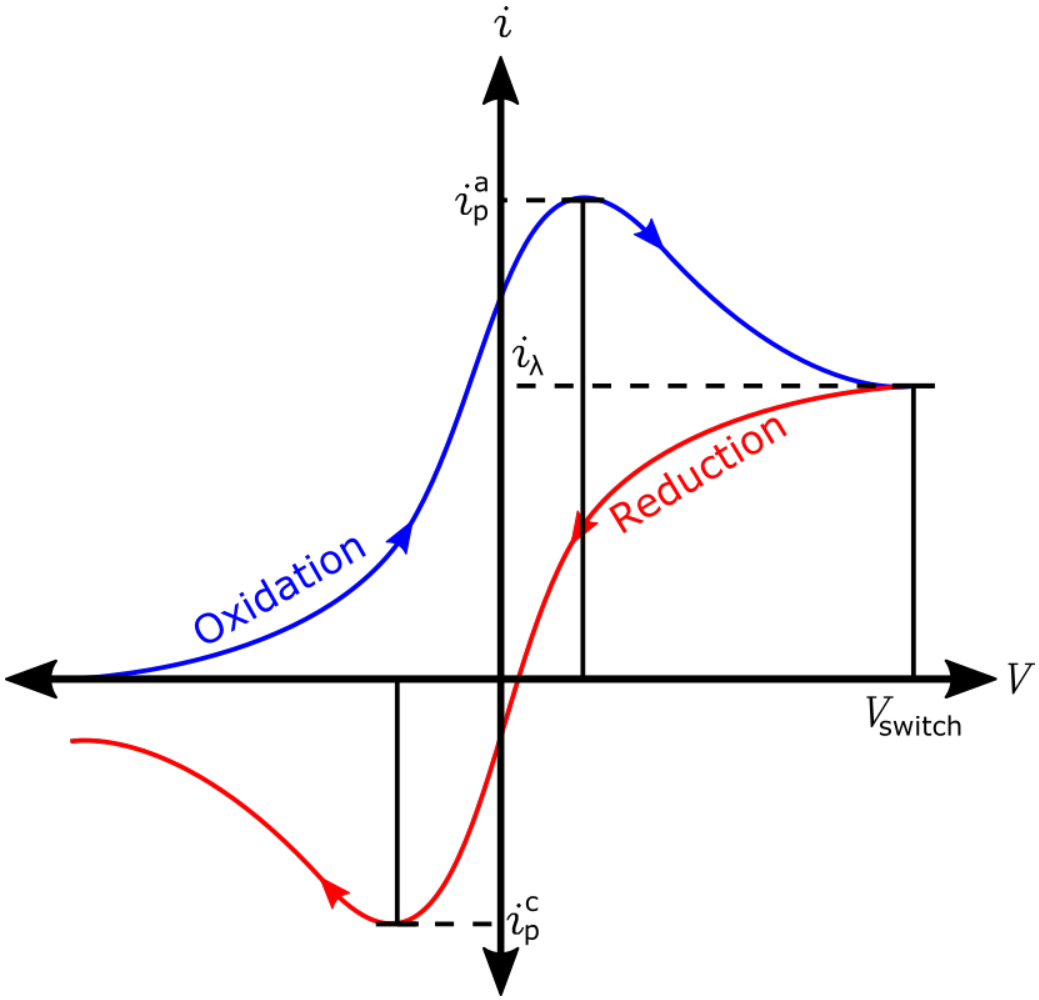


Figure 5.6: An illustrated example of a cyclic voltammetry curve, with the direction of the scan given by the arrows on the curve and the regions of (**blue**) oxidation and (**red**) reduction labelled. The peak cathodic and peak anodic currents, i_p^c and i_p^a respectively, are annotated, along with the current, i_λ, at the switching voltage, V_{switch}.

ions, $FeCN_6^{3-}$ and $FeCN_6^{4-}$ respectively, is,

$$FeCN_6^{3-} + e^- \rightleftharpoons FeCN_6^{4-} \tag{5.4}$$

A commercial, glass RE was used, along with a platinised titanium mesh CE. Either ENIG or $AgCl$-plated pads acted as the WE. An Au-coated microscope slide (Sigma) was also used as a WE as a benchmark. Measurements were made with a VersaStat 3 potentiostat.

Polarisation Curves

For reliable RE operation, the potential of the electrode must vary minimally with applied current density [1]. This can be characterised with polarisation curves of potential against current density [55], for which a flat region at low current densities is desired. Polarisation curves were obtained with the $Ag/AgCl$ pad acting as the WE, a commercial glass RE, and a $100\,mM\ KCl$ test solution. Measurements were made with a VersaStat 3 potentiostat.

5.4 Results

5.4.1 Fabricated Prototypes

ENIG

ENIG plating was successfully conducted as exemplified by Figure 5.7. The microscope image shows an Au coating on the bond-pad. The surface profile data contained in Figure 5.8 shows that the plated surface has risen above the level of the passivation, creating the expected 'bump-pad' profile, demonstrating that the autocatalytic Ni plating has progressed well. The presence of Au is also confirmed with EDX analysis of the surface.

To assess the adhesion of the underlying layers, tape tests were performed alongside wirebonding tests. In the majority of attempts, no delamination of the ENIG coating occurred. However, where delaminations did occur, analysis of the pad using SEM found that in some instances the underlying Al pad had delaminated from the array of vias connecting it to the circuitry underneath, as can be seen in Figure 5.9. This points towards issues with the processing of the Al to remove the Al_2O_3 and apply the Zn layer. It is possible that over-etching of the pad has resulted in the weakness of this layer, which must be optimised going forwards. There were also instances where the ENIG layer delaminated from the Al pad[4].

[4]Supporting figures from the adhesion tests can be found in Appendix E

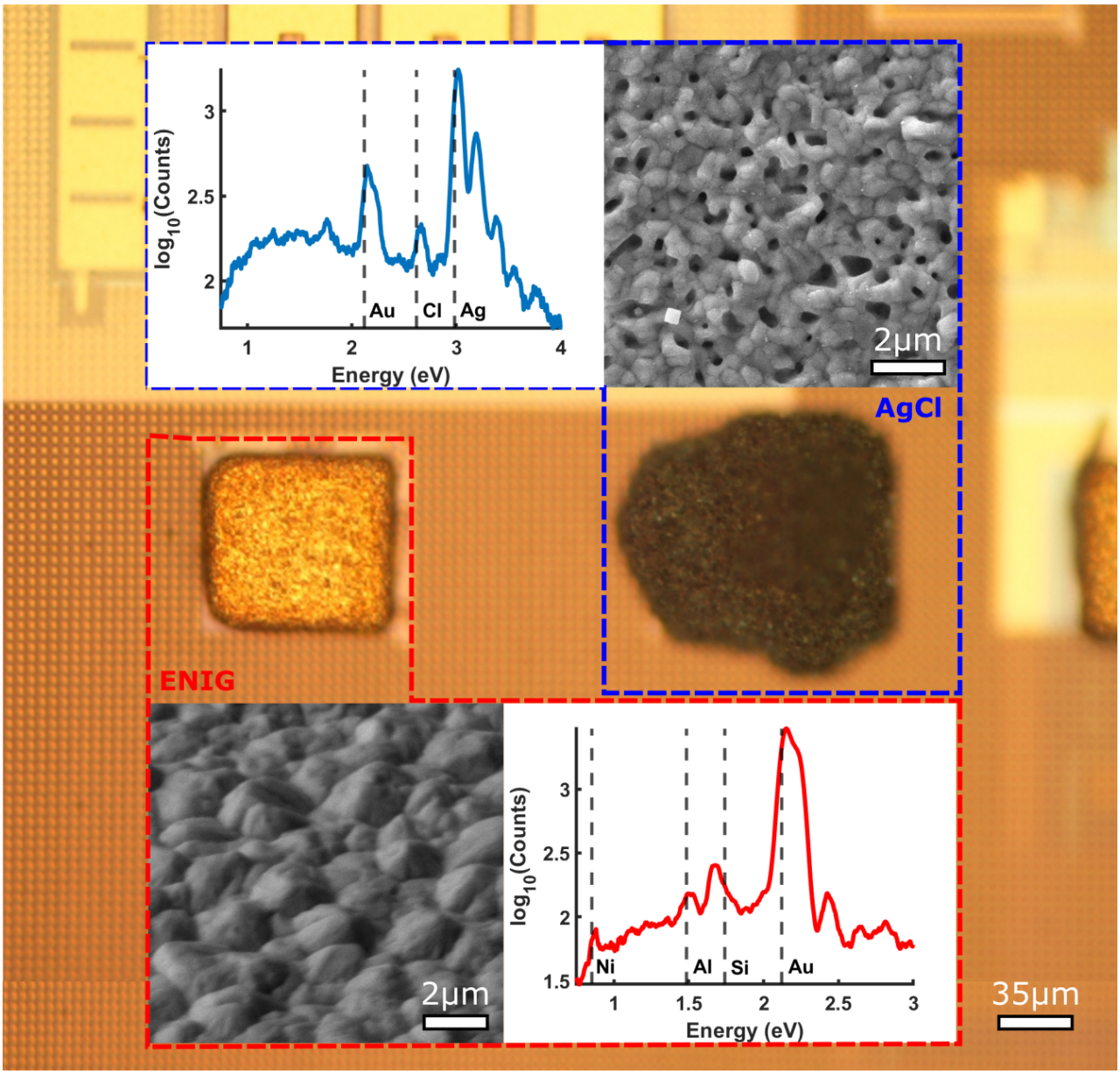


Figure 5.7: A microscope image of an ENIG-plated and an $AgCl$-plated pad. SEM close-up images of the surface topology were obtained with a beam energy of $10\,kV$. The white scale bars in the SEM images represent $2\,\mu m$. EDX spectra of the surfaces are provided, annotated with the elements corresponding to certain peaks.

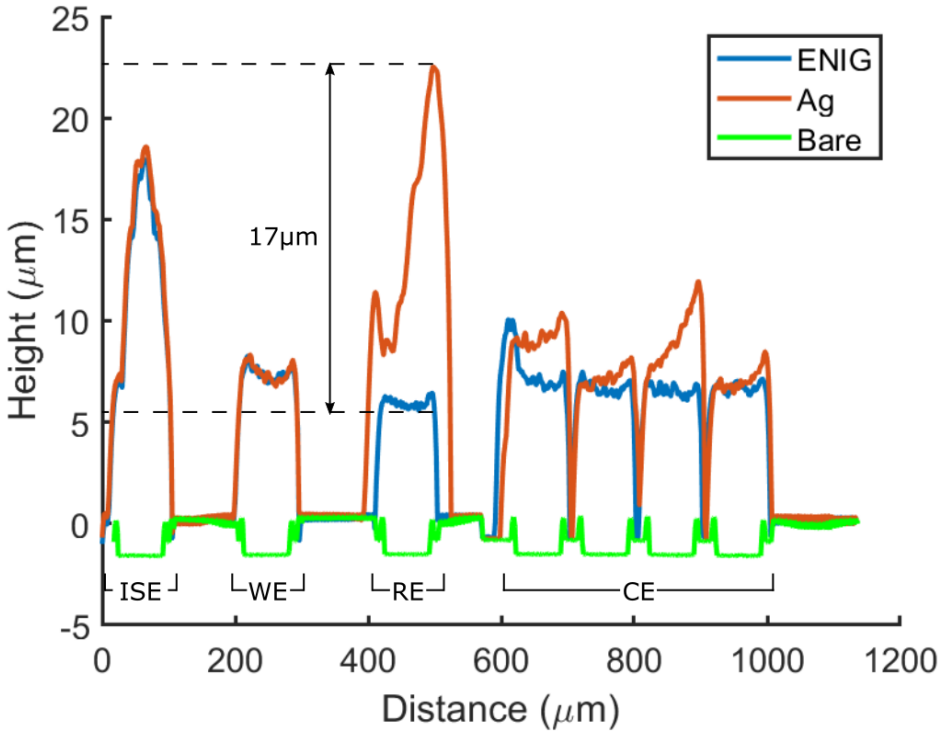
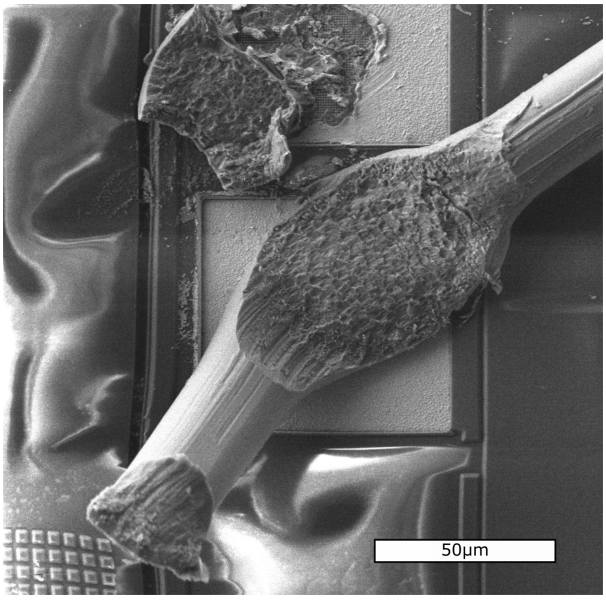
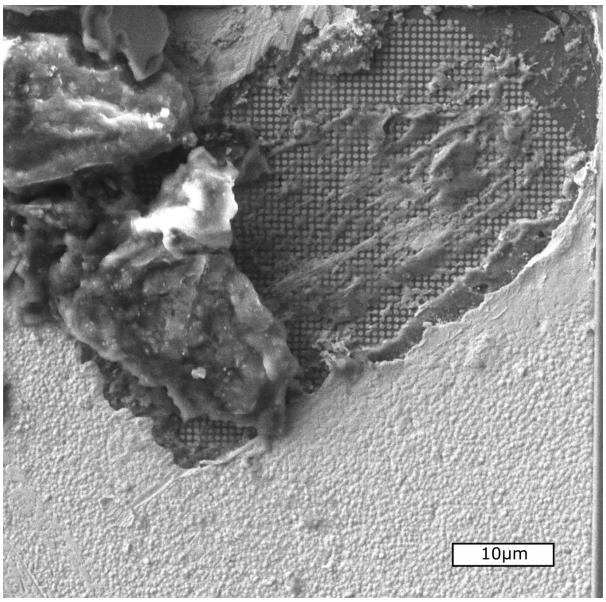


Figure 5.8: A graph of surface profiles of the DAPPER ISE, WE, RE, and CE. Profiles are shown for the (**green**) bare chip and the chip (**blue**) after ENIG plating of all electrodes and *Ag* plating of the RE only (**red**).



(a) Before



(b) After

Figure 5.9: Scanning electron microscope images of an ENIG plated pad with a bonded wire, and after this wire has been pulled, causing bond failure. (**a**) shows successful wirebonding and (**b**) shows delamination of the underlying *Al* bondpad from the silicon and *Al* vias underneath after the wire has been pulled off. SEM images were obtained with a 10 kV beam energy. White scale bars have been provided.

Test Subject	Peak-to-peak	Peak ratio	Cathode peak linearity (r^2)	Anodic peak linearity (r^2)
Ideal	$57\,mV$	1	1	1
Au slide	$116.6\,mV$	1.1920	0.9986	0.9998
ENIG pad	$163.6\,mV$	0.9198	0.9840	0.9630
$AgCl$ pad	$336.3\,mV$	2.4874	0.7070	0.9901

Table 5.2: A table summarising parameters for CV experiments on the Au-coated slide, ENIG-coated pad, and $AgCl$-coated pad, averaged over all scan rates, for which parameter values are independent.

Ag/AgCl

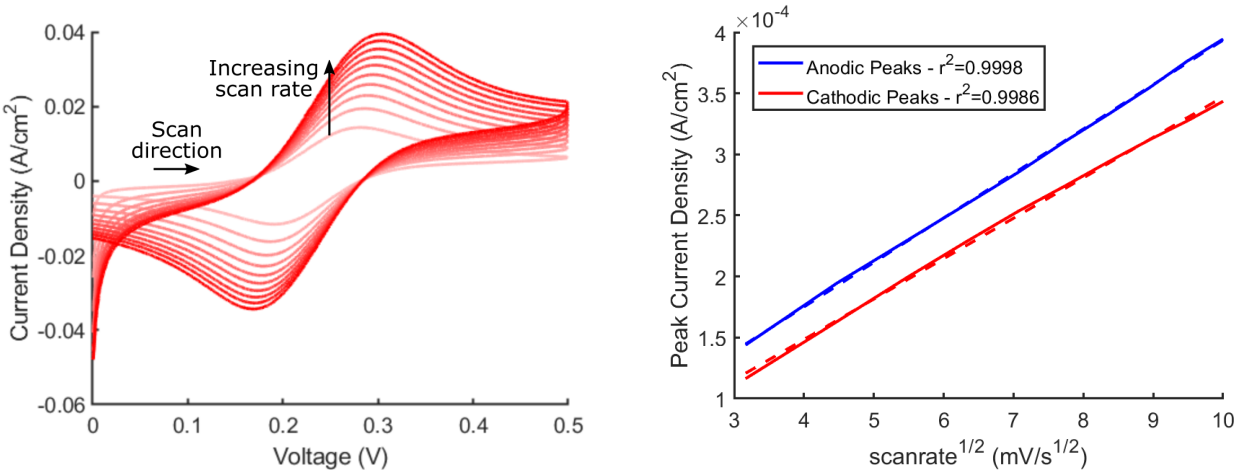
Ag was successfully plated and chlorinated, as demonstrated in Figure 5.7. $AgCl$ has a black appearance and the presence of both Ag and Cl is confirmed with EDX analysis. The Ag peak is roughly 4× greater than the Cl peak, which is similar to results seen in the literature [56]. The final $Ag/AgCl$ showed good adhesion, as it passed all tape tests. Wirebonding was not attempted. The surface profile of an Ag-plated RE, shown in Figure 5.8, indicates that the Ag layer is between 5-17 μm thick.

5.4.2 Electrochemical Performance

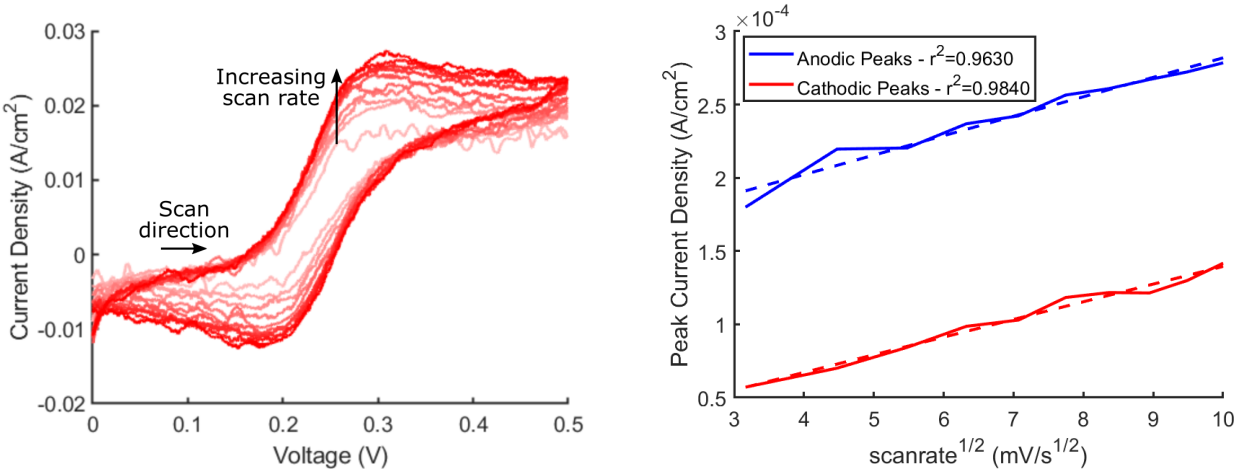
ENIG

CV was conducted on an ENIG-coated ISE pad on DAPPER. In doing so, the electrochemical performance of the underlying ENIG layer was separated from that of the full $Ag/AgCl$ electrode. An Au-coated microscope slide was also used to provide a comparison, with results for both provided in Figures 5.10a and 5.10b.

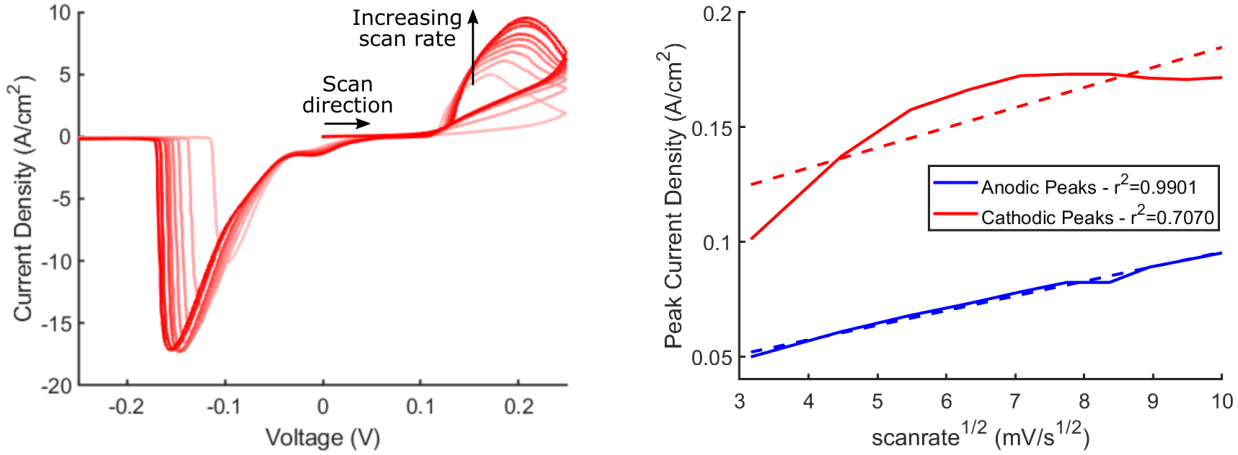
Similar performance was exhibited between the ENIG-coated pad and the Au-coated slide. Less prominent peaks detected by the pad are the consequence of convergent diffusion, which increases the transport rate of reactants from the bulk solution to the electrode surface. Subsequently, the current decreases slower with increasing voltage as the reactants are being replenished [57]. The estimates of peak current from Equation 5.3 for the ENIG-coated pad range from 7.27×10^{-5}-$2.30 \times 10^{-4}\,Acm^{-2}$ between scan rates of 10-100 $mV\,s^{-1}$, which are in reasonable agreement with the measured results. The CV curve parameters, collected in Table 5.2, indicate that electron transfer is slower in the ENIG-coated pad.



(a) *Au* slide

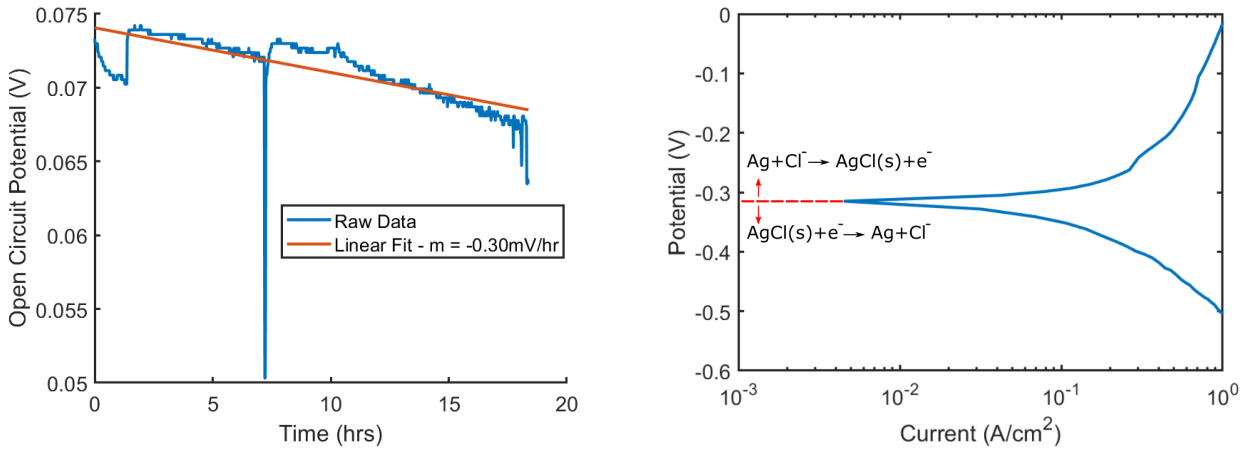


(b) ENIG pad



(c) *AgCl* pad

Figure 5.10: CV analysis for the (**a**) *Au*-coated slide, (**b**) ENIG-plated pad, and (**c**) *AgCl*-plated pad. (**left**) Graphs of five-point moving means of CV curves using a commercial *Ag/AgCl* RE. A *Pt* mesh was used as a counter electrode and the solution is $0.1\,M\ KCl$, $0.1\,mM\ K_3FeCN_6$, and $1\,mM\ K_4FeCN_6$. 10 scan rates from $10 - 100\,mV/s$ were run. Increasing scan rate direction is shown by increasing opacity of the line and is annotated on the graphs, along with the direction of the scans. (**right**) Graphs of (**red**) absolute peak cathodic and (**blue**) anodic current against the square-root of scan rate. Linear fits are provided, along with their r^2 values.



(a) OCP (b) Polarisation

Figure 5.11: Electrochemical characterisation of the plated $Ag/AgCl$ RE. (**a**) A graph of OCP versus time measured over an 18 hr period. A linear fit is provided along with the drift rate. (**b**) A polarisation curve. Both are measured against a commercial $Ag/AgCl$ glass electrode in 100 mM KCl solution.

Ag/AgCl

The OCP of one of the fabricated REs is shown in Figure 5.11a. The potential varied between 75-65 mV over 18 hrs of measurement, with an overall drift rate of 0.3 mV/hr. A large discontinuity can be seen at around 7 hrs which is believed to be caused by bubble formation. The polarisation curve produced in Figure 5.11b contains a low-gradient region at low current densities, which indicates stable behaviour of the RE to environmental fluctuations. This is comparable to the $Ag/AgCl$ RE polarisation curve seen in Khullar *et al.* 2015 [55].

The CV analysis of the $Ag/AgCl$-coated pads, seen in Table 5.2, suggests slow electron transfer, particularly when compared to the performance of the underlying ENIG layer. This is further reinforced by the non-linearity of $i_p - \sqrt{v}$ that is demonstrated in Figure 5.10c. However, the CV spectrum for the $Ag/AgCl$ electrode will be dominated by the reaction shown in Equation 1, with peak current densities almost three orders of magnitude larger than observed for the ferro/ferricyanide system using the ENIG-coated pad. As such, the CV spectrum contains similar characteristics to the polarisation curve in Figure 5.11b and the large peak separation is not necessarily caused by slow electron transfer.

A full demonstration of the on-chip three-electrode system is compared to off-chip system CV performance in Figure 5.12, with a scan rate of 25 mV/s. The on-chip system demonstrates similar behaviour to the off-chip equivalent, with consistent current values and graph shape, albeit with an offset in potential, likely derived from the different working potentials of the reference electrodes.

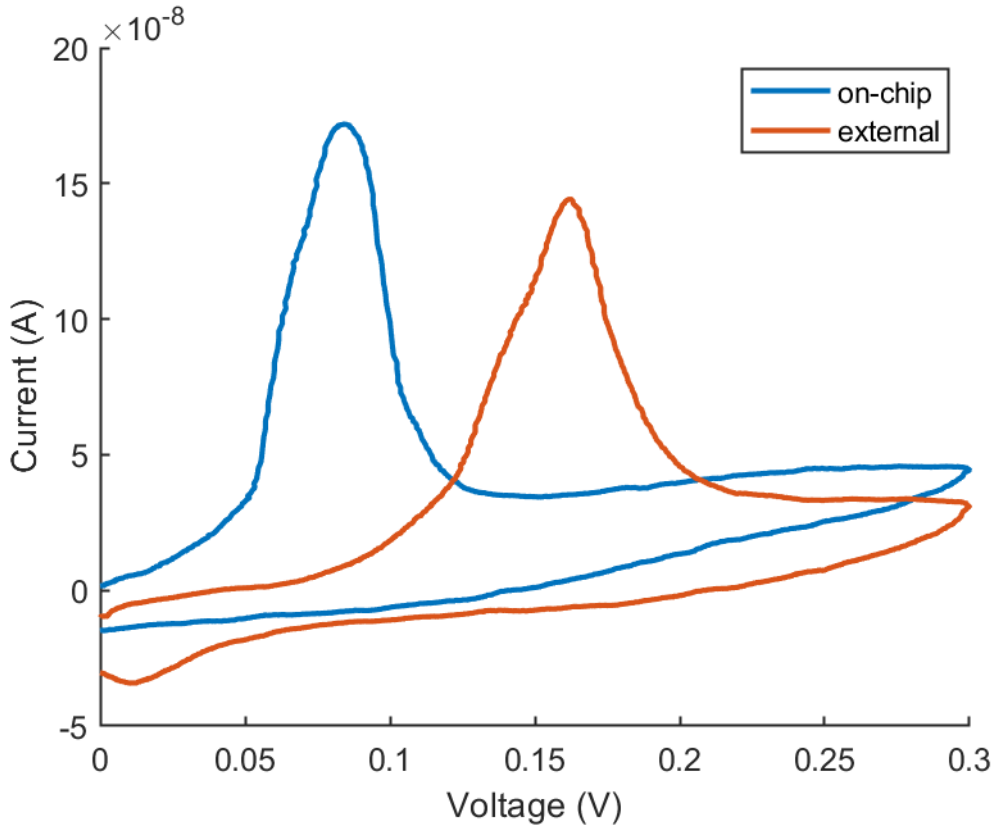


Figure 5.12: CV curves for (**blue**) on-chip and (**red**) off-chip three-electrode systems. The on-chip system used ENIG-plated WE and CE pads and an $Ag/AgCl$-plated RE pad. The off-chip system used an ENIG-plated WE pad, a platinised titanium mesh CE, and a commercial glass RE. The test solution was $0.1\,M\ KCl$, $0.1\,mM\ K_3FeCN_6$, and $1\,mM\ K_4FeCN_6$. A scan rate of $25\,mV/s$ was used.

5.5 Discussion

It has been shown that an $Ag/AgCl$ RE can be electroplated onto an Al bond-pad and that it can provide a stable potential. The observed drift rate of $0.3\,mV/hr$ is comparable to other thin-film $Ag/AgCl$ REs in the literature, found in Table 5.1. The lifetime of the plated RE, which extends up to a day, is sufficiently long for the majority of biosensing applications, which typically require between a few hours to a few days of operation. Fabrication of more REs is required to demonstrate the repeatability of the process in terms of the electrode characteristics.

The CV analysis of the final $Ag/AgCl$ electrode points towards slow electron transfer properties, with further optimisation of the electrode required moving forwards. The problem likely stems from the $Ag/AgCl$ layer, as the underlying ENIG layer demonstrated relatively quick electron transfer that compared favourably to Au-coated slides under CV analysis. It is worth investigating the use of a constant plating current to produce a more porous Ag layer and seeing whether this improves electrode performance.

The ENIG plating progressed well, as evidenced by the 'bump' profile obtained and the CV analysis. However, a number of ENIG-plated pads failed adhesion tests, with the ENIG layer or the underlying Al pad delaminating after removal of adhesive tape or during wirebonding. It was noted that adhesion test performance was worse for pads with a bump-profile or where thermal regulation of plating baths was sub-optimal. Thermal regulation of the plating baths would be more straightforward with specialised tanks and immersion heaters, which is an advantage of scaling up the process. The bump-profile is also unnecessary for RE functionality and thus shorter Ni plating times should be used. Shorter etching times of the Al pad and zincated layers, or more diluted etchants, should be used to avoid Al delamination.

5.6 Future Vision: Towards Multi-wafer Level, Electroless RE Fabrication for Wireless ISFET Arrays

The $Ag/AgCl$ RE fabricated within this chapter is the first that is 'fully' electroplated, based upon the Al bond-pads of a commercial CMOS process. All of these steps, bar the electroplating of Ag on Au, are electroless and do not require electrical connections to supply a current to the electrodes.

The vision is to have a fully electroless process, whereby creation of REs on CMOS chips would simply require immersion of a wafer into a sequence of different chemicals. This could then be significantly scaled up to a multi-wafer level process. As many wafers as can fit in the chemical tank are able to be plated at once, which far outstrips the production capability of other

thin-film $Ag/AgCl$ REs. There are also benefits to accessibility with an electroless process, as there is no need for expensive equipment. To realise this vision, an autocatalytic electroless Ag plating solution must become commercially available. An autocatalytic Ag process has been developed by Polymer Kompositer and is now being marketed by AutocatSilver AB [58].

A key limitation of a fully electroless process is the lack of specificity over which bond-pads are plated. Photoresists could be used to expose desired pads to the plating solutions. But having produced the photopattern, sputtering of an Au metal base would be the more efficient solution. The major issue with plating all bond-pads is the need to wirebond the chip to allow communication with it. The viability of wirebonding to $AgCl$ is yet to be investigated, but it is likely to produce sub-optimal performance.

However, there is currently a movement towards wirelessly operated microchips, with power, inputs, and outputs transmitted via an inductive coil [59]. In this case, the need for wired connections to the chips is removed, and the only bond-pads present would be for the electrochemical sensing electrodes. For a two or three-electrode set-up, $Ag/AgCl$ is not a popular choice as a WE or CE, although it does have its applications [36, 55]. Instead, it is wireless sensors such as FETs and ISFETs, where only a single electrode, the RE, is exposed to the electrolyte, that stand to benefit most from a fully electroless QRE fabrication process.

5.7 Summary

A survey of thin-film $Ag/AgCl$ RE fabrication approaches found that the metal bond-pads of commercial CMOS processes were yet to be exploited as a base for Ag electroplating. Industry-standard zincate and ENIG electroless surface processing was conducted on the Al pads to provide an Au surface onto which Ag could be electroplated and then chlorinated. This underlying ENIG layer was shown to have good electron-transfer properties through CV analysis. The final $Ag/AgCl$ electrode was able to sustain an OCP around $70\,mV$ for up to $18\,hrs$ with a drift rate of $0.3\,mV/hr$, which is comparable to thin-film $Ag/AgCl$ QREs in the literature.

Bibliography

[1] M. W. Shinwari et al. "Microfabricated reference electrodes and their biosensing applications". In: *Sensors* 10 (3 Mar. 2010), pp. 1679–1715. ISSN: 14248220.

[2] B. J. Polk et al. "Ag/AgCl microelectrodes with improved stability for microfluidics". In: *Sensors and Actuators, B: Chemical* 114 (1 Mar. 2006), pp. 239–247. ISSN: 09254005.

[3] E. T. S. G. D. Silva et al. "Simple on-plastic/paper inkjet-printed solid-state Ag/AgCl pseudoreference electrode". In: *Analytical Chemistry* 86 (21 Oct. 2014), pp. 10531–10534. ISSN: 15206882.

[4] S. Papamatthaiou et al. "Ultra stable, inkjet-printed pseudo reference electrodes for lab-on-chip integrated electrochemical biosensors". In: *Scientific Reports 2020 10:1* 10 (1 Oct. 2020), pp. 1–10. ISSN: 2045-2322.

[5] A. Moya et al. "Stable Full-Inkjet-Printed Solid-State Ag/AgCl Reference Electrode". In: *Analytical Chemistry* 91 (24 Dec. 2019), pp. 15539–15546. ISSN: 15206882.

[6] W.-Y. Liao and T.-C. Chou. "Fabrication of a Planar-Form Screen-Printed Solid Electrolyte Modified Ag/AgCl Reference Electrode for Application in a Potentiometric Biosensor". In: *J. K. Meas. Sci. Techol* 76 (1 2004), p. 43.

[7] D. Moschou et al. "Surface and Electrical Characterization of Ag/AgCl Pseudo-Reference Electrodes Manufactured with Commercially Available PCB Technologies". In: *Sensors* 15 (8 July 2015), pp. 18102–18113. ISSN: 1424-8220.

[8] H. R. Lim et al. "Ultrathin, long-term stable, solid-state reference electrode enabled by enhanced interfacial adhesion and conformal coating of AgCl". In: *Sensors and Actuators, B: Chemical* 309 (Apr. 2020), p. 127761. ISSN: 09254005.

[9] Q. Li et al. "Stable thin-film reference electrode on plastic substrate for all-solid-state ion-sensitive field-effect transistor sensing system". In: *IEEE Electron Device Letters* 38 (10 Oct. 2017), pp. 1469–1472. ISSN: 07413106.

[10] R. Mamińska, A. Dybko, and W. Wróblewski. "All-solid-state miniaturised planar reference electrodes based on ionic liquids". In: *Sensors and Actuators, B: Chemical* 115 (1 May 2006), pp. 552–557. ISSN: 09254005.

[11] H. Suzuki et al. “Problems associated with the thin-film Ag/AgCl reference electrode and a novel structure with improved durability”. In: *Sensors and Actuators, B: Chemical* 46 (2-3 Feb. 1998), pp. 104–113. ISSN: 09254005.

[12] H. Suzuki et al. “An integrated three-electrode system with a micromachined liquid-junction Ag/AgCl reference electrode”. In: *Analytica Chimica Acta* 387 (1 Apr. 1999), pp. 103–112. ISSN: 00032670.

[13] H. Suzuki and T. Taura. “Thin-Film Ag/AgCl Structure and Operational Modes to Realize Long-Term Storage”. In: *Journal of The Electrochemical Society* 148 (12 Nov. 2001), E468. ISSN: 00134651.

[14] A. Hiratsuka et al. “Integration of microfabricated needle-type glucose sensor devices with a novel thin-film Ag/AgCl electrode and plasma-polymerized thin film: Mass production techniques”. In: *Analyst* 126 (5 Jan. 2001), pp. 658–663. ISSN: 00032654.

[15] T. Matsumoto, A. Ohashi, and N. Ito. “Development of a micro-planar Ag/AgCl quasi-reference electrode with long-term stability for an amperometric glucose sensor”. In: *Analytica Chimica Acta* 462 (2 July 2002), pp. 253–259. ISSN: 00032670.

[16] I. Y. Huang, R. S. Huang, and L. H. Lo. “Improvement of integrated Ag/AgCl thin-film electrodes by KCl-gel coating for ISFET applications”. In: *Sensors and Actuators, B: Chemical* 94 (1 Aug. 2003), pp. 53–64. ISSN: 09254005.

[17] S. I. Park et al. “Application of a new Cl-plasma-treated Ag/AgCl reference electrode to micromachined glucose sensor”. In: *IEEE Sensors Journal* 3 (3 June 2003), pp. 267–273. ISSN: 1530437X.

[18] D. S. Kim et al. “Field effect transistor-based bimolecular sensor employing a Pt reference electrode for the detection of deoxyribonucleic acid sequence”. In: *Japanese Journal of Applied Physics, Part 1: Regular Papers and Short Notes and Review Papers* 43 (6 B June 2004), pp. 3855–3859.

[19] F. L. Almeida et al. “Fabrication Process of Ag/AgCl Reference Pseudo-Electrode Based on Electrodeposition of Au on Pt Surfaces from Formaldehyde Baths: Chemical Stability and Adherence”. In: *ECS Transactions* 23 (1 Dec. 2009), pp. 255–262. ISSN: 1938-6737.

[20] J. Zhou et al. “Fabrication of a microfluidic Ag/AgCl reference electrode and its application for portable and disposable electrochemical microchips”. In: *ELECTROPHORESIS* 31 (18 Aug. 2010), pp. 3083–3089. ISSN: 01730835.

[21] J. Schnitker et al. “Planar reference electrodes on multielectrode arrays for electrochemical measurements of ionic currents”. In: *physica status solidi (a)* 210 (5 May 2013), pp. 892–897. ISSN: 18626300.

[22] A. Baraket et al. "Diazonium modified gold microelectrodes onto polyimide substrates for impedimetric cytokine detection with an integrated Ag/AgCl reference electrode". In: *Sensors and Actuators, B: Chemical* 189 (Dec. 2013), pp. 165–172. ISSN: 09254005.

[23] Y. Abbas et al. "No more conventional reference electrode: Transition time for determining chloride ion concentration". In: *Analytica Chimica Acta* 821 (Apr. 2014), pp. 81–88. ISSN: 18734324.

[24] T. Kim, S. Hong, and S. Yang. "A Solid-State Thin-Film Ag/AgCl Reference Electrode Coated with Graphene Oxide and Its Use in a pH Sensor". In: *Sensors* 15 (3 Mar. 2015), pp. 6469–6482. ISSN: 1424-8220.

[25] T. S. Monteiro et al. "PDMS encasing system for integrated lab-on-chip Ag/AgCl reference electrodes". In: Institute of Electrical and Electronics Engineers Inc., Apr. 2015. ISBN: 9781479982691.

[26] S. J. Wu et al. "ISFET-based pH sensor composed of a high transconductance CMOS chip and a disposable touch panel film as the sensing layer". In: Institute of Electrical and Electronics Engineers Inc., Dec. 2015. ISBN: 9781479982028.

[27] E. Garcia-Cordero et al. "Heterogeneous integration of low power pH FinFET sensors with passive capillary microfluidics and miniaturized Ag/AgCl quasi-Reference Electrode". In: vol. 2016-October. Editions Frontieres, Oct. 2016, pp. 452–455. ISBN: 9781509029693.

[28] N. Wang et al. "Microfabricated thin-film reference electrode for disposable electrochemical sensors". In: vol. 2017-December. Institute of Electrical and Electronics Engineers Inc., Dec. 2017, pp. 1–3. ISBN: 9781509010127.

[29] T. Rahman and T. Ichiki. "Fabrication and Characterization of a Stabilized Thin Film Ag/AgCl Reference Electrode Modified with Self-Assembled Monolayer of Alkane Thiol Chains for Rapid Biosensing Applications". In: *Sensors* 17 (10 Oct. 2017), p. 2326. ISSN: 1424-8220.

[30] L. N. Q. Hoa, H.-R. Chen, and T. T.-C. Tseng. "An Arrayed Micro-glutamate Sensor Probe Integrated with On-probe Ag/AgCl Reference and Counter Electrodes". In: *Electroanalysis* 30 (3 Mar. 2018), pp. 561–570. ISSN: 10400397.

[31] B. Bao et al. "Development and characterisation of electroplating silver/silver chloride modified microelectrode arrays". In: *Micro and Nano Letters* 14 (3 Mar. 2019), pp. 299–303. ISSN: 17500443.

[32] N. Wang et al. "Investigation of a Thin-Film Quasi-Reference Electrode Fabricated by Combined Sputtering-Evaporation Approach". In: *Electroanalysis* 31 (3 Dec. 2018). ISSN: 1040-0397.

[33] T. M. Huynh et al. “Fabrication of thin film Ag/AgCl reference electrode by electron beam evaporation method for potential measurements”. In: *Advances in Natural Sciences: Nanoscience and Nanotechnology* 10 (1 Feb. 2019), p. 15006. ISSN: 20436262.

[34] A. B. Rosli et al. “Fabrication of integrated solid state electrode for extended gate-FET pH sensor”. In: *Materials Research Express* 6 (1 Jan. 2019), p. 016419. ISSN: 20531591.

[35] J. Yin et al. “Batch microfabrication and testing of a novel silicon-base miniaturized reference electrode with an ion-exchanging nanochannel array for nitrite determination”. In: *RSC Advances* 9 (34 June 2019), pp. 19699–19706. ISSN: 20462069.

[36] K. C. E. Tjon and J. Yuan. “Impedance characterization of silver/silver chloride microelectrodes for bio-sensing applications”. In: *Electrochimica Acta* 320 (Oct. 2019). ISSN: 00134686.

[37] K. Xu et al. “Preparation and performance of a solid-state thin-film Ag/AgCl quasi-reference electrode modified by chitosan-graphene”. In: *Materials Technology* (Feb. 2020), pp. 1–9. ISSN: 1066-7857.

[38] J. Dai et al. “Microfluidic sensor integrated with nanochannel liquid conjunct Ag/AgCl reference electrode for trace Pb(II) measurement”. In: *Analytica Chimica Acta* 1164 (June 2021).

[39] Z. Wang et al. “A Dual-Sensing CMOS Array for Combined Impedance-pH Detection of DNA with Integrated Electric Field Manipulation”. In: *2021 IEEE International Symposium on Circuits and Systems (ISCAS)*. 2021, pp. 1–5.

[40] V. Torres-González, J. A. Ávila-Niño, and E. Araujo. “Facile fabrication of tailorable Ag/AgCl reference electrodes for planar devices”. In: *Thin Solid Films* 757 (Sept. 2022). ISSN: 00406090.

[41] P. Tirado, I. R. Chavez-Urbiola, and J. J. Alcantar-Peña. “Ionic gel effect on a reference electrode in a flexible solid-state pH sensor”. In: *MRS Communications* 13 (1 Feb. 2022), pp. 41–46. ISSN: 21596867.

[42] J. Burgess. “Electroplating onto aluminium and its alloys”. In: *Transactions of the IMF* 97.6 (2019), pp. 285–288.

[43] J. F. Rohan, P. A. Murphy, and J. Barrett. “Zincate-Free, Electroless Nickel Deposition on Aluminum Bond Pads”. In: *Journal of The Electrochemical Society* 152.1 (Dec. 2004), p. C32.

[44] D. A. Hutt et al. “Electroless nickel bumping of aluminum bondpads - Part I: Surface pretreatment and activation”. In: *IEEE Transactions on Components and Packaging Technologies* 25 (1 Mar. 2002), pp. 87–97. ISSN: 15213331.

[45] D. Charyk et al. *Optimizing immersion silver chemistries for copper*. Tech. rep. 2007.

[46] E. Long and L. Toscano. *Electroless nickel/immersion silver - A new surface finish for PCB applications*. Tech. rep. MacDermid, 2012.

[47] B. J. Polk et al. "Microelectroplating Silver on Sharp Edges toward the Fabrication of Solid-State Nanopores". In: *Journal of The Electrochemical Society* 151.9 (Aug. 2004), p. C559.

[48] B. Rostami et al. "Development of an enhanced porosity AgAgCl reference electrode with improved stability". In: *Engineering Research Express* 1.1 (Sept. 2019), p. 015039.

[49] D. Ma, S. S. Ghoreishizadeh, and P. Georgiou. "DAPPER: A Low Power, Dual Amperometric and Potentiometric Single-Channel Front End". In: *2020 IEEE International Symposium on Circuits and Systems (ISCAS)*. 2020, pp. 1–5.

[50] S. G. Robertson and I. M. Ritchie. "The role of iron(III) and tartrate in the zincate immersion process for plating aluminium". In: *Journal of Applied Electrochemistry* 27 (7 1997), pp. 799–804. ISSN: 0021891X.

[51] S. K. Lee, J. H. Lee, and Y. H. Kim. "Nucleation and growth of zinc particles on an aluminum substrate in a zincate process". In: *Journal of Electronic Materials* 36 (11 Nov. 2007), pp. 1442–1447. ISSN: 03615235.

[52] X. Chen et al. "Electroless nickel bath for wafer bumping: influence of additives". In: *International Symposium on Electronic Materials and Packaging (EMAP2000) (Cat. No.00EX458)*. 2000, pp. 12–17.

[53] N. N. Elgrishi et al. "A Practical Beginner's Guide to Cyclic Voltammetry". In: (2017). DOI: 10.1021/acs.jchemed.7b00361. URL: https://pubs.acs.org/sharingguidelines.

[54] R. S. Nicholson. "Semiempirical Procedure for Measuring with Stationary Electrode Polarography Rates of Chemical Reactions Involving the Product of Electron Transfer". In: *Analytical Chemistry* 38 (10 1966), p. 1406. ISSN: 15206882.

[55] P. Khullar, J. V. Badilla, and R. G. Kelly. "The use of a sintered Ag/AgCl electrode as both reference and counter electrode for electrochemical measurements in thin film electrolytes". In: *ECS Electrochemistry Letters* 4 (10 Aug. 2015), pp. C31–C33. ISSN: 21628734.

[56] E. M. Robbins, E. Castagnola, and X. T. Cui. "Accurate and stable chronic in vivo voltammetry enabled by a replaceable subcutaneous reference electrode". In: *iScience* 25 (8 Aug. 2022), p. 104845. ISSN: 2589-0042. DOI: 10.1016/J.ISCI.2022.104845.

[57] C. Sandford et al. "A synthetic chemist's guide to electroanalytical tools for studying reaction mechanisms". In: *Chemical Science* 10 (26 July 2019), pp. 6404–6422. ISSN: 20416539.

[58] S. Shukla, N. Gomathi, and R. George. "Autocatalytic silver-plating of aluminium radio frequency waveguides with autocatalytic nickel as the undercoat for space applications". In: *Surface Topography: Metrology and Properties* 2 (4 Nov. 2014), p. 045004. ISSN: 2051-672X.

[59] M. Zargham and P. G. Gulak. "Fully Integrated On-Chip Coil in 0.13 μm CMOS for Wireless Power Transfer Through Biological Media". In: *IEEE Transactions on Biomedical Circuits and Systems* 9.2 (2015), pp. 259–271.

Chapter 6

Conceptualisation of an Electrokinetic Lab-on-CMOS Diagnostic Device

As alluded to in the future vision section of Chapter 4, the application of DNA DEP to microchip-based diagnostic devices will increasingly focus on sample preparation, a field in which electrodes have a proven ability. The challenge is to conduct as many sample preparation stages within the confines of the CMOS chip itself, thus marrying sample handling with target detection as part of the same system, with the hope of increasing the speed and ease of operation.

The concept of an electrokinetic lab-on-CMOS is not new, with Medoro and Manaresi publishing multiple papers in the early 2000s on a microchip for cell manipulation and detection [3, 4]. Subsequent electrokinetic lab-on-CMOS devices have been developed that focus on cells for monitoring or analytical purposes [5, 6, 7, 8, 9]. DEP manipulation of cells requires lower DEP forces and hence electrodes can be designed in CMOS top-metal without needing to remove the passivation, simplifying the implementation. Such an approach is not feasible for DNA.

To this end, an electrode array can be fabricated by utilising bond-pads of the native CMOS process to expose top-metal to the test solution and exert sufficiently strong electrokinetic forces to effectively manipulate DNA. As demonstrated by the FRY microchip in chapter 4, the bond-pads require surface treatment to ensure their longevity within the samples. A bond-pad electrode array that can induce a variety of electrokinetic effects, combined with sensors on-chip, is an ideal candidate to produce a sample-to-result lab-on-CMOS diagnostic device.

This chapter will highlight key capabilities of electrode systems within the sample-to-result pipeline and their feasibility for on-chip implementation. A concept for an electrokinetic lab-on-CMOS diagnostic will then be presented, supported by the first experimental demonstration

Fluorescence microscopy was conducted at the Hamlyn Centre, Imperial College London. The DAPPER microchip used for electrokinetic trapping of DNA was designed by Dr. Ma [1]. A combined pH-impedance DNA detection microchip was developed by Zhengyu Wang during their master's project [2].

of DEP using a bond-pad electrode, utilising the ENIG plating process developed in the previous chapter.

6.1 Electrokinetic Sample Preparation

The ability to move and trap DNA, as well as other material, with electric field interactions can be applied to the preparation of diagnostic samples for testing. By moving as many of these sample preparation stages on-chip as possible, the accessibility and reliability of a diagnostic device can be improved, with responsibility taken away from the end-user and equipment requirements reduced. However, all sample preparation steps must be achievable at a low voltage and should not require additional or highly specialised electrode systems, to maintain the simplicity and scalability of the final device.

6.1.1 Cell Lysis

In the presence of an electric field, ions build up on either side of cellular membranes and create a potential difference. If this potential increases beyond a threshold value, the membrane will breakdown and the cell will expel its contents into the surrounding medium. Cell lysis is a key component of sample preparation as it provides a larger amount of DNA or RNA than circulates freely in blood.

Cheng *et al.* were able to demonstrate lysis of *Escherichia Coli* (*E. coli*) in their 1998 paper using an array of circular electrodes [10]. With *E. coli* being held at the electrode surface, 400 $50\,\mu s$ pulses of $500\,V$ were used to break apart the cellular membrane and release the DNA held within. To enable lysis at low voltages, small electrode features are required to exert the necessary electric field strengths. Graphene was used to form microwells in Kabiri Ameri *et al.* 2014 to lyse cells at $3\,V$ with a DC signal applied for $8\,s$ with almost $100\,\%$ efficiency [11]. Riaz et al. used nanospikes in their 2017 paper fabricated from Al imprinted by a Si mould and achieved almost $100\,\%$ lysing efficiency with a $5\,V$, $13\,ms$ pulse [12]. In Punjiya *et al.* 2020, a cell lysis system was designed using CMOS metal layers to create a multi-layer electrode well [13]. After being etched using RIE, the electrodes were able to lyse cells with $3\,V$ applied. Thus, low-voltage lysing is achievable on a CMOS platform, but may require specialised systems.

6.1.2 Sample Purification

Isolating DNA from a complex mixture of particles is vital for reliable amplification. Both haemoglobin and heparin are substances found in blood that take up amplification reagents

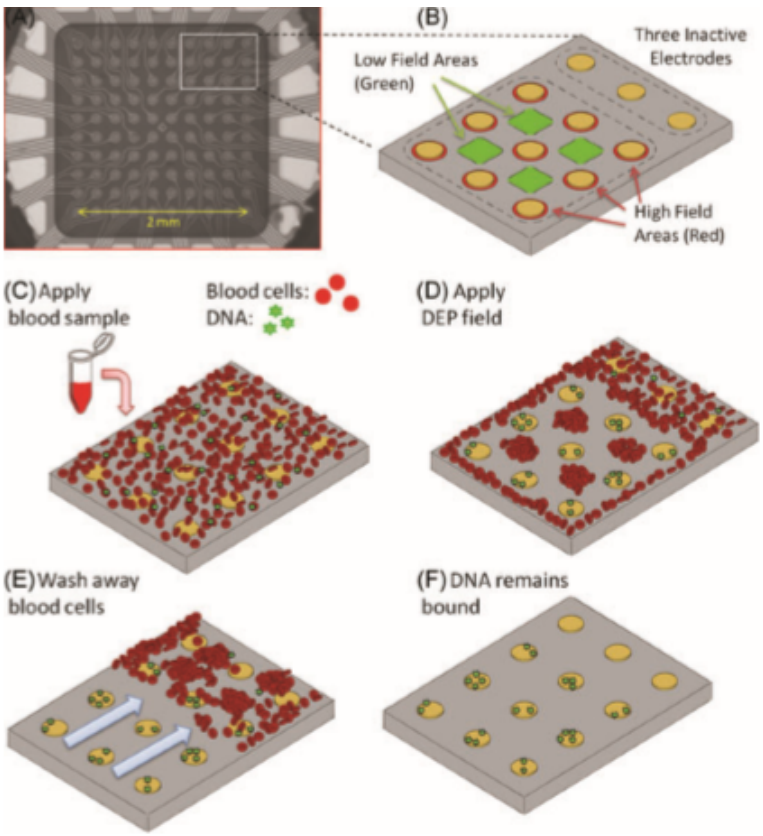


Figure 6.1: A series of diagrams detailing the process of DNA isolation from blood carried out in Sonnenberg *et al.* 2012 [14], using an array of circular electrodes to form quadrupoles.

Year	Paper	Concentration	Time (s)	Voltage
1998	Asbury *et al.* [15]	5×	30	$200\,V$
2001	Kawabata *et al.* [16]	2.25×	125	$7\,V$
2002	Asbury *et al.* [17]	16×	240	$3\,V_{pp}$
	Hölzel *et al.* [18]	11×	3000	$7.5\,V$
2006	Bakewell *et al.* [19]	1.22×	2	$4.5\,V$
	Bown *et al.* [20]	6.5×	100	$4\,V_{pp}$
	Tuukkanen *et al.* [21]	40×	240	$4.5\,V_{rms}$
2008	Du *et al.* [22]	36×	4	$20\,V_{pp}$
2009	Yeo *et al.* [23]	1.36×	60	$20\,V_{pp}$
2013	Martinez-Duarte *et al.* [24]	8×	20	$16\,V_{pp}$
2018	Velmanickam *et al.* [25]	3×	50	$10\,V_{pp}$

Table 6.1: Table presenting concentration factors that have been either been quoted in the literature or can be discerned from graphs provided in the text. Both the voltage used and the time that the DEP field was applied to achieve it are shown for context.

and can inhibit reactions, increasing the ttp or false negatives. A DEP trap is capable of separating particles based on differing CM functions, so that desired particles move to high intensity field regions under pDEP and undesired particles to low intensity field regions by nDEP. nDEP trapping is weaker and so by applying a fluid flow the undesirable particles can be washed away, as illustrated in Figure 6.1.

In Sonnenberg *et al.* 2012 [14], an array of hydrogel-coated, circular Pt electrodes polarised to form quadrupoles was used to separate DNA and nanoparticles from red blood cells, which experienced pDEP and nDEP respectively, in physiological solutions with high conductivity between 0.74-1.15 Sm^{-1}. If DNA has a similar CM function to the other particle then separation becomes more complex. However, it is apparent that DNA attracted to electrodes under pDEP should be separable from cells undergoing nDEP in the majority of conditions. Other extracellular matter may be trapped along with the DNA, but is unlikely to impact on subsequent detection methods. A checkerboard polarisation pattern like that used in Sonnenberg *et al.* 2012 is easily implemented in CMOS with electrical connections made in the underlying IC.

6.1.3 DNA Concentration

The low concentrations at which target DNA may be present in blood samples provides an obstacle to detection and can lead to long ttps or false negatives. Increasing the concentration of DNA in samples is thus an important objective. An electrokinetic trap is able to increase sample concentrations by accumulating DNA at electrodes as more of the sample is passed over it. Table 6.1 contains concentration factors of DNA achieved by microelectrode systems in the literature. In cases where factors are not explicitly stated, it is possible to estimate them from fluorescent intensity graphs provided in the text.

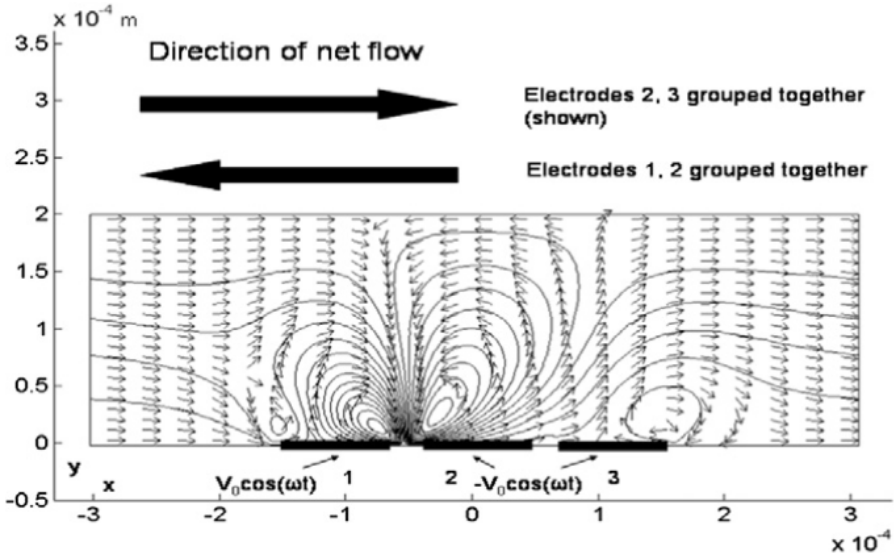


Figure 6.2: Simulated electric field strength and ACEO fluid flow direction caused by asymmetric electrode pairs [28].

The increase in DNA concentration is dependent on the electrokinetic trap capacity, which is determined by size of the region where the trapping force is larger than other forces exerted on DNA. As DNA is trapped, the molecules will aggregate. As this aggregation grows, it will reach the limit of effective trapping. Further DNA will be physically impeded from travelling closer to the electrode edge and instead will remain in regions where it experiences a weak electrokinetic force and can be carried away by other forces. To maximise trap capacity, either larger voltages can be applied or an electrode geometry with a larger trapping area can be used. A larger trapping area could be created by adding castellations to a line IDE or using 3D electrodes that extend deeper into the test solution.

6.1.4 Sample Transport and Mixing

When sample handling is brought down to the microfluidic scale, the mixing of molecules in a solution becomes challenging with the laminar, non-turbulent flow typically encountered. There are many approaches to sample mixing that involve microfluidic design [26]. But the vortices created by ACEO possess the ability to mix samples on-demand through application of an electric field [27], offering a more straightforward approach.

The transport of samples through microfluidic channels can also be enabled through electro-osmosis. DC electro-osmosis can be used for sample pumping over long distances, but requires large voltages [29]. Typically, ACEO performed by symmetric planar electrodes only allows local fluid transport. However, an asymmetric electrode design, as was used in Loucaides *et al.* 2012 [28], is capable of creating an unidirectional and reversible fluid flow, with an example of simulated ACEO pumping provided in Figure 6.2. Another approach to transporting samples

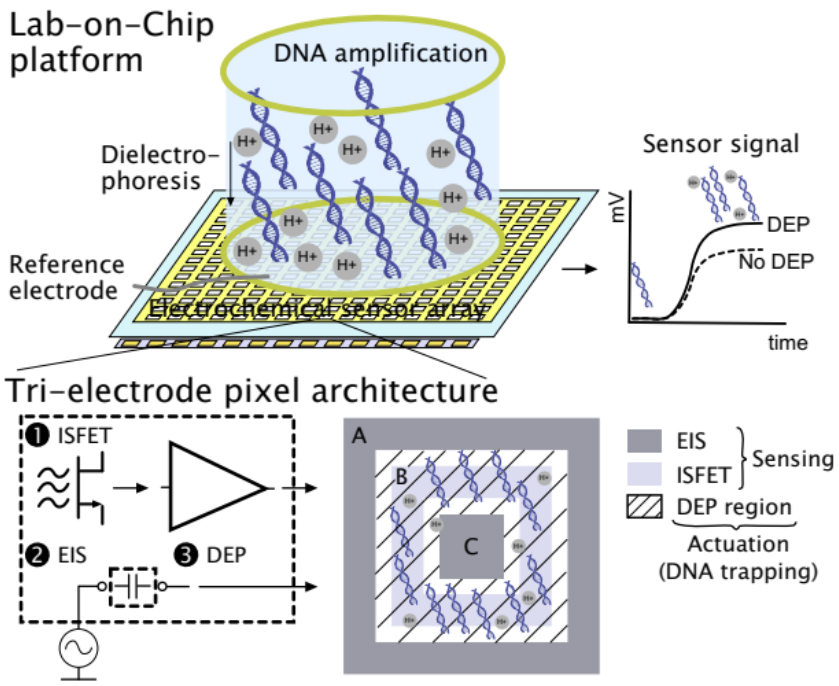


Figure 6.3: A graphical summary of the combined ISFET-impedance pixel for DNA detection, with integrated DEP positioning, developed in Wang *et al.* 2021.

focusses not on fluid flow, but instead on moving the target molecule itself. Travelling-wave DEP (twDEP) uses consecutive sets of electrodes with a 90° shifted sinusoidal potential to draw targets down a channel. This has previously been implemented in CMOS, using top-metal electrodes for transporting cells [30, 31].

6.2 Alternative Electrochemical Sensing Modalities

It is possible to exploit the on-CMOS electrodes used for electric field manipulation of DNA for impedance sensing as well. Many combined DEP-impedance systems have separate electrodes for manipulation and sensing [32], but both functions can be conducted by the same electrodes, as in Velmanickam *et al.* 2019 [33] and Pungetmongkol *et al.* 2019 [34] for RNA and DNA detection respectively. The CE for the impedance sensing system is used to produce an AC excitation signal, whose voltage could be increased to induce DEP motion. In doing so, targets will be drawn to regions of high electric field intensity and will produce a greater impedance change.

Impedance sensing has been a popular approach to DNA detection, typically involving a binding event of target DNA with an immobilised probe [35, 36]. However, the increase in DNA concentration during amplification reactions will provide a change in solution impedance that can be be detected [37]. Such an approach would pair well with ISFET-based DNA detection.

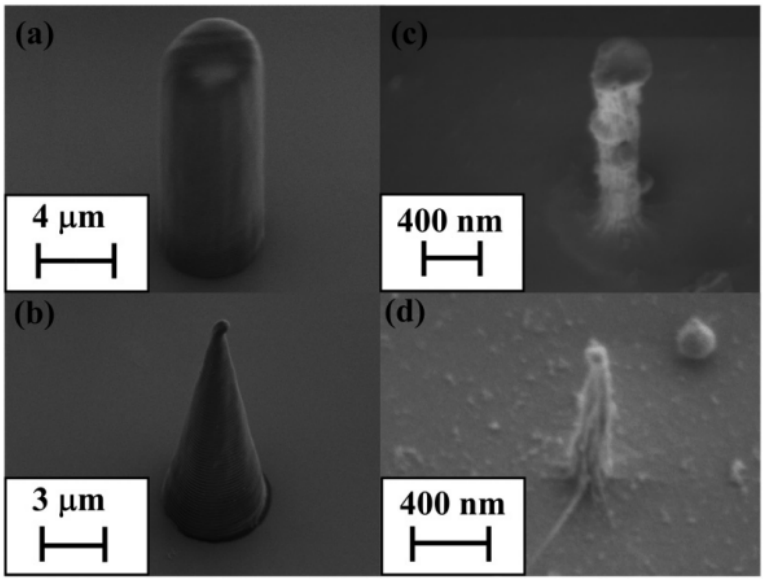


Figure 6.4: Examples of carbonised 2PP structures produced in Haque *et al.* 2020 [43].

A combined ISFET-impedance sensing system would possess greater dynamic range, on top of improved diagnostic decision making through concurrent analysis of the two sensing modes. A dual-sensing CMOS array for combined ISFET and impedance-based detection of DNA was designed in Wang *et al.* 2021 [38].

6.3 On-CMOS 3D Carbon Electrodes

Martinez Duarte *et al.* demonstrated the exceptional ability of 3D carbon electrodes as a sample preparation system [24], supported by further studies from the group in a variety of applications [39, 40, 41]. However, as previously discussed, the high carbonisation temperatures of the precursor structures (900° C) used by Martinez Duarte prohibited their implementation on CMOS [42].

A recent paper by Haque *et al.* provided a technique for low-temperature polymer carbonisation to create conducting carbon structures through two-photon polymerisation (2PP) [43]. 2PP, as opposed to standard photolithography, consists of a photosensitive material that absorbs two photons, instead of one, to activate the photoinitiators. This allows a two-beam set-up to selectively polymerise points within the bulk of the photoresist and create 3D polymer structures. Haque *et al.* carbonised these precursor polymer structures through thermal treatment in Ar and O_2 atmospheres at $500°C$, which is a CMOS-compatible temperature. Examples of the conducting carbon structures produced in Haque *et al.* can be seen in Figure 6.4.

The 3D structuring possible with 2PP enables the fabrication of electrodes with sub-micron feature sizes. For instance, the nanospike array used by Riaz *et al.* for cellular lysis [12],

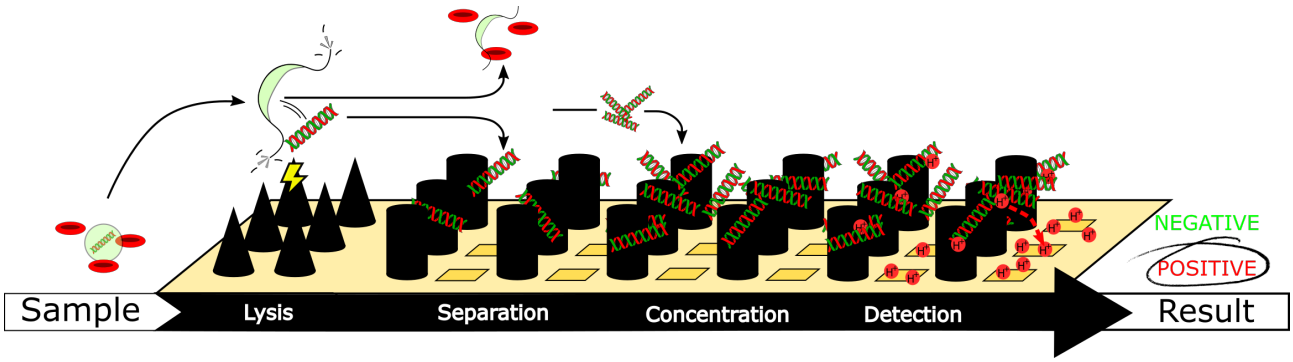


Figure 6.5: A schematic illustrating the sample-to-result pipeline envisaged in BUFFY.

could be replicated in carbon on CMOS to lyse cells electrically. Furthermore, the creation of electrodes with nanoscale features could provide the key to the electrokinetic trapping of DNA in high conductivity LAMP solutions.

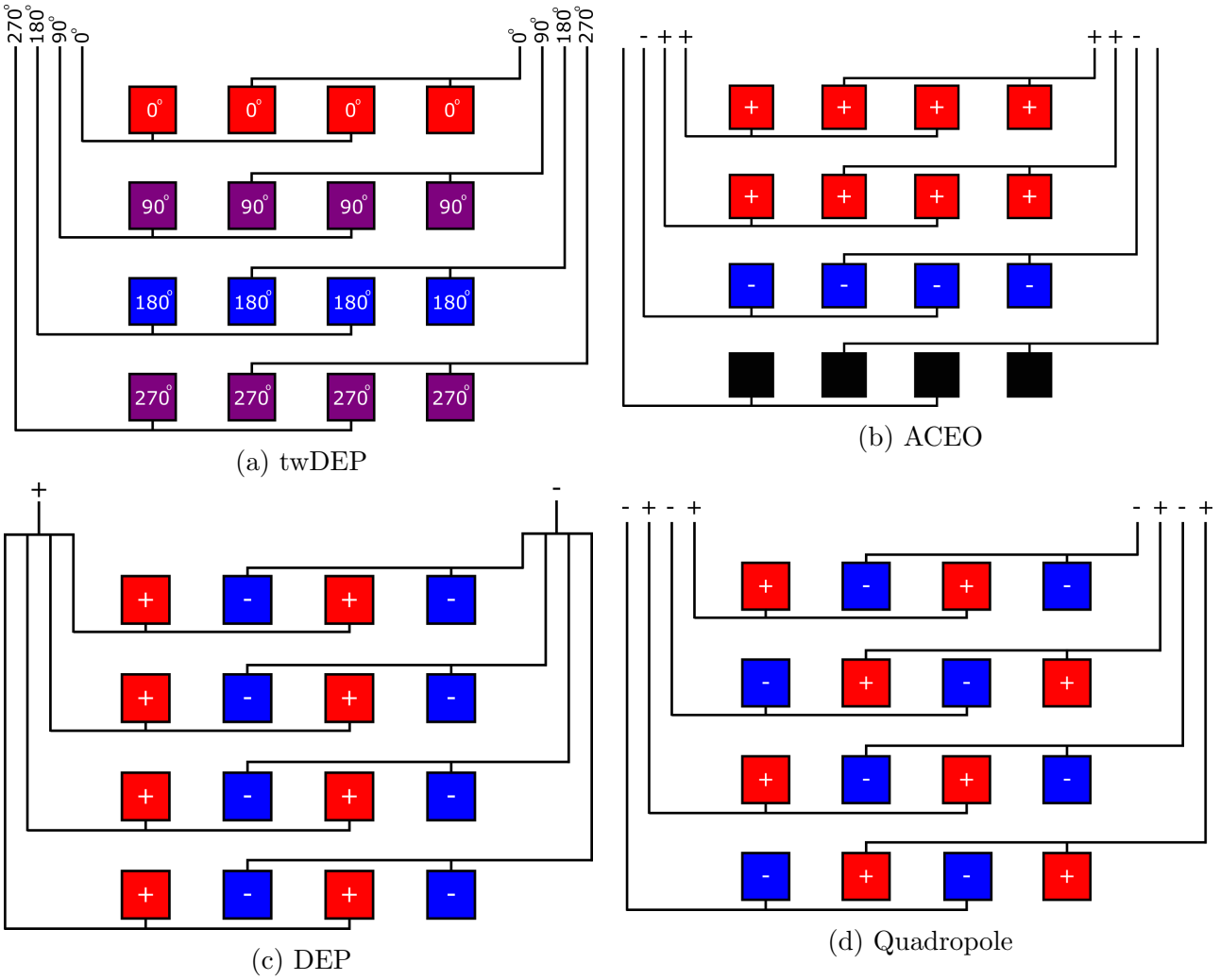
6.4 BUFFY: An Electrokinetic Lab-on-CMOS Diagnostic Device

Taking into account all the functionality discussed previously, it is possible that a single electrode array could be used to carry out:

- **Transport**: via twDEP or ACEO.
- **Mixing**: via ACEO.
- **Lysis**: via electric field-induced cell membrane breakdown.
- **Concentration**: via pDEP.
- **Purification**: separation of DNA and cellular material via pDEP and nDEP respectively.
- **Sensing**: Impedance sensing with a 3-electrode set-up.

This is summarised in Figure 6.5. An array of 3D carbon electrodes sitting on bond-pads will be able to carry out these functions effectively. Reconfigurable polarisation patterns can be implemented as part of the CMOS IC to induce different electrokinetic effects.

The design of BUFFY is made more complex with the incompatibility of high AC voltages with CMOS transistors, which define the voltage limits of a microchip. With switches, the reconfiguration of electrode polarisations to conduct different stages of sample preparation is straightforward, requiring MCU control of row and column decoders via a SPI. Specialised high



(a) twDEP

(b) ACEO

(c) DEP

(d) Quadropole

Figure 6.6: A schematic illustrating the planned electrode polarisations and the electrokinetic effects for which they are used.

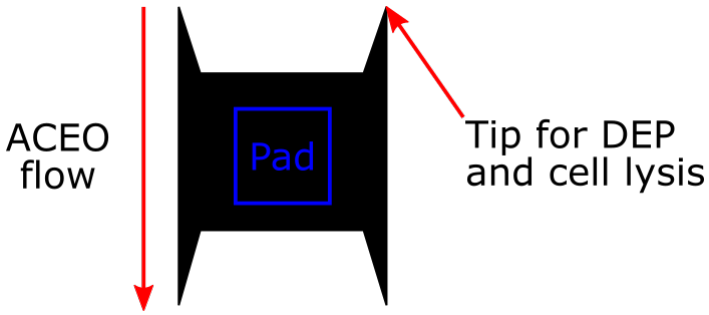


Figure 6.7: An illustration of the square pillar electrode design imagined for the BUFFY microchip.

voltage CMOS processes could be used to permit the use of CMOS-based switches, but this is sub-optimal for the design of the sensing circuits. Instead, switches can be omitted from the design, with electrode polarisation patterns 'hard-wired'. Drawbacks of this approach include limits on the number of connections that can be made, an increase in the number of input pads, and polarisation control being moved off-chip. Furthermore, to incorporate the negative portions of the AC voltages, the electrokinetic input lines will not be able to have electrostatic discharge (ESD) protection, leaving the chip vulnerable.

The four proposed polarisation schemes, illustrated in Figure 6.6, require eight connections in total, with a repeating 4×2 electrode array. twDEP needs four polarisations across four neighbouring rows of electrodes with 0^o, 90^o, 180^o, and 270^o phase-shifted sinusoidal signals. Sample transport could also be conducted using ACEO pumping, which requires asymmetric electrode sizes. In this case, two electrodes are grouped with one polarisation, leaving one in the opposite polarity and the remaining electrode floating. The electrode polarities could be reversed to change the direction of pumping, as in Loucaides *et al.* 2012 [28]. A checkerboard polarity for electric quadropoles can also be implemented to separate DNA and cells as in Sonnenberg *et al.* 2012 [14]. For trapping DNA from a fluid flow, alternating rows or columns can be polarised positively and negatively, similar to the pattern used in Martinez Duarte *et al.* 2013 [24]. Finally, for cellular lysis, all electrodes will be provided with a DC voltage pulse.

The electrodes will be fabricated using the 2PP approach developed by Haque *et al.*. These carbon electrodes will take the form of square pillars, modified with a sharp tip running down the vertices, as depicted in Figure 6.7. Such a geometry provides a flat electrode surface for efficient ACEO flow whilst also containing a tip capable of producing sufficiently intense electric fields to lyse cells, as well as strong DEP trapping. The bare *Al* pads reside below the level of the passivation and this may block the exposure of resists within this region. If this is the case, ENIG processing of the pads can be carried out to extend the electrodes above the passivation layer, on top of which the electrodes can be fabricated. If cellular lysis cannot be conducted by the square pillar electrodes, then a separate, specialised electrode system is required. To allow

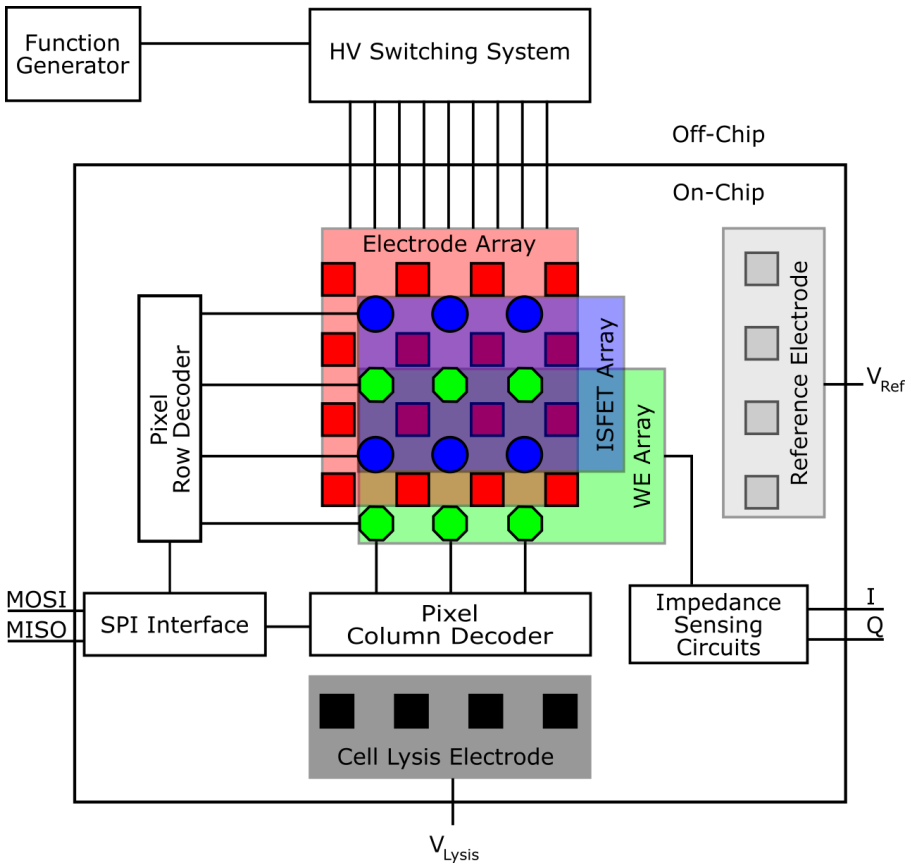


Figure 6.8: A system-level illustration of the planned BUFFY chip.

for this eventuality, another row of bond-pads will be provided to create a carbon nanospike structure akin to that used in Riaz *et al.* 2017 [12].

The carbon pillars themselves will act as the CEs of the impedance sensing system. The WEs will take the form of ENIG-plated pads, which will be connected to impedance sensing circuits. ENIG-plated pads functionalised with probes have previously been used for CMOS-based impedance detection of DNA in Manickam *et al.* 2010. The impedance system will output in-phase, I, and in-quadrature, Q, signals that can be used to determine impedance magnitude and phase. The pixel selected for output, in both the impedance and ISFET systems, will be controlled by row and column decoders and a SPI, which is possible as the high-voltage input will not run through these circuits.

$Ag/AgCl$ bond-pads will be created to provide the reference potential needed for both ISFET and impedance sensing systems. These will be fabricated using the process that was introduced in Chapter 5, but with Ag plating carried out using AutocatSilver AB's autocatalytic Ag solution. The polymer precursors of the carbon electrodes could be utilised to protect the pads from the electroplating process, before then being pyrolysed to form conducting carbon structures.



(a) Before (b) During

Figure 6.9: Fluorescence microscope images of an ENIG-plated bond-pad before (**a**) and during (**b**) the application of a $2\,V$, $500\,Hz$ electric field, trapping $400\,pM$ YOYO-1-dyed $\lambda-$DNA.

6.5 DNA DEP Using ENIG-Plated Bond-pads

The ability to conduct DEP of DNA using standard CMOS bond-pads was tested using the DAPPER microchip. The bond-pads were ENIG plated through the process developed in Chapter 5 to ensure electrochemical stability. The experimental set-up from Chapter 4 was used for fluorescence microscopy of YOYO-dyed λ-DNA. The RE pad of DAPPER was connected to a $2\,V$, $500\,Hz$ signal, with the ISE and WE pads receiving a 180^o phase-shifted signal.

High fluorescence intensity at the corners of the bond-pad with the voltage applied, as can be seen in Figure 6.9, indicated that DEP trapping of DNA was successful. This is the first demonstration of DEP using the standard bond-pads of a commercial CMOS process and supports the use of an array of pad-based electrodes to form an electrokinetic sample preparation system. After the electric field was turned off, DNA drifted away from the electrode, apart from in places around the edge of the WE, suggesting imperfections in the Au coating. The increase in DNA concentration at the electrode edges is less pronounced when compared with that achieved by the electrode systems in Chapter 4. This is due to the profile of the ENIG-plated electrode, which is thicker and with more rounded edges, causing a decrease in electric field strength. Reducing the thickness of the ENIG-plated layer is a straightforward way to improve trapping efficiency.

6.6 Summary

In this chapter, the concept for an electrokinetic sample-to-result lab-on-CMOS diagnostic device was developed. By surveying the literature for examples of electrode-based sample preparation, key functionality was established. As part of this survey, the opportunity to fabricate 3D carbon electrodes on CMOS for the first time was identified, with the intention of producing a 3D carbon electrode array based on bond-pads to perform electrokinetic sample preparation.

Bringing these aspects together, the design for a prototype microchip, named BUFFY, was outlined. The concept was given further credence by the first experimental observation of DEP trapping using the ENIG-plated bond-pads of a commercial CMOS process.

Bibliography

[1] D. Ma, S. S. Ghoreishizadeh, and P. Georgiou. "Concurrent Potentiometric and Amperometric Sensing With Shared Reference Electrodes". In: *IEEE Sensors Journal* 21.5 (2021), pp. 5720–5727.

[2] Z. Wang. "A Dual-Sensing CMOS Array for Combined Impedance-pH Detection of DNA with Integrated Electric Field Manipulation". MA thesis. Imperial College London, 2020.

[3] G. Medoro et al. "CMOS-only sensors and manipulators for microorganisms". In: *Technical Digest - International Electron Devices Meeting* (2000), pp. 415–418. ISSN: 01631918.

[4] N. Manaresi et al. "A CMOS Chip for Individual Cell Manipulation and Detection". In: *IEEE Journal of Solid-State Circuits* 38 (12 Dec. 2003), pp. 2297–2305. ISSN: 00189200.

[5] K. Park, S. Kabiri, and S. Sonkusale. "Dielectrophoretic lab-on-CMOS platform for trapping and manipulation of cells". In: (2016).

[6] K. Mohammad et al. "CMOS single cell dielectrophoresis cytometer". In: *Sensors and Actuators, B: Chemical* 249 (2017), pp. 246–255. ISSN: 09254005.

[7] J. Chung, Y. Chen, and S. J. Kim. "High-density impedance-sensing array on complementary metal-oxide-semiconductor circuitry assisted by negative dielectrophoresis for single-cell-resolution measurement". In: *Sensors and Actuators B: Chemical* 266 (Aug. 2018), pp. 106–114. ISSN: 0925-4005.

[8] T. Mitsunaka et al. "CMOS biosensor IC with 360-sensing elements using 63-GHz LC-oscillator and DEP for label-free single-cell detection". In: *Asia-Pacific Microwave Conference Proceedings, APMC* 2018-November (Jan. 2019), pp. 243–245.

[9] Y. S. Chan et al. "A Traveling-Wave Dielectrophoresis Bio-Chip for Cell Manipulation in Standard CMOS Process". In: *IEEE Transactions on Circuits and Systems II: Express Briefs* 69 (3 Mar. 2022), pp. 1582–1586. ISSN: 15583791.

[10] J. Cheng et al. "Preparation and hybridization analysis of DNA/RNA from E. coli on microfabricated bioelectronic chips". In: *Nature Biotechnology* 16 (1998), pp. 541–6.

[11] S. K. Ameri, P. Singh, and S. Sonkusale. "Utilization of graphene electrode in transparent microwell arrays for high throughput cell trapping and lysis". In: *Biosensors and Bioelectronics* 61 (2014), pp. 625–630. ISSN: 0956-5663.

[12] K. Riaz et al. "Low-Cost Energy-Efficient 3-D Nano-Spikes-Based Electric Cell Lysis Chips". In: *Journal of Microelectromechanical Systems* 26.4 (2017), pp. 910–920. ISSN: 1057-7157.

[13] M. Punjiya et al. "CMOS microcavity arrays for single-cell electroporation and lysis". In: *Biosensors and Bioelectronics* 150 (Feb. 2020), p. 111931. ISSN: 0956-5663.

[14] A. Sonnenberg et al. "Dielectrophoretic isolation of DNA and nanoparticles from blood". In: *Electrophoresis* 33.16 (2012), pp. 2482–2490.

[15] C. L. Asbury and G. van den Engh. "Trapping of DNA in Nonuniform Oscillating Electric Fields". In: *Biophysical Journal* 74.2 (1998), pp. 1024–1030. ISSN: 0006-3495.

[16] T. Kawabata and M. Washizu. "Dielectrophoretic detection of molecular bindings". In: *IEEE Transactions on Industry Applications* 37.6 (2001), pp. 1625–1633. ISSN: 0093-9994.

[17] C. L. Asbury, A. H. Diercks, and G. van den Engh. "Trapping of DNA by dielectrophoresis". In: *Electrophoresis* 23.16 (2002), pp. 2658–2666.

[18] R. Holzel. "Single particle characterization and manipulation by opposite field dielectrophoresis". In: *Journal of Electrostatics* 56.4 (2002), pp. 435–447. ISSN: 0304-3886.

[19] D. J. Bakewell and H. Morgan. "Dielectrophoresis of DNA: time- and frequency-dependent collections on microelectrodes". In: *IEEE Transactions on NanoBioscience* 5.1 (2006), pp. 1–8. ISSN: 1536-1241.

[20] M. R. Bown and C. D. Meinhart. "AC electroosmotic flow in a DNA concentrator". In: *Microfluidics and Nanofluidics* 2.6 (2006), pp. 513–523. ISSN: 1613-4990.

[21] S. Tuukkanen et al. "Carbon Nanotubes as Electrodes for Dielectrophoresis of DNA". In: *Nano Letters* 6 (Aug. 2006), pp. 1339–43.

[22] J.-R. Du et al. "Long-range and superfast trapping of DNA molecules in an ac electrokinetic funnel". In: *Biomicrofluidics* 2.4 (2008), p. 044103.

[23] W.-H. Yeo et al. "Size-Specific Concentration of DNA to a Nanostructured Tip Using Dielectrophoresis and Capillary Action". In: *The Journal of Physical Chemistry B* 113.31 (2009), pp. 10849–10858.

[24] R. Martinez-Duarte et al. "Dielectrophoresis of lambda-DNA using 3D carbon electrodes". In: *Electrophoresis* 34.7 (2013), pp. 1113–1122.

[25] L. Velmanickam, I. T. Lima, and D. Nawarathna. "High Throughput and Low-Cost Detection of Short Nucleic Acid Biomarkers in Serum using Dielectrophoretic Biosensor". In: *2018 IEEE Research and Applications of Photonics In Defense Conference (RAPID).* 2018, pp. 1–3.

[26] Y. K. Suh and S. Kang. "A Review on Mixing in Microfluidics". In: *Micromachines 2010, Vol. 1, Pages 82-111* 1 (3 Sept. 2010), pp. 82–111. ISSN: 2072-666X.

[27] W. Y. Ng et al. "DC-biased AC-electroosmotic and AC-electrothermal flow mixing in microchannels". In: *Lab on a Chip* 9 (6 Mar. 2009), pp. 802–809. ISSN: 1473-0189.

[28] N. Loucaides, A. Ramos, and G. E. Georghiou. "Configurable AC electroosmotic pumping and mixing". In: *Microelectronic Engineering* 90 (Feb. 2012), pp. 47–50. ISSN: 01679317.

[29] Y. Okamoto et al. "On-Chip CMOS-MEMS-Based Electroosmotic Flow Micropump Integrated with High-Voltage Generator". In: *Journal of Microelectromechanical Systems* 29 (1 Feb. 2020), pp. 86–94. ISSN: 19410158.

[30] P. W. Yen et al. "A Low-Power CMOS Microfluidic Pump Based on Travelling-Wave Electroosmosis for Diluted Serum Pumping". In: *Scientific Reports 2019 9:1* 9 (1 Oct. 2019), pp. 1–8. ISSN: 2045-2322.

[31] Y. S. Chan et al. "A Traveling-Wave Dielectrophoresis Bio-Chip for Cell Manipulation in Standard CMOS Process". In: *IEEE Transactions on Circuits and Systems II: Express Briefs* 69 (3 Mar. 2022), pp. 1582–1586. ISSN: 15583791.

[32] C. Páez-Avilés et al. "Combined dielectrophoresis and impedance systems for bacteria analysis in microfluidic on-chip platforms". In: *Sensors (Switzerland)* 16 (9 Sept. 2016). ISSN: 14248220.

[33] L. Velmanickam et al. "Label free MicroRNA biomarker detection in serum samples for diagnosis applications at point-of care". In: *2019 IEEE Research and Applications of Photonics in Defense Conference, RAPID 2019 - Proceedings* (Aug. 2019).

[34] P. Pungetmongkol and T. Yamamoto. "Single-Molecule Detection of DNA in a Nanochannel by High-Field Strength-Assisted Electrical Impedance Spectroscopy". In: *Micromachines 2019, Vol. 10, Page 189* 10 (3 Mar. 2019), p. 189. ISSN: 2072-666X.

[35] F. Patolsky, A. Lichtenstein, and I. Willner. "Detection of single-base DNA mutations by enzyme-amplified electronic transduction". In: *Nature Biotechnology 2001 19:3* 19 (3 2001), pp. 253–257. ISSN: 1546-1696.

[36] F. Lucarelli, G. Marrazza, and M. Mascini. "Enzyme-based impedimetric detection of PCR products using oligonucleotide-modified screen-printed gold electrodes". In: *Biosensors and Bioelectronics* 20 (10 Apr. 2005), pp. 2001–2009. ISSN: 0956-5663.

[37] E. Salm et al. "Electrical detection of dsDNA and polymerase chain reaction amplification". In: *Biomedical microdevices* 13.6 (Dec. 2011), pp. 973–982. ISSN: 1387-2176.

[38] Z. Wang et al. "A Dual-Sensing CMOS Array for Combined Impedance-pH Detection of DNA with Integrated Electric Field Manipulation". In: *2021 IEEE International Symposium on Circuits and Systems (ISCAS)*. 2021, pp. 1–5.

[39] M. D. C. Jaramillo et al. "On-line separation of bacterial cells by carbon-electrode dielectrophoresis". In: *ELECTROPHORESIS* 31 (17 Sept. 2010), pp. 2921–2928. ISSN: 1522-2683.

[40] M. Islam et al. "Enrichment of diluted cell populations from large sample volumes using 3D carbon-electrode dielectrophoresis". In: *Biomicrofluidics* 10 (3 June 2016), p. 033107. ISSN: 19321058.

[41] Y. Yildizhan et al. "Dielectrophoretic Separation of Live and Dead Monocytes Using 3D Carbon-Electrodes". In: *Sensors 2017, Vol. 17, Page 2691* 17 (11 Nov. 2017), p. 2691. ISSN: 1424-8220.

[42] R. Martinez-Duarte. "Fabrication challenges and perspectives on the use of carbon-electrode dielectrophoresis in sample preparation". In: *IET Nanobiotechnology* 11 (2 Mar. 2017), pp. 127–133. ISSN: 1751-875X.

[43] M. A. Haque et al. "Carbonization of 3D printed polymer structures for CMOS-compatible electrochemical sensors". In: *Journal of Vacuum Science & Technology B* 38.5 (2020), p. 052203.

Chapter 7

Conclusion

Over the course of this thesis, the opportunities arising from the combination of on-CMOS microelectrode systems with an ISFET-based DNA detection platform have been explored. Three areas of improvement have been targeted: device ttp, RE integration, and sample preparation. Some of these opportunities, namely RE integration using an $Ag/AgCl$-plated bond-pad, have been realized, with the others shown to be plausible through CMOS-based electrokinetic trapping of DNA and supporting simulations.

Despite the lack of success when transferring the electrokinetic DNA trapping system to LAMP solutions in this thesis, it is still feasible with modifications to the electrode design. Indeed, it was the shortcomings of the FRY microchip that proved pivotal in forming the idea of using ENIG-plated bond-pads for electrokinetic trapping. In turn, the surface processing required for this inspired the creation of the $AgCl$ RE bond-pad.

Whilst opening up the underlying IC to the electrolyte is a potentially fraught process, by increasing the interaction between CMOS circuitry and the test sample, powerful capabilities in sensing and sample preparation can be added. The multiple facets of this thesis have come together in the vision for the BUFFY electrokinetic lab-on-CMOS, which defines the path ahead for on-CMOS microelectrode systems.

7.1 Contributions

Chapter 3: Spatio-Temporal Simulation of ISFET-based DNA Detection

In this chapter, proton diffusion was incorporated within an existing LAMP reaction model so that the effects of DNA positioning on ISFET detection could be estimated. A novel Monte-Carlo simulation based on the first-passage distribution was developed that showed

good agreement with a random walk ground truth with run-times 3 orders of magnitude lower. This first-passage simulation estimated modest improvements in ttp with DNA trapped at the ISFET sensing surface. A FEM model based on the level-set method was also created that has the potential to simulate many of the phenomena that form the DNA amplification and ISFET detection mechanisms.

Chapter 3: Original contributions to the field

1. The first random walk simulation for ISFET sensing.
2. The first Monte-Carlo first-passage simulation for electrochemical sensing.
3. The first level-set simulation for electrochemical sensing.

Chapter 4: Electrokinetic Manipulation of DNA to Enhance ISFET-based Detection

In this chapter, on-chip electrode systems were developed for electrokinetic trapping of DNA. IDEs fabricated on the surface of an ISFET array through photolithography conducted the first example of both DEP and ACEO trapping of DNA on-CMOS. Trapping was successful at low solution conductivity, but was not observed in high-conductivity LAMP reaction solutions and is yet to be demonstrated. To better integrate the DNA trapping and ISFET sensing systems, a microchip was designed that attempted to trap DNA using CMOS top-metal for the first time, with successful trapping unable to be confirmed.

Chapter 4: Original contributions to the field

1. The first example of on-CMOS DEP and ACEO trapping of DNA.
2. The first use of a one-sided sawtooth electrode for electrokinetic trapping.
3. The first attempt to use CMOS top-metal for electrokinetic DNA trapping.
4. The first attempt to conduct electrokinetic DNA trapping in LAMP reaction solutions.

Chapter 5: An Electroplated *Ag/AgCl* Reference Electrode based on CMOS Top-Metal

In this chapter, an on-chip $Ag/AgCl$ QRE was fabricated using CMOS top-metal bond-pads as a base of a fully electroplated process. The bond-pad RE is the first of its kind and was shown to produce a reference potential with a comparable stability to those in the literature.

Chapter 5: Original contributions to the field

1. The first $Ag/AgCl$ QRE based on an electroplated bond-pad of a commercial CMOS process.
2. The first demonstration of an on-CMOS, electroplated bond-pad three-electrode system.

Chapter 6: Conceptualisation of an Electrokinetic Lab-on-CMOS Diagnostic Device

In this chapter, the concept for the first electrokinetic lab-on-CMOS diagnostic device was proposed, combining sample preparation, performed by 3D carbon electrodes on a bond-pad array, with pH-impedance target detection. To support this approach, the first demonstration of electrokinetic DNA trapping using CMOS bond-pads, which were ENIG-plated, was conducted.

Chapter 6: Original contributions to the field

1. The concept for the first electrokinetic lab-on-CMOS diagnostic device.
2. The first demonstration of electrokinetic trapping using standard CMOS bond-pads.

7.2 Recommendations for Future Work

A future vision at the end of each chapter charted the road ahead for each research area. The work required to achieve these visions is summarised in this section.

7.2.1 Amplification Model and Hotspot Validation

A key requirement to validate the amplification model developed by Dr. Moniri and which forms the basis of the simulations in Chapter 3 is to experimentally observe the formation and growth of DNA clusters. This could be achieved by using a microfluidic system or electrokinetic trapping to provide a defined starting point for cluster growth. Fluorescence microscopy could be used to determine the existence of DNA clusters before confirming their presence on an ISFET array. After proving DNA behaves as modelled during LAMP reactions, efforts to apply the hotspots technique to real-time ISFET array data and improve diagnostic performance can begin.

7.2.2 Electrokinetic DNA trapping in LAMP Solutions

Electrokinetic trapping of DNA in high conductivity solutions, such as LAMP reaction solutions, is required to realise the full sample preparation functionality of the conceptual BUFFY lab-on-CMOS as well as the improvement in ISFET-based DNA detection predicted in Chapter 3 and sought in Chapter 4. The best approaches to achieve this involve the development of low-conductivity LAMP reaction solutions, redesign of electrodes to maximise field gradients, and the use of more electrochemically stable electrode materials. Electrode coatings, such as hydrogels and oxides, could assist in avoiding electrode dissolution, but would increase manufacturing complexity. Higher voltages may ultimately be required for electrokinetic trapping in LAMP solutions, but for the sake of CMOS-compatibility, this should be a last resort. However, no approach should be taken off the table to achieve electrokinetic trapping.

7.2.3 On-CMOS 3D Carbon Electrode Fabrication for Electrokinetics

Successful fabrication of 3D carbon electrodes on-CMOS through 2PP is fundamental to the creation of the BUFFY lab-on-CMOS. As a first step, the ability of a 3D carbon electrode array, fabricated through the process laid out in Haque *et al.* 2020, to conduct the various electrokinetic interactions required for sample preparation must be confirmed off-chip. These experiments can be carried out one-by-one, with individual electrode arrays specialised for a single electrokinetic effect, before eventually being combined into one design that is capable of all steps. Then, this design will be produced on-CMOS, with the survival of the chip after the fabrication process to be verified.

7.2.4 Standard CMOS-Compatible High-Voltage Electrokinetics

The ability to conduct all stages of sample preparation on-CMOS may be dependent on the use of higher voltages than the tolerance limits of the microchip. The implementation of high-voltage AC electrokinetics through the use of hard-wired, transistor-free IC connections to electrodes must be tested on a small scale, to ascertain what is possible with standard CMOS processes. These tests may indicate that specialised, high-voltage CMOS is required for BUFFY. On the other hand, if it is found that the electrokinetics can be performed at CMOS-compatible voltages, then the added functionality that can incorporated into the electrokinetic system due to combination with CMOS IC is immense.

7.2.5 Fabrication of Full Sample-to-Result Electrokinetic Lab-on-CMOS

BUFFY will combine multiple electrode systems with varying fabrication processes. A key obstacle in fabrication of the final chip is the compatibility of the different post-processing steps. Many tests of the full BUFFY post-processing will have to be run to determine the optimum order of steps. Compromises in functionality may have to be made for the sake of manufacture.

Appendix A

Publications Arising from this Thesis

A. Jaccottet, P. Feng, K. Szostak-Lipowicz, **L. Keeble**, T. Constandinou, 'Towards a wireless micropackaged implant with hermeticity monitoring', Proceedings BioCAS, 2022, pp 500-504

Z. Wang, **L. Keeble** *et al.*, '*A Dual-sensing CMOS Array for Combined Impedance-pH Detection of DNA with Integrated Electric Field Manipulation*', Proceedings IEEE ISCAS, 2021, pp 1-5

L. Keeble *et al.*, '*A Combined ISFET-Electric Field Actuation System for Enhanced Detection of DNA: A Proof-of-Concept*', Proceedings IEEE ISCAS, 2020

L. Keeble *et al.*, '*ISFET-Based Sensing and Electric Field Actuation of DNA for On-Chip Detection: A Review*', IEEE Sensor Journal, 2020, Vol. 20, Iss. 19

N. Moser, **L. Keeble** *et al.*, '*ISFET arrays for lab-on-chip technology: A review*', Proceedings IEEE ICECS, 2019, pp 57-60

Appendix B

GitHub Repository

All code and data used in this thesis will be made available at the GitHub repository, github.com/LewisKeeb
This will include:

- MATLAB code for the random walk simulation of ISFET-based DNA detection.
- MATLAB code for the first-passage simulation of ISFET-based DNA detection.
- MATLAB code for the initialisation of the level-set simulation in COMSOL Multiphysics 5.5 (Requires MATLAB Livelink).
- MATLAB code for the post-processing and extraction of data from the level-set simulation in COMSOL Multiphysics 5.5 (Requires MATLAB Livelink).
- MATLAB code for the initialisation of the 1D stationary surface site concentration simulation (Requires MATLAB Livelink).
- Data and MATLAB post-processing code for all simulations.
- Data and MATLAB post-processing code for all experiments.

Appendix C

Supplementary Data for Section 3.7.2

Full-scale simulations were carried out with both reflecting and absorbing boundaries and then compared to experimental output to determine which type of boundary performed better. The 1×10^3 copy number experiments were chosen for comparison to reduce simulation times. In the simulations, A scaling factor was applied to the number of protons detected by the ISFETs so that the total number of protons released over the course of the reaction matched the experimentally observed pH change, to account for stochasticity.

The shape of the signals in Fig. C.1 indicate that reflecting boundary conditions better mimic the temporal response of experimental data. Absorbing boundaries have a signal that saturates sooner and more abruptly. The final voltages at saturation are $13.2mV$ and $39.4mV$ for absorbing and reflecting boundaries respectively. When compared to the final experimental voltage of 15.6mV, this points towards absorbing boundaries being better suited. However, this must be balanced with the discrepancies between the first-passage and random walk models showing an overestimation of around double for the absorbing boundaries.

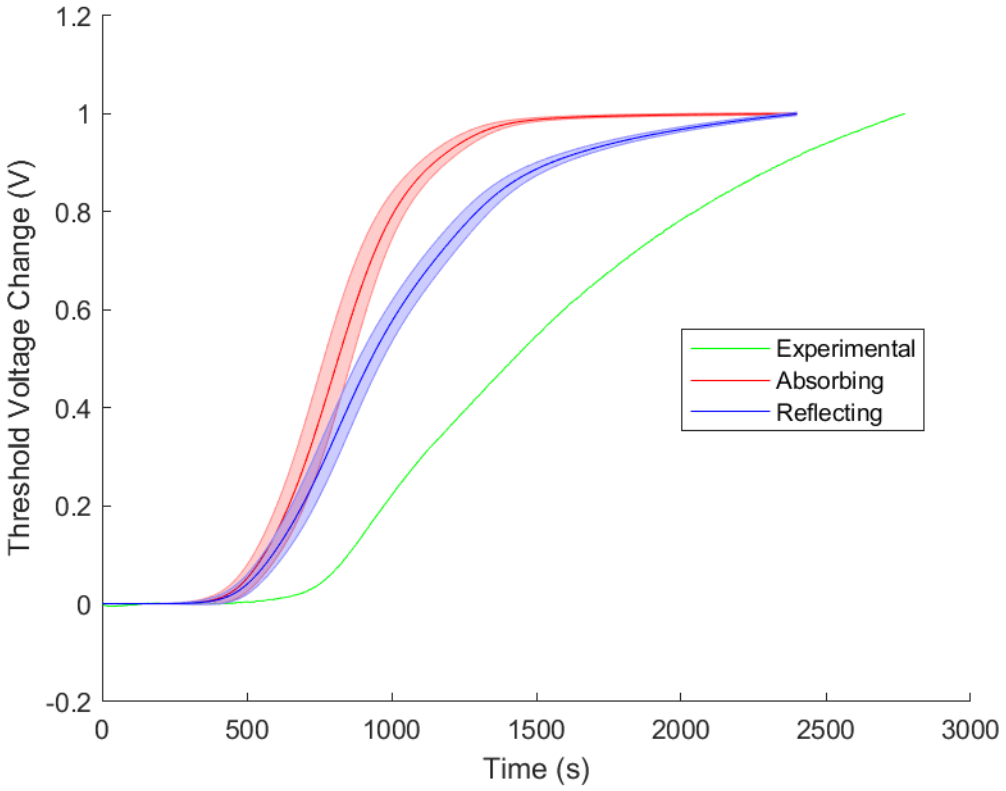


Figure C.1: A comparison of first passage simulations with absorbing (red) and reflecting (blue) boundary conditions with experimental results (green). 1×10^3 DNA copies were used.

Appendix D

Supplementary Data for Section 4.4.3

The following section provides supporting figures for observations of electrokinetic DNA trapping using photolithographically fabricated on-CMOS electrodes in section 4.4.3. The figures show fluorescence microscope images of $400pM$ YOYO-dyed $\lambda-$DNA. The applied voltages are stated in the captions. DNA is shown to be concentrated at the centre of the electrode.

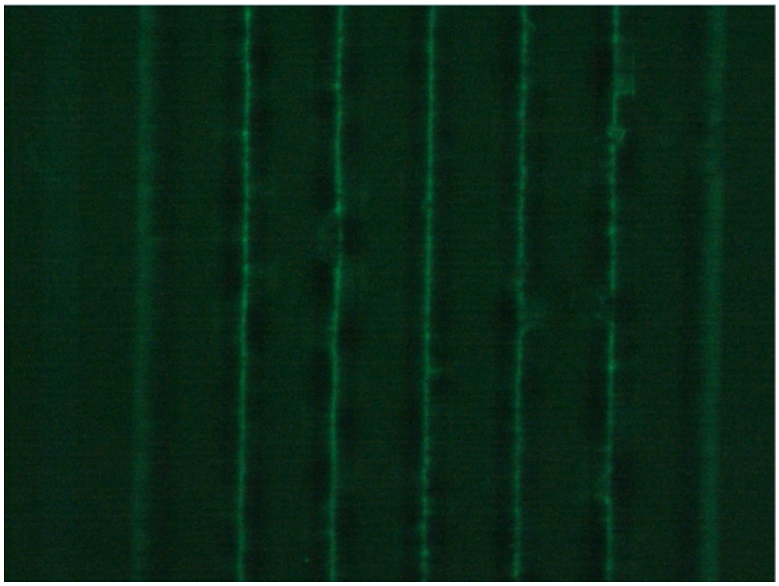


Figure D.1: Fluorescence microscope image of line electrodes with a 4V, 10kHz electric field applied, trapping 400pM YOYO-1-dyed $\lambda-$DNA.

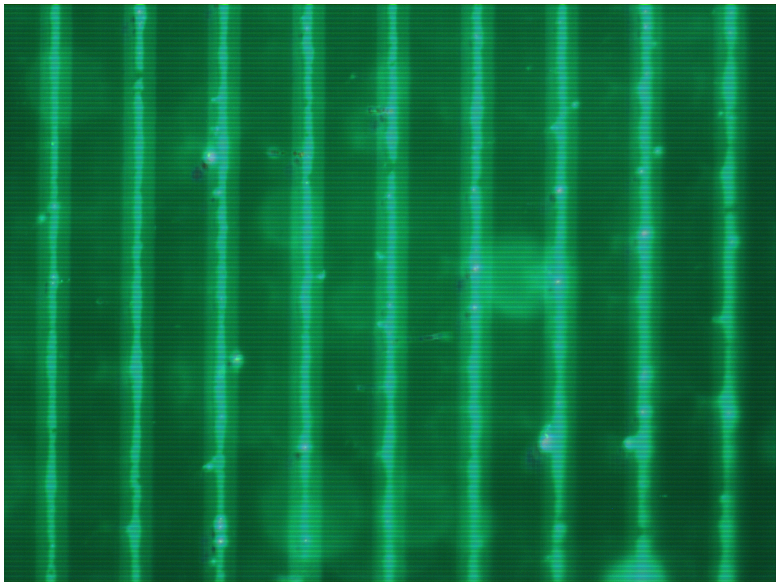


Figure D.2: Fluorescence microscope image of line electrodes with a 500Hz electric field applied, trapping 400pM YOYO-1-dyed $\lambda-$DNA and an applied voltage of $900mV_{pp}$ with a 900mV offset (varying from 0-1.8V).

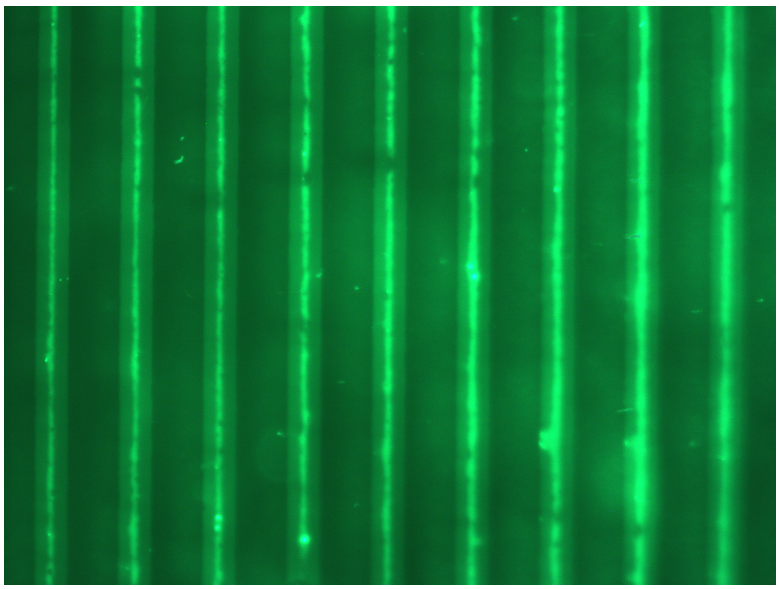


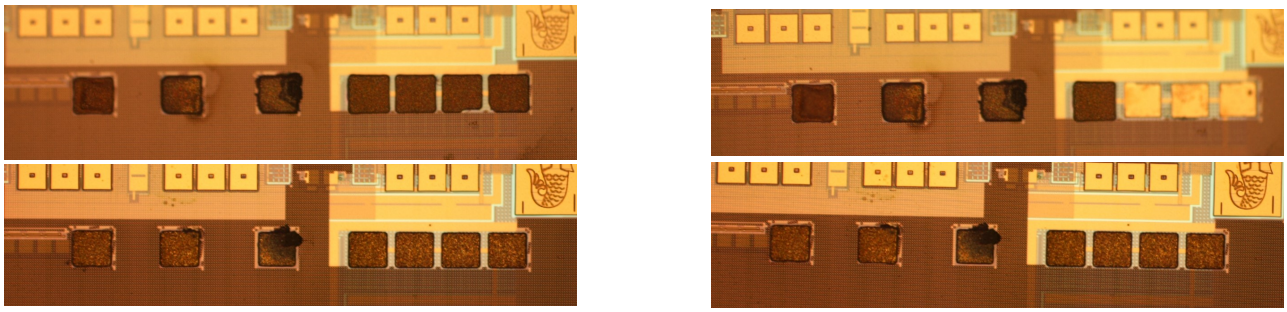
Figure D.3: Fluorescence microscope image of line electrodes with a 500Hz electric field applied, trapping 400pM YOYO-1-dyed $\lambda-$DNA and an applied voltage of $1.8V_{pp}$.

Appendix E

Supplementary Data for Section 5.4.1

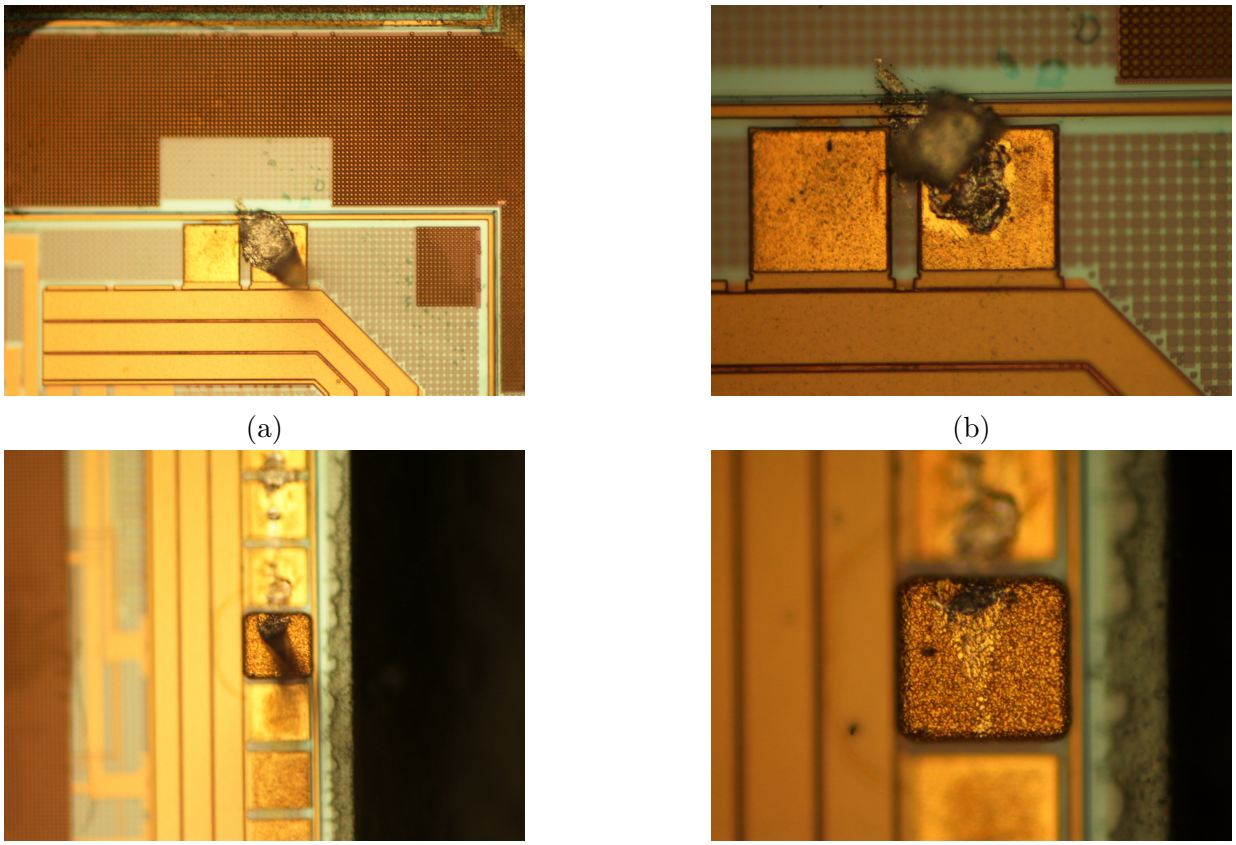
The following section provides further observations and figures for the adhesion tests of the ENIG-plated bond-pads in section 5.4.1.

It is notable that there is an inconsistency in the plating thickness between different pads on the same chip, with some having a profile above the passivation and some remaining beneath the top of the passivation. More reliable bonding performance was achieved with the smoother, non-bumped pads as compared to the bumped pads, where the ENIG layer sometimes delaminated when bonding was attempted. Reduced plating thicknesses are likely linked to higher electrode impedances.



(a) Before (b) After

Figure E.1: Microscope images of two tape tests with (a) before and (b) after.



(a) (b)

(c) Before (d) After

Figure E.2: Microscope images of ENIG plated pads with bonded wires, and after these wires have been pulled, causing bond failure. (b) shows the bond wire breaking after being pulled. (c) shows delamination between the bonded wire and the Au surface.